

AD-A237 057



RL-TR-1991-156, Vol II (of two)
In-House Report
April 1991



PROCEEDINGS OF THE 1990 ANTENNA APPLICATIONS SYMPOSIUM

Paul Mayes, et al.



Sponsored by
DIRECTORATE OF ELECTROMAGNETICS
ROME LABORATORY
HANSCOM AIR FORCE BASE
AIR FORCE SYSTEMS COMMAND

APPROVED FOR PUBLIC RELEASE; DISTRIBUTION UNLIMITED.

91-02500



Rome Laboratory
Air Force Systems Command
Griffiss Air Force Base, NY 13441-5700

This report has been reviewed by the Rome Laboratory Public Affairs Division (PA) and is releasable to the National Technical Information Service (NTIS). At NTIS it will be releasable to the general public, including foreign nations.

RL-TR-91-156, Volume II (of two) has been reviewed and is approved for publication.

APPROVED:



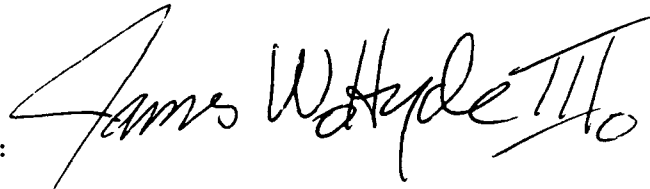
ROBERT J. MAILLOUX
Chief, Antennas & Components Division
Directorate of Electromagnetics

APPROVED:



JOHN K. SCHINDLER
Director of Electromagnetics

FOR THE COMMANDER:



JAMES W. HYDE III
Directorate of Plans & Programs

If your address has changed or if you wish to be removed from the Rome Laboratory mailing list, or if the addressee is no longer employed by your organization, please notify Rome Laboratory (EEAS) Hanscom AFB MA 01731-5000. This will assist us in maintaining a current mailing list.

Do not return copies of this report unless contractual obligations or notices on a specific document require that it be returned.

REPORT DOCUMENTATION PAGE

Form Approved
OMB No. 0704-0188

Public reporting burden for this collection of information is estimated to average 1 hour per response, including the time for reviewing instructions, searching existing data sources, gathering and maintaining the data needed, and completing and reviewing the collection of information. Send comments regarding this burden estimate or any other aspect of this collection of information, including suggestions for reducing this burden, to Washington Headquarters Services, Directorate for Information Operations and Reports, 1215 Jefferson Davis Highway, Suite 1204, Arlington, VA 22202-4302, and to the Office of Management and Budget, Paperwork Reduction Project (0704-0188), Washington, DC 20503

1. AGENCY USE ONLY (Leave blank)	2. REPORT DATE April 1991	3. REPORT TYPE AND DATES COVERED Scientific Interim Volume II	
4. TITLE AND SUBTITLE Proceedings of the 1990 Antenna Applications Symposium		5. FUNDING NUMBERS PE 62702F PR 4600 TA 14 WU PE	
6. AUTHOR(S) Paul Mayes, et al		8. PERFORMING ORGANIZATION REPORT NUMBER RL-TR-91-156 (II)	
7. PERFORMING ORGANIZATION NAME(S) AND ADDRESS(ES) Rome Laboratory Hanscom AFB, MA 01731-5000 Project Engineer: John Antonucci/EEAS			
9. SPONSORING / MONITORING AGENCY NAME(S) AND ADDRESS(ES)		10. SPONSORING / MONITORING AGENCY REPORT NUMBER	
11. SUPPLEMENTARY NOTES Volume I consists of pages 1 - 296; Volume II consists of pages 297 - 573			
12a. DISTRIBUTION / AVAILABILITY STATEMENT Approved for public release; distribution unlimited		12b. DISTRIBUTION CODE	
13. ABSTRACT (Maximum 200 words) The Proceedings of the 1990 Antenna Applications Symposium is a collection of state-of-the-art papers relating to phased array antennas, multibeam antennas, satellite antennas, microstrip antennas, reflector antennas, HF, VHF, UHF and various other antennas.			
14. SUBJECT TERMS Antennas Satellite antennas Broadband antennas		Microstrip Reflector HF, VHF, UHF	Multibeam antennas Array antennas
		15. NUMBER OF PAGES 284	
		16. PRICE CODE	
17. SECURITY CLASSIFICATION OF REPORT Unclassified	18. SECURITY CLASSIFICATION OF THIS PAGE Unclassified	19. SECURITY CLASSIFICATION OF ABSTRACT Unclassified	20. LIMITATION OF ABSTRACT SAR

Accession For	
NTIS GRA&I	<input checked="" type="checkbox"/>
DTIC TAB	<input type="checkbox"/>
Unannounced	<input type="checkbox"/>
Justification _____	
By _____	
Distribution/	
Availability Codes	
Dist	Avail and/or Special
A-1	



Contents

WEDNESDAY, SEPTEMBER 26, 1990

OVER-THE-HORIZON RADAR

- * **Keynote: "HF Antennas: Application to OTH Radars," J. Leon Poirier**
1. "A Thinned High Frequency Linear Antenna Array to Study Ionospheric Structure" by Anthony J. Gould, Capt, USAF 1
 2. "Coherence of HF Skywave Propagation Wavefronts," by John B. Morris and James R. Barnum 41
 3. "Adaptive Nulling of Transient Atmospheric Noise Received by an HF Antenna Array," by Dean O. Carhoun 61
 4. "Near End Fire Effects in a Large, Planar, Random Array of Monopoles," by R. J. Richards 77
 5. "Antenna Designs for the AN/FPS-118 OTH Radar," by K. John Scott 107

Contents

ARRAYS

6. "Phased Array Calibration by Adaptive Nulling," by Herbert M. Aumann and Frank G. Willwerth 131
7. "Applications of Self-Steered Phased Arrays," by Dean A. Paschen 153
8. "Array Thinning Using the Image Element Antenna," by Joe Kobus, Robert Shillingburg and Ron Kielmeyer 172
9. "Distributed Beamsteering Control of Monolithic Phased Arrays," by S. F. Nati, G. T. Cokinos and D. K. Lewis 202
10. "Analysis of Edge Effects in Finite Phased Array Antennas," by Steven M. Wright 217
11. "Multimode Performance From a Single Slotted Array Antenna," by John Cross, Don Collier and Len Goldstone 244
12. "An Adaptive Array Using Reference Signal Extraction," by Jian-Ren E. Wang and Donald R. Ucci 261

THURSDAY, SEPTEMBER 27, 1990

SHF/EHF ANTENNAS

13. "Optically Linked SHF Antenna Array," by Salvatore L. Carollo, Anthony M. Greci and Richard N. Smith 275
14. "A Modularized Antenna Concept for a Ku-Band Ferrite Phased Array," by F. Lauriente, A. Evenson and M. J. Kiss 297
15. "A Matrix Feed Beam Steering Controller for Monolithic EHF Phased Array Systems," by G. T. Wells, S. T. Salvage and S. R. Oliver 322
16. "Omnidirectional Ku-Band Data Link Antenna Design," by F. Hsu and A. J. Lockyer 353
17. "A Retrospective on Antenna Design via Waveguide Modes," by K. C. Kelly 372
- * 18. "Conformal Microstrip Antennas," by M. Oberhart and Y. T. Lo
19. "A Dual Polarized Horn With a Scanning Beam," by Zvi Frank 396

* NOT INCLUDED IN THIS VOLUME

Contents

ANTENNA ELEMENTS

- 20. "Multi-Octave Microstrip Antennas," by Victor K. Tripp and Johnson J. H. Wang 414
- 21. "External Lens Loading of Cavity-Backed Spiral Antennas for Improved Performance," by George J. Monser 444
- 22. "A Compact Broadband Antenna," by Sam C. Kuo and Warren Shelton 457
- 23. "Reduced Profile Log Periodic Dipole Antenna Designed for Compact Storage and Self Deployment," by G. D. Fenner, J. Rivera and P. G. Ingerson 486
- 24. "A Printed Circuit Log Periodic Dipole Antenna With an Improved Stripline Feed Technique," by Jeffrey A. Johnson 504
- 25. "Half Wave "V" Dipole Antenna," by Valentin Trainotti 512

FRIDAY, SEPTEMBER 28, 1990

ANALYSIS AND PROCESSING

- 26. "Compact Highly Integrated Dual Linear Antenna Feed," by Joseph A. Smolko, Daniel M. Earley, Daniel J. Lawrence and Michael J. Virostko 538
- 27. "Shaped Beam Design With a Limited Sized Aperture," by F. Rahman 552
- 28. "Adaptive Algorithms for Energy Density Antennas in Scattering Environments," by James P. Phillips and Donald Ucci 558
- * 29. "Finding the Sources of Momentary HF Signals From a Single Site," by A. F. L. Rocke

* NOT INCLUDED IN THIS VOLUME

A MODULARIZED ANTENNA CONCEPT

FOR A

KU-BAND FERRITE PHASED ARRAY

**F. Lauriente and A. Evenson,
Microwave Applications Group, Inc.
Santa Maria, CA**

and

**M.J. Kiss
Martin Marietta Corp.
Orlando, FL**

ABSTRACT

A modularized antenna concept for a two-axis scanning, polarization diverse, Ku-Band ferrite phased array is presented. The design concept is predicated upon a module of the array being a basic building block which is replaceable at the depot-level in order to effect a reduction in life-cycle antenna cost.

The array design centers upon a novel modular concept whereby, the array aperture is divided into a number of modules containing two rows of approximately 80 elements each. The design of the driver circuitry for control of the ferrite phase shifters and polarization switch provides provision for storage of collimation data thereby making each module independent and permitting module interchangeability without recollimation of the array. This feature represents a significant improvement in maintainability of electronically scanned phased arrays, since a module can be replaced at the depot level and the antenna returned to service with no further adjustments.

Polarization diversity and independent control over the sum and difference mode distributions are incorporated into the design. Two array modules were designed, fabricated and tested in order to validate the design concept.

© Martin Marietta, 1990

297

1.0 Introduction

In a conventional two-axis ferrite phased array architecture; each phase shifter is usually fitted with its own individual driver prior to installation in the antenna. The drivers are arranged to plug into a circuit board carrying power and command signals to each phase control element. In a large array of several thousand elements, a complex multi-layer board consisting of several shielded layers is normally needed. Hence the antenna assembly and integration task becomes very complicated and costly.

An alternate array architecture for use in the next generation ferrite phased arrays is a modular design concept (1) as depicted in Figure 1. In this approach; multi-channel drivers and collimation memory components are mounted on a circuit board and integrated with the phase shifters and RF distribution manifold into a module which accommodates two rows (or columns) of the antenna. The advantages of this approach are increased reliability, maintainability, and reduced life-cycle costs.

An array module for use in a polarization diverse, two-axis electronically scanned phased array was designed, fabricated and tested. The module design is fully form factored in accordance with array requirements listed in Table 1, and the physical layout of the full array shown in Figure 2. A full module consists of two rows of 80 elements each on an equilateral triangular grid. The 160 elements in each module consist of phase shifters integrated with polarization switch and radiating elements. The design philosophy, which is predicated on complete interchangeability within the array, requires that each module contain memory for the storage of

TABLE 1

ARRAY RF PERFORMANCE PARAMETERS

BEAMWIDTH	~ 1.3° @ f ₀
SCAN COVERAGE	± 45 DEGREES
GAIN VARIATION VS. SCAN ANGLE	LESS THAN 4dB RELATIVE TO BROADSIDE
BANDWIDTH OPERATING INSTANTANEOUS	1.0 GHz 320 MHz
BEAM SCAN VS. INSTANTANEOUS BANDWIDTH	MINIMUM
BEAM BROADENING	LESS THAN 0.2 DEGREE
POLARIZATION	VERTICAL LINEAR, RCP, LCP WITH 1.0dB AXIAL RATIO IN CP
SIDELOBE LEVELS	SUM: -30dB PEAK, -45dB AVERAGE DIFFERENCE: -25dB PEAK, -40dB AVERAGE
POWER HANDLING (MODULE LEVEL)	500 W AVERAGE, 7.5KW PEAK
VSWR	1.5 : 1
BEAM SWITCHING	60μsec @ 1KHz RATE

collimation data, phase shifter linearization tables, and polarization switch settings. Use of orthogonal product illumination functions and a rectangular aperture, permits the use of a single module design as a basic building block. In fact, a single module itself consists of two identical halves assembled with one half rotated 180 degrees. A picture of a half module is shown in Figure 3 and an assembled module in the pattern test fixture shown in Figure 4. Two complete modules were fabricated and tested.

The sidelobe levels specified for the sum and difference modes and the requirement for minimum beam scan over the instantaneous bandwidth require a feed manifold with equal line lengths and independent control over the sum and difference mode excitations. While the overall array conceptual design is a result of a number of trade studies including thermal analysis, structural analysis, and architecture, this paper concentrates on the basic module design and test results. The array conceptual design studies may be presented in a later paper.

2.0 Array Module Design

2.1 General Considerations

The detail designs of the module are governed by the array performance requirements shown in Table 1, with the major design drivers being instantaneous bandwidth, sidelobe levels and polarization diversity. In order to provide sufficient performance margin in an array assembled from a number of modules, it was decided to design each module with a Taylor 35 db, $N = 4$ distribution for the sum and a Bayless 30 dB, N

- bar = 4 distribution for the difference.

2.2 Feed Network

The RF design of the module to be used as a basic building block in a phased array antenna centers around the use of a compact traveling wave feed network which feeds two rows of 80 elements each. Each element consists of a dual mode latching ferrite phase shifter with an integrated radiating element and latching polarization switch. Scan requirements dictate the need for an equilateral triangular lattice spacing of 0.472 inch on a side so that no grating lobes enter the visible region. Because of the small interelement spacing, ridge waveguide is required at the phase shifter inputs.

Independent control of the sum and difference distributions is obtained with a Lopez Feed (2), the schematic embodiment of which is shown in Figure 5. This is based upon the geometrical representation shown in Figure 6. The two contiguous 3-4-5 right triangles ensure that the path length from the input at the A-line or B-line to any of the radiating elements are equal. In the usual technique for equalizing the line lengths in a traveling wavefeed, where the main guide is at 45 degrees with respect to the array axis, the wide dimension of the coupled guides is foreshortened by a factor of $\sqrt{2}$. In this approach no such foreshortening occurs.

The feed consists of a series of cross-guide couplers connected in tandem, with the main waveguide being reduced height WR-62 guide. Adjacent elements are coupled from opposite sides of the main guide as shown in Figure 7. Well-matched loads in the isolated arm of each coupler provide

a low reflection termination of each element for good RCS characteristics. The primary line coupler values are chosen to produce the desired sum distribution and the secondary line values are chosen in conjunction with the primary couplers to produce the desired difference distribution.

Since the efficiency of the feed network is directly dependent on the maximum coupler value used in the primary and secondary lines, a trade-off study was made of efficiency versus maximum coupler value. Plotted in Figure 8 are the efficiencies of the sum and difference modes. Since it is desired to make the feed as efficient as possible, high coupling is desired. However, this presents severe design problems for the couplers in that it becomes very difficult to achieve tight coupling with minimal coupling variation with frequency and high directivity. Previous experience indicates that a reasonable compromise is to limit the maximum value of coupling to -12 dB. This then gives a sum mode efficiency of 97.9 percent and a difference mode efficiency of 97.4 percent.

A plot of the required secondary line coupler values is shown in Figure 9. As can be seen a sign reversal occurs in the coupler values near coupler number 50. Since implementation of the needed 180 degree phase shift would be difficult, it was decided to terminate the secondary line couplers after coupler number 48, where the required coupling value is about -28 dB. The effects of this are shown in the computed pattern of Figure 10.

2.3 Coupler Design

With the dimensions of the lattice geometry and other mechanical

constraints in mind, the waveguide configuration shown in Figure 11 was chosen for realization of the couplers. Coupling values in the range of -12 dB to -25 dB were required with directivity in excess of 20 dB. In addition it was desired that return loss of each coupler be greater than 26 dB.

The design of the cross-guide couplers is especially difficult in view of the limited amount of common wall area available between the two guides for placement of coupling apertures. Coupling fixtures were constructed in order to obtain coupling aperture data over the range of values needed. The coupling variation and directivity are shown in Figures 12 and 13 respectively. Figure 14 shows the minimum return loss as a function of mean coupler value. Flat coupling, high directivity, and good VSWR characteristics were maintained over the required range of coupling values.

2.4 Phase Shifter/Polarization Switch/Radiating Element

The phase shifter polarization switch and radiating element are integrated into a single package. A block diagram is shown in Figure 15 and Figure 16 shows a photograph of the unit. The radiating element is a dielectrically loaded circular waveguide which is matched in a number of waveguide simulators. Radiation patterns of the element in the array environment were verified in a 121 element subarray. The phase shifter and polarization switch are realized on a circular ferrite rod which is metalized to form a ferrite-filled waveguide. The polarization switch is composed of a cascade connection of a switched 45 degree Faraday rotator and a nonreciprocal circular polarizer. When the Faraday rotator is in an

unbiased state, the linearly polarized r-f energy propagates through the rotator and experiences no rotation.

The polarization is rotated ± 45 degrees when the rotator is biased in one direction or the other. Note that the direction of polarization rotation is independent of the direction of propagation through the rotator for a fixed bias direction.

2.5 Electronics Design

The block diagram of the module driver board is shown in Figure 17. All I/O lines are differential for maximum noise immunity. Further immunity is achieved thru the use of data and address latches that are controlled by a PAL with an on-board clock. The PAL is activated by the four system control lines. Look-up tables that contain phase shifter characterization data are contained in the on-board memory.

Data is programmed into the PROMs via a test socket, and addressing one half-module board out of several is done by setting the board DIP switch so that each board in the system has a unique address. Temperature data from three thermistors is digitized and returned to the BSC over the data bus as required and is also latched on-board to form part of the PROM address. Each of the 20 8-channel phase shifter drivers controls four phase shifters and their associated polarization switches. Built-in-test is provided from the drivers and is monitored by the BSC.

3.0 Test Results

3.1 General

The test program was generally divided into 2 general categories (a) detail-in-process tests and (b) final module acceptance tests. The in-process tests consisted of tests on each phase shifter/polarization switch unit, half module feed tests and sub-array verification tests. The final acceptance testing of the module consisted mainly of radiation pattern tests.

3.2 Phase Shifter/Polarization Switch Tests

Comprehensive test data were measured on each PCM. The parameters measured were: insertion loss, return loss, RF phase characteristics versus phase command (look up tables) and cross polarization at eight frequencies throughout the operating frequency band.

3.3 Sub-Array Verification Tests

A test subarray was constructed for the purpose of verifying the radiating element design in the array environment. The sub-array consists of 121 elements arranged on an equilateral triangular lattice of 0.472 - inch on a side. All elements except six are terminated in loads. The remaining six elements are brought out the rear of the array into waveguide ports for purposes of measuring the imbedded element pattern and mutual coupling. The arrangement is shown in Figure 18. This figure also shows the maximum measured mutual coupling between the various six elements. Measured E- and H- plane patterns are shown in Figure 19 and 20 for the center band frequency and center element for vertical polarization and in Figures 21 and 22 for horizontal polarization.

3.4 Feed Network

Each half of the linear array feed was tested for its coupling and match characteristics. The measured amplitude distribution for the sum (A-) line of a typical half-module feed is shown in Figure 23. As can be seen, the distribution agrees quite well with the Taylor 35 dB, $N = 4$ distribution which has an edge illumination of -15.5 dB.

The amplitude distribution for the difference (B-) line of the feed was measured. When combined with the measured sum line distribution with a weighting factor of -3.5 dB, the difference distribution of Figure 24 results.

3.6 Module Acceptance Tests

The final acceptance tests on each of the two deliverable modules were performed at the Martin Marietta Antenna Range facility in Orlando, Florida. Shown in Figure 25 is a collage of the measured sum and difference patterns in linear polarization for module 2 as the beam is scanned from -45 degrees to +45 degrees. The data shown in the figure are typical of the performance of both modules in linear polarization.

The tests on the modules consisted of linear polarization, RHCP and LHCP patterns for both the sum and difference channels at low mid and high band frequencies. In addition instantaneous bandwidth tests were made in linear polarization.

Radiation patterns and axial ratio measurements were made also in RHCP and LHCP at various scan angles. The results for module No. 1 are shown in Table 2, while those for module 2 are shown in Table 3.

TABLE 2: AXIAL RATIO (dB)

MODULE NO. 1

Frequency (GHz) and Sense	SCAN ANGLE								
	0°			-45°			+45°		
	-θ _{3dB}	0°	θ _{3dB}	-θ _{3dB}	-45°	θ _{3dB}	-θ _{3dB}	45°	θ _{3dB}
15.9 (RHLP)	0.50	0.82	0.76	1.41	1.25	1.13	0.98	1.07	1.56
15.9 (LHLP)	3.80	3.64	3.73	2.67	2.47	2.46	2.74	2.56	2.44
16.4 (RHLP)	0.46	0.55	0.70	1.22	1.32	1.61	1.31	1.56	2.08
16.4 (LHLP)	2.54	2.50	2.60	0.98	0.95	1.10	1.33	1.02	0.95
16.9 (RHLP)	0.16	0.36	0.25	1.67	1.76	2.06	2.10	2.13	2.57
16.9 (LHLP)	1.55	1.56	1.65	0.52	0.59	0.66	1.04	0.83	0.84

TABLE 3: AXIAL RATIO (dB)

MODULE NO. 2

Frequency (GHz) and Sense	SCAN ANGLE					
	0°			45°		
	-θ _{3dB}	0°	θ _{3dB}	-θ _{3dB}	45°	θ _{3dB}
15.9 RHCP	1.4	1.2	1.6	1.0	1.4	1.7
15.9 LHCP	3.7	3.7	3.7	2.6	2.7	2.7
16.4 RHCP	0.7	0.7	1.0	1.5	2.4	0.8
16.4 LHCP	2.3	2.0	1.8	1.3	2.1	1.0
16.9 RHCP	0.6	0.8	0.9	2.0	2.1	2.5
16.9 LHCP	1.3	1.2	1.0	1.1	1.1	1.0

3.0 Conclusions

The results of the work reported herein have demonstrated that a high performance phased array antenna can be constructed using a modularized building block concept. This study has conclusively shown that an array module capable of meeting the specified array requirements can be built.

REFERENCES

(1) C.R. BOYD

Ferrite Phased Array Antenna's: Toward a More Affordable Design Approach (1987) IEEE AP-S International Symposium Digest, Blacksburg, VA.

(2) LOPEZ, ALFRED R.

(1968) "Monopulse Networks for Series Feeding an Array Antenna," IEEE Trans. on Antennas and Propagation, Vol. AP-16, No. 4, July 1968, pp. 436-440.

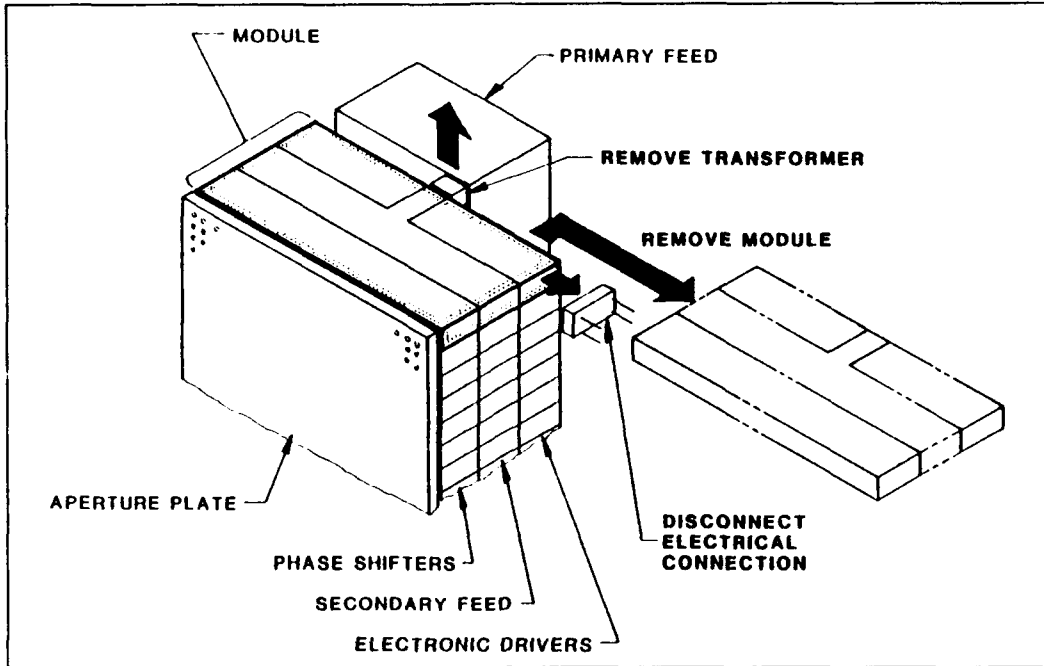


FIGURE 1 - Conceptual Design of Modular Array.

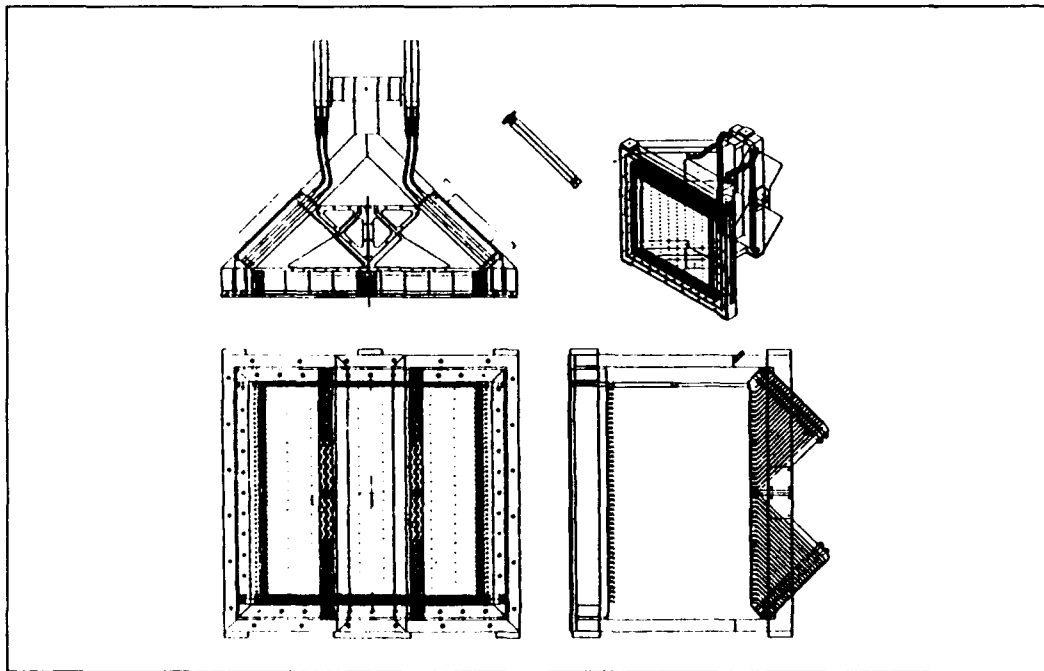


FIGURE 2 - Array Layout.

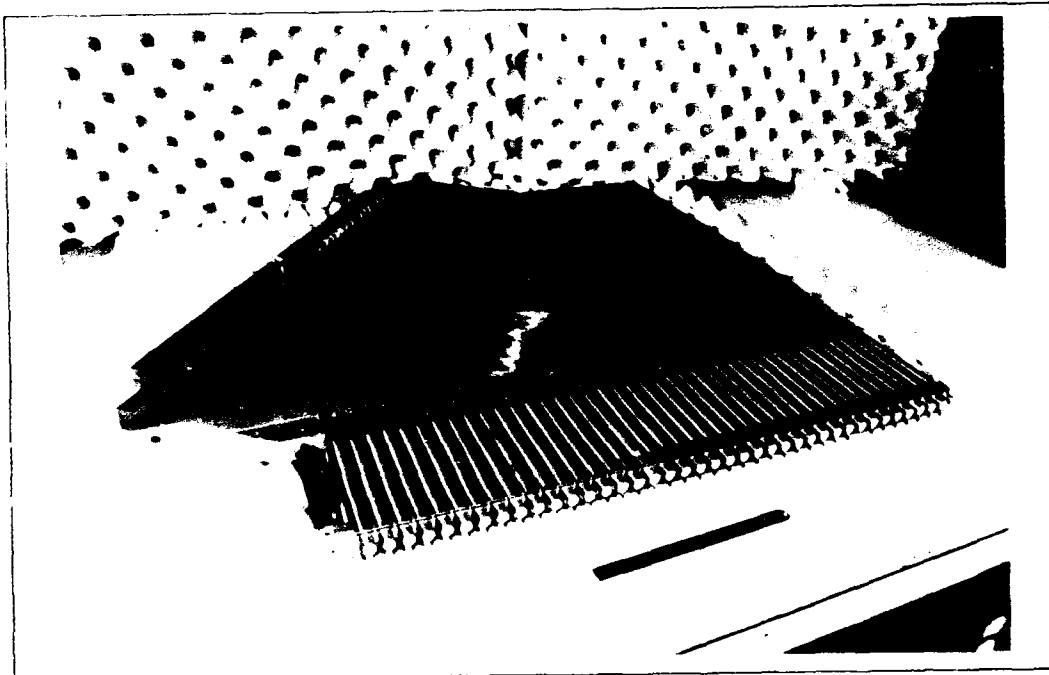


FIGURE 3 - Half-Module.

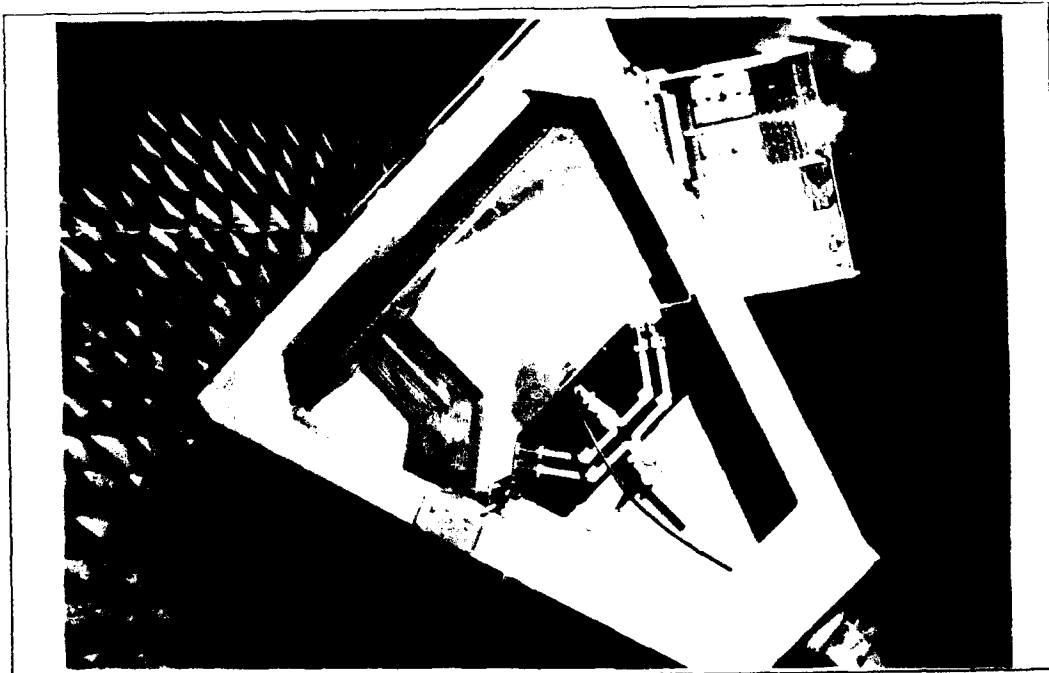


FIGURE 4 - Assembled Module in Pattern Test Fixture.

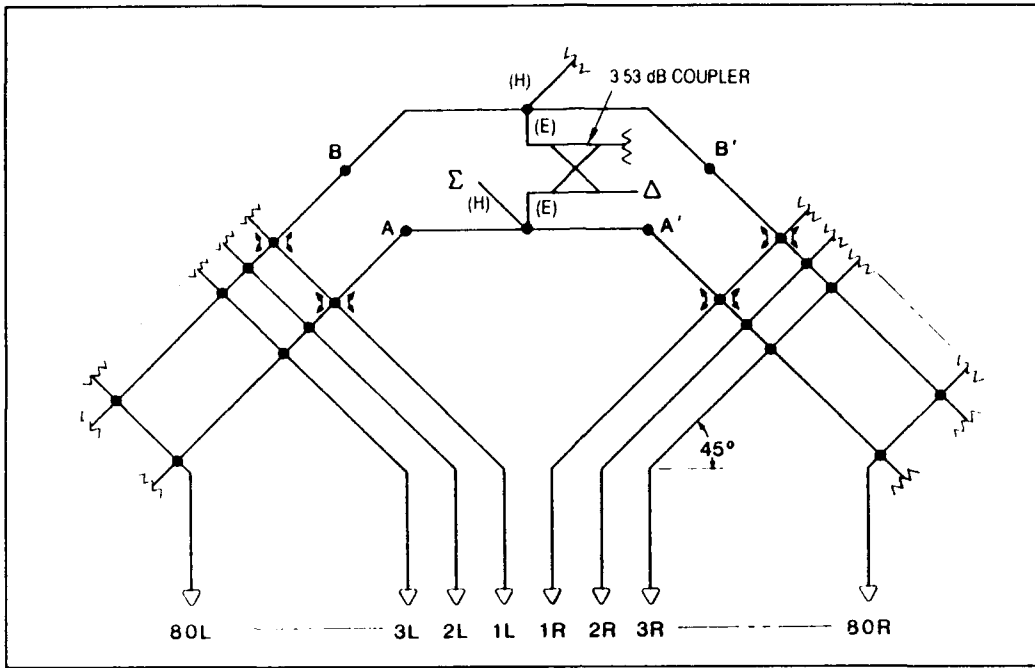


FIGURE 5 - Equal Path Length Lopez Feed.

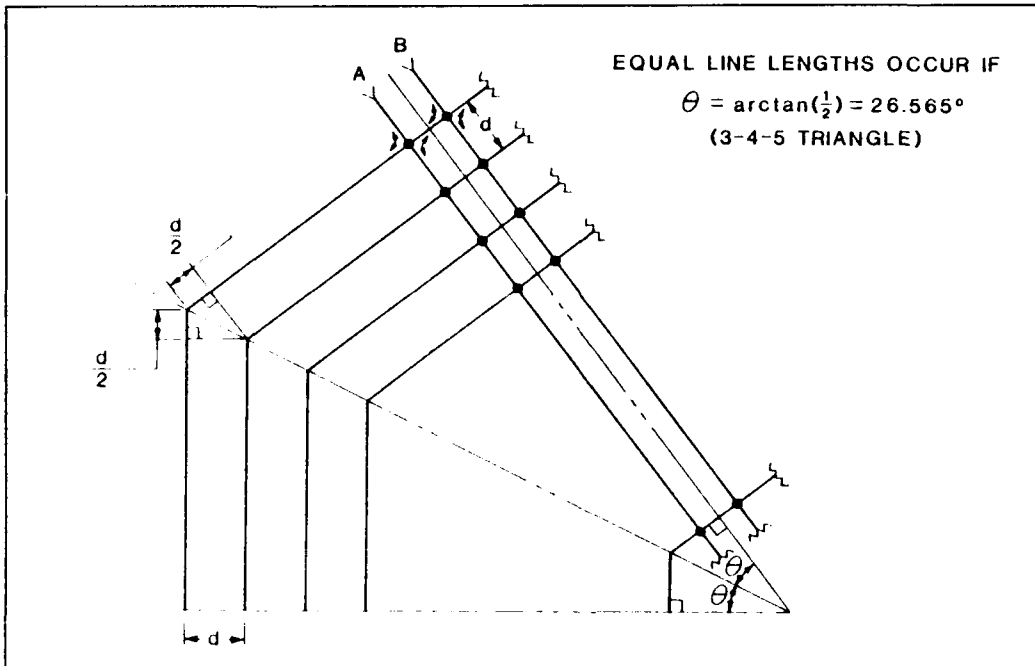


FIGURE 6 - 3-4-5 Triangle.

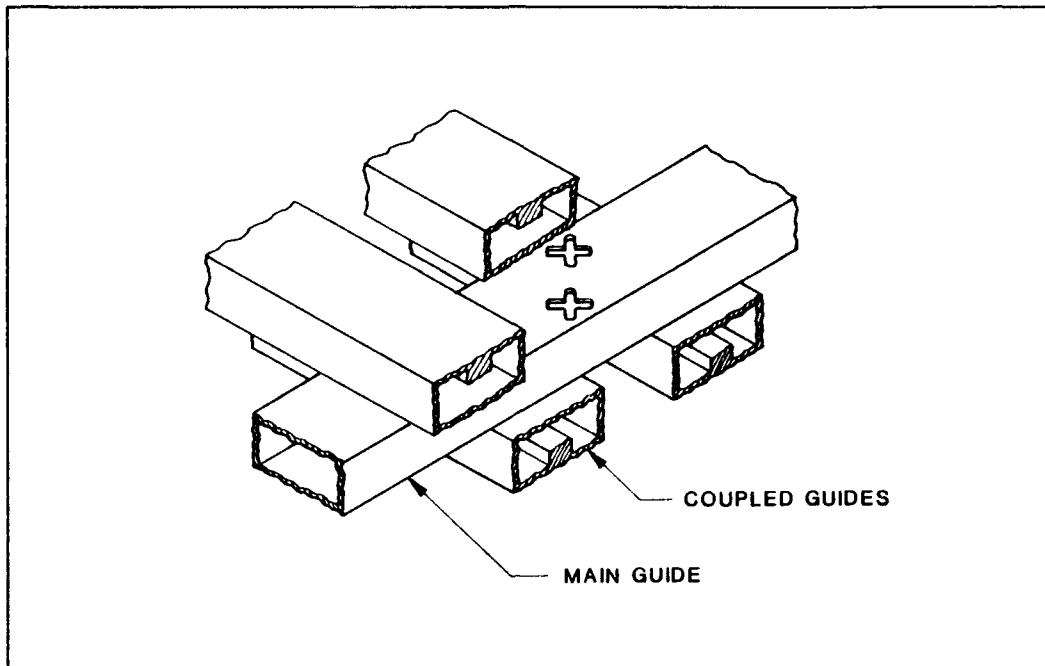


FIGURE 7 - Module Feed Concept.

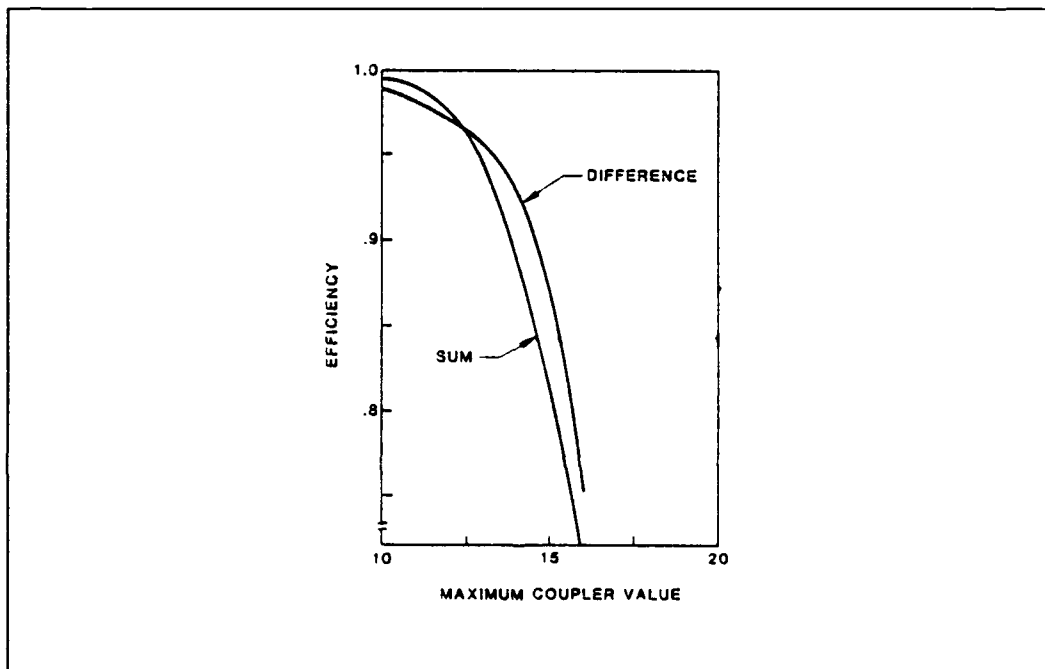


FIGURE 8 - Feed Efficiency vs. Maximum Coupler Value.

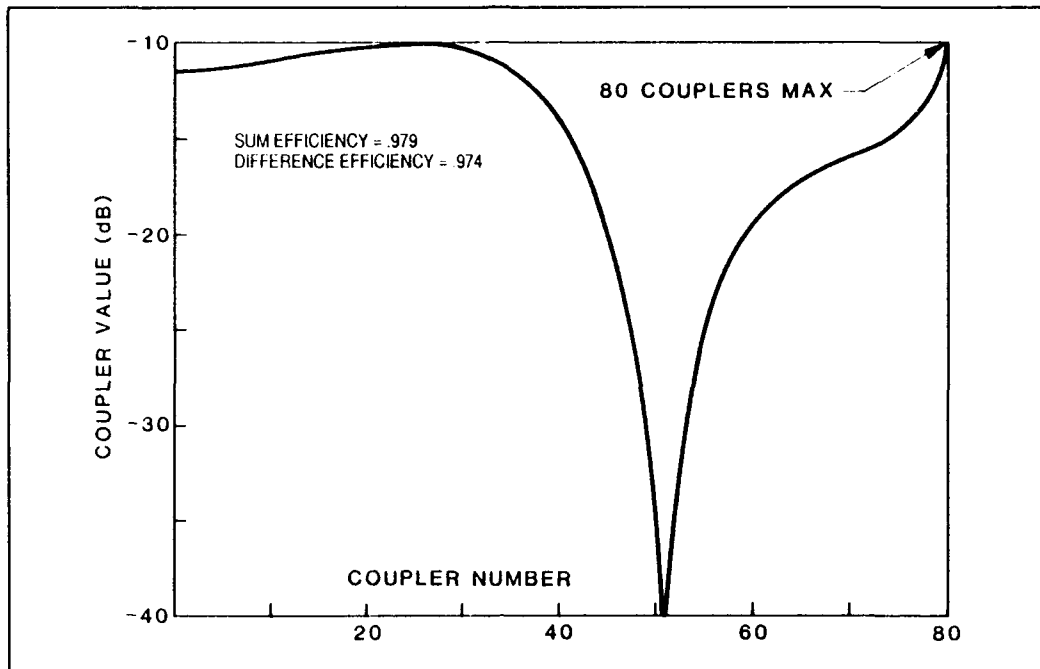


FIGURE 9 - Lopez Feed Secondary Line Coupler Values.

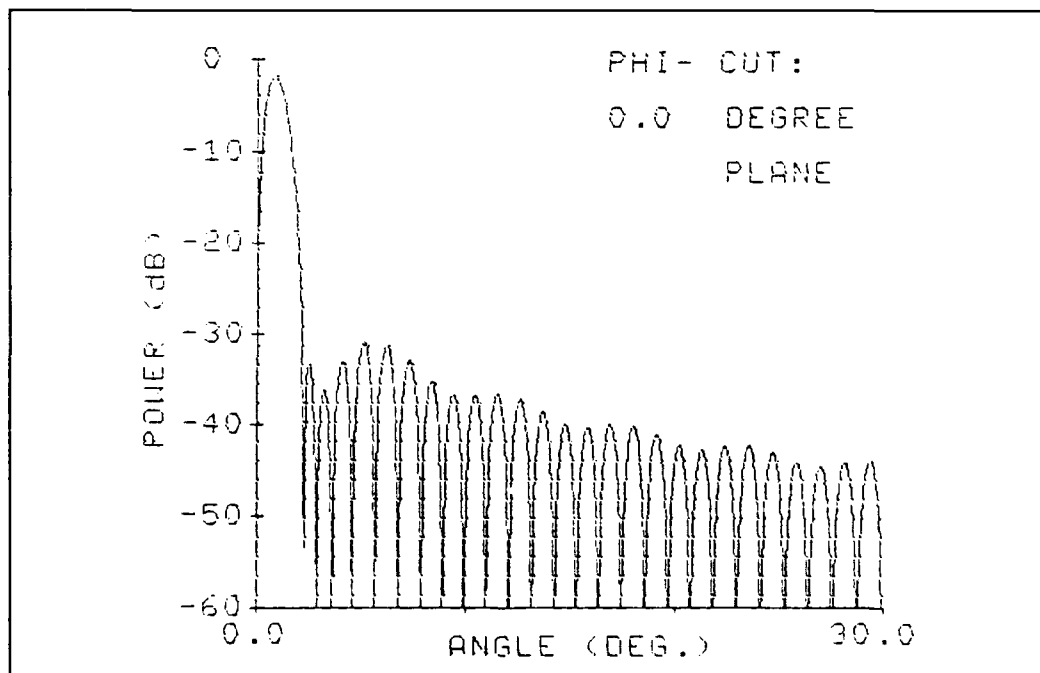


FIGURE 10 - Difference Pattern, Secondary Lopez Feed.

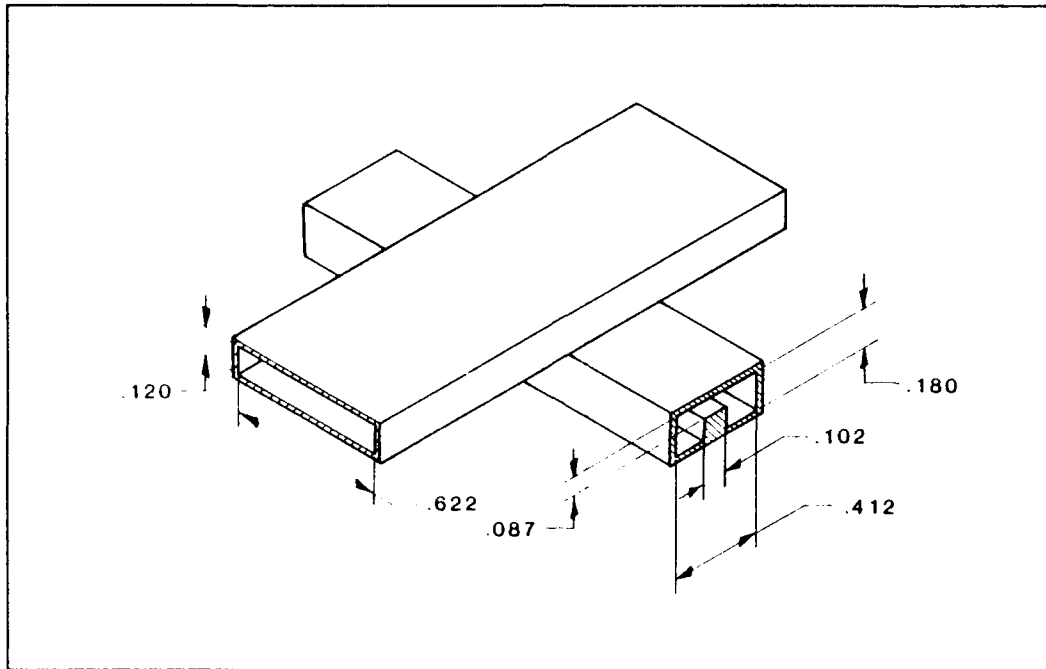


FIGURE 11 - Coupler Configuration.

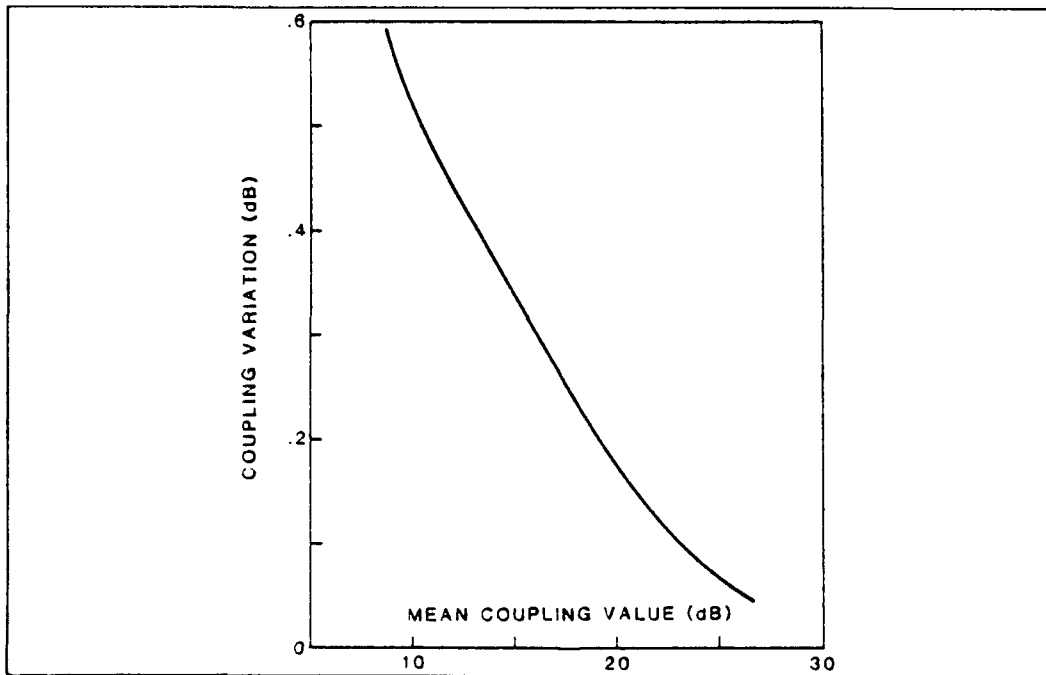


FIGURE 12 - Coupling Variation vs. Mean Coupling Value.

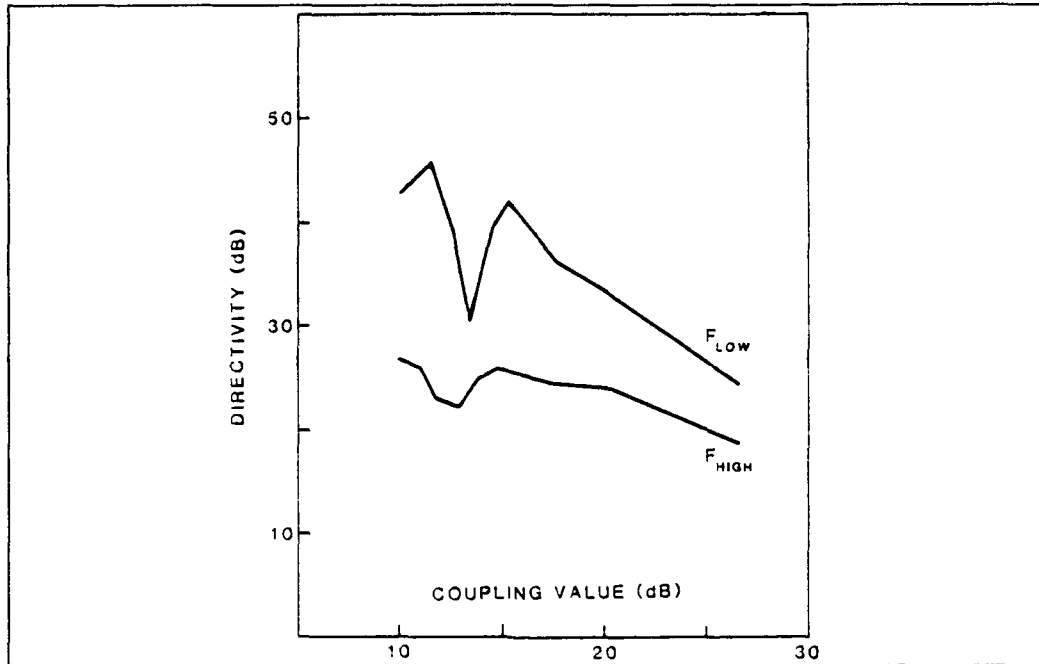


FIGURE 13 - Directivity vs. Mean Coupling Value.

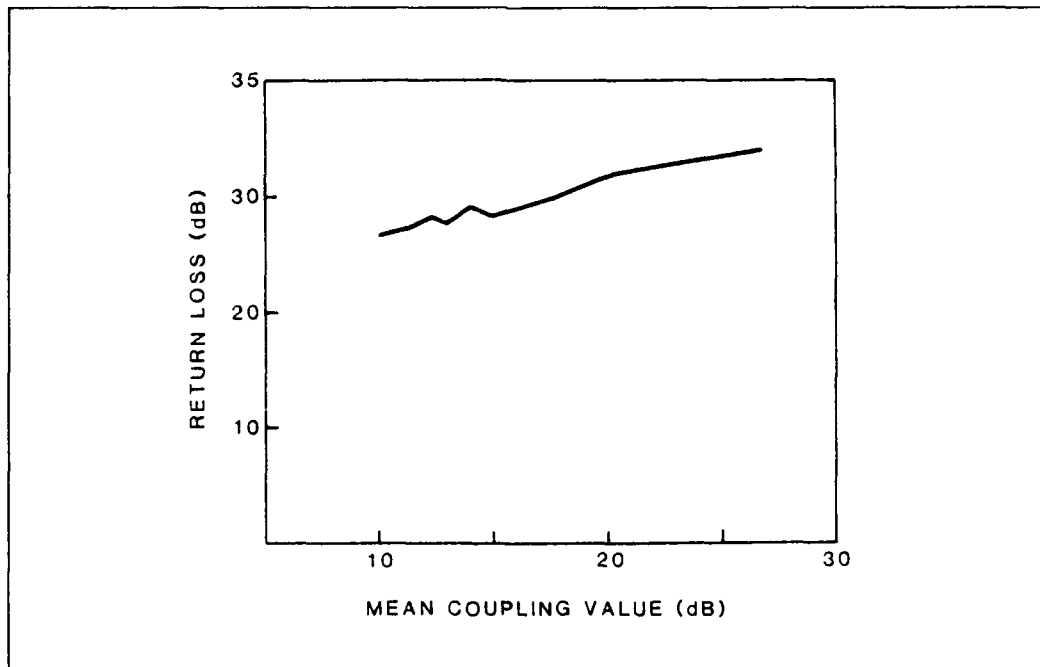


FIGURE 14 - Maximum Return Loss vs. Mean Coupling Value.

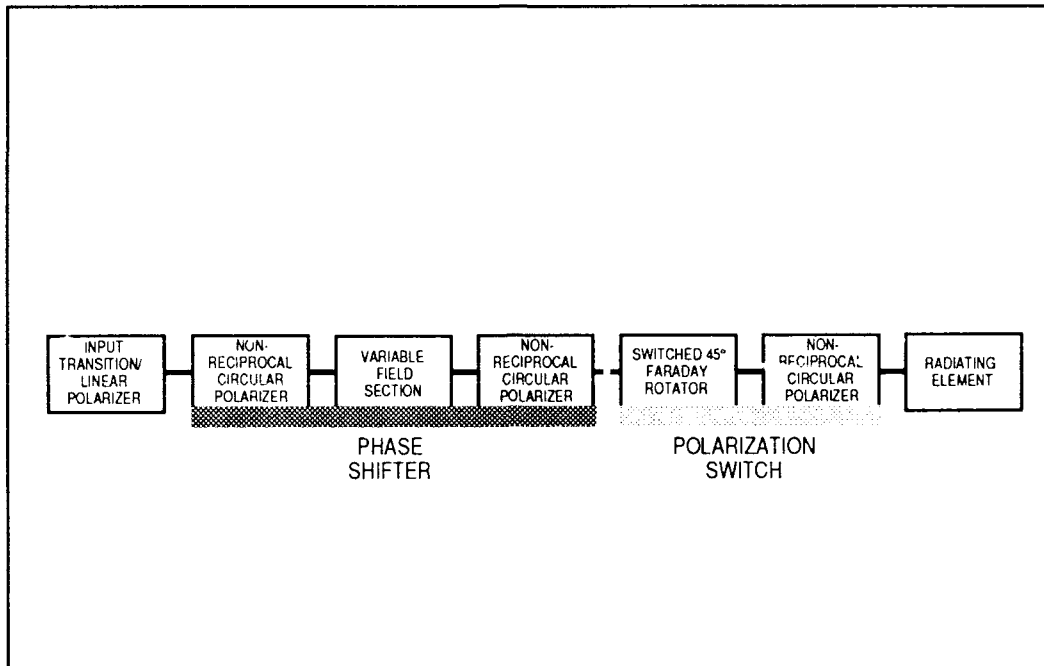


FIGURE 15 - Phase Shifter/Polarization Switch Block Diagram.

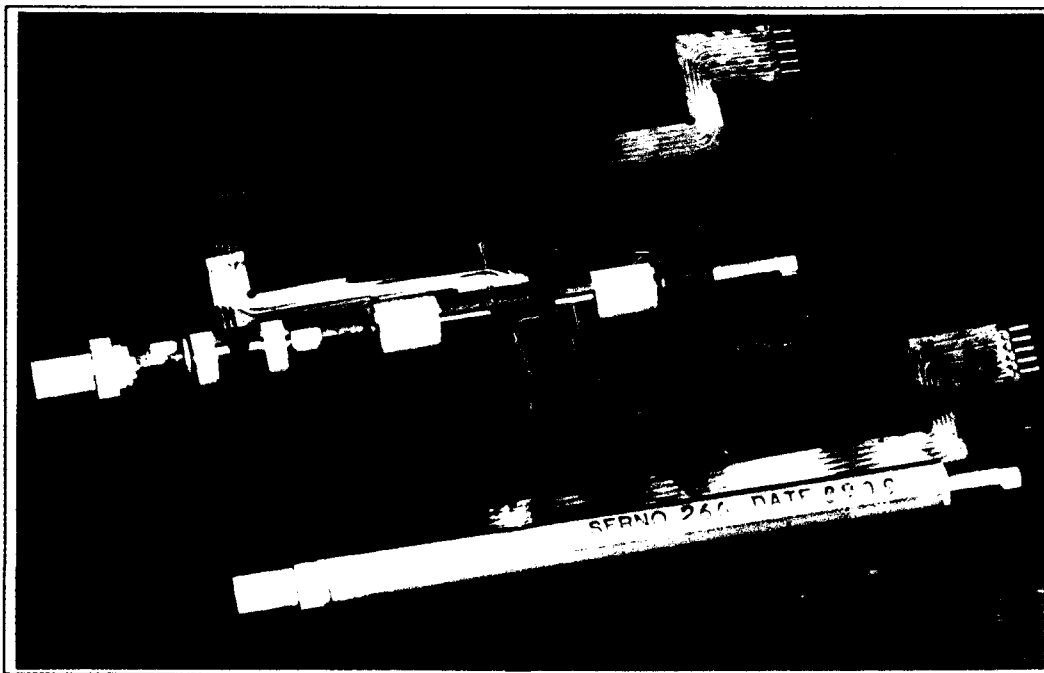


FIGURE 16 - Phase Shifter/Polarization Switch.

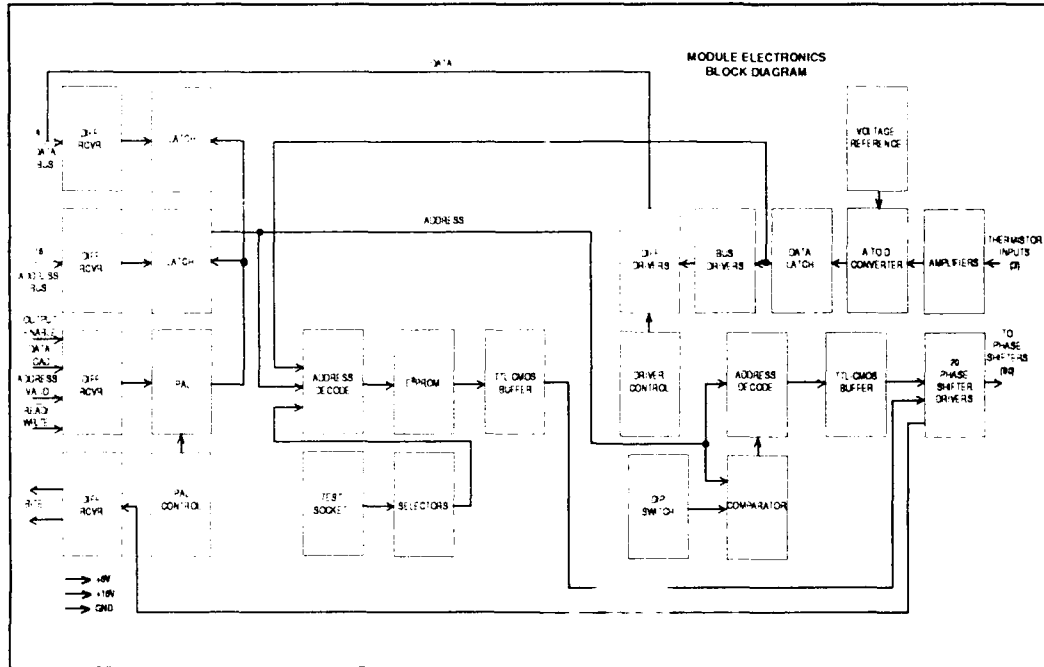


FIGURE 17 - Module Electronics Block Diagram.

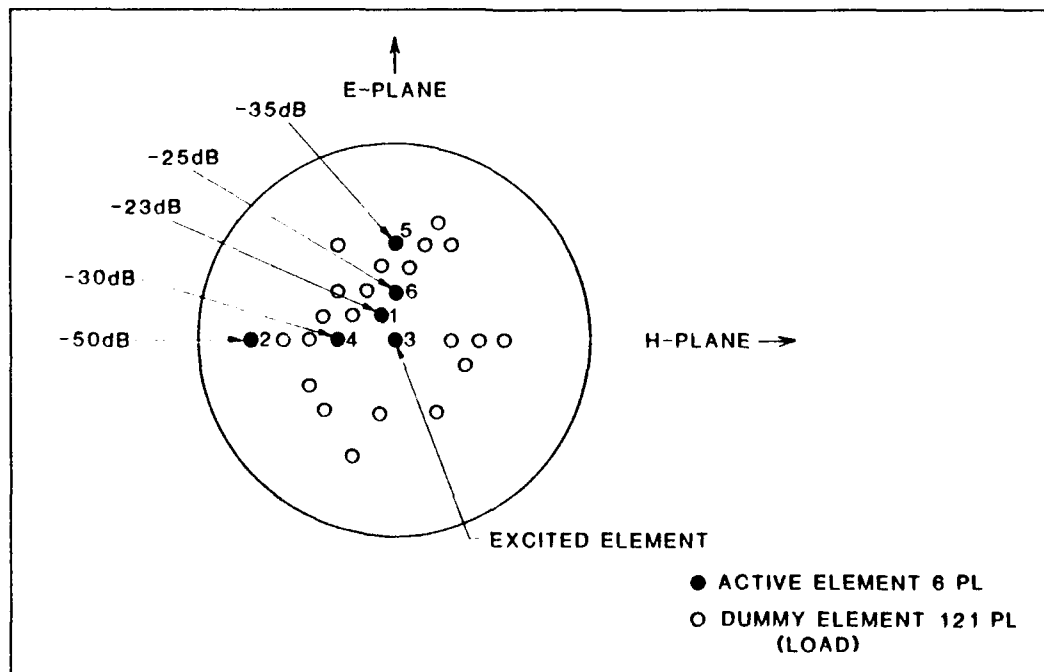


FIGURE 18 - Subarray Layout.

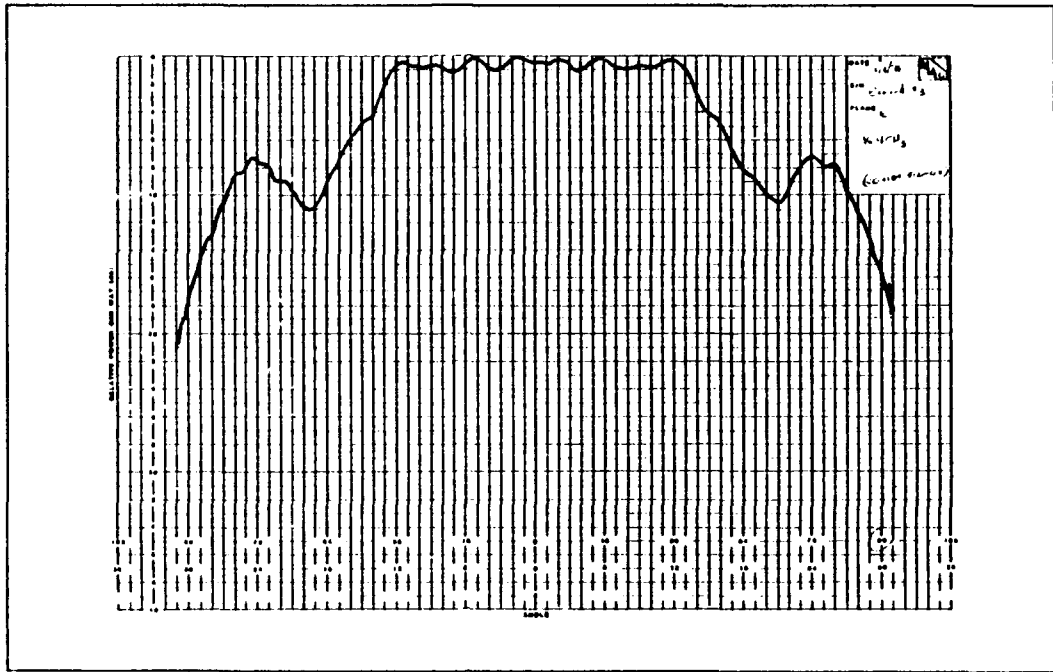


FIGURE 19 - Center-Band E-Plane Element Pattern (Vertical Polarization).

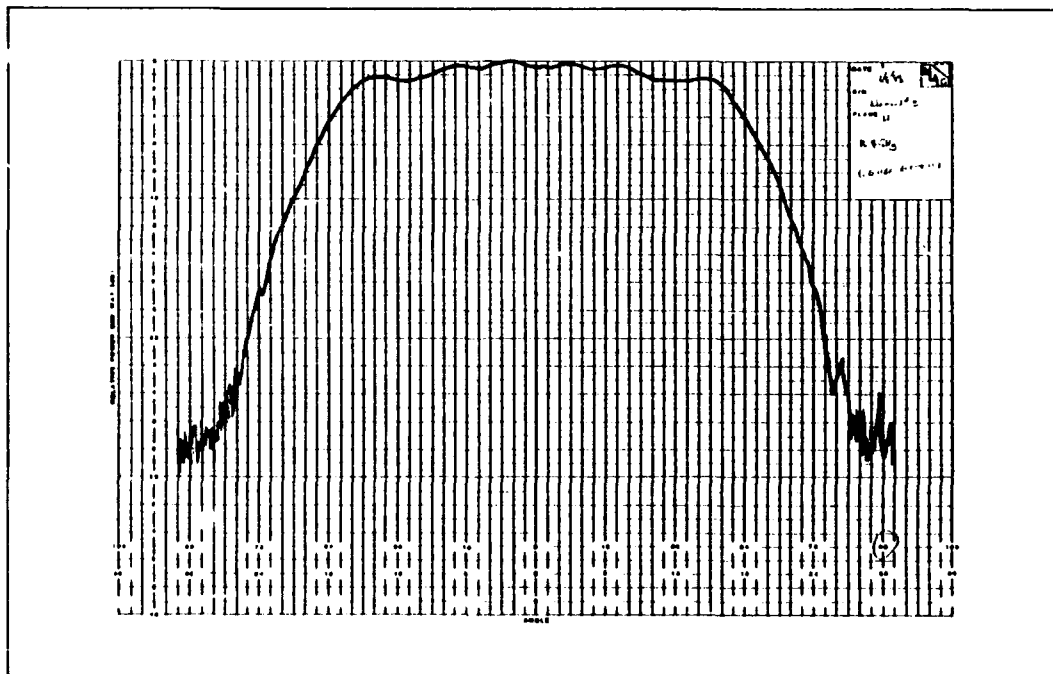


FIGURE 20 - Center-Band H-Plane Element Pattern (Vertical Polarization).

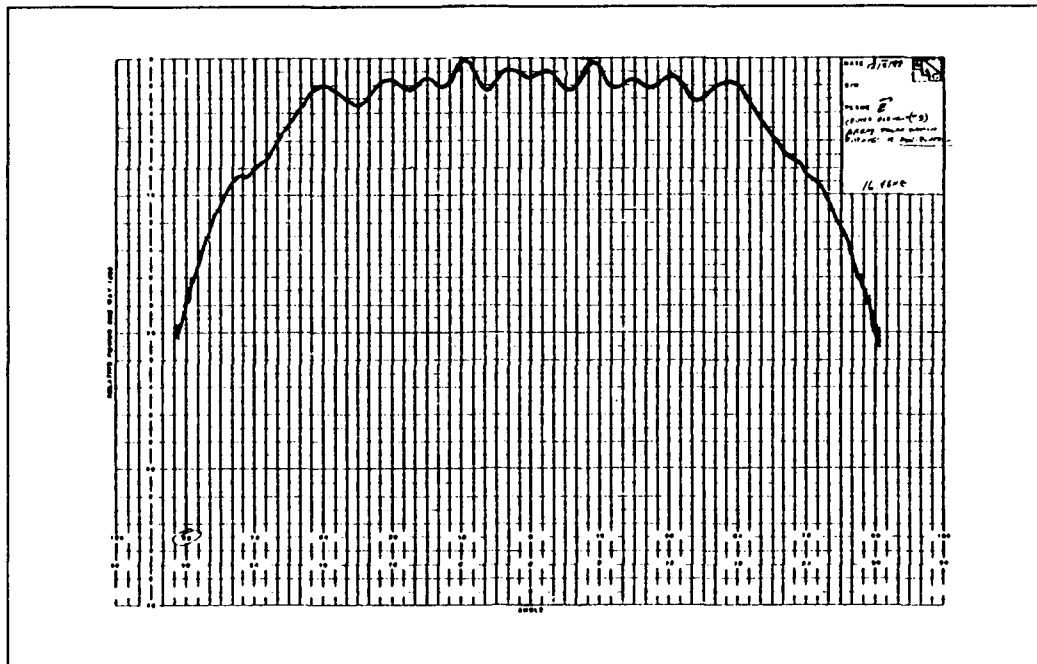


FIGURE 21 - Center-Band E-Plane Element Pattern (Horizontal Polarization).

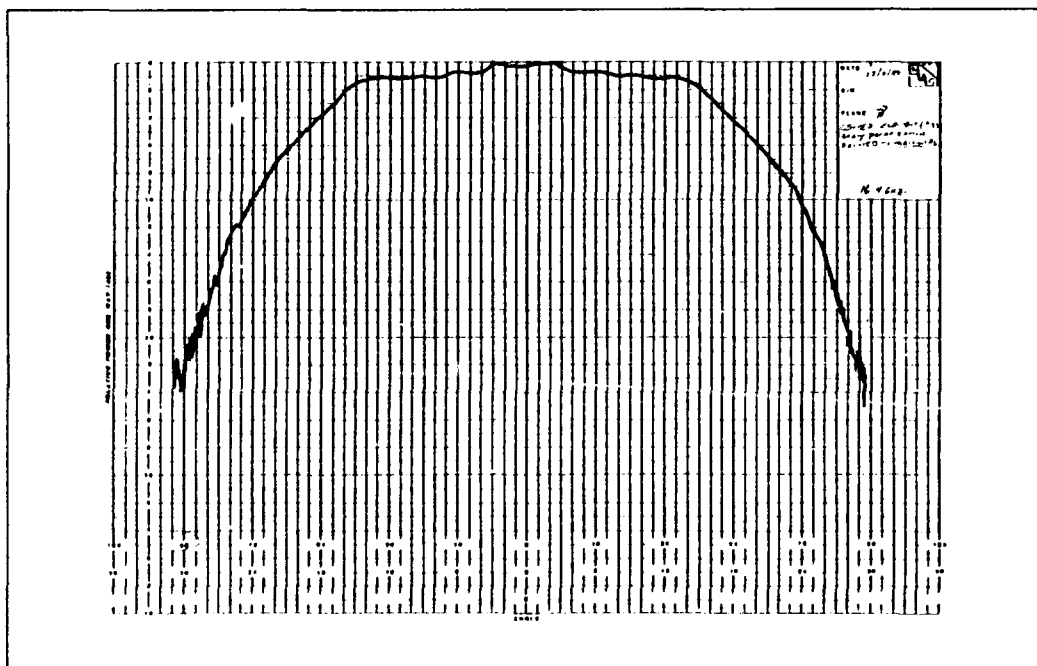


FIGURE 22 - Center-Band H-Plane Element Pattern (Horizontal Polarization).

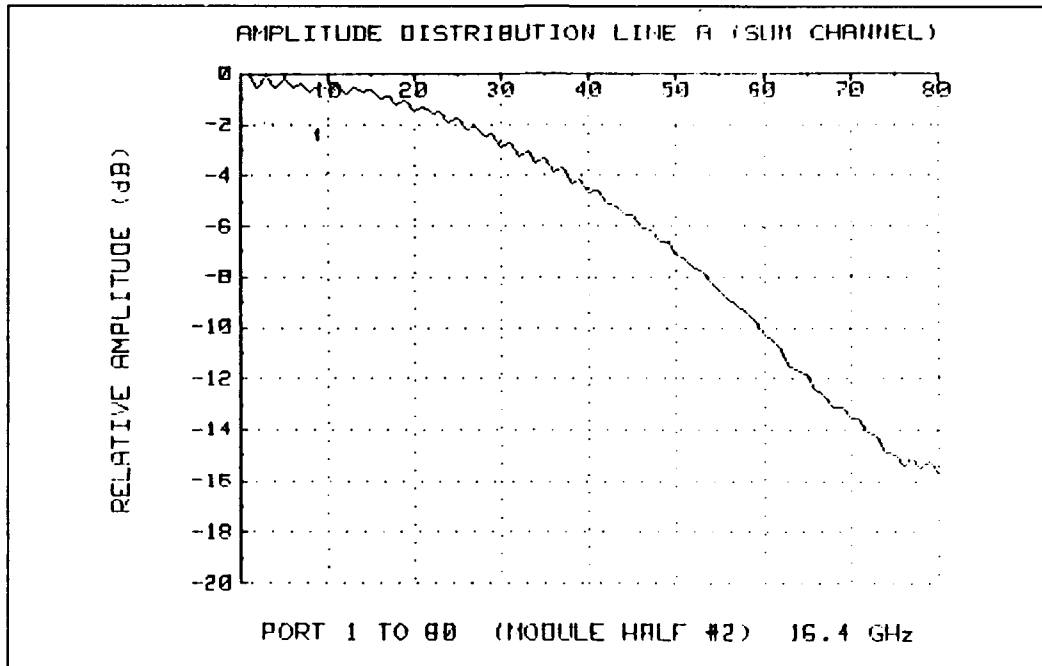


FIGURE 23 - Half-Module Sum Distribution.

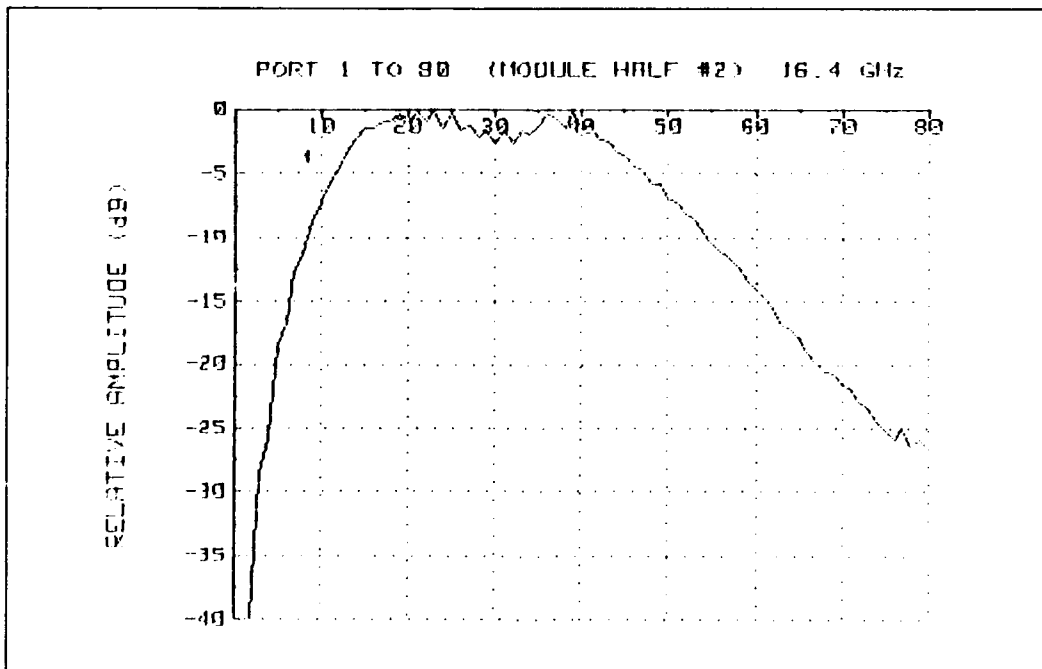


FIGURE 24 - Difference Distribution.

Module 2 Linear Pol. Broadside Beam
A890911A.REP
A: H1 (n)
FREQUENCY = 16.4 GHz

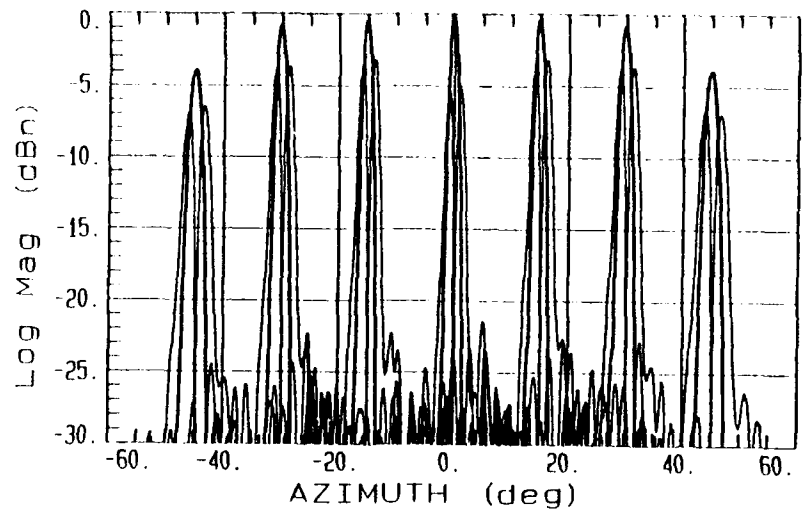


FIGURE 25 - Measured Sum and Difference Patterns.

A MATRIX-FEED BEAM STEERING CONTROLLER FOR
MONOLITHIC EHF PHASED ARRAY SYSTEMS

G. T. Wells, S. T. Salvage, S. R. Oliver
Harris Government Communications Systems Division
P. O. Box 91000
Melbourne, FL 32902

1990 Symposium on Antenna Applications
September 26-28, 1990
Allerton Park
Monticello, Illinois

A MATRIX-FEED BEAM STEERING CONTROLLER FOR
MONOLITHIC EHF PHASED ARRAY SYSTEMS

G. T. Wells, S. T. Salvage, S. R. Oliver

Harris Government Communications Systems Division

ABSTRACT

The design, fabrication, and test of a Beam Steering Controller (BSC) system for a monolithic 44 GHz phased array antenna is presented. This system is based on a Matrix-Feed approach to distributing phase shift data to a large number (1024) of GaAs subarrays which integrate multiple antenna elements with phase shifters, amplifiers, and power combiners. The Matrix-Feed approach realizes the following advantages over alternate controller concepts: It greatly reduces the number of interconnects to the subarrays. The effect on yield is minimized due to the simplicity of the digital circuitry contained on the subarray. The subarray chips are completely interchangeable. The flexibility provided by this architecture eases expansion for alternative applications.

Test results are presented which prove that the phase state for each individual element of a 4096 element array can be calculated, distributed, and latched into position in less than 44 microseconds. This corresponds to an array update time of greater than 22.7 KHz.

1.0 INTRODUCTION

Future monolithic phased array systems are envisioned to consist of numerous identical subarray chips set into place upon the phased array surface. Each subarray chip would contain four or more radiating elements, phase shifters, and amplifier gain stages. This approach offers the reliability, cost, and size advantages associated with the integration of several array functions on the same chip.

However, the need to distribute phase shift commands from a central controller to each of the individual phase shifters can add significantly to the array cost, while detracting from its reliability, due to the requirement for many thousands of bond wire connections. For this reason, it is desirable to reduce the number of connections to a practical level.

In this paper, a method of reducing the number of connections from a central phased array controller to 1024 subarray chips distributed over the face of the array is discussed. This method has been applied to the design of a 44 GHz monolithic phased array, in which each subarray chip contains four antenna elements, four power amplifiers, four phase shifters, and a power dividing network. Although the 44 GHz application discussed is fairly specific, the method is general enough to find

applicability in other types of systems, such as the "brick" (modular) types of phased array concepts as well.

The beam steering control (BSC) approach discussed in this paper is called the Matrix-Feed Method. The Matrix-Feed Method is identified by the method of data transfer to the subarrays through a network of row and column lines to each subarray. The column connection provides a clock which allows data to be synchronously transferred through the row connections. A centralized controller board calculates and transfers phase-state data to 32 subarrays at a time. The primary benefit of this design is that it requires only 2 pin connections per subarray and only 64 wires between the controller board and the subarrays for a 4096 element array. It uses a simple low risk digital design, allowing the use of algorithms which are flexible enough for applications such as null steering and multiple beam forming. The method is capable of providing digital self test. Using currently available technology, this architecture is capable of array updates at rates greater than than 20 KHz.

In order to realize the Matrix-Feed approach, a limited amount of digital circuitry must be fabricated, along with the RF power amplifiers and phase shifters, on the subarray chips. Fewer than 100 digital gates are required per subarray. It has been calculated that the subarray digital circuitry will consume less

than 45% of the unused area on a 44 GHz subarray, ensuring low impact on future monolithic integration of the RF subarrays and the BSC design. It is essential to maintain a low gate count on the face of the subarray, to keep from adversely affecting the yield and power dissipation of the chips.

In addition to developing this approach on paper, a hardware system has been built, demonstrating that the Matrix Feed method accurately transfers data to a 4096 element array at an update rate faster than 20 KHz. The following sections will detail the design, fabrication and test of this concept.

2.0 DESCRIPTION OF THE MATRIX-FEED BSC CONCEPT

The Matrix-Feed Controller System can be functionally divided into two main sections, i.e. the subarray circuitry and the central controller. The subarray circuitry consists of the digital gates which are to be fabricated along with the power amplifiers and phase shifters on the face of the phased array. The central controller is more complex, and is broken down into identifiable subsections. They are:

- The Coordinate Transformation block
- The Phase Computation sections (for element level phase computation)

- The Matrix Interface sections (for serial data distribution)
- The Timing section

The relationships between these sections and the subarray chips are shown in Figure 1.

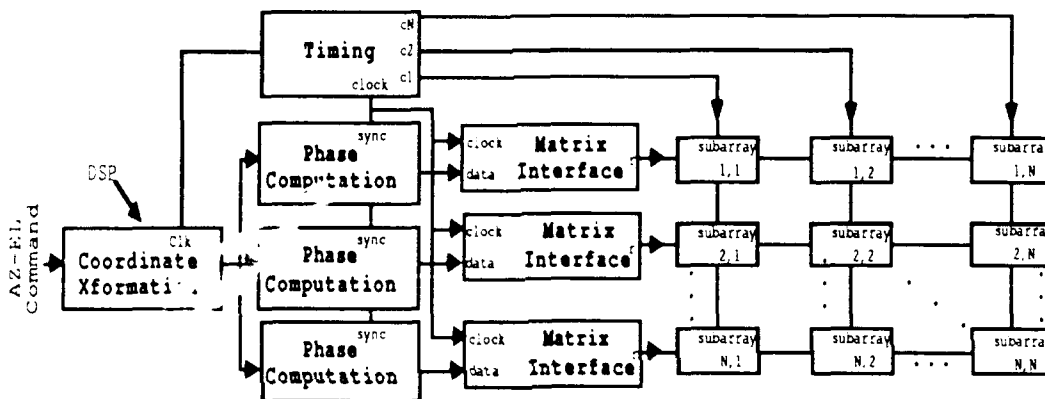


Figure 1 Matrix-Feed BSC Architecture

2.1 COORDINATE TRANSFORMATION BLOCK

In this phased array system, an initial beam position is assumed to have been given in spherical coordinate angles (Θ, \emptyset) . The phase at the i_{th} and k_{th} elements of an m -row by n -column flat phased array is described by the following equations.

$$\emptyset_{ik} = i(f/f_0)\pi\sin\emptyset_x + k(f/f_0)\pi\sin\emptyset_y \quad (1)$$

$$\theta_x = \sin^{-1}[\sin(\Theta)\cos(\emptyset)/(\sin^2(\Theta)\cos^2(\emptyset) + \cos^2(\Theta))^{1/2}] \quad (2)$$

$$\theta_y = \sin^{-1}[\sin(\Theta)\sin(\emptyset)/(\sin^2(\Theta)\sin^2(\emptyset) + \cos^2(\Theta))^{1/2}] \quad (3)$$

where f/f_0 is a factor to account for frequency shift in a frequency hopping system.

The solution of equations (2) and (3), the calculation of the sine of equations (2) and (3), and the multiplication of equations (2) and (3) by π and (f/f_0) , need be performed only once for the entire array, and is accomplished in the coordinate transformation block as soon as the command is received. The output of this block consists of two single 10 bit words, representing $(f/f_0)\pi\sin(\theta_x)$ and $(f/f_0)\pi\sin(\theta_y)$. These words are then transferred to the Phase Computation section where the subsequent multiplication of these words by the individual row and column numbers (i and k) occurs.

2.2 PHASE COMPUTATION AND MATRIX-FEED SECTIONS

The two words generated in the coordinate transformation section are used to calculate the phase state for each individual element of the array. The phase computation block performs the multiplication of the first word, $(f/f_0)\pi\sin(\theta_x)$, by the row number of the element (i), and the second word, $(f/f_0)\pi\sin(\theta_y)$ by

its column number (k). Addition of the two numbers is then performed. The multiplication of the element locations, i and k , by $(f/f_0)\pi\sin(\theta_x)$ and $(f/f_0)\pi\sin(\theta_y)$ continues, column by column until the last subarray in each row is reached.

The multiplication of $(f/f_0)\pi\sin(\theta_x)$ and $(f/f_0)\pi\sin(\theta_y)$ by i and k for each phased array element can be time consuming for a large array. It is therefore desirable to parallel as much of this operation as is possible. The division of effort which was selected in the 44 GHz study was to allocate a Phase Computation block in the central controller for each of the 32 subarray rows. By configuring the Phase Computation sections in this manner, the array update rate was increased by a factor of 32.

As the multiplication is performed for each column of the array, the data is transferred to the Matrix Interface block. The Matrix Interface block directs the flow of the calculated phase state data from the controller to the individual subarrays. The entire transfer is accomplished with only two connections per subarray in the following manner:

The data for any four, four-bit phase shifters contained in a given row of subarrays (locations $\{i,k\}$, $\{i,k+1\}$, $\{i+1,k\}$, and $\{i+1,k+1\}$) is shifted serially to each subarray as the desired

subarray column line is clocked. The selected column line is used as a clock and the row line as data to provide the synchronous transfer. All subarrays in a given row receive data on the row line simultaneously, but only one subarray receives the data and an enabling clock at the same time. All other row and column lines which do not receive the simultaneous row and column signals are automatically driven to a 'LOW' state. Since the subarray address is determined entirely by the row and column combination, there is no need to set an address on the subarray. This allows all subarray chips to be manufactured identically.

2.3 SUBARRAY CIRCUITRY

On the subarrays which have not yet received simultaneous row and column commands, the digital circuitry remains in a "wait" state for a "Start-Bit" pattern. When the "Start-Bit" pattern is received, a 16 bit stream of data immediately follows, representing (in this case), the phase state of the four, four bit phase shifters contained on that subarray. When the counter's output is equal to a specified number of bits transferred, the shift register and the counter's gates are disabled. The phase shift data is transferred to the phase shifters only after all of the data for all of the subarrays of the array has been transferred. A single latch command which globally shifts all of the rows and columns high realizes the final transfer. It will

receive no more information until a new "Start-Bit" pattern is received.

3.0 IMPLEMENTATION OF THE MATRIX-FEED BSC

A hardware implementation of the Matrix-Feed BSC scheme was completed to verify the speed with which the scheme could update a 4096 element array consisting of 1024 subarrays with 4 elements each. A top level diagram of a single row of the beam steering controller design is shown in Figure 2. This figure is a block diagram of the actual hardware implementation of the system discussed in Figure 1. Table 1 is a quick reference table which explains the terms of the block diagram. Contained within the dotted lines of figure 2 is all of the circuitry used to perform the phase computation and distribution of phase state information to the individual subarrays. This circuitry is contained on a single card. A photograph of this card in the test environment is shown in Figure 3.

The subsection in Figure 2 called the "BSC Array Chips" will eventually be built in GaAs. For the hardware demonstration, this circuitry was built using off-the-shelf silicon components, so they could be used to test the controller and the overall Matrix-Feed concept.

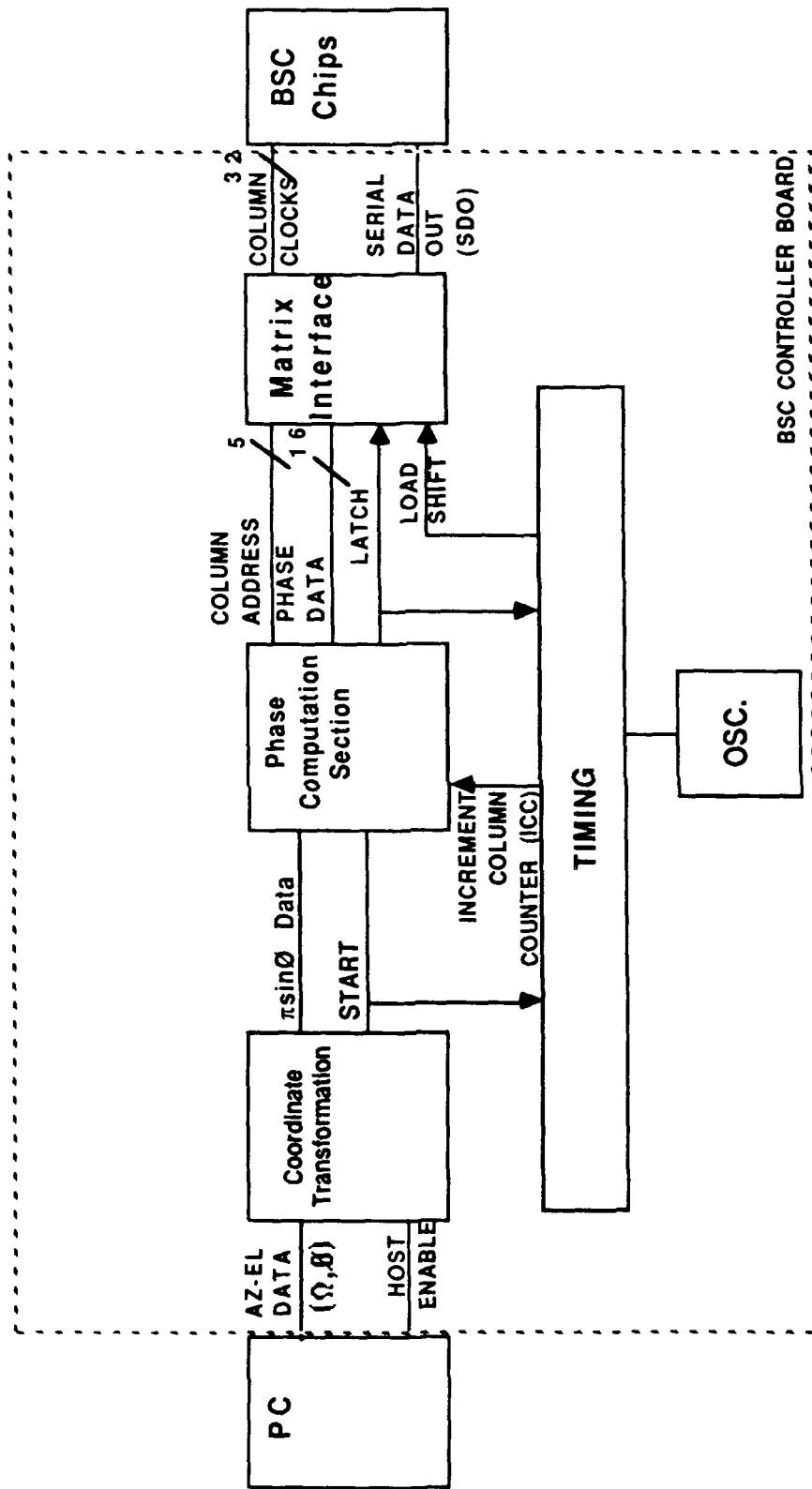


Figure 2 Overall BSC Block Diagram

PC:	An IBM AT Personal Computer or equivalent (includes custom PC comm card)
AZ-EL DATA:	Azimuth and Elevation Pointing Vector (Spherical Coordinates)
HOST ENABLE:	Processing card interrupt signal, AKA: HEN
DSP:	Digital Signal Processor (Motorola 56000)
Pointing DATA:	Pointing Vector (Converted from Spherical Coordinates to θ x and ϕ y)
START:	Control signal which initiates the Processing Section and Matrix Interface
Processing Section:	Circuits which compute the phase data for each element in a row of antenna subarrays
Column Address:	A 5 bit parallel signal that represents the address of the subarray column
PHASE DATA:	A 16 bit parallel signal that represent the four 4 bit phase commands for the four elements located in the subarray located at the column address
LATCH:	A control signal that directs the Matrix Interface to send the "LATCH" command to all the BSC chips in that row which synchronizes the new phase data
LOAD/SHIFT:	A control signal which directs the Matrix Interface to either load in the parallel phase data from the Processing Section or shift the phase data out to the chips
Increment Column Contrl:	A control signal that directs Processing Section to compute phases for next column
Matrix Interface:	Circuits which distribute the phase data to the subarrays for one row
Column Clocks:	The array column interconnects which carry the clock signals to the subarrays
Serial Data Out:	The array row interconnect which carries the data to the subarrays
BSC Array Chips:	Digital communication circuits which will eventually be on the monolithic subarrays

Table 1 Definition of Terms used on BSC Block Diagram

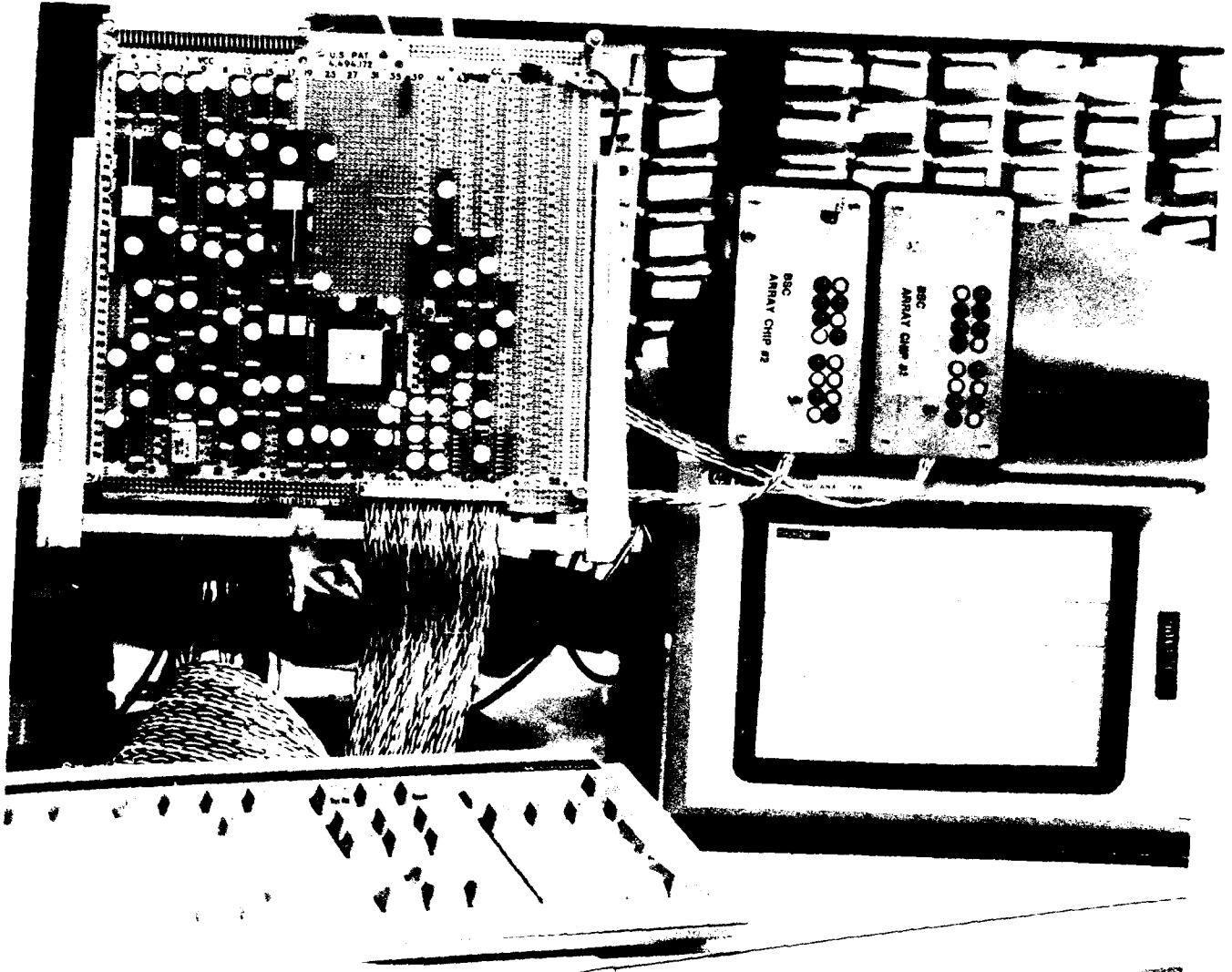


Figure 3 Photograph of BSC Test Equipment

3.1 COORDINATE TRANSFORMATION CIRCUITS

The Coordinate Transformation block shown in Figure 2 is used to transform the azimuth and elevation beam pointing information into the coordinate system the controller is designed to process (paragraph 2.2).

The key component of this section is the Motorola 56001 digital signal processor (DSP). In addition to managing the coordinate transformation, this section provides the interface to a personal computer (PC). The PC is used to download DSP firmware, send the array update command, and in a test mode, read data back from the DSP. The DSP runs at 20 MHz and processes 10 million instructions per second (MIPS). The conversion algorithm runs in 5.5 microseconds.

The DSP algorithm was designed to meet the speed criteria of the BSC. To do this, lookup tables were used to store sine, cosine, and the inverses of the squareroots corresponding to a known set of input commands. The lookup tables were designed to store lookup values for any angle between 0 and 360 in 0.2 degree increments and possible inverse-squareroot values accurate to 11 bits. This set of values can be easily expanded by using more memory. The DSP receives the azimuth, elevation, frequency hop (FHOP) factor in the form of a pointer address that points

directly to the memory location containing a sine, cosine, or frequency hopping factor. This is accomplished by passing integer values representing 1 of 1800 points around a 360 degree circle and an integer 0-7 for one of 8 possible FHOP factors. The algorithm uses a minimal number of instruction cycles using this pointer method.

3.2 PHASE COMPUTATION CIRCUITS

The $(f/f_0)\pi\sin\theta_x$ and $(f/f_0)\pi\sin\theta_y$ data generated by the Coordinate Transformation section is used to calculate the phase state for each element of each subarray contained in a single row of subarrays making up the array. The Phase Computation section (Figure 2) is responsible for coordinating the column address with its corresponding data. The output of this section is a parallel 16 bit word describing the 4 bit phase state of each of the four elements on a 4 element subarray, as well as parallel five bit column address corresponding to the subarray for which the data was calculated.

Figure 4 is a data flow diagram depicting the digital multiplication which takes place in the processing section. This design is a key component to the Harris Beam Steering Controller which enables it to complete the computations rapidly.

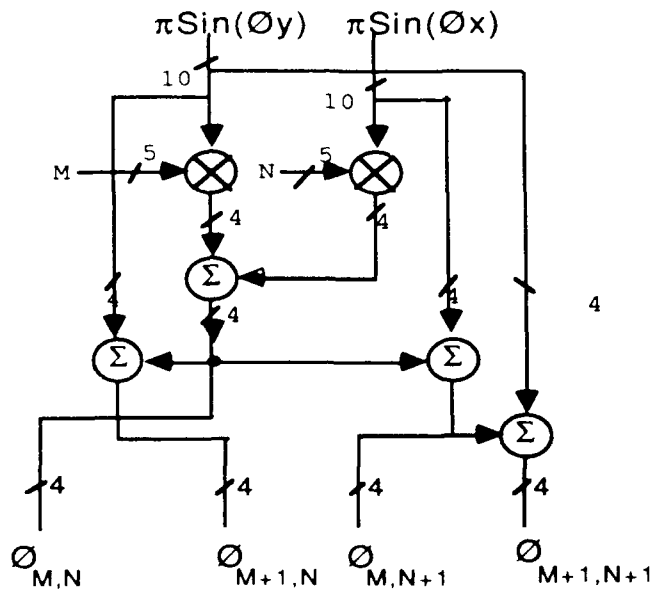


Figure 4 Processing Section Multiplier Data Flow Diagram

For the initial proof-of-concept, the data flow diagram shown in Figure 4 was implemented with off-the-shelf full multiplier chips and adders. Many of the carry functions of these chips are unnecessary. All of the processing functions required by the total array could be more efficiently implemented in a single gate array and one microprocessor. This has been proposed for future developments of this concept.

3.3 MATRIX INTERFACE CIRCUITS

The Matrix Interface Section receives the 16 bit parallel data word and the eight bit address from the Phase Computation

Section and converts the parallel data to a serial data stream which is output to each subarray. Simultaneously the address bits activate the clock for the column of the array to which the data is directed.

The Matrix Interface Section uses a clock distribution circuit that is comprised of four 1-of-8 Demux chips which together form a simple 1-of-32 demux. The address held in a latch of the processing section determines which of the 32 lines will receive a clock signal. A signal is sent which will circumvent the demux and cause all 32 clocks to be activated simultaneously when the array update is complete. This final signal instructs all of the subarrays to send their data to the phase shifters which cause the direction of the beam to change at that instant.

3.4 MATRIX-FEED BSC ARRAY CHIP

The digital circuitry which will eventually reside on the monolithic substrate with the RF components is referred to as the "array chip". The method in which it operates is critical to the design of the BSC system. Figure 5 shows the schematic diagram of the array chip.

The Matrix Interface transfers the calculated subarray phase shifter settings to each appropriate subarray using a

synchronous serial protocol. In steady state operation, the subarray circuitry is waiting for a designated "Start-Bit" pattern on the Rx line. After the pattern is received, the timing block gates a data bit counter and a serial to parallel shift register. This allows all other transitions on the column line to clock the data into the shift register and increment the count in the data bit counter. When the counter's output is equal to a specified number of bits transferred, the shift register and the counter's gates are disabled. The timing block then clears the counter and prepares for the next block to be sent.

Additional bits are needed to provide for array synchronization and subarray digital self test. These functions can be implemented by providing control bits prior to the data bits within a block transfer previously described. For this proof-of-concept, only a latch bit was implemented (it is used for array synchronization). It is recommended that future development of this architecture include the digital self-test feature.

The latch bit will alert the subarray that the block of data to be transferred represents either phase shifter data or synchronization control. If it is the synchronization control, the subarray will send previously received data to update the phase shifters to their new value. If the block is phase shifter data, the subarray will load the data in preparation for transfer

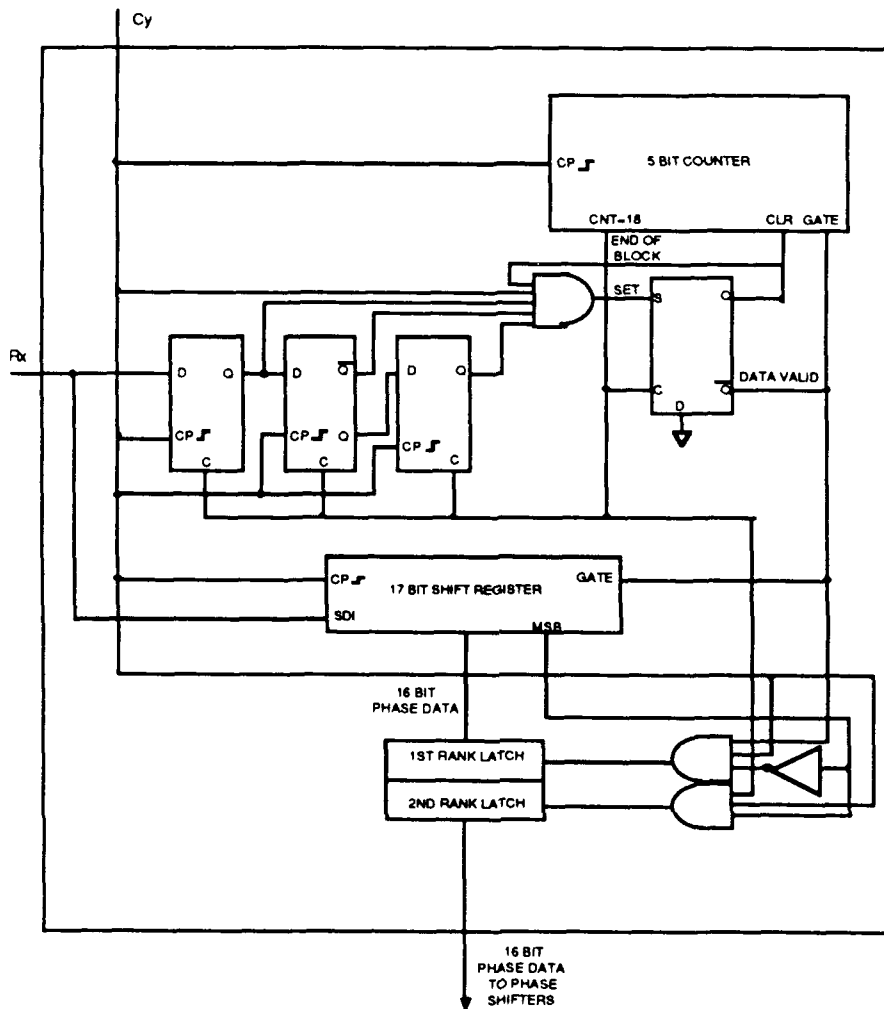


Figure 5 Matrix-Feed Approach Array Chip Design

to the phase shifters. The two latch (more commonly referred to as "dual-ranked") design provides the means to sequentially update columns of subarrays, without updating their phase shifters, and then updating all of the second latches of the subarrays, providing array synchronization.

As the Phase Computation section calculates phase settings and distributes them to their corresponding phase shifters (through the Matrix Interface), the subarrays load the transferred data into a holding latch, or first rank latch. After all of the subarrays have been updated, the Matrix Interface and Timing sections will transmit a control word to all of the subarrays, thereby loading the DAC latch (second rank) with the data contained in the holding latch (first rank). In this way the subarrays columns can be written sequentially, while the phase shifters are updated simultaneously.

4.0 TEST RESULTS

There are two critical aspects of the beam steering controller that needed to be verified by the proof-of-concept hardware. First, it was important that the BSC be shown to exceed an update rate of 20 kHz. Second it was important to establish the accuracy of the system. Both the method of testing and the results will be presented in this section.

4.1 ARRAY UPDATE RATE

The update rate is calculated from three processing tasks: the coordinate transformation, the subarray phase calculation, and the subarray phase data distribution time. Figure 6 shows how

these three components contribute individually to the total array update time.

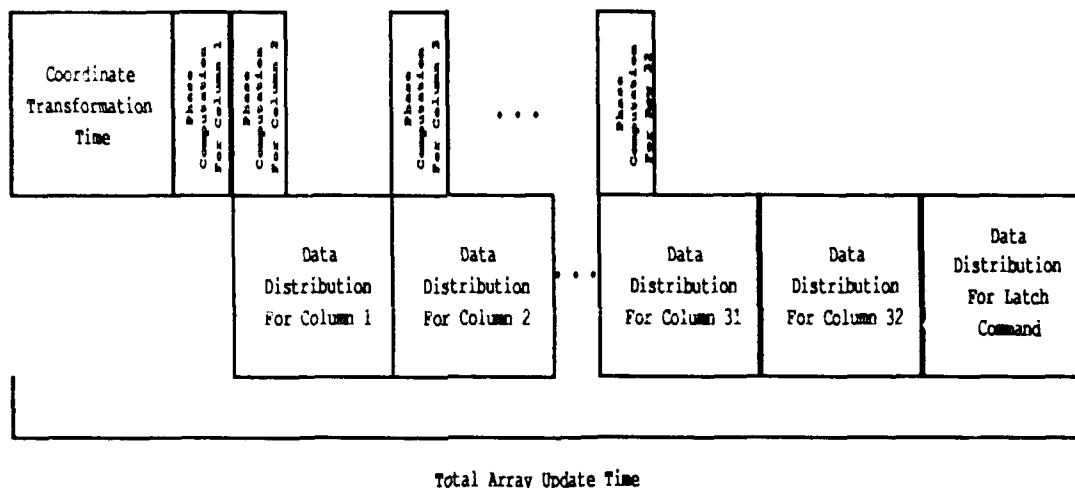


Figure 6 Contributing Components to the Array Update Time

The coordinate transformation time is the processing time required for the BSC digital signal processor (DSP) to transform the input beam pointing command from azimuth and elevation angles to θ_x and θ_y .

The subarray phase computation time is the amount of time it takes the Phase Computation section to take the $(f/f_0)\pi\sin\theta_x$ and $(f/f_0)\pi\sin\theta_y$ data, multiply them by the appropriate row and column number, truncate the unnecessary bits to the correct four bits, round them to achieve the most accurate four bits, and finally add them.

The subarray data distribution time is the amount of time it takes the Matrix Interface section to perform the following tasks.

- Convert the 16 bit data word from a parallel to a serial signal
- Serially send the signal to the appropriate subarray
- Read the five bit column address from the Phase Computation section
- Send the clock to appropriate subarray

Figure 7 shows that the Coordinate Transformation time is 5.5 microseconds. That is the amount of time between the "O" marker (which is 100 nanoseconds before the rising edge of the "HOST ENABLE" signal) and the "X" marker (which marks the rising edge of the "START" pulse).

Figure 8 shows that the Phase Computation time is 240 nanoseconds. That is the amount of time between the trigger (which is on the rising edge of the "START" signal) and the "X" marker (which marks the falling edge of the "LOAD/SHIFT" pulse).

Figure 9 shows that the Data Distribution time is 1.15 microseconds. That is the amount of time between the "O" and "X" markers (which mark the rising edges of sequential LOAD/SHIFT signals).

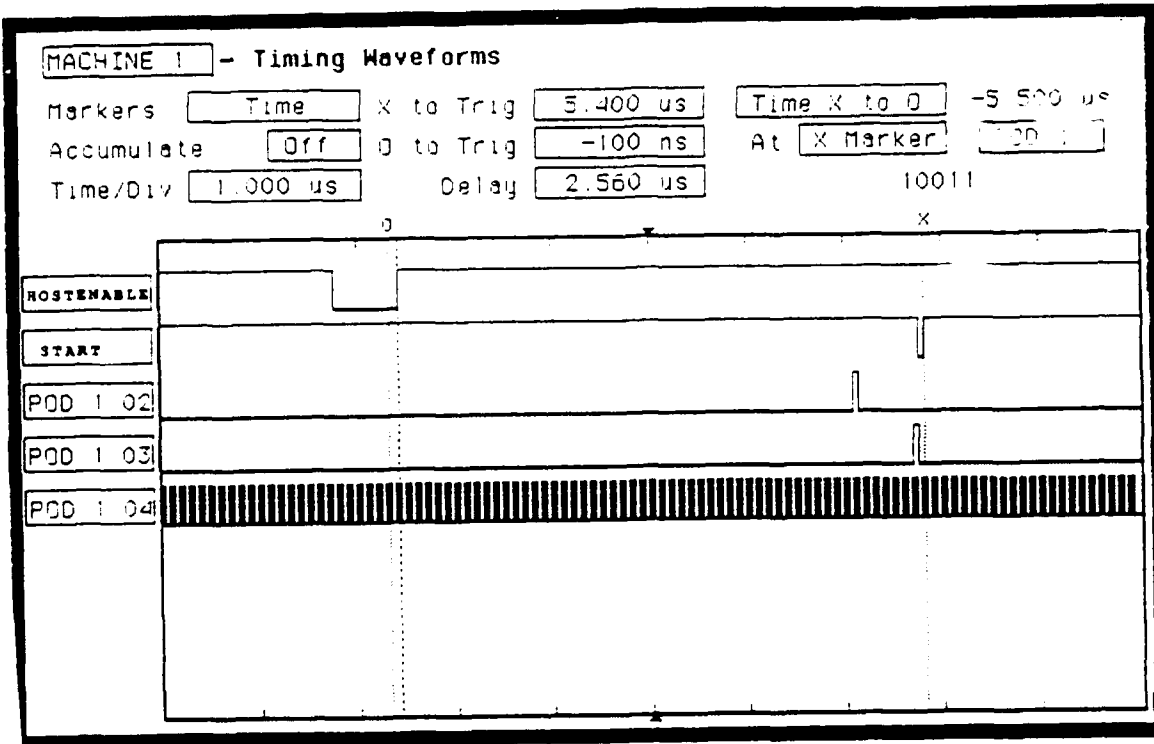


Figure 7 The Coordinate Transformation Time equals 5.5 u seconds.

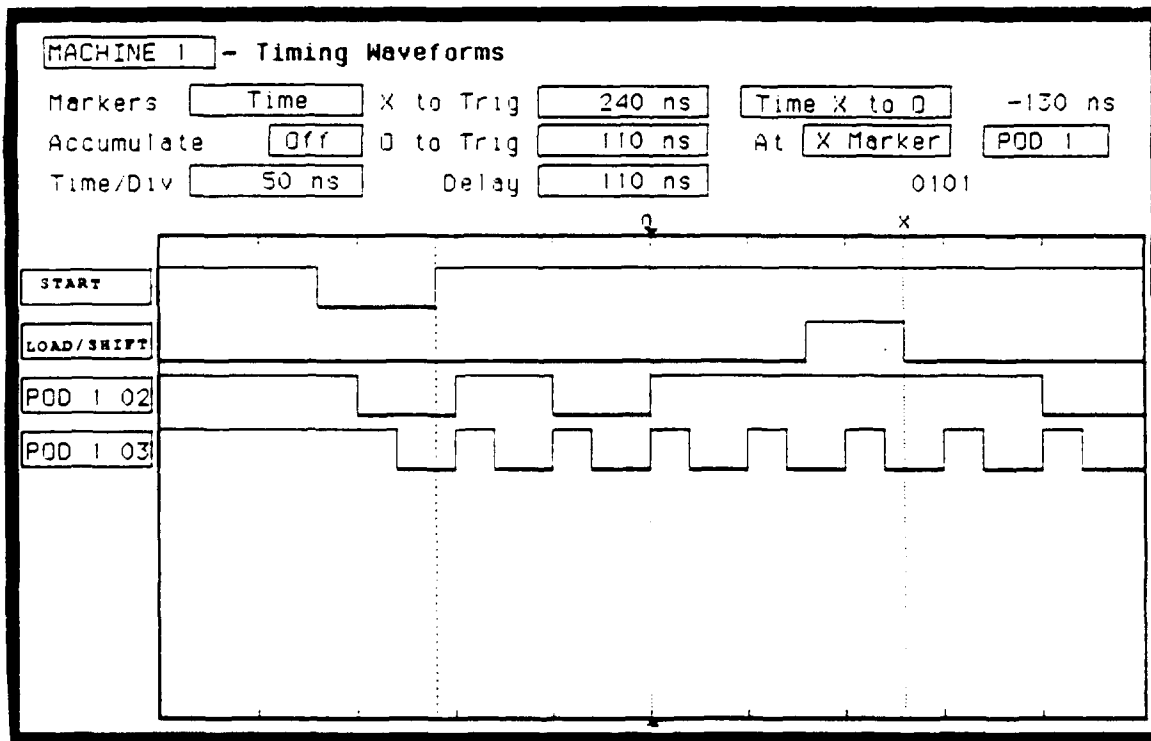


Figure 8 The Phase Computation Time equals 240 nanoseconds.

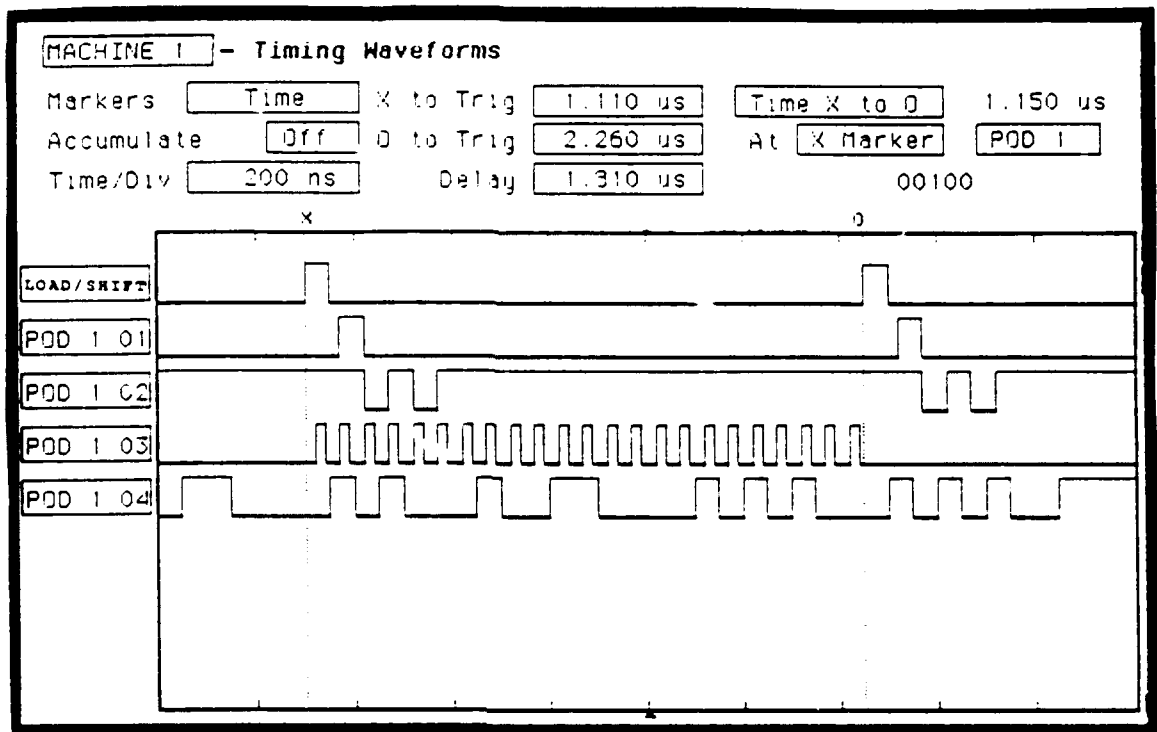


Figure 9 The Data Distribution Time Equals 1.15 Microseconds.

The total array update time is the sum of all the components (shown above) required to update the entire array with a new set of phase commands and issue the final latch command. Figure 10 shows that the Update time time is 43.7 microseconds. That is the amount of time between the trigger (which marks the rising edge of the "START" pulse) and the "X" marker (which marks the rising edge of the final latch pulse on the Array Chip).

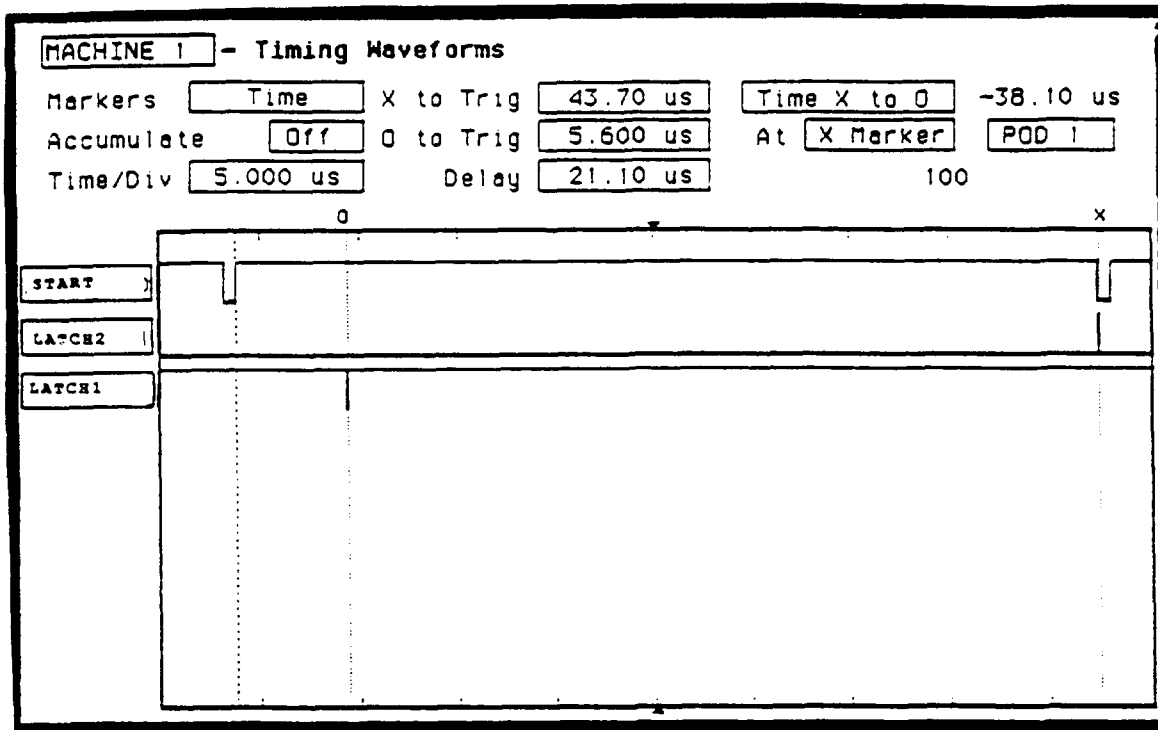


Figure 10 BSC Update Time Equals 43.7 μ seconds

(Update rate=22.9 kHz)

4.2 DATA ACCURACY

The second characteristic of the BSC which was tested was the accuracy of the system. This was tested in two ways. First, the system was simulated so that the results of the digital implementation of the BSC could be compared to a more accurate floating point computation. This determined the pointing accuracy of the design as it was implemented. The second test verified that the system actually yielded the expected results. A test station was built to automatically send in an exhaustive set of data points, read back the results and verify that the hardware

achieved the same results as the software simulator. Using this simulator the pointing space of the array has been thoroughly tested and found to include no errors in calculation for any element of the array.

4.2.1 ACCURACY ANALYSIS

Every point in the pointing space of the array has been considered in this analysis. Each θ_x and θ_y (simulated as would be computed by the DSP) was compared to the theoretical θ_x and θ_y . The maximum error was stored and printed in a file as the total system was evaluated. Two programs were written which perform this analysis. One program calculated the pointing error for every 0.2 degree increment in the Az-El space. Since the angles checked were exactly those for which there were sine and cosine values, this error is due only to the resolution of the squareroot-inverse tables. The second program calculated the pointing error on the odd angles (e.g. 0.1, 0.3, 0.5 degrees etc.). This error is the worst case pointing error due to both lookup tables. Table 2 shows the results of these programs. The maximum pointing error due only to the squareroot-inverse table is 0.12 degrees. The maximum pointing error due to both tables is 0.28 degrees. However, this error can be reduced to any desired level by increasing the size of the lookup tables. It should be

noted that the largest errors occur when the elevation is close to its extreme. (The maximum elevation tested was 60 degrees from zenith.) Greater elevations can be accurately achieved by increasing the lookup memory.

THE LARGEST POINTING ERROR DUE TO THE RESOLUTION OF THE SQRT INVERSE TABLES IN THE PHI-X DIRECTION OCCURRED AT:							
AZ	EL	PHIX	PHIX-T	PHIY	PHIY-T	ACCURX	
358.4	59.8	59.9095	59.7903	-2.7988	-2.7466	-0.1192	
THE LARGEST POINTING ERROR DUE TO THE RESOLUTION OF THE SQRT INVERSE TABLES IN THE PHI-Y DIRECTION OCCURRED AT:							
AZ	EL	PHIX	PHIX-T	PHIY	PHIY-T	ACCURY	
268.4	59.8	-2.7988	-2.7466	-59.9095	-59.7903	-0.1192	
THE LARGEST POINTING ERROR DUE TO THE RESOLUTION OF TRIG & SQRT INVERSE TABLES IN THE PHI-X DIRECTION OCCURRED AT:							
AZ	EL	PHIX	PHIX-T	PHIY	PHIY-T	ACCURX	
110.9	59.1	-30.5182	-30.7977	57.3304	57.3548	-0.2795	
THE LARGEST POINTING ERROR DUE TO THE RESOLUTION OF TRIG & SQRT INVERSE TABLES IN THE PHI-Y DIRECTION OCCURRED AT:							
AZ	EL	PHIX	PHIX-T	PHIY	PHIY-T	ACCURY	
20.9	59.1	57.3304	57.3548	30.5182	30.7977	0.2795	

Table 2 Pointing Error Analysis

4.2.2 ACCURACY VERIFICATION TESTS

A five hour exhaustive test was run to determine if the hardware was actually producing the expected simulated results.

In this test all combinations of azimuth and elevation angles (in one degree increments) were tested (21,600 test points). With this procedure the pointing space of the array has been thoroughly tested. No errors in calculation were found for any element of the array.

5.0 CONCLUSIONS

A Matrix-Feed method of controlling a monolithic phased array system has been presented. It offers several advantages over traditional approaches.

- It has a low subarray pin count (2 signal pins per subarray).
- It has a low number of interface signals between the controller board and the subarrays (64 wires for 1024 subarrays).
- It is a low risk approach for a monolithic BSC design due to a simple, low gate count architecture.
- It provides a flexible architecture by providing processing external to the subarrays.
- It provides array update at rates faster than 20 KHz.
- It can provide for self test without additional subarray connections.
- It provides for array synchronization without additional subarray connections.

- It provides a design that assures identical subarrays.
- It provides a phased array system concept that allows for graceful degradation, insuring higher reliability than conventional BSC's.
- It provides for low power and heat dissipation due to the minimal number of digital gates on the substrate.

Hardware has been built and tested which demonstrates the concept, and proves that update rates of greater than 20KHz are achievable for a large (4096 element) phased array. There are now a number of efforts which are being considered to make this method of control practical. First of all, improvements are being considered which will substantially reduce the size of the controller. Size reduction can be accomplished through the use of a single gate array. It has been calculated that, except for the DSP chip and associated EPROMS and support logic, the entire controller board can be realized in a gate array with fewer than 12,000 gates. Using hybrid packaging techniques, the entire controller area can be reduced to less than four square inches.

Practical integration of the digital and RF subarray circuitry must be considered as well. HEMT (High Electron Mobility Transistor) technology is required for the RF circuitry at 44 GHz, and therefore any digital circuitry which is contained on the same chip must be realized using this same technology.

There is at least one advantage to using HEMT technology in combining RF and Digital circuitry on the same chip, since it has been shown that HEMTs are much less susceptible to threshold variation with gate length than are MESFETs [1]. High yield one micron technology HEMTs can therefore be used for the digital circuitry, while reserving high performance (but lower yield) 1/4 micron gate lengths for the RF circuitry.

Other considerations include the logic family to be used on the subarray. If threshold voltages can be held constant, DCFL (Direct Coupled FET Logic) is ideal, due to the small size of the circuitry and the low power dissipation.

As GaAs chip yields improve, a point may be reached where the phased array controller can be entirely integrated onto the same chip as the RF circuitry. Today however, the Matrix-Feed method offers a practical alternative which can be put into place with current chip yields, and yet is flexible enough to adapt to the requirements of the future.

6.0 Acknowledgements

The authors would like to acknowledge the support of RADC under contract F19628-89-C-053, and several helpful discussions with RADC-Hanscom personnel.

7.0 References

- [1] Masayki Abe et al., "Recent Advances in Ultrahigh-Speed HEMT LSI Technology", *IEEE Transactions On Electron Devices*, Vol. 35, No. 10, Oct. 1989 pp.2021-2031

OMNIDIRECTIONAL KU-BAND DATA LINK ANTENNA DESIGN

F. Hsu

A. J. Lockyer

Northrop Aircraft Division

One Northrop Ave,

Hawthorne, CA 90250

ABSTRACT

An antenna fabricated from a conventional Ku-band rectangular waveguide $TE_{1,0}$ mode feed, transitioned into a circular waveguide for propagation is described. The transition radius from the rectangular to the circular waveguide was dimensioned for $TM_{0,1}$ mode propagation to achieve maximum omnidirectional coverage. This design was conceived for an aircraft application, and has the following advantages over other techniques: 1) greater power handling, 2) simplicity of construction, 3) ease of installation, and 4) reliability and maintainability. The antenna makes use of an impedance tunable device to optimize bandwidth within the required beamwidth coverage. Analytical methods for predicting antenna patterns are described and compared with actual measurement data taken on a 5 foot diameter ground plane to simulate the aircraft/antenna installation. Finally, design modifications to achieve 4π steradian coverage are also presented.

1. INTRODUCTION

Airborne data link system integration is placing increasingly severe requirements on antennas such as providing (1) anti-jam, (2) surveillance, (3) intra-flight communication, (4) unmanned airborne vehicle for target acquisition, (5) narrowband detection beyond a specified detection range (normally 50 nm), (6) reliable communications up to a specified range (normally 30 nm). These requirements are mandatory for many airborne applications involving high speed fighter aircraft.

The design of an omni-directional Ku-band data link aircraft antenna, based on simplicity of construction and ease of installation, is briefly described. A conventional Ku-Band rectangular waveguide (WR-62) with $TE_{1,0}$ mode feed, transitioned into a $TM_{0,1}$ mode circular waveguide forms the basis of the design generating essentially a monopole pattern. The results of practical antenna measurements taken on a 5 feet ground plane for VSWR, radiation patterns, gain and power handling are presented. Theoretical modeling of the antenna performance installed on the aircraft is explained and predicted pattern distortion due to airframe interaction calculated. Finally, design modifications to achieve 4π steradian pattern coverage are also presented for a future special program.

2. OVERALL AIRCRAFT ANTENNA DESIGN REQUIREMENTS

An aircraft must be designed to meet mechanical, electrical, reliability, maintainability, safety, quality assurance (QA), electromagnetic compatibility (EMC) performance requirements and cost effectiveness. Both mechanical and aerodynamic requirements impose severe constraints in terms of static and dynamic stress, size, shape, weight and a heavy burden for the environmental control systems (ECS).

Important electrical requirements for aircraft antenna design are: frequency of operation, bandwidth, beamwidth, radiation pattern, polarization,

gain, VSWR, power handling, and radar cross section (RCS). An electromagnetic compatibility (EMC) assessment must be performed for all airborne antennas primarily to ensure that out-of-band electromagnetic cross coupling does not degrade system performance. Reliability, maintainability and safety (RMS), and QA are important considerations also to be observed during aircraft antenna installation. But perhaps the single most important factor featured in the antenna design described is cost effectiveness.

3. ANTENNA DESIGN

Several types of antenna were considered. Since microstrip lines are not well suited for high power handling applications, a waveguide type of antenna was chosen. A conventional rectangular waveguide (WR-62) and a circular waveguide were used. Whenever it is desired to couple two different waveguides together, either in the same or different modes, some type of transition unit is needed. For this application the rectangular waveguide was fed with $TE_{1,0}$ mode. (See Figure 1), and transitioned into the circular waveguide. The transition radius from the rectangular to circular waveguide was dimensioned for $TM_{0,1}$ mode (see Figure 2) propagation to achieve maximum omni-directional pattern coverage.

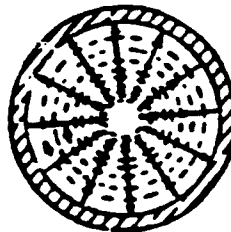
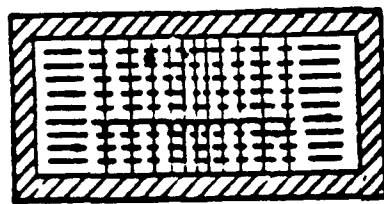


Figure 1: $TE_{1,0}$ Mode Figure 2: $TM_{0,1}$ Mode

The radius of the circular waveguide was determined by the standard formular for the $TM_{0,1}$ mode:

$$\lambda_c = \frac{2\pi a^\dagger}{\mu_{m,n}} \quad (1.1)$$

where λ_c is the cut-off wavelength, a is the radius of the waveguide and $\mu_{m,n}$ is the n root of the Bessel equation $J_m(\mu) = 0$. Evaluating the constant $\mu_{m,n}$ for values of m and n equal to 0 and 1 respectively we have the result that $\mu_{0,1} = 2.405^{\dagger\dagger}$. Substituting this value for the root of the Bessel function in equation (1-1) enables the radius of the circular waveguide to be calculated as a function of the required wavelength.

$$\lambda_c = \frac{2\pi a}{2.405} \quad (1.2)$$

$$a = .383\lambda_c \quad (1.3)$$

The primary impedance matching section was designed at the end of the rectangular waveguide with a movable short tuning block. This type of external tuning device is much better and easier than the matching window method which uses an iris^{††} inside of the waveguide between rectangular and circular waveguide. The secondary impedance matching device uses a dielectric cap placed on the output of the circular waveguide. This cap was specially shaped with dielectric material to form a radome and has a dual purpose in that 1) it serves as a weather shield, and 2) provides a means of impedance matching to improve the radation pattern. The primary impedance matching device is a movable tuning block shown in Figure 3.

This type of antenna design was conceived for an aircraft application and has the following advantages over other techniques: 1) high power handling (as

[†] - "Microwave Transmission Design Data," see [1] for details.
^{††} - "Electrical Enginnering Handbook," see [2] for details.

no sharp corners are presented to cause corona or electrical breakdown, 2) simplicity of construction, 3) ease of installation and access and 4) cost effectiveness.

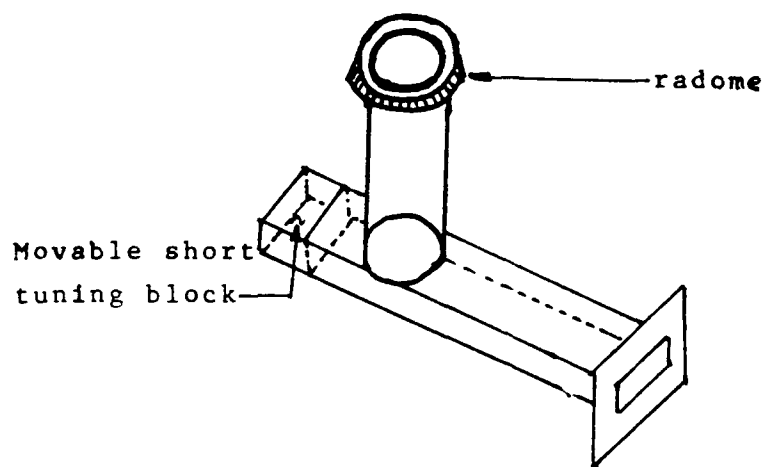


Figure 3: Antenna Assembly

4. ANTENNA TEST

An engineering model unit consists of a six inch long rectangular waveguide (WR-62) with choke flange (UG 541 A/U) and a 3 inch long circular waveguide with a radome. The unit was fabricated and successfully evaluated prior to the fabrication of the production units. The item weight amounted to approximately one pound per unit. The impedance matching devices at the end of the rectangular waveguide and at the end of the circular waveguide were used to optimize for the best possible VSWR as shown in Figure 4.

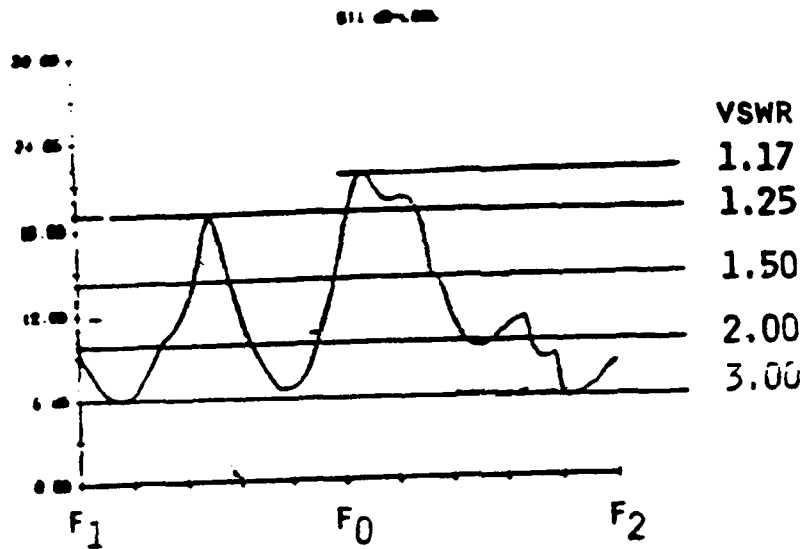


Figure 4: Antenna VSWR

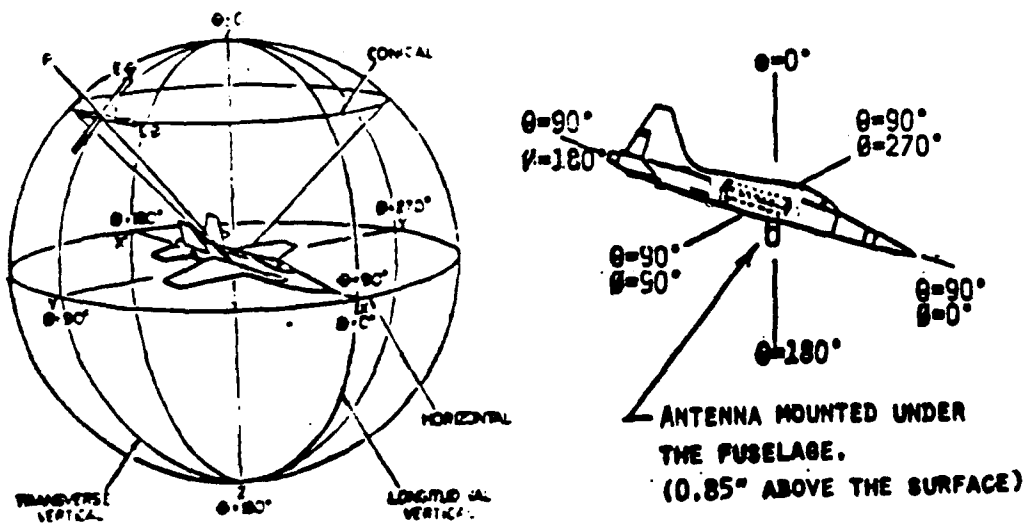


Figure 5: Antenna/Aircraft Coordinate System

The test results showed the VSWR of less than 3:1 within the entire frequency of operation. The best VSWR for the center frequency was 1.7 to 1, however a VSWR of 1.25 to 1 was chosen for the transmitting and receiving

frequencies. The VSWR tests were repeated after the impedance tuning short block position was determined and permanently sealed. A pre-production antenna was fabricated and tested for VSWR, power handling, radiation pattern and gain measurements. The production antennas were tested for VSWR only prior to installation on the aircraft.

The antenna radiation patterns measurements were conducted on a five feet diameter ground plane to simulate the aircraft antenna installation. The antenna radiation patterns were taken per aircraft/antenna coordinate system, Figure 5, for an elevation (pitch cut) and azimuth (conical cut) planes evaluation to verify the proper polarization on omnidirectional coverage.

A total of 16 radiation patterns including pitch cuts, conical cuts ($\theta = 90^\circ$ to $\theta = 140^\circ$ with 10° increments) and cross polarization cuts for both transmitting and receiving frequencies, F_T and F_R , are presented in Figure 6 through 21.

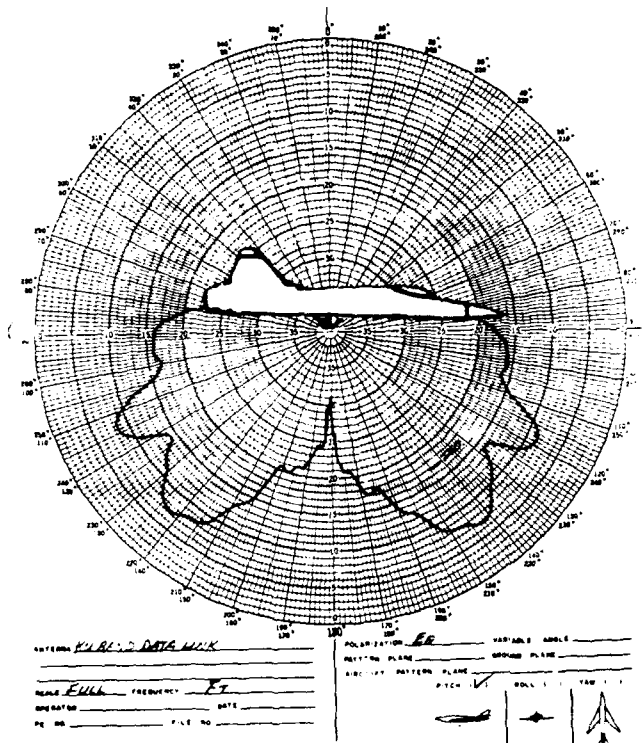


FIGURE 6
 POL. -VERTICAL
 FREQ. -FT
 PITCH CUT

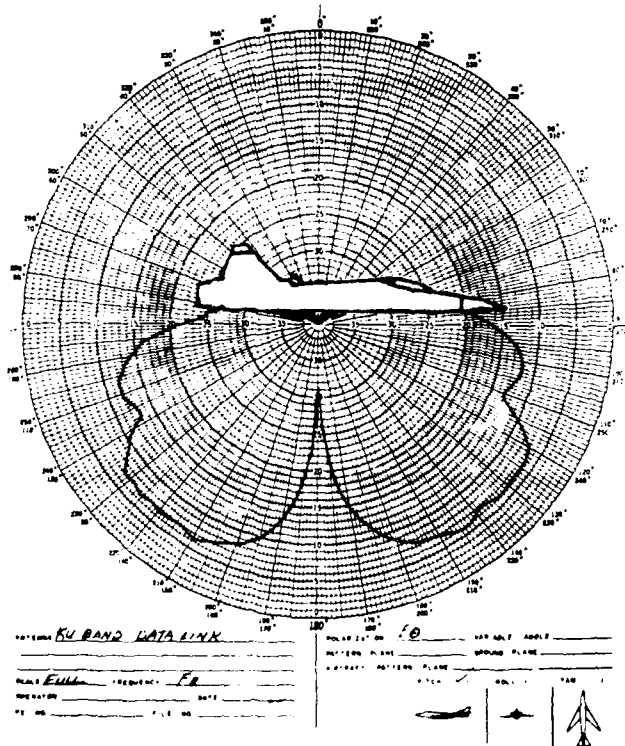


FIGURE 7
 POL. -VERTICAL
 FREQ. -FR
 PITCH CUT

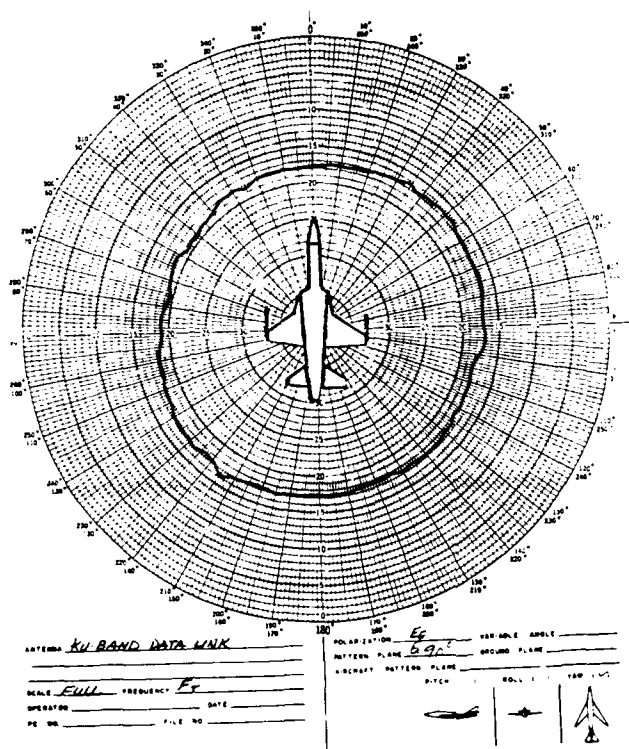


FIGURE 8
 POL. -VERTICAL
 FREQ. -FT
 CONIC CUT- $E\theta=90^\circ$

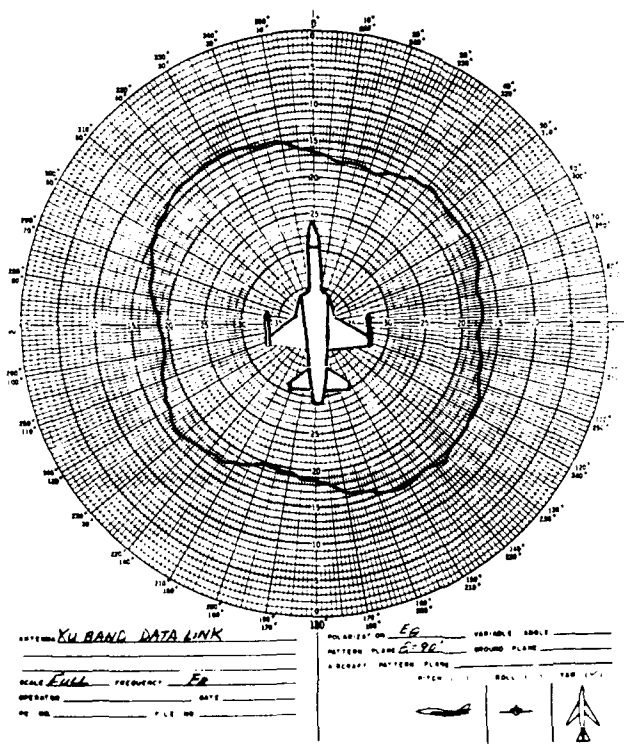


FIGURE 9
 POL. -VERTICAL
 FREQ. -FR
 CONIC CUT- $E\theta=90^\circ$

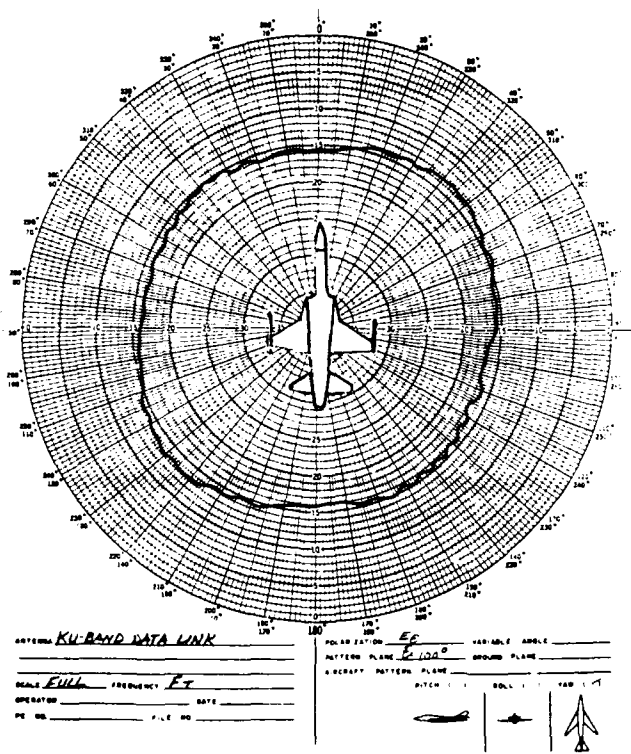


FIGURE 10
 POL. -VERTICAL
 FREQ. -FT
 CONIC CUT- $E\theta=100^\circ$

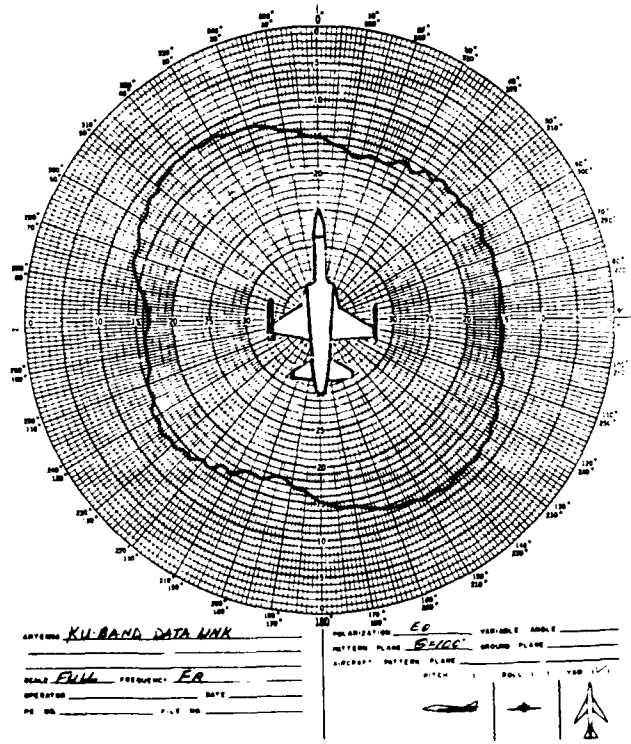


FIGURE 11
 POL. -VERTICAL
 FREQ. -FR
 CONIC CUT- $E\theta=100^\circ$

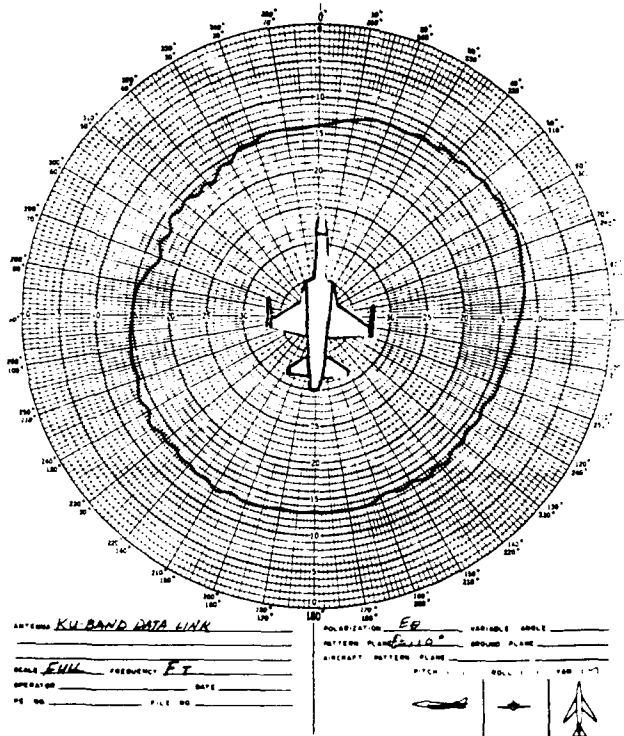


FIGURE 12
 POL. -VERTICAL
 FREQ. -FT
 CONIC CUT- $E\theta=110^\circ$

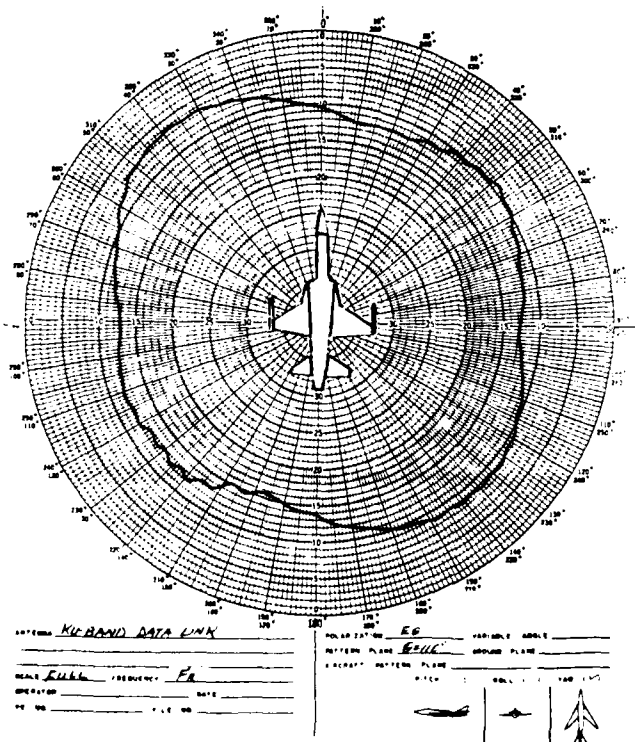


FIGURE 13
 POL. -VERTICAL
 FREQ. -FR
 CONIC CUT- $E\theta=110^\circ$

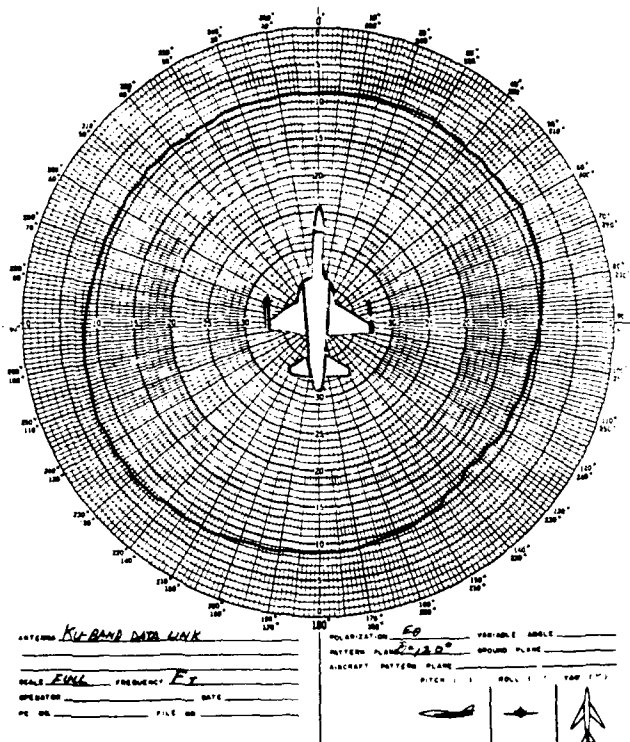


FIGURE 14
 POL. -VERTICAL
 FREQ.-FT
 CONIC CUT- $E\theta=120^\circ$

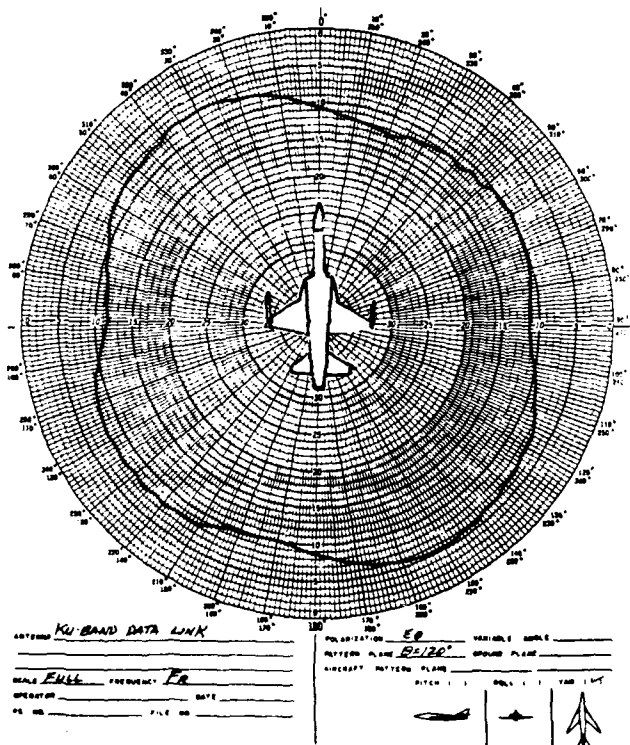


FIGURE 15
 POL. -VERTICAL
 FREQ.-FR
 CONIC CUT- $E\theta=120^\circ$

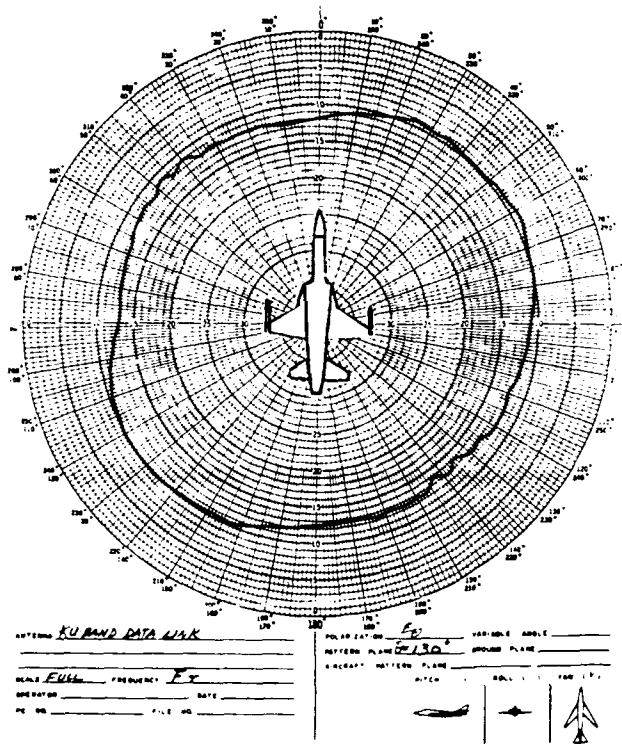


FIGURE 16
 POL. - VERTICAL
 FREQ. - FT
 CONIC CUT - $E_{\theta} = 130^{\circ}$

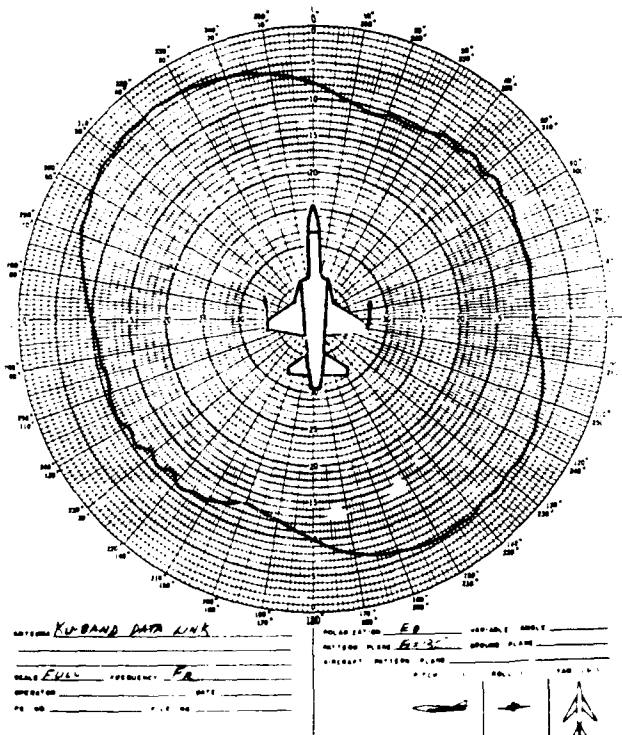


FIGURE 17
 POL. - VERTICAL
 FREQ. - FR
 CONIC CUT - $E_{\theta} = 130^{\circ}$

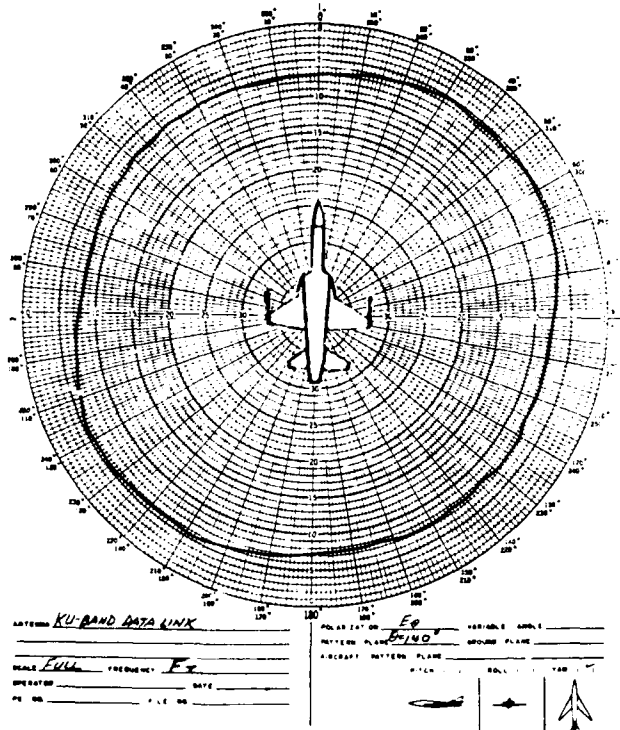


FIGURE 18
 POL. -VERTICAL
 FREQ.-FT
 CONIC CUT- $E\theta=140^\circ$

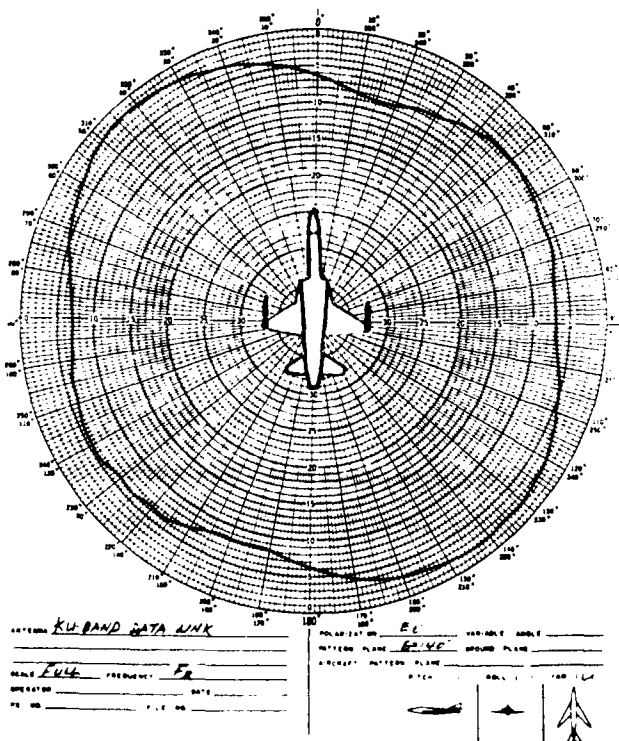


FIGURE 19
 POL. -VERTICAL
 FREQ.-FR
 CONIC CUT- $E\theta=140^\circ$

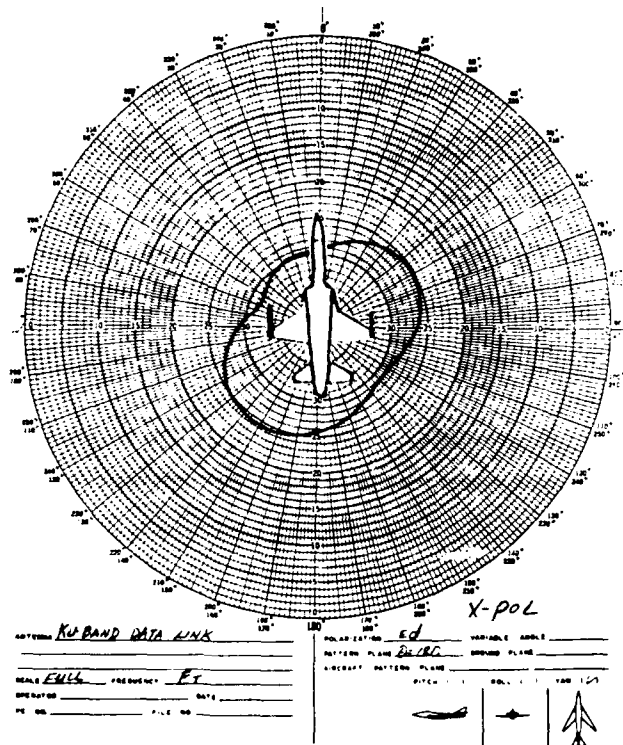


FIGURE 20
 POL. -HORIZONTAL
 FREQ.-FT
 CONIC CUT- $E\theta=130^\circ$

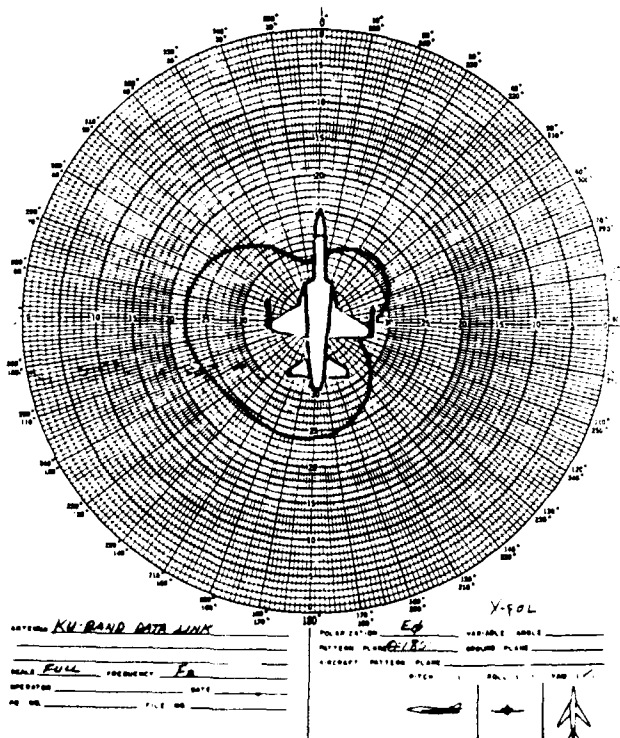


FIGURE 21
 POL. -HORIZONTAL
 FREQ.-FR
 CONIC CUT- $E\theta=130^\circ$

5. ANTENNA TO AIRFRAME INTERACTION

As the antenna tested was not mounted on a full scale mock-up during the antenna radiation pattern measurements the aircraft interaction from wings, fuselage and other aircraft structures was modeled with the General Electromagnetic Model for the Analysis of Complex Systems (GEMACS) [3]. Resident within the single GEMACS code are four widely used and fairly general physics formulations which give the code extensive applicability to a large variety of electromagnetic problems. These physics formulations include (1) the method of moments (MOM) (low frequency model) which applies to the analysis of an aerospace vehicle's interaction with EM phenomena whose wavelength is large compared to the vehicle resonant region, (2) the geometrical theory of diffraction (GTD) (high frequency model) for frequencies where the vehicle is electrically large, (3) and a finite difference technique which allows fields coupled through apertures into interior regions to be quantitatively assessed. GEMACS also possesses the capability to hybridize all of the physics formulations described above [4].

The hybrid MOM/GTD formulation of GEMACS was used to model antenna performance on 1) a five foot ground plane for measurement comparison purposes, and 2) on an actual aircraft structure to predict the airframe distortion effects of the pattern in the lower hemisphere. Figure 22 shows a low frequency GEMACS MOM model close to the airframe's resonant frequency while Figure 23 shows how this structure, derived from the low frequency MOM model, was built with basic GTD elements which include plates, cylinders and end caps. Figures 24 and 25 are the results of the ground plane analysis showing that the GEMACS simulated patterns in azimuth and elevation compare very closely to measured results. The airframe distortion effects are presented in Figures 26 and 27 which show that the azimuth pattern shape is retained while the elevation pattern is distorted in the third quadrant and the null is filled in, due to reflections and diffraction from the wings, tail and local fuselage structure.

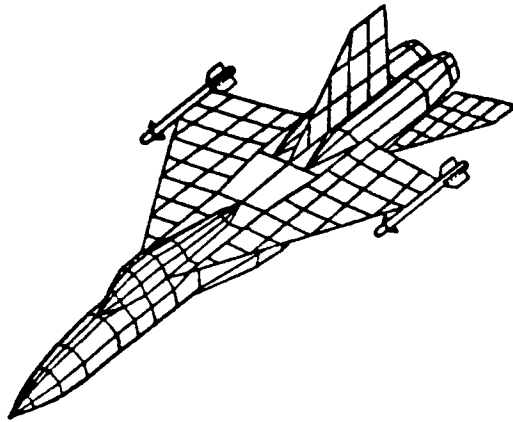


Figure 22: GEMACS MOM Model

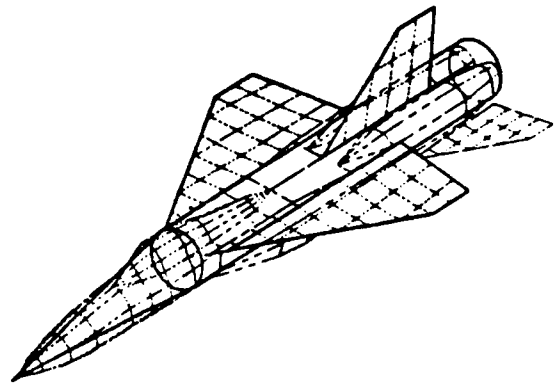


Figure 23: MOM/GTD Hybrid Model

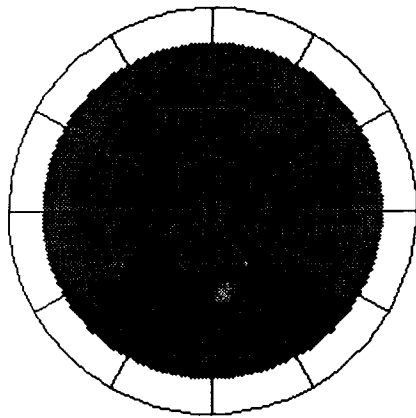


Figure 24: Yaw Cut (Ground Plane)

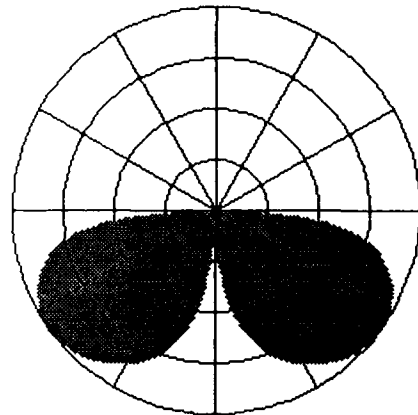


Figure 25: Pitch Cut (Ground Plane)

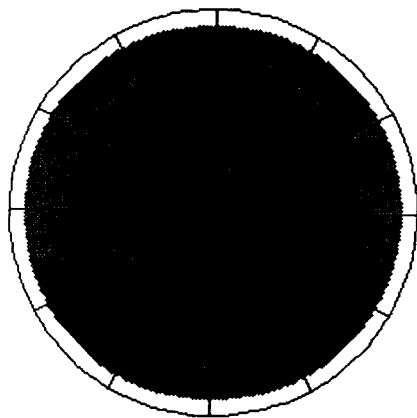


Figure 26: Yaw Cut (on Aircraft)

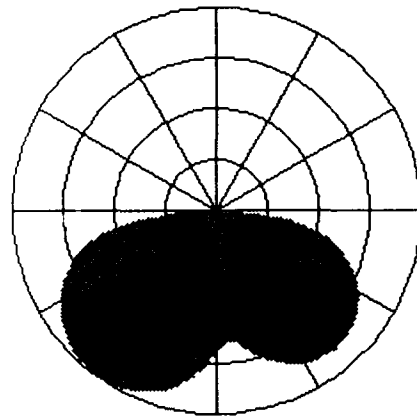


Figure 27: Pitch Cut (on Aircraft)

6. SUMMARY AND CONCLUSIONS

It has been demonstrated that a relatively simple cost effective, robust antenna for data link applications can readily be fabricated by transitioning from a rectangular to circular waveguide for efficient propagation. Test results and analysis show that all electrical performance requirements including radiation patterns, VSWR, gain, bandwidth, beamwidth and high power capabilities imposed by aircraft applications can be met. Although not discussed in detail here, an EMC analysis was also performed to ensure that the antenna installation did not interfere with other aircraft antennas or couple to other sensitive avionic equipments. Pattern distortion due to the aircraft installation was predicted by analytical means and found not to be significant.

During the antenna evaluation, a precaution was taken in the radiation pattern characteristics to ensure that only the $TM_{0,1}$ mode radiated. A critical design parameter was to make sure that the diameter of the circular waveguide at the transition corresponded to the cut off wavelength for $TM_{0,1}$ mode of operation.

The test results showed that the antenna bandwidth was 12% within the VSWR range of 1.5 to 1. This bandwidth can be improved. An experimental effort has been initiated to broaden the bandwidth by using double ridged waveguides. A design using the $TM_{0,1}$ and $TE_{1,1}$ excitation modes of a circular waveguide will provide hemispherical pattern coverage. The full 4π steradian can thus be achieved by installing upper and lower antennas on the aircraft fuselage.

ACKNOWLEDGEMENT

Valuable assistance for the design, test and fabrication of this antenna were provided by Dr. S. Govind and Messrs A. B. Hitterdal, S. Lalande, N. Mitsuoka, K. Smith and J. Marczinco.

REFERENCES

1. Moreno Theodore, "Microwave Transmission Design Data," Chapter 7, page 121, Dover Publications Inc. March, 1948.
2. Pender and Mallivain, "Electrical Engineering Handbook," Fourth Edition, page 10-26, John Wiley and Sons, Inc. August, 1957.
3. Kadlec, D.L. and Coffey, E.L., "General Electromagnetic Model for the Analysis of Complex Systems (GEMACS), User Manual (V4)," The BDM Corporation, RADC-TR-87-68, Volumes I,II, and III, May 1987. Vol I: ADB114131L; Vol II: ADB113530L; Vol III: ADB113531L
4. Coffey, E. L. "Solution of Multi-Region, Aperture-Coupled Problems with GEMACS 4.0," presented at the Fourth Annual Review of Progress in Applied Computational Electromagnetics at the Naval Postgraduate School, Monterey, CA, March 1988.

**A RETROSPECTIVE ON
ANTENNA DESIGN VIA WAVEGUIDE MODES**

K. C. Kelly
Radar Systems Group
Hughes Aircraft Company
El Segundo, CA

ABSTRACT

This text presents a revisit, spanning 35 years, of a variety of antenna problems which have been solved with lesser used waveguide geometries and/or lesser used waveguide modes in common waveguide geometries. The aim has been to achieve rather natural solutions to the realization of specified antenna radiation patterns, polarizations, or frequency band(s) of operation while also accomplishing some specified physical shape, interlacing of frequency bands and/or polarizations, or fabrication concept.

In particular, interlaced multiband slotted waveguide array antennas, radial waveguide fed slot array antennas, conformal array antennas using conical waveguides, square multimode horn antennas, and dual polarization slot array antennas are described.

1. RECTANGULAR WAVEGUIDE MULTIBAND SLOT ARRAYS¹

1.1 Slotted Rectangular Waveguide S and X band Array - Because of the vintage of the writer we here use the rectangular waveguide nomenclature and geometry of Marcuvitz². The inside dimension height, b , of rectangular waveguide is measured along the y axis and the inside dimension waveguide width, a , along

the x axis.

Since S band wavelength is nominally three times that of X band, there is no difficulty in causing a rectangular waveguide to operate in the $TE_{1,0}$ mode for S band and the $TE_{3,0}$ mode for X band. The b dimension of the waveguide was kept to less than one half a free space wavelength at X band to assure that only $TE_{m,0}$ modes would be possible at X band. An exciter at one end of this small height rectangular waveguide launched the S band energy, while another exciter launched the X band $TE_{3,0}$. Both modes generate purely longitudinal, z direction, current in the center of the broad wall. Thus, longitudinal S band slots half waveguide wavelength spaced along that center line of the broad wall will not radiate either S band or X band energy since those longitudinal slots cut no wall currents. The S band slots are then probe excited by placing probes on the lines $x=a/3$ and $2\cdot a/3$ along which lines the electric fields for the X band $TE_{3,0}$ are always zero. The probes do not affect the X band energy. Tapering of the excitation of the S band linear array is achieved by varying the probe length according to position along the S band array.

Now, broad wall X band slots whose centers lie on the lines $x=a/3$ and $2\cdot a/3$ will not couple to the X band energy if they are transverse slots, parallel to the x direction. Pairs of such slots may be spaced a half wavelength at the X band frequency and are made to radiate the desired amount of X band energy by rotating the X band slots a few degrees from being purely transverse. The directions of rotation are chosen to cause the radiation from all X band slots to be in phase. The X band slots do not couple to S band energy because they are too far below resonant length for the S band energy.

Once excited by the $TE_{3,0}$ mode, the X band slots scatter energy which couples

to the $TE_{1,0}$ mode. Because all of the X band slots are in phase but only half wave-length spaced at X band, there is no reinforcement of coupling to the longitudinal top wall currents of the 1,0 mode. The directions of the X band slot rotations, however, is such that reinforced coupling to the transverse currents of the unwanted $TE_{1,0}$ is produced and that energy would couple to the S band slots which are three half wavelengths at X band. Because of this, X band $TE_{1,0}$ mode suppressors were built into the bottom broad wall of the waveguide.

This design approach to a dual frequency band linear array produces broadside S and X band beams which are orthogonally polarized to each other.

1.2 Copolarized X and K Band Rectangular Waveguide Array - A K band array has been integrated into a standard offset longitudinal shunt slots X band array in the following way. The $TM_{1,1}$ rectangular waveguide mode has field components such that there are only longitudinal currents in the broad walls, associated with there being only H_x at those wall. That being so, coupled with the fact that normal X band waveguides support the $TM_{1,1}$ at K band, allows the simple step of adding K band $TM_{1,1}$ mode exciters to an X band array and cutting pairs of K band series slots through the broad wall to achieve copolarized broadside beams at both X and K band. The X band slots do not couple to the K band energy because the X band slots are parallel to the K band wall currents and thus do not cut any.

Again, consideration must be given to other higher order modes generated by the existence of the excited K band slots. Of the several possible modes which propagate in this waveguide that supports the $TM_{1,1}$, it can be shown that only the $TE_{0,1}$ is excited, posing a potential problem. Fortunately, that mode is completely suppressed by inserting wires parallel to the x axis from narrow wall to narrow wall, at $y=b/2$. Those wires have absolutely no effect upon the X band 1,0 mode

or the K band 1,1 mode.

Investigators have demonstrated other types of multiple frequency band slotted waveguide antennas. The two types mentioned here are simply illustrative of the concept for which there are innumerable solutions.

2. RADIAL WAVEGUIDE FED SLOT RADIATOR ANTENNAS

The attractiveness of the radial waveguide³ as the basis for slot array antennas lies in two facts. First, regardless of the size of the antenna, the feeding of the radial waveguide remains the same simple center point feed. Next, the top plate of the radial waveguide is readily accessible for punching or etching all slots at once. The down side is that the single center point feed is incompatible with the idea of corporate feeding to increase the antenna's useful frequency bandwidth.

2.1 Antennas Using Lowest Order Radial Waveguide Mode - The dominant radial waveguide mode is a TEM and has simple E and H field configurations. Adopting an $r\phi z$ coordinate system in which propagation is in the r direction, ϕ is the angular azimuthal position, and z is the vertical direction perpendicular to the parallel plates, the inner surface of one plate is $z=0$ while the inner surface of the second plate is $z=\text{constant}$. Then, the only field components will be E_z and H_ϕ . The currents induced in the plates are purely radial, resulting from the cross product of H_ϕ and z -directed normals to the plates.

2.1.1 Linear polarization at the peak of a broadside pencil beam results when a set of half wavelength long slots perpendicular to radii are cut along a circular arc of 180° , and a second set of similar slots cut in the remaining 180° but at a radius one half wavelength different. Radial waveguides produce radial propagation whose phase and amplitude are described by the Hankel functions, so

the meaning of "half wavelength" is not simply c/f , the velocity of light divided by the frequency.

Concentric half rings of slots can be arrayed to fill the aperture for higher directivity designs. The linear polarization will be in the plane that bisects the 180° sector groups of half wavelength slots. Clearly, the slots at the ends of the 180° sectors contribute only undesired cross polarization. Tests showed an overall improvement in the desired polarization's radiation patterns and a reduction of cross polarized lobes when the individual slots forming the 180° sectors were all rotated to 45° relative to its radial line with the sign of the 45° being controlled by quadrants.

2.1.2 Circularly polarized pencil beam peaks were obtained by using circular hole radiators instead of slots. The holes are closely spaced and their centers lie along a single turn or multiturn spiral⁴ of one wavelength pitch. One wavelength is defined by the length for 360° in phase for the Hankel function between the start radius and finish radius for a complete turn of the spiral(s). The radial waveguide must be terminated in a matched load.

2.2 Antennas Using Higher Order Radial Waveguide Mode(s)⁵ - A radial waveguide with a full circle of round hole or crossed slot radiating elements would produce pure linear polarization if purely radial currents in the plates had a $\cos \phi$ dependence in amplitude, while purely circumferential currents at the same radius were controlled by $\sin \phi$.

2.2.1 The standing wave $E_{1,0}$ radial waveguide mode produces equal amplitude I_r and I_ϕ currents at discrete radii in the top and bottom plates. Furthermore, the currents have the $\cos \phi$ and $\sin \phi$ amplitude variations for the r-directed and the ϕ -directed currents. Thus, at those discrete radii the net current is every-

where parallel to a single plane. In tests of the principle using crossed slots equally spaced around a circle of the proper radius, experimental units displayed measured cross polarization levels as good as 34 db below the peak of the beam for the desired linear polarization.

At other than a set of specific radii, the standing wave $E_{1,0}$ radial waveguide mode's I_r is much larger than the azimuthal current, I_ϕ . When the mode is operating as a travelling wave, the I_r is dominant at all radii. Because of that fact, it is not possible to build an $E_{1,0}$ mode radial waveguide fed array of several concentric radiators, have the radial waveguide matched looking into the radial waveguide from a feed located at the center, and have pure linear polarization, all at the same time. A high degree of linear polarization purity was demonstrated with an array of five concentric rings of radiators, however, by using radiators that coupled to the mode very lightly, resulting in a large mismatch being presented to the feed point.

The $E_{1,0}$ radial waveguide mode is readily excited by simply making a tee joint between a circular waveguide, operating in the dominant $TE_{1,1}$ circular waveguide mode, at the center of the lower plate of the radial waveguide. The spacing of the plates must be well below one half a free space wavelength to assure that only the $E_{1,0}$ radial waveguide mode is launched.

2.2.2 It has been analyzed and demonstrated that pure traveling wave $E_{1,1}$ and $H_{1,1}$ radial waveguide modes may be excited in a single radial waveguide in such a manner as to produce $I_r \cdot \cos \phi$ and $I_\phi \cdot \sin \phi$ at all radii. An array of any number of rings of radiating elements, and matched looking into the radial waveguide, can produce pure linear polarization when the 1,1 radial waveguide mode pair is used. Launching the 1,1 mode pair is considerably more difficult than

launching either the 0,0 or the 1,0 E-type radial waveguide modes.

2.3 Polarization Options With Radial Waveguide Fed Arrays - The linearly polarized radial waveguide fed arrays, described above, which use the $E_{1,0}$ or combined $E_{1,1}/H_{1,1}$ radial waveguide modes will produce circular polarization by simply placing a circular polarizer into the input waveguide. For example, a quarter wave plate or other circular polarizer inserted into the dominant mode circular waveguide that launched the $E_{1,0}$ radial waveguide mode makes the standing wave antenna's beam circularly polarized. Similarly, if instead of a circular polarizer an orthomode junction is attached to the $TE_{1,1}$ circular waveguide, one then gets two coincident beams made independent by orthogonality of their linear polarizations. Connecting those two ports from the orthomode junction to a network containing a power divider and a phase shifter enables the antenna to select any arbitrary polarization characteristic for the main beam of the antenna.

2.4 Monopulse Antenna Excited By Radial Waveguide - The $H_{0,1}$ radial waveguide mode has just one electric field component, namely E_ϕ . That means that the electric field lines close on themselves, forming circles around the z axis. It follows, then, that slicing that radial waveguide with conducting planes containing the z axis will not affect the mode since the electric field is always perpendicular to those conducting planes.

Two conducting sheets were placed in an $H_{0,1}$ radial waveguide at right angles to each other to create four 90° sectoral regions. A single slot, parallel to the z axis, at the vertex of each 90° sector provided independent excitation for each sector. Radiating slots were cut in the top plate for each quadrant. When the four mode excitation slots, one in each quadrant, were connected to a Σ and Δ network below the bottom plate, a light weight flat plate monopulse antenna was produced.

In all of the radial waveguide fed antennas discussed thus far, it had not been mentioned that arrays of concentric rings of radiators, quasi-annular slots, are spaced a full waveguide wavelength apart. That full wavelength spacing is used because there is, for radial waveguide fed arrays, no equivalent phase reversal mechanism such as that which allows half waveguide wavelength spaced slots in antennas fed by rectangular waveguides. In order to achieve aperture filling with the monopulse antenna discussed in this section, the rings were spaced only one half wavelength apart but the innermost ring of slots were all shorter than resonant length. The next ring had slots longer than resonant. The third ring, again shorter than resonant, etc. By this means, instead of having the phase of successive rings alternate $0, \pi, 0, \pi$ producing considerable destructive interference, a much more benign $-\pi/4, +\pi/4, -\pi/4, +\pi/4$ phasing was achieved.

Again, it needs to be stated that in discussing radial waveguide transmission lines here, the term "wavelength" is being used without repeatedly stating that radial waveguide "wavelength" is a function of position along the transmission direction because of the Hankel function's characteristics.

3. CONICAL CONFORMAL SLOT ARRAY

The conical waveguide⁶ is suggestive of the shape of the nose of high speed aircraft or missiles. A thin walled 40 degrees total angle conical shell, $\theta_2=20^\circ$, and an inner cone of total angle 20 degrees, $\theta_1=10^\circ$, were combined to form a conical waveguide. Furthermore, the inner cone was coated with paraffin wax finished so as to have the wax's surface at $\theta_{inner}=13^\circ$. Similarly, the inner surface of the outer cone had a wax sleeve with the surface of the wax at $\theta_{outer}=17^\circ$.

At the common vertices, a coaxial line excited the dominant TEM wave in the

conical waveguide. Half wavelength long slots cut in the outer conical shell were arranged in 180° circular arcs on one half of the cone and spaced to create a forward looking pencil beam on the axis of the outer cone when both the inner cone and the outer cone were coaxial. A similar set of slotted 180° arcs on the other half of the cone are positioned to reinforce the peak of the beam produced by the first set. When the inner cone's axis was moved off of the outer cone's axis, keeping the cone vertices coincident, the beam is scanned off of the outer cone's axis.

This lowest order mode approach to the use of the conical waveguide has the same strong generation of cross polarized fields for the same reason as given in section 2.1.1 above. Though it might be possible to reduce the cross polarized fields by the use of higher order conical waveguide modes, no attempt was made.

4. EQUALIZING E- AND H-PLANE BEAM WIDTHS OF SQUARE HORNS

4.1 General - The square pyramidal horn has been a popular antenna, and also a widely used type of feed for both focal point fed and Cassegrain type reflector antennas. Though the square horn will handle any type of polarization, it is useful to discuss only one linearly polarized component being present and parallel to two opposite walls. Excited with only the $TE_{1,0}$ mode and built with a small flare angle, the square horn produces the well known -13 dB sidelobes in the E-plane, -23 dB sidelobes in the H-plane, and an E/H 3 dB beamwidth ratio of 0.73:1.

For decades the E- and H-plane differences have been practically eliminated by adding the proper ratio and phase of both the $TE_{1,2}$ and $TM_{1,2}$ modes to the dominant $TE_{1,0}$ mode in the square horn. A very common method of achieving the desired result is illustrated and described in Johnson and Jasik⁷. An enlarging step

in the cross sectional dimensions of the square waveguide leading to the horn throat generates the 1,2 modes, and a following straight section continues for the purpose of phasing those modes relative to the 1,0 mode. The length of that phasing section can be quite long and make it impossible to package a feed in the space available.

4.2 A "Zero Length" $TE_{1,2}/TM_{1,2}$ Launcher/Phaser - The original 40 KW CW feeds for the 30' diameter Unified S-band Cassegrain earth station antennas, used to support the Apollo man-on-the-moon missions, were switchable RHCP/LHCP monopulse feeds. Packaging two monopulse networks formed of S-Band waveguide, plus incorporating three large high reliability S-Band waveguide switches left no room for a conventional 1,0/1,2 mode phasing section.

In a square waveguide a magnetic line source which is transverse and full width in the top wall, plus an identical in-phase magnetic line source in the bottom wall, will together scatter only the 1,n modes. Because both magnetic line sources are in phase (but the direction of their E field vectors are oppositely directed) only even n numbers can result. If those line sources are located in a square waveguide that supports only modes lower than $n=4$, one is assured of having only the $TE_{1,0}$ and $TE_{1,2}/TM_{1,2}$ modes.

Implementation of this concept was achieved with an $a \times a$ square waveguide by interrupting all four walls (to handle both polarizations) of the square waveguide. The interruptions were made by waveguides of width a and height b , where $b \ll a$, making tee junctions with the square waveguide. The incident $TE_{1,0}$ longitudinal currents are interrupted by the waveguides stubbed into the square waveguide and the stubs are thus excited, creating magnetic line sources in the square waveguide's walls. The discontinuity at the mouth of the stub waveguides

and the length, L , of the stubs are adjusted to create resonant cavities. Adjustments of b , L , and sometimes the placement of small inductive irises at the mouth of in the stub waveguides, give the needed control for adjusting the amplitude and phase of the 1,2 modes relative to the 1,0 mode. The H-plane patterns are unaffected by the 1,2 modes.

E-plane patterns matching the H-plane patterns were obtained for the Unified S-Band feeds for the 30' Cassegrain antennas which were positioned around the globe for communicating with Apollo spacecraft when in earth orbit.

5. RECTANGULAR WAVEGUIDE DUAL POLARIZATION FLAT PLATE^{8,9}

An effort was initiated to find a dual polarization flat plate antenna of the slotted rectangular waveguide type that would have a removable top plate that would permit punching or etching all slots at one time. One solution to that specification is based on the use of the rectangular waveguide mode of the standard $TE_{1,0}$ type but with the subscript index "1" replaced by a large number. In the initial design and experiments, the figure "10" was used and thus a $TE_{10,0}$ waveguide was constructed, ten times as wide as a standard $TE_{1,0}$ rectangular waveguide but of height no greater than for standard waveguide.

Looking at the $TE_{10,0}$ mode in an E-plane view one sees the E field of ten narrow-wall-to-narrow-wall $TE_{1,0}$ waveguides which have been alternately fed with phase 0 or π radians and all the narrow walls removed except for the outboard narrow walls of the first and last $TE_{1,0}$ waveguides.

Exciters at both ends of a $10 \cdot \lambda_0 / \sqrt{2}$ length of $TE_{10,0}$ waveguide, each exciter consisting of ten slots in the plane $y=b/2$ and phased alternately 0 and π , are used to launch the $TE_{10,0}$ mode. That mode propagates in the z axis direction. Ten other

exciter slots are cut through each of the narrow side walls of that z-axis-direction propagating $TE_{10,0}$ to launch a second $TE_{10,0}$ mode, this time in the x axis direction. These two orthogonal $TE_{10,0}$ modes will hereafter be referred to as the $zTE_{10,0}$ and $xTE_{10,0}$ modes, both propagating in a $10 \cdot \lambda_0 / \sqrt{2}$ square cavity-like region. It can be shown that in a lossless system the two modes are orthogonal in every sense and thus do not couple to each other. Furthermore, the exciter slots for each mode are invisible to each other.

The exciter network for the $zTE_{10,0}$ has its own input port and is completely independent of a second similar port for the $xTE_{10,0}$ that has its own network. Next, it will be explained that a set of offset longitudinal shunt slots parallel to the z axis can be positioned so as to couple to the $zTE_{10,0}$ exclusively, and similarly for a second set of longitudinal shunt slots parallel to the x axis coupling to the $xTE_{10,0}$ exclusively.

The exclusivity of coupling with either set of slots is a result of the fact that the slots which couple to one of the two modes have their center points precisely on the virtual wall, the plane of zero E field, of the other mode. There is only one component of H field at all virtual walls and that component is parallel to the virtual wall. Thus, the only current component in the slotted top wall at the center of the slots for coupling to the first mode, are absolutely parallel to the currents excited by in the top wall by the second mode and vice versa. Slots are not excited by wall current parallel to themselves or H fields perpendicular to themselves.

As mentioned above, there is one input port of this antenna which is associated with the radiating slots parallel to one axis, and another port associated with the orthogonal radiating slots. The two ports may be used to provide two independent coincident pencil beams in orthogonal linear polarizations, or the ports may be

combined via a 3 dB quadrature coupler to produce coincident independent RHCP and LHCP beams, etc.

A unit constructed to operate over a band centered at 12.5 Ghz was built employing the x and y TE_{20,0} modes. This uniform aperture illumination design achieved a measured peak aperture efficiency of 88% and an efficiency of not less than 77% over a 4% total bandwidth, including feed networks losses.

ACKNOWLEDGEMENTS

Many people aided or influenced my work over the long period indicated. I thank the following people for their help, ideas, encouragements, or discussions in the work presented: Robert S. Elliott, Charles W. Chandler, Seymour B. Cohn, John J. Erlinger, Frank J. Goebels, Jr., Charles Lindsay, Virginia T. Norwood, and Harold A. Rosen. I'm sure that memory fails me on important others. Thanks also to Hughes Aircraft Co. and Rantec Division of Emerson Electric Co.

REFERENCES

1. Kelly, K. C. (1963) Microwave Antennas for Operation at Two Frequencies. Master's Thesis, UCLA
2. Marcuvitz, N. (1951) Waveguide Handbook, McGraw-Hill Book Co., Inc., New York, N. Y.: 57.
3. Marcuvitz, N., op. cit.: 90-96.
4. Kelly, K. C. (1957) Recent Annular Slot Array Experiments, IRE National Convention Record, Part 1:144-151.
5. Goebels, F. J. and Kelly, K. C. (1961) Arbitrary Polarization from Annular Slot Planar Antennas, IRE Trans. AP-9:342-349.
6. Marcuvitz, N., op. cit.:98
7. Johnson, R. C. & Jasik, H. (1984) Antenna Engineering Handbook, McGraw-Hill Book Co., New York, N. Y.:15-25 - 15-27.
8. K. C. Kelly, (1988) U. S. Patent 4,716,415, Dual Polarization Ant.
9. K. C. Kelly, (1986) Dual Polarization Flat Plate Antenna, 1986 IEEE Aerospace Applications Conf. Digest, Steamboat Springs, CO.

A DUAL POLARISED HORN
WITH A SCANNING BEAM

ZVI FRANK

ELBIT COMPUTERS LTD.

NES-ZIONA.

ISRAEL

Abstract

The proposed antenna is a special type of Multi-Beam Antenna (MBA). Such antennas are of course well known in the literature. The unique feature of this particular antenna is that beam scanning is achieved within the confines of a single horn. The additional advantages of compactness and high gain are clearly evident in this design.

The antenna described is a compact quad-ridged Horn. Each ridge in the horn is fed separately at four orthogonal inputs to a square waveguide.

By means of an R.F. network consisting of a number of 180 degrees Hybrids and delay lines, the beam of the horn can be switched in azimuth over 110 degrees. The nominal gain of the Horn is more than 8 dBi. The aperture size is about 0.6 x 0.6 wavelengths at the low end of the band. The length of the antenna is less than three quarter of a wavelength at the low end. The antenna is extremely rugged and is designed to operate under severe environmental conditions.

1 Description of Antenna

2.3

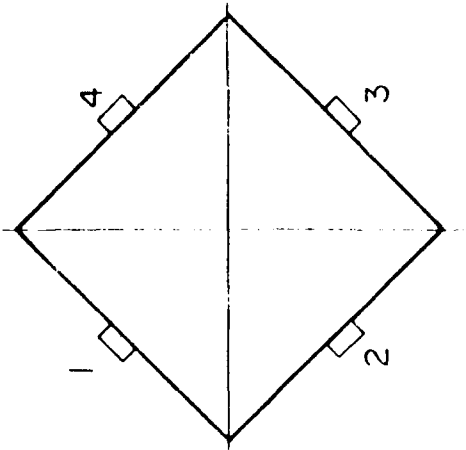
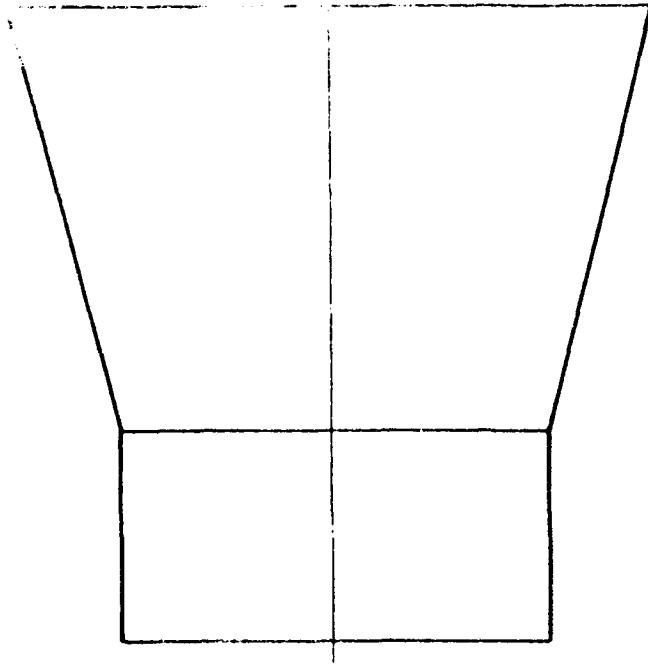
A sketch of the quad-ridged horn is shown in Fig 1. A square waveguide with four orthogonal inputs provides a launcher for the compact horn. The horn is mounted diagonally as shown schematically in Fig 2. This is necessary to provide two phase centers in the horizontal plane required for steering the beam. The summation matrix together with the switching arrangement are also shown in Fig 2.

From the vector diagram of Fig. 3 it is observed that the output ports of the 180 degree hybrids "A" and "B" yield vertical and horizontal polarisations.

It is also clear that each pair of vertical and horizontal polarisations are out of phase. Direct summation of these outputs via a second set of 180 degree hybrids provides vertical and horizontal polarisations at output "X" and "Y" respectively.

Switching of the beam in azimuth is attained by means of the four transfer switches and suitable delay lines.

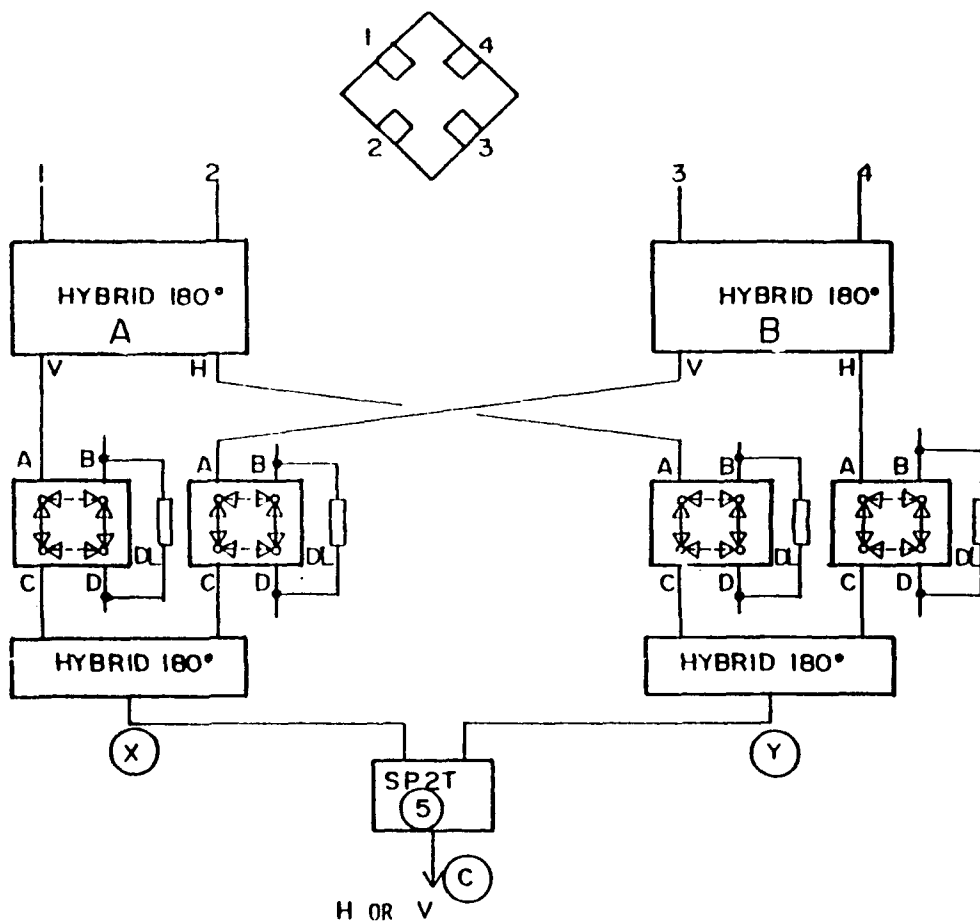
Each polarisation can be steered to the left or right by switching in a suitable delay line. The arrangement in Fig 2 is for a three beam antenna. However more beams are possible with a more complex



SKETCH OF QUAD-FED HORN

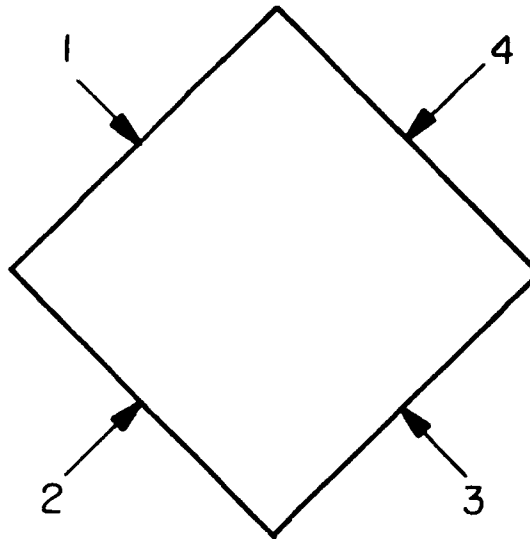
FIG 1

FIG. 2
 CONFIGURATION NO. 1
 BLOCK DIAGRAM OF FEED MATRIX



Pol.	Beam.	SWITCH				
		1	2	3	4	5
Vert.	CENTER	0	0			0
	LEFT	1	0			0
	RIGHT	0	1			0
Hor.	CENTER			0	0	1
	LEFT			1	0	1
	RIGHT			0	1	1

VECTOR DIAGRAM FOR FEED MATRIX



$A = \overset{\rightarrow}{1} + \overset{\rightarrow}{2}$	\rightarrow	HORIZONTAL POLARISATION	(RIGHT)
$B = \overset{\rightarrow}{1} - \overset{\rightarrow}{2}$	\downarrow	VERTICAL POLARISATION	(DOWN)
$C = \overset{\rightarrow}{3} + \overset{\rightarrow}{4}$	\leftarrow	HORIZONTAL POLARISATION	(LEFT)
$D = \overset{\rightarrow}{3} - \overset{\rightarrow}{4}$	\uparrow	VERTICAL POLARISATION	(UP)
$\vec{A} - \vec{C} =$	\rightarrow	HORIZONTAL POLARISATION	(RIGHT)
$\vec{B} - \vec{D} =$	\downarrow	VERTICAL POLARISATION	(DOWN)

FIG. NO. 3

feed matrix.

An alternative arrangement for this horn as shown in Fig. 4 yields a steerable circularly polarised horn.

The present design operates over an octave bandwidth. An antenna with a wider bandwidth is at present being designed.

2.0 Modal Analysis

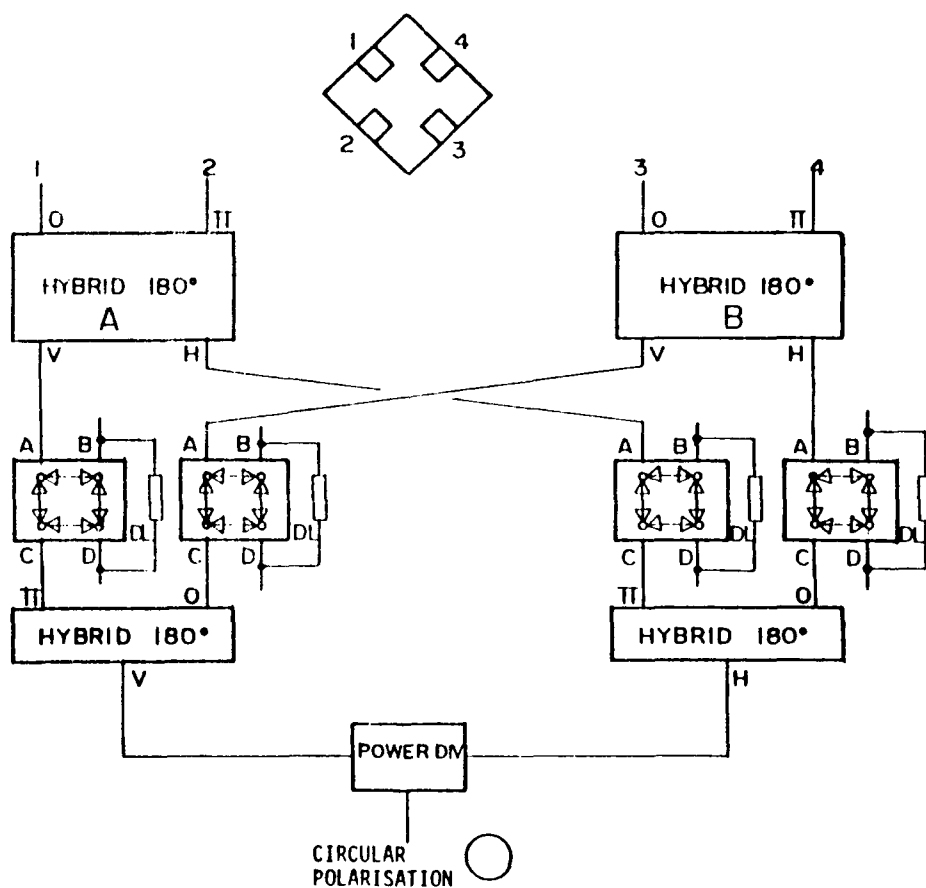
A modal analysis has been made on this horn, the mathematical details of which will not be presented in this paper. However, the results of the analysis show that the vertical and horizontal polarisations are generated by TE and TM modes respectively. The consequence of this analysis predicts a wide beamwidth for the horizontal polarisation and a narrow beam for the vertical polarisation. Our measurements on the antenna model verified this analysis.

3.0 Results (Configuration 1)

3.1 VSWR

The VSWR at port "X" is shown in Fig. 5. The VSWR at the input to the Hybrid Port "Y" is shown in Fig. 6. The VSWR is better than 3:1 over the band. Over

FIG. NO. 4
 CONFIGURATION NO. 2
 BLOCK DIAGRAM OF FEED MATRIX
 FOR CIRCULAR POLARISED MODEL



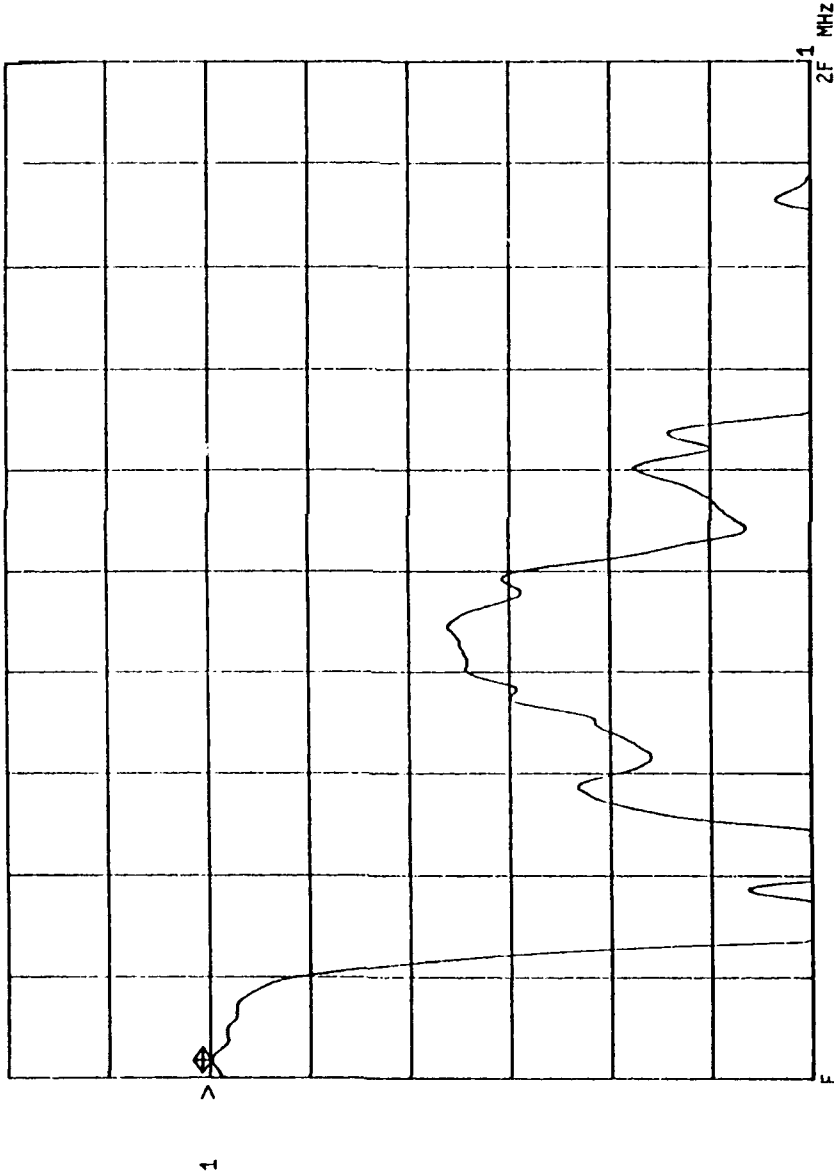
POL.	BEAM POSITION	SWITCH POSITION			
		1	2	3	4
CIRCULAR	CENTER	0	0	0	0
	LEFT	1	0	1	0
	RIGHT	0	1	0	1

CONFIGURATION NO. 1

VSWR AT OUTPUT X
POLARISATION - H

CH1: B -M 3.001 SWR
2.0 dB/ REF - 6.00 dB

FIG. NO. 5



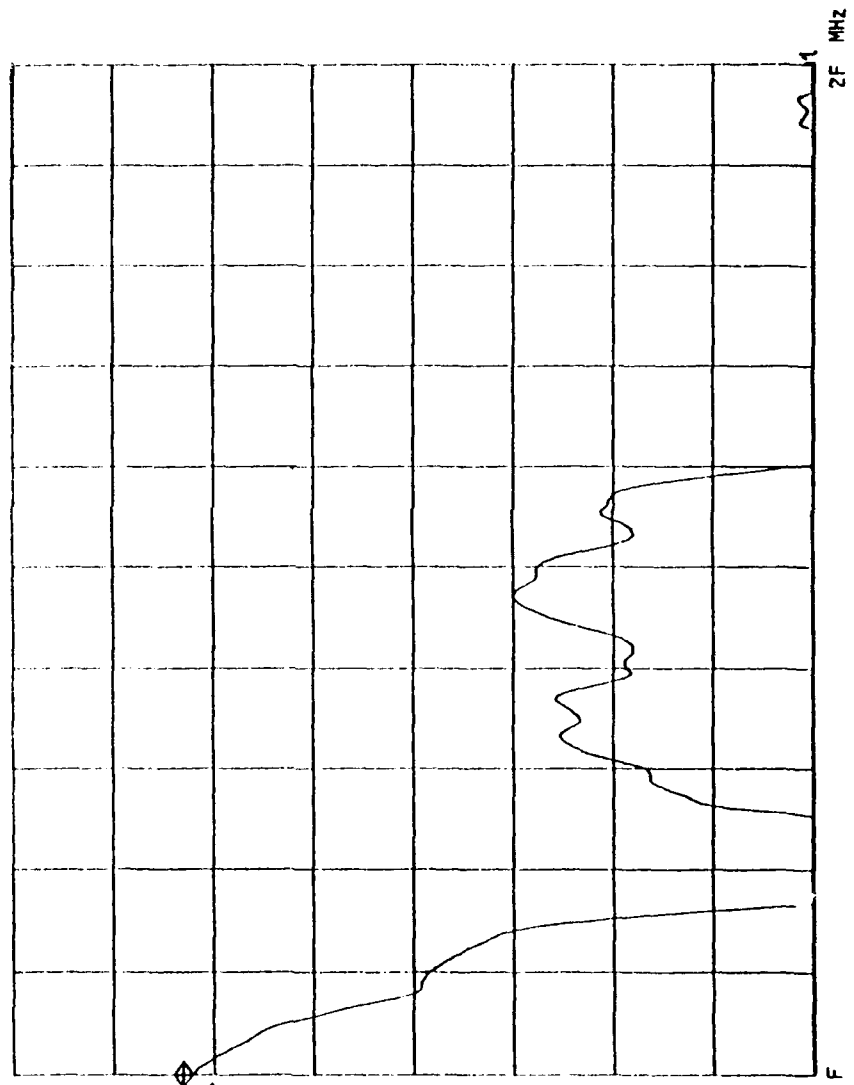
CONFIGURATION NO. 1

VSWR AT OUTPUT Y

POLARISATION - V

CH1: B -M REF - 3.226 SWR
2.0 dB/ REF - 6.00 dB

FIG. NO. 6



most of the band the VSWR is better than 2:1

3.2 Gain

The swept gain of the antenna for both Vertical and Horizontal polarisations is shown in Fig 7. The gain is above 8 dB over most of the band. At the low end there is a degradation in gain due to the high VSWR of the launcher.

3.3 Radiation Patterns

3.3.1 Horizontal Polarisation Patterns

In the horizontal polarisation the beamwidths are very wide and for this reason the beam switching was not of great help. Figs 8 to 10 show typical patterns for the three beam antennas.

A later model of this antenna has the switches for horizontal polarisation removed. No significant degradation in performance was observed.

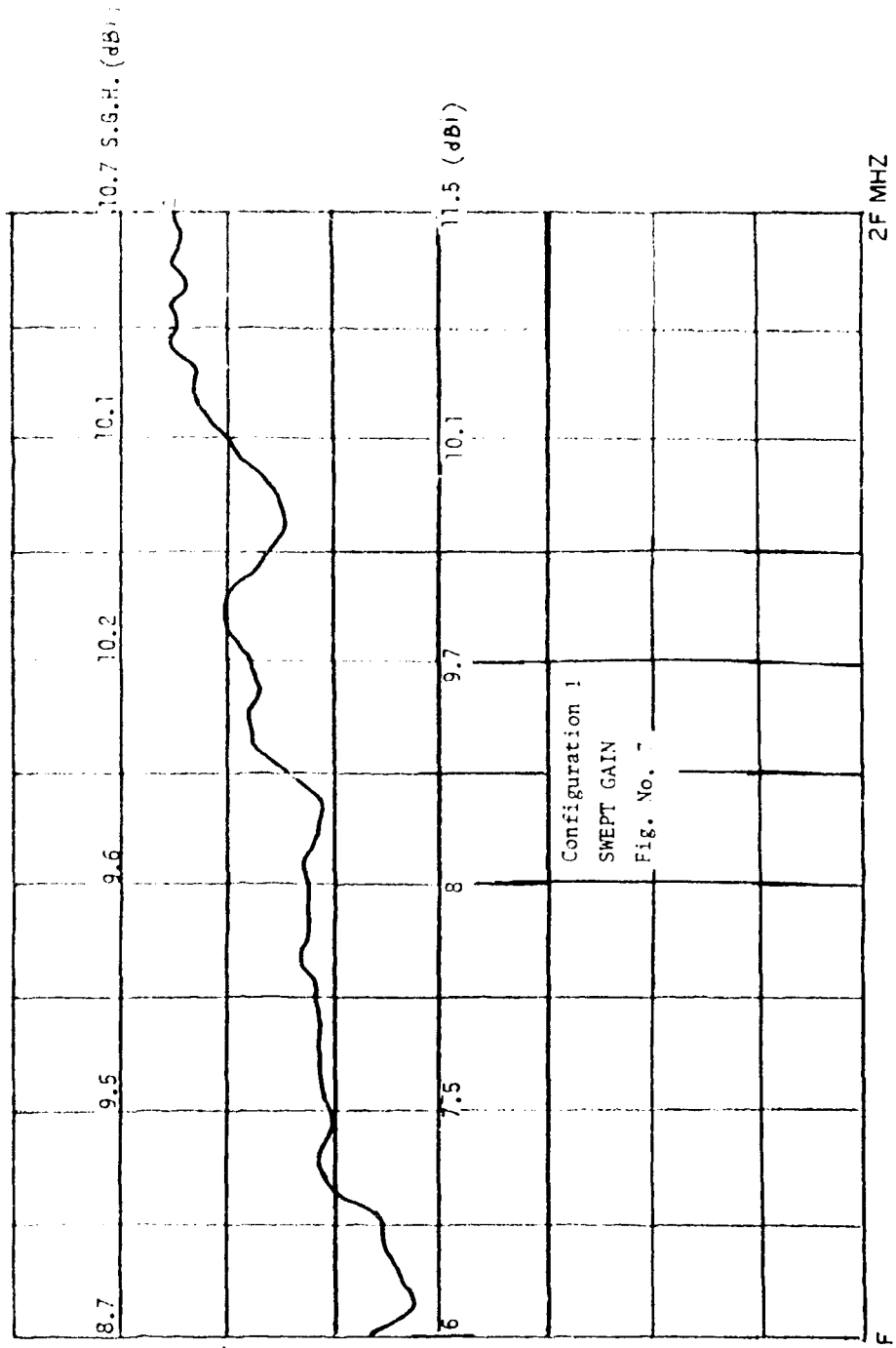
3.3.2 Vertical Polarisation

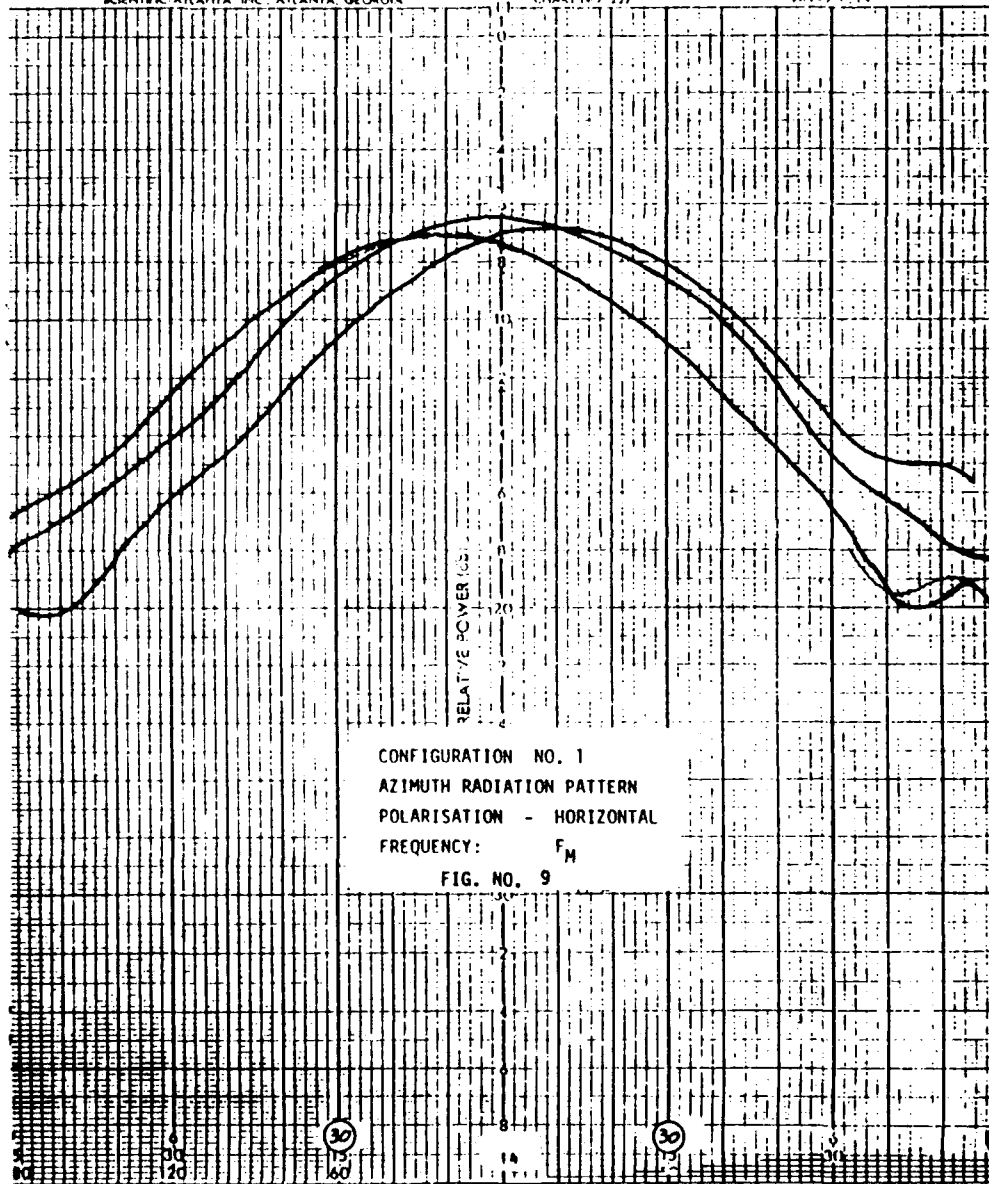
The patterns 11 to 13 show the three beams at frequencies low, mid and high ends of the band. The advantage of the beam switching is very clear here.

4.0 Configuration 2 - Circularly Polarised Horn

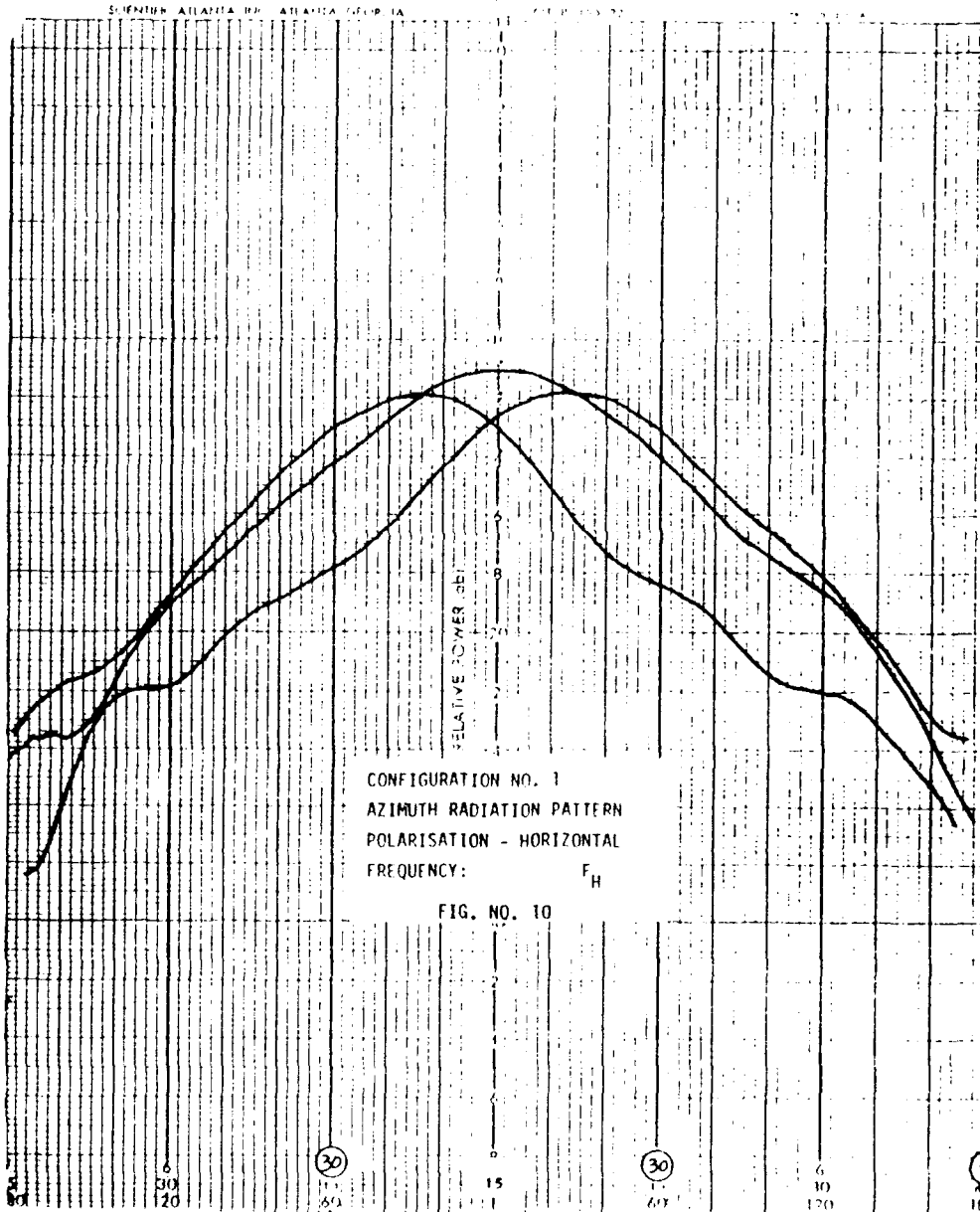
The VSWR and Gain and Axial Ratio of the Circularly Polarised Horn are shown in Figs 14, 15 and 16. The rather low gain at the low end of the

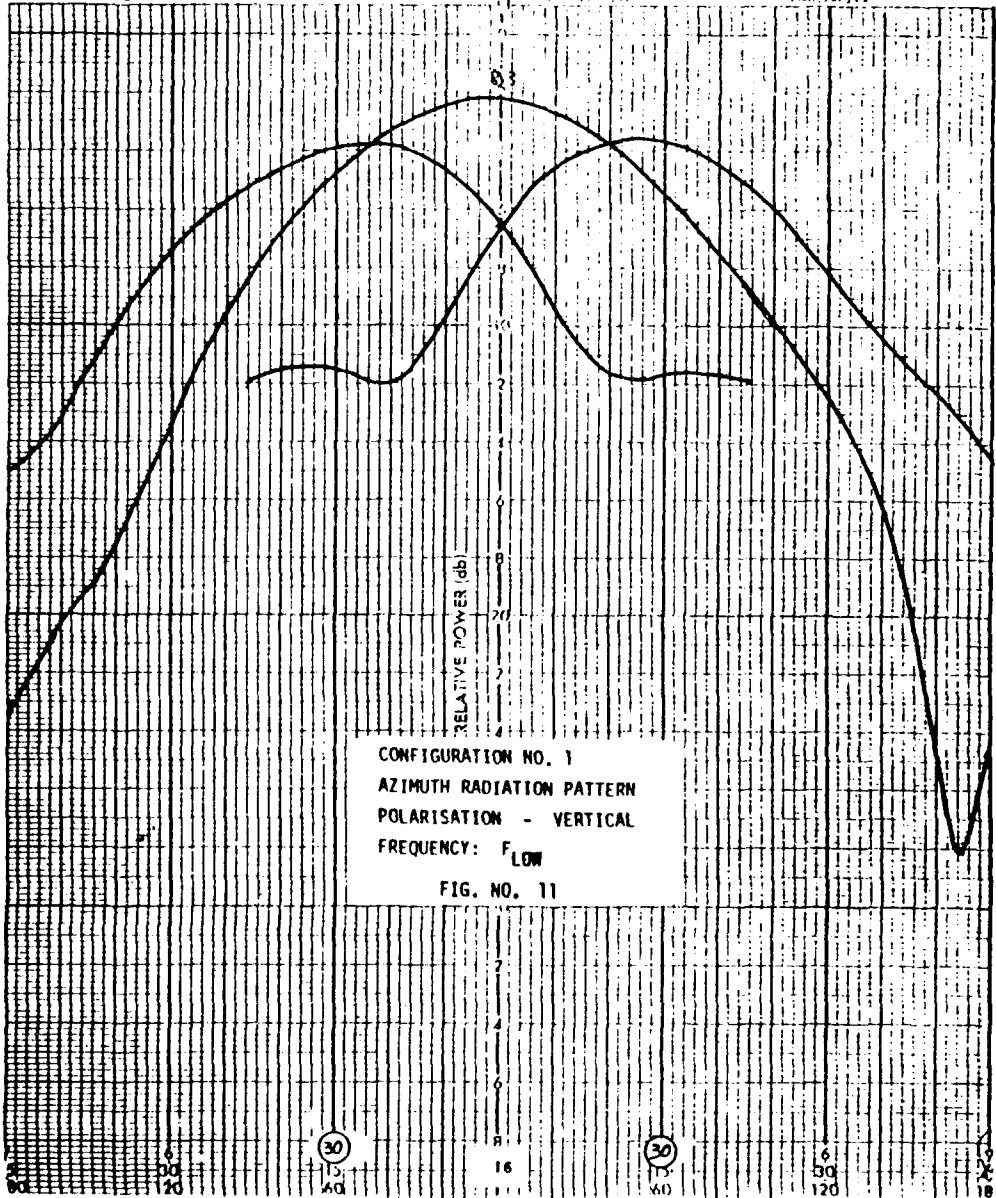
Gain vs. Frequency
Sweep Rate: 10.00 dB

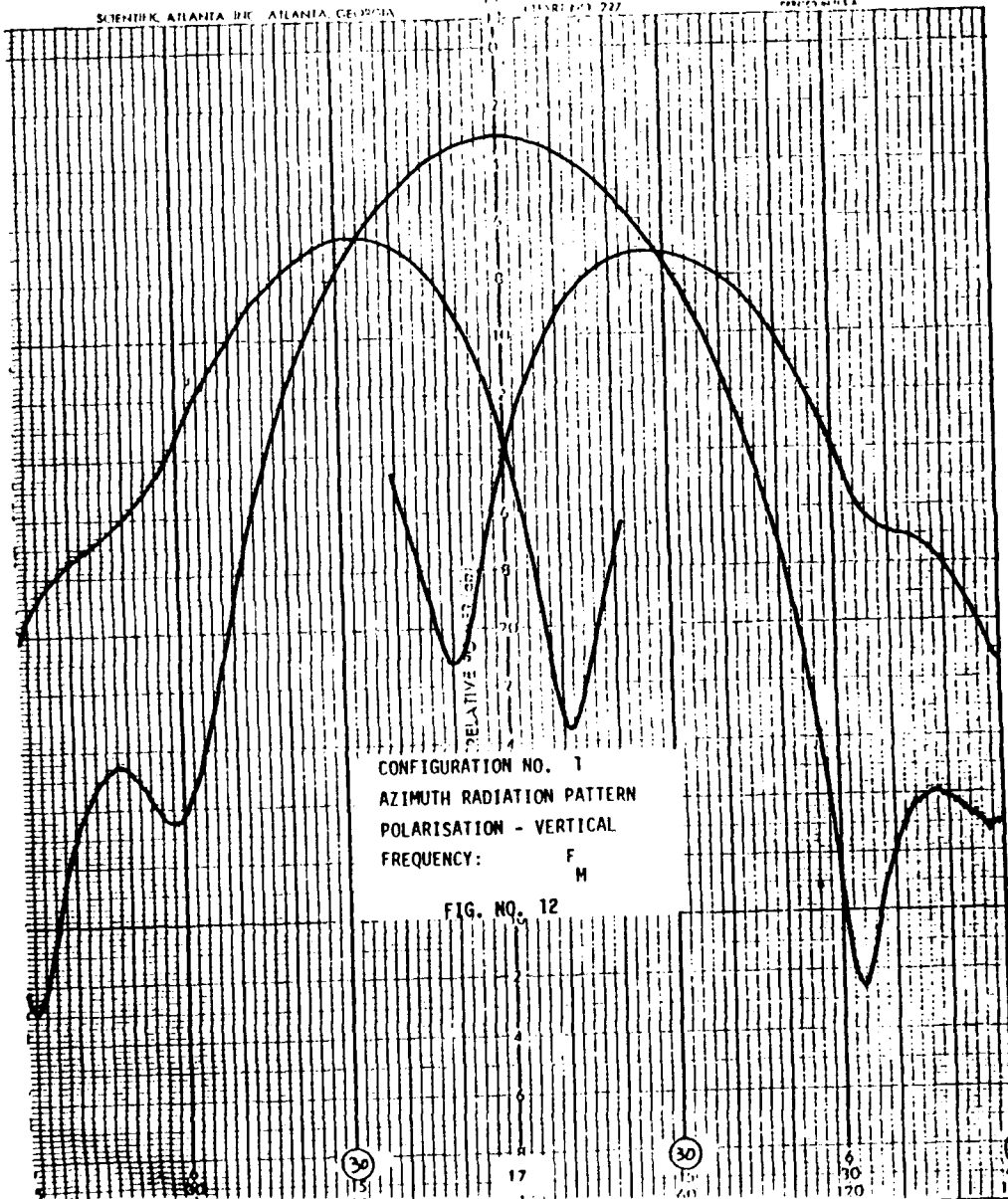




CONFIGURATION NO. 1
AZIMUTH RADIATION PATTERN
POLARISATION - HORIZONTAL
FREQUENCY: F_M
FIG. NO. 9







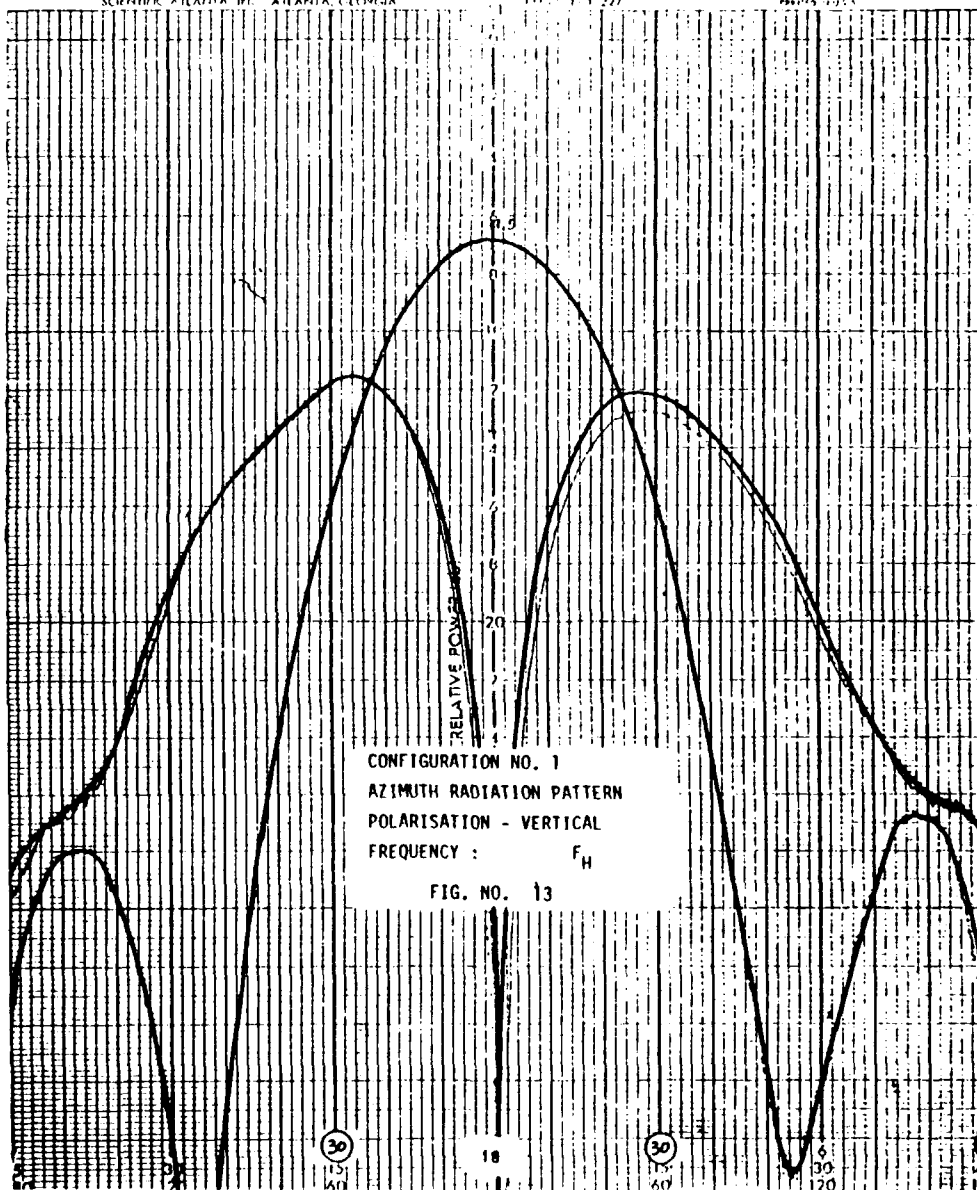
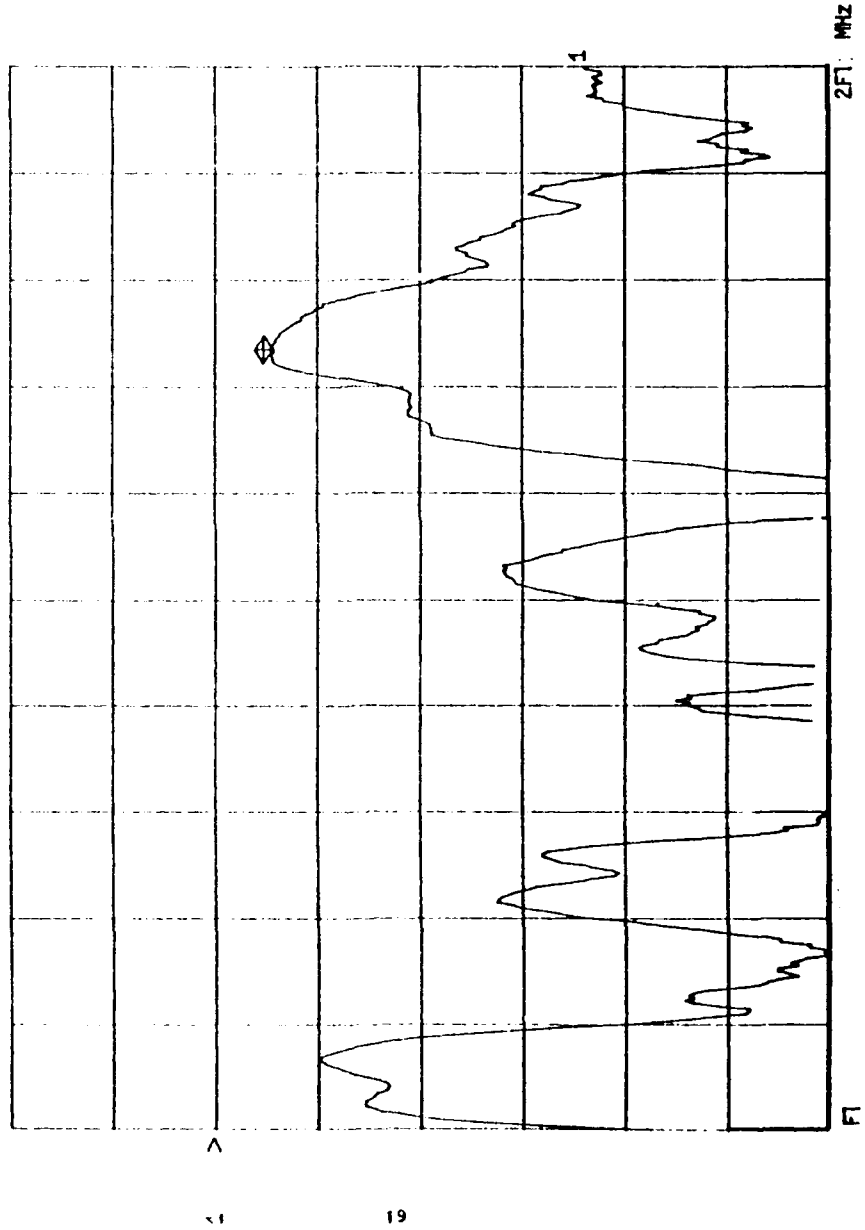


FIG. NO. 14
CONFIGURATION NO. 2
VSWR AT INPUT

CH1: A -M 1.324 SWR
2.0 dB/ REF -16.00 dB



CONFIGURATION NO. 2
 CIRCULARLY POLARISED ANTENNA
 GAIN OF VERTICAL OR
 HORIZONTAL POLARISATION

CH1: A -M S - 3.80 dB
 2.0 dB/ REF + .00 dB

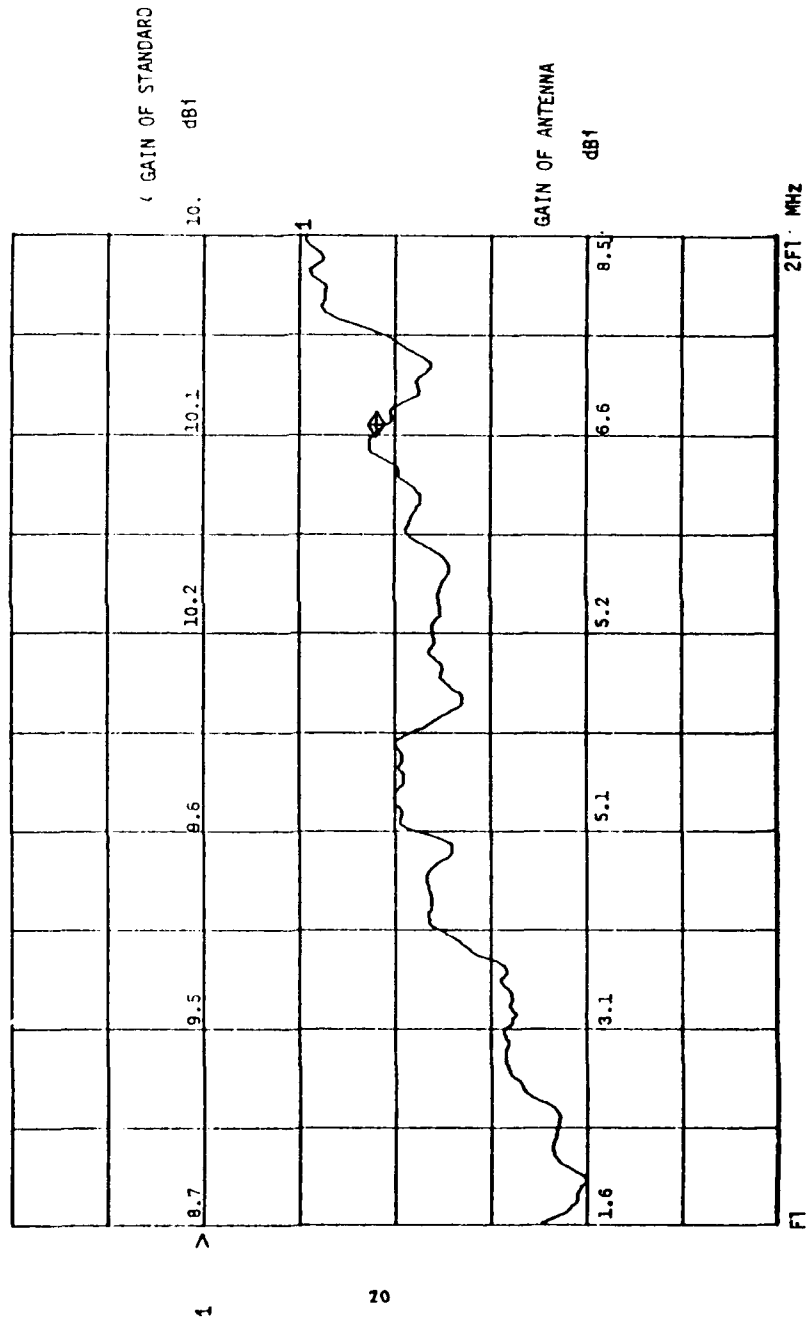
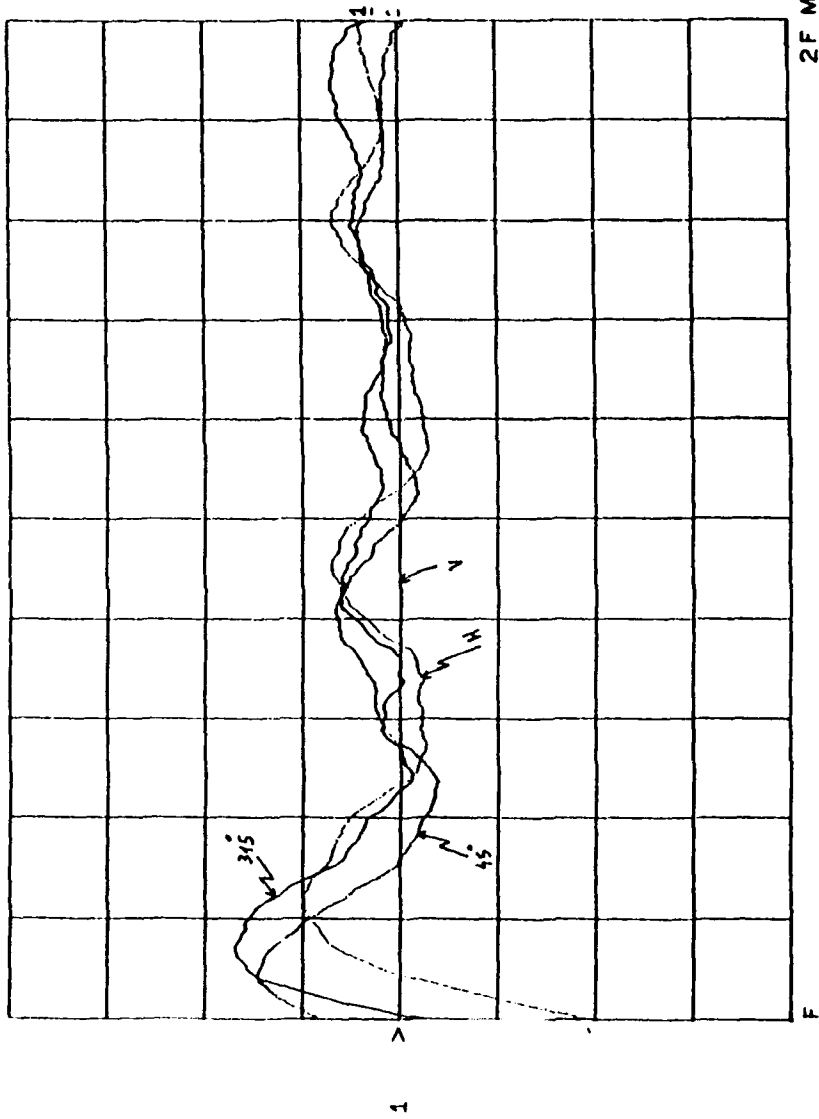


Fig. 15

CONFIGURATION NO. 2
GAIN VERSUS POLARISATION

CH1: A -M S
2.0 dB/ REF - .00 dB

FIG. NO. 16



band is due to the poor axial ratio. This could be improved with a larger feed adaptor.

5.0 Alternative Feeding Arrangement

5.1 Feed Matrix

An alternative feed matrix was designed and is shown in Fig. 17. The new arrangement known as Configuration 3 has the advantage that no delay lines are required. This arrangement is facilitated by the fact that each ridge of the guide when fed separately tends to squint off center.

5.2 VSWR and Gain

The VSWR and gain of Configuration 3 is basically identical to Configuration 1 and hence is not shown separately.

5.3 Radiation Patterns

Typical radiation patterns for vertical and horizontal patterns at the extremities of the band are shown in Figures 18 to 21. These patterns tend to give better azimuth coverage and high gain at angles up to ± 45 degrees. For wide angular coverage there is not much difference between the two configurations.

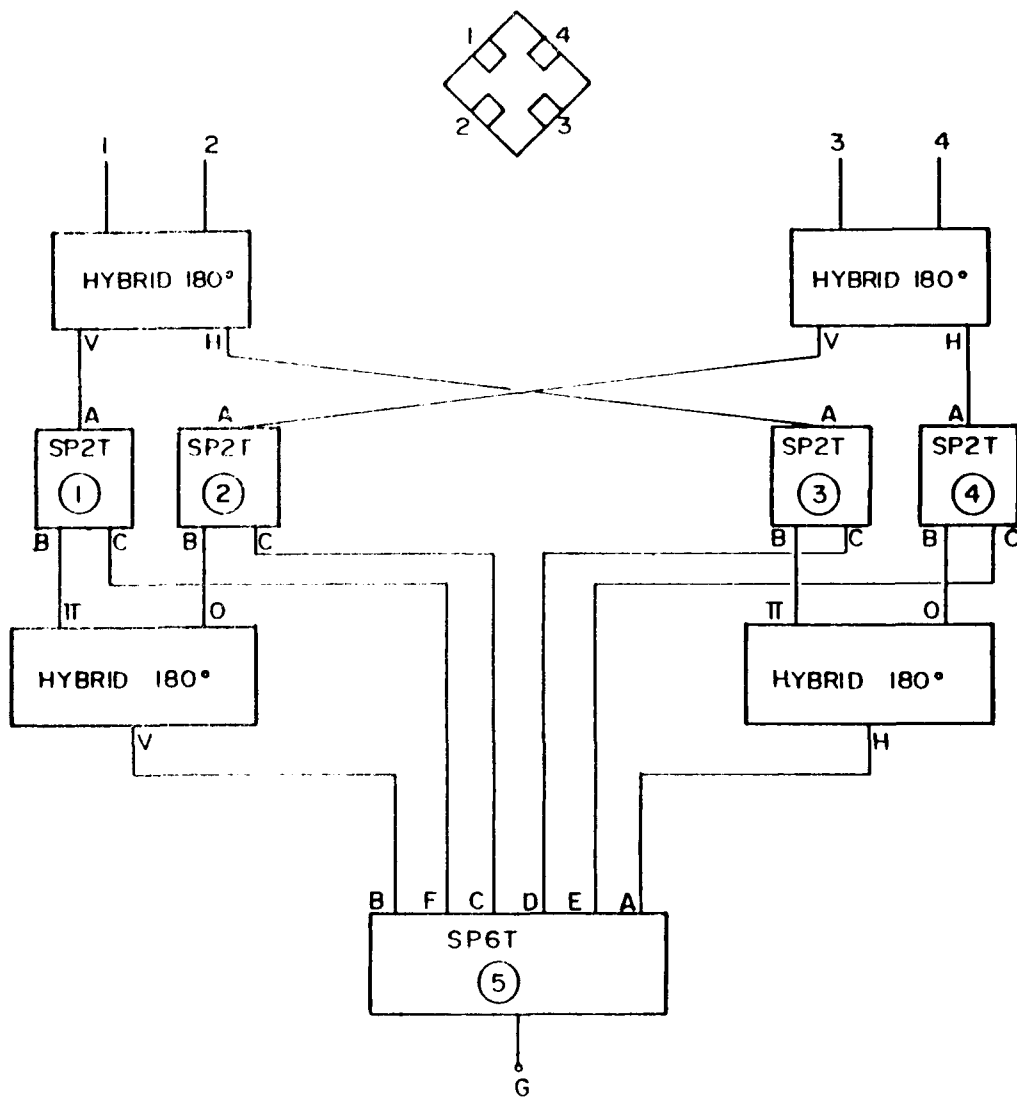
6.0 Conclusion

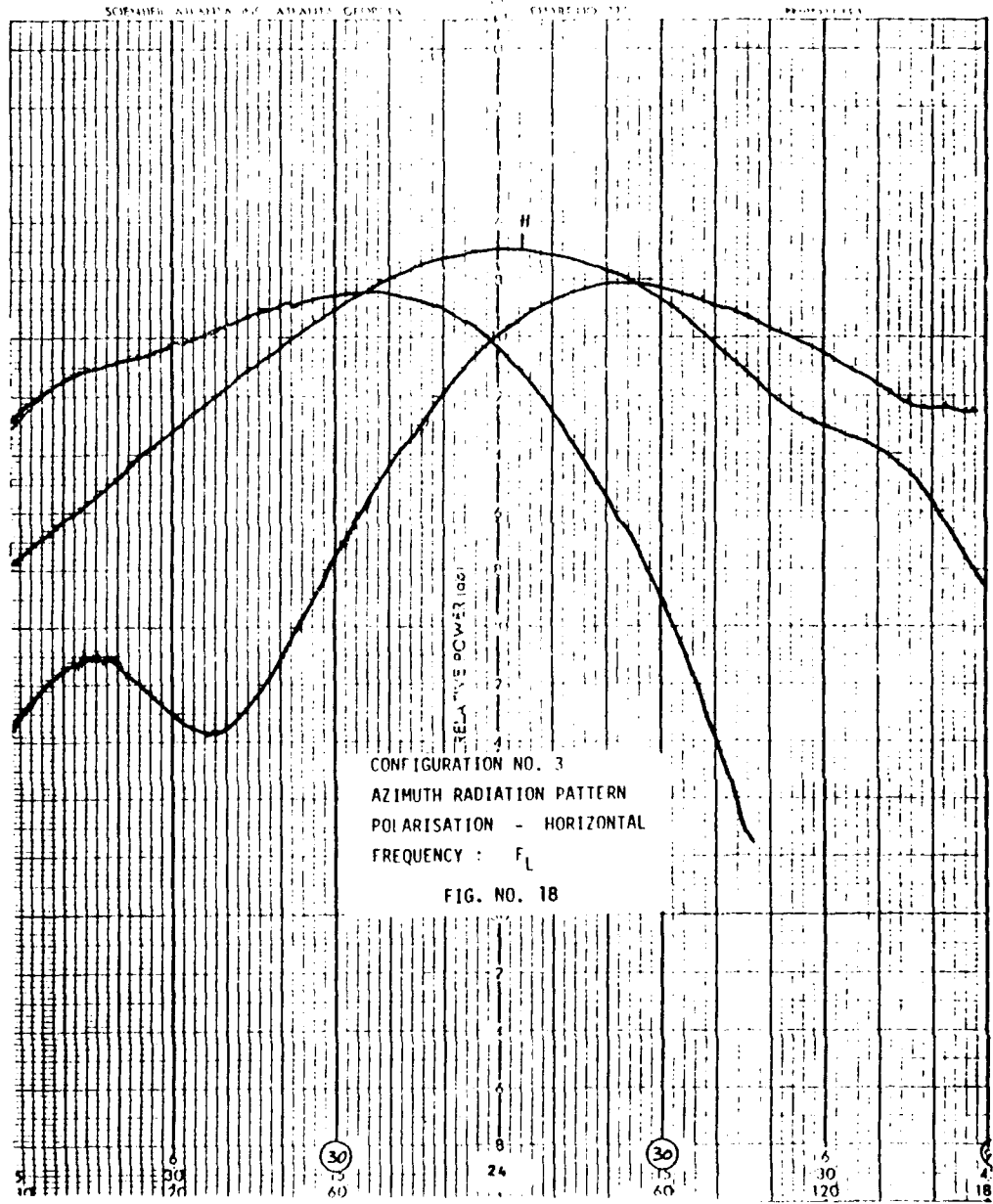
A quad-fed quad-ridged dual polarised horn has been described. The horn operates over an octave

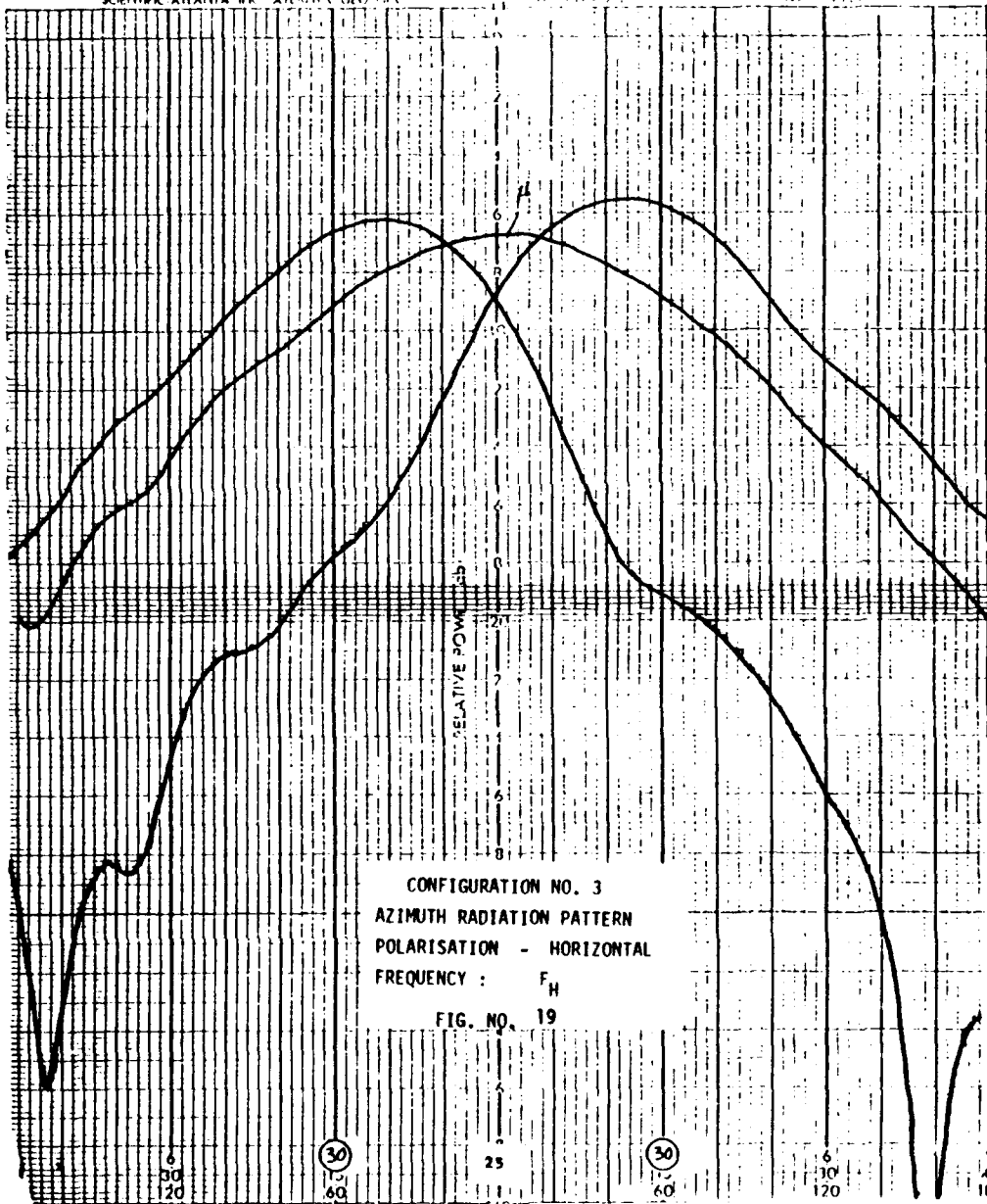
CONFIGURATION NO. 3

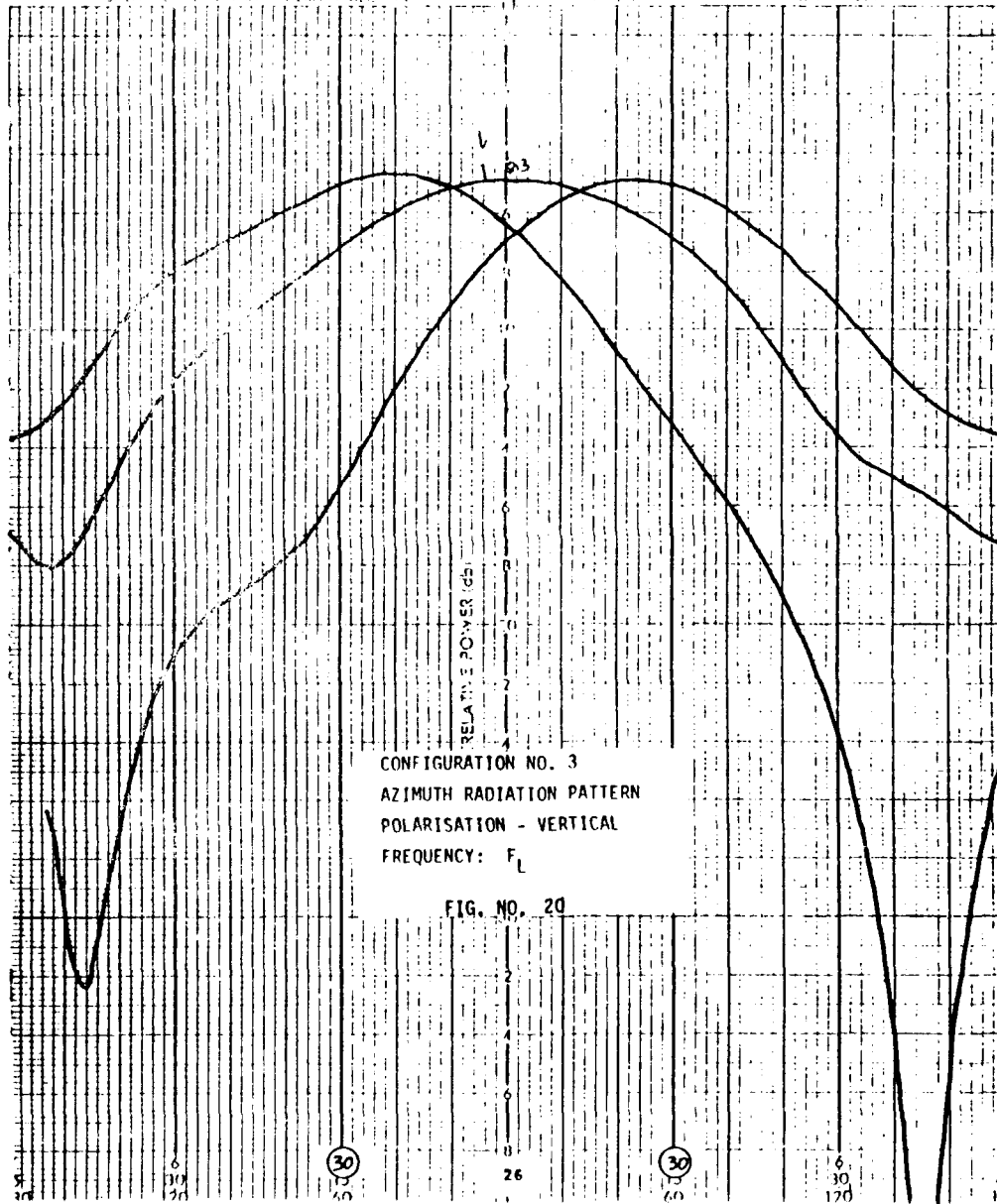
BLOCK DIAGRAM OF FEED MATRIX

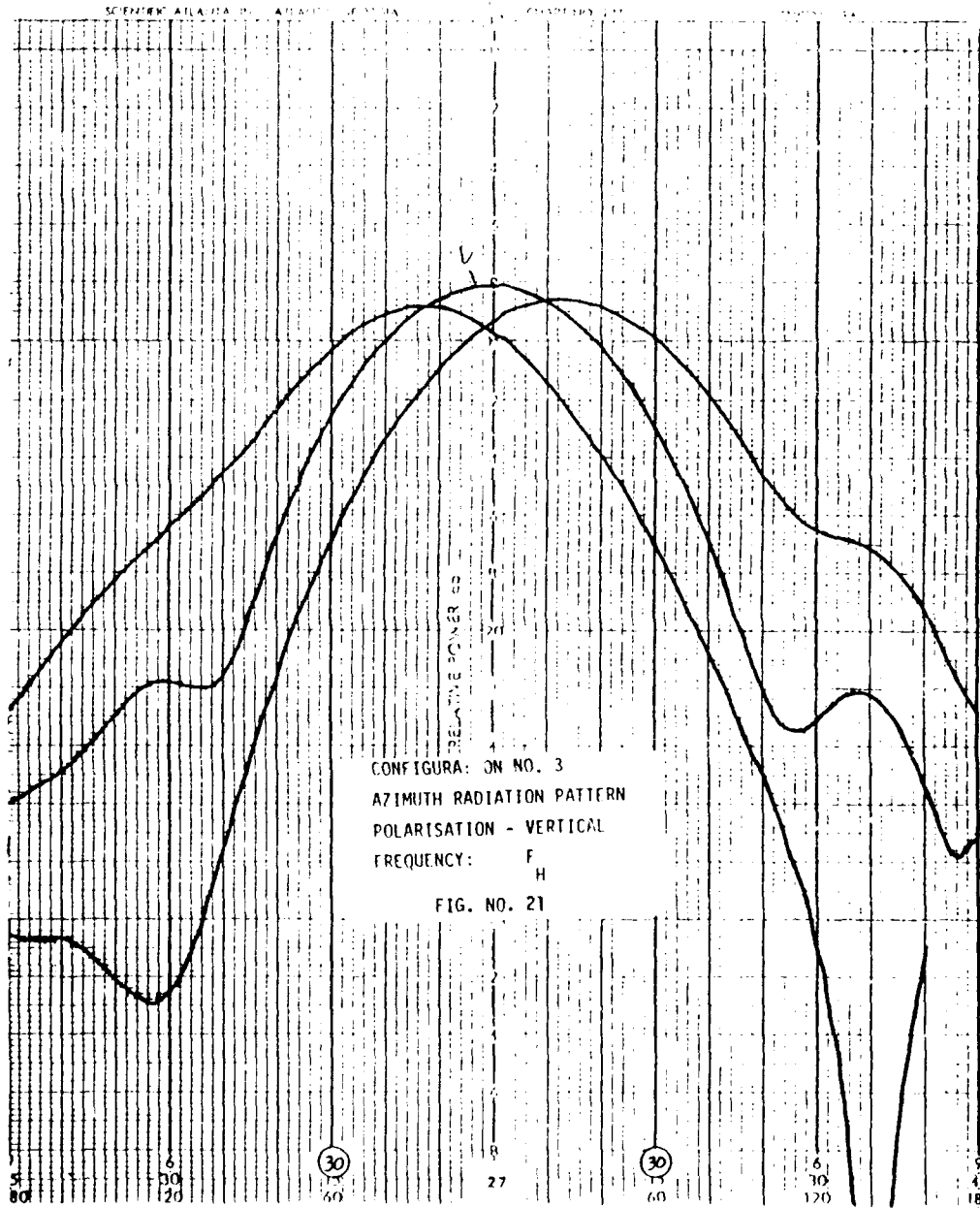
FIG. NO. 17











bandwidth. Arrangement for steering the beam in azimuth has been described. The horn is particularly useful when small size, high gain and wide angular coverage is required.

8 0 Acknowledgment

The author is indebted to the Management of Elbit Computers Ltd. for permitting him to publish this report.

9 0 References

1. The Handbook of Antenna Design Chapter 6 pp 466 to 505. Multibeam Antennas. Published by Peter Peregrinus Ltd.
2. Sexon T. (1968) Quadruply Ridged Horn. Rep. EDL - MI160. Cont. DAA B07-67-C-0181 par. 2.1.
3. Johnson and Jasik Antenna Engineering Handbook. Chap. 40, Second Edition. Published by McGraw Hill Book Company.

MULTI-OCTAVE MICROSTRIP ANTENNAS

Victor K. Tripp
and
Johnson J. H. Wang

Electromagnetic Science and Technology Lab
GEORGIA TECH RESEARCH INSTITUTE

Georgia Institute of Technology
Atlanta, Georgia 30332

ABSTRACT

The microstrip equi-angular spiral antenna has been previously demonstrated by the present authors to provide a gain enhancement bandwidth of more than 5:1 when compared with the conventional absorber-loaded cavity-backed spiral. In this paper, the Archimedean spiral microstrip antenna is demonstrated to have similar performance. As with cavity-backed antennas, these antennas lose efficiency at the lower frequencies. The gain performance is thus investigated as a function of the substrate thickness, edge loading techniques, and dielectric constant of the substrate.

1. INTRODUCTION

Many applications require antennas to be low-profile or even flush-mounted to a smooth conducting surface. Aircraft and missiles are most notable in this respect, due to aerodynamic requirements. Further advantages of low-profile installations include their low cross-section presented to radar and even to birds. The microstrip antenna ¹ is generally the antenna of choice for such applications and has been widely used. However, existing microstrip antennas are limited to a very narrow bandwidth of less than 10%. For low-profile applications requiring large bandwidth, such as ESM antennas, effort has been expended in recent years to broaden the bandwidth of the microstrip antenna ^{2,3}, but little has been accomplished without increasing substrate thickness, thus increasing the height of the antenna.

On the other hand, the planar spiral antenna, especially the equi-angular type, has a very wide frequency bandwidth ⁴. Unfortunately, this simple design radiates to both sides of the spiral plane, while most applications require a unidirectional pattern. To overcome this difficulty over a large bandwidth, the usual approach is to place a lossy cavity on one side of the spiral to absorb undesired radiation. This cavity-backed planar spiral was perfected more than a decade ago at several industrial firms. It yields wideband frequency coverage of 2 - 18 GHz or more.

The recently developed sinuous antenna ⁵ resembles the cavity-backed spiral in both electrical and physical characteristics and is capable of radiating linear polarizations that do not rotate with frequency. This means that such antennas having more than two arms can produce dual polarization of either the linear or circular type.

The lossy cavity of the spiral and sinuous antennas has two undesirable effects:

1. At least half of the radiated power is lost in the dissipative cavity, and
2. The cavity is deeper than the radius of the spiral, thus rendering it unsuitable for low-profile surface mounting.

To avoid the gain loss and system noise increase due to the lossy cavity, the planar spiral can be designed with the backing of a lossless cavity⁶ or a conducting plane⁷. However, only very modest bandwidths of less than 40% have been reported for such designs to date.

When a low-profile and a broad bandwidth are of primary consideration, one wonders whether a spiral-shaped microstrip antenna could achieve both characteristics. Wood³ initially investigated this possibility. One of his experimental models was a single microstrip line wound as an Archimedian spiral to a radius of about one wavelength at 10 GHz on a polyguide substrate 1.59 mm thick. He concluded that the achievement of wideband operation analogous to the conventional spiral is not feasible because the radiation patterns tend to exhibit a large axial ratio.

Other researchers have made significant contributions leading to the present state of the art, but their zeal was probably dampened by Wood's disappointing conclusion. At least that was the case for the co-author of this paper who demonstrated⁸ an excellent impedance match over a 2.7:1 band for a spiral only 0.032 wavelengths above a groundplane at the lowest frequency. The electrical thickness of the dielectric substrate was about 0.066 wavelengths.

About the same time, Waller and Mayes⁹ were experimenting with single arm spirals over flat (microstrip configuration) and conical ground surfaces. Their demonstration of a 2:1 pattern bandwidth was promising enough to lead to

further research. Drewniak and Mayes' measurements on a single-arm log-spiral over a conical ground surface provided insight into how such antennas work ¹⁰, though their best performance came from an annular-sector radiating line antenna ¹¹. To date all the single-arm models have suffered from the skewing of patterns off broadside.

Recently Nakano ⁴ reported a theoretical investigation which indicated that poor radiation patterns are due to the residual power after the electric current on the spiral has passed through the first-mode radiation zone (which is on a centered ring about one wavelength in diameter). Thus if we can remove the residual power from radiation, we should be able to obtain excellent radiation patterns over a very wide bandwidth.

A simple technique for removing the residual power is to place a ring of absorbing material at the truncated edge of the spiral outside the radiation zone. This scheme allows the absorption of the residual power which would radiate in "negative" modes, causing deterioration of the radiation patterns, especially their axial ratio. Also the first-order rotational asymmetry of patterns can be eliminated by the use of two arms rather than one. This approach makes feeding less convenient, but it is a more reliable remedy than increasing the single-arm wrap rate.

This paper presents the experimental results of a study of two-arm spiral antennas closely spaced over a ground surface. Various dielectric substrates, edge loading techniques, and ground spacings are considered.

2. BANDWIDTH

Before examining the parametric studies, we will discuss performance bandwidth since that is the motivation for this effort. As there are many definitions of bandwidth, each important for a different application, we characterize bandwidth by presenting an array of patterns for a rather arbitrarily selected hardware configuration. The configuration is similar to that shown in Figure 1,

except that the spiral is Archimedian, with a separation of about 1.9 lines per inch. Figure 2 demonstrates that for a spacing of 0.145 inch the impedance band is very broad -- more than 20:1 for a VSWR below 2:1. The band ends depend on the inner and outer terminating radii of the spiral. The feed was a broadband balun ¹² made from a 0.141 inch semi-rigid coaxial cable, which made a feed radius of 0.042 inch. It was necessary to create a narrow cavity in the ground-plane in order to clear the balun. The cavity's radius was 0.20 inch, and its depth, 2 inches. This cavity also affects the high frequency performance.

These parameters worked well, though they were by no means optimal. Better matches were obtained over narrower bands for other configurations. Figure 3 shows the VSWR of a log-spiral 0.3 inch above a similar ground plane and balun. Both spirals, incidentally, were complementary.

The outer radius was 1.5 inch with foam absorbing material extending from 1.25 to 1.75 inches. It seems intuitive that if this terminating absorber is good enough, the antenna match can be extended far below the frequencies at which the spiral radiates significantly. More importantly, at the operating frequencies, the termination eliminates currents that would be reflected from the outer edge of the spiral and disrupt the desired pattern and polarization. These reflected waves are sometimes called negative modes because they are polarized in the opposite sense to the desired mode. Thus, their primary effect is to increase the axial ratio of the patterns.

The patterns for this antenna ($d = 0.145$) are shown in Figures 4 through 11. The patterns are normalized to the actual gain of the antenna. Since we are measuring circular polarization with a linear probe antenna, the levels recorded are about 3 dB below the actual gain. The scale is marked "dBiL" to remind us of this fact.

For an engineering model, the antenna operates well from 2 to 14 GHz, a 7:1 band. It is to be expected that the detailed engineering required to produce a

commercial antenna would yield excellent performance over this range. The gain is higher than that of a 2.5" commercial lossy-cavity spiral antenna up through 12 GHz, as shown in Figure 12. (We feel that the dip at 4 GHz is an anomaly.) This figure also shows gain curves for a groundplane spacing of 0.3 inch. The Archimedian version of this design demonstrates a gain improvement over the nominal loaded-cavity level of 4.5 dBi (with matched polarization) over a 5:1 band. The gain of the 0.145 inch spaced antenna is lower because the substrate was a somewhat lossy cardboard material rather than the light foam used for the 0.3 inch example.

Similar pattern performance for other spiral configurations has been reported elsewhere. The log-spiral has been shown to behave in an essentially identical manner to the Archimedian design in microstrip configurations ^{13,14}. It has also been shown to perform very well when conformed to a curved surface ^{13,15}. Log-periodic antennas have recently been developed in circular shapes and with loaded cavities similar to the standard broadband spiral antennas. Examples are the interlog ¹⁶ and the sinuous antennas ⁵. We have no reason to believe that these antennas cannot be configured as broadband microstrip antennas similar to the spirals. We have designed and built a microstrip sinuous antenna, and it is presently being tested.

3. EFFECT OF SUBSTRATE

Only two basic parameters of the substrate have been studied to date: thickness, and dielectric constant. We found, as expected, that a decrease in thickness caused the band of high gain to move upward in frequency, subject to the limitation imposed by the inner truncation radius. Figure 13 shows gain plotted at several frequencies as a function of spacing for the "substrate" air. At low frequencies, the spiral arms act more like transmission lines than radiators as they are moved closer to the groundplane. They carry much of their energy into the absorber ring, and the gain decreases.

At high frequencies, gain generally increases with reduced spacing, indicating that the lines are better radiators when they are less than a quarter wavelength from the groundplane. This is consistent with our theory ¹⁵, but differs from the apparent assumption of Nakano, et al. ⁷ that the optimum spacing should be a quarter wave. For these types of antennas, we have found that efficient radiation generally takes place when the spacing is far below the quarter wave "optimum". We have observed a gain enhancement over that of a loaded cavity for frequencies that produce a spacing of less than 1/20 wavelength. If one is willing to tolerate gain degradation down to 0 dBi at the low frequencies, as found in most commercial spirals, the spacing can be as small as 1/60th wavelength.

The effect of the presence of high-dielectric-constant material was studied in two ways: with and without a groundplane. To investigate the case of no groundplane both calculations and measurements were used, and the results are reported elsewhere ¹⁵. The basic conclusion was that patterns degrade in the presence of a dielectric substrate; the higher the dielectric constant, and the thicker the substrate, the more seriously the patterns degrade. In this paper, we will show that, even though dielectric substrates cause pattern degradation, it is possible to design spiral microstrip antennas with acceptable performance over a narrower frequency band.

The case of dielectric substrates between the spiral and the groundplane was studied for materials of relatively small dielectric constant, the greatest being 4.37. As is shown in Figures 14 through 17, little degradation was found at these frequencies. The upper pattern in each of these figures was measured on the configuration of Figure 1; while the lower patterns are for the same configuration, with 0.063 inches of fiberglass substituted for 0.145 inches of air. In both of these configurations the electrical spacing is the same (within 10 %). If the electrical spacing is considered to be more important the other spiral dimen-

sions, the upper pattern at 9 GHz can be compared with the lower pattern at 10 GHz (also 10 with 11 and 11 with 12), where the electrical spacings are nearly the same.

4. EFFECT OF EDGE LOADING

The use of edge loading to suppress reflections from the outer ends of the spiral arms is well known. We investigated several configurations, most notably foam absorbing material and magnetic RAM material.

For the foam case, we compared log-spirals terminated with a simple circular truncation (open circuit) and a thin circular shorting ring. There was no discernable difference in performance. The magnetic RAM absorber was tried on open-circuit Archimedian and log-spirals with spacings of 0.09 and 0.03 inches. Figures 18 and 19 show the VSWR for 0.10 inch foam and 0.09 RAM respectively. Clearly, the magnetic RAM is not nearly so well behaved as the foam. In addition to the gain loss caused by the VSWR spikes, the patterns showed a generally poor axial ratio, indicating that the magnetic RAM did not absorb as well as the foam. In our measurements, the loading materials were always shaped into a half-inch wide annulus, half within and half outside the spiral edge. The thickness was trimmed to fit between the spiral and the groundplane or in the very close configurations it was mounted on top of the spiral. Since this top-mounting partially defeats the purpose of the low-profile approach, an alternative loading technique is being sought. Materials under consideration include Aquadag.

5. CONCLUSION

The spiral microstrip antenna has been demonstrated to work well over a multi-octave band. It provides gain enhancement over the conventional loaded-cavity configuration over a 5:1 band and the desired stability of input impedance over a 20:1 band. A gain of 0 dBi can be achieved at frequencies where the

spacing is as little as 0.02 wavelength in air, and dielectrics can be used with minimal pattern degradation provided that the dielectric constant is low. Moderate edge loading can be obtained with absorbing foam.

ACKNOWLEDGEMENTS

The authors are pleased to acknowledge the support and encouragement of Mr. Robert L. Davis for this research. They also thank Jason Goth, Robert Zimmer and Amy Jacoby for assembly and measurement work.

REFERENCES

1. Munson, R. E. (1974) Conformal Microstrip Antennas and Microstrip Phased Array, *IEEE Trans. Ant. Prop.*, Vol. AP-22, pp. 74-78.
2. Pascen, D. A. (1983) Broadband Microstrip Matching Techniques, *Proc. 1983 Antenna Appl. Symp.*, EM Laboratory, Univ. of IL, Urbana, IL.
3. Wood, C. (1979) Curved Microstrip Lines as Compact Wideband Circularly Polarized Antennas, *IEE Microwaves, Optics and Acoustics*, Vol. 3, pp. 5-13.
4. Rumsey, V. H. (1966) *Frequency Independent Antennas*, Academic Press, New York.
5. DuHamel, R. H. (1986) Dual Polarized Sinuous Antennas, European Patent Application No. 019 8578, (U.S. Patent No. 703042, 1985.)
6. Hansen, R. C., Ed. (1966) *Microwave Scanning Antennas, Vol. 2, Array Theory and Practice*, Academic Press, New York, pp. 116-127.
7. Nakano, H., Nagami, K., Arai, S., Mimaki, H., and Yamauchi, (1986) J. A Spiral Antenna Backed by a Conducting Plane Reflector, *IEEE Trans. Ant. Prop.*, Vol. AP-34, pp. 791-796.
8. Wang, J. J. H. (1985) A Study of the Spiraphase and Anisotropic Substrates in Microstrip Antennas, Interim Report RADC-TR-85-146, Rome Air Development Center, Griffiss AFB, N.Y. ADA159862
9. Waller, R. W., and Mayes, P. E. (1985) Development of a Flush-Mounted Equiangular Spiral Antenna, Electromagnetics Lab Report No. 85-3, Univ. of IL, Urbana, IL.
10. Drewniak, J. L., Mayes, P., Tanner, D., and Waller, R. (1986) A Log-Spiral, Radiating-Line Antenna, *IEEE AP-S International Symposium Digest*, Philadelphia, p 773.
11. Drewniak, J. L., and Mayes, P. E. (1989) ANSERLIN: A Broad-Band, Low-Profile, Circularly Polarized Antenna, *IEEE Trans. Ant. Prop.*, Vol. 37, pp. 281 - 288.
12. Duncan, J. W., and Minerva, V. P. (1960) 100:1 Bandwidth Balun Transformer, *Proc. of IEEE*, Vol. 48, p. 156 - 164.

13. Wang, J. J. H. and Tripp, V. K. (1990) Design of Broadband, Conformal, Spiral Microstrip Antennas, *1990 URSF Radio Science Meeting*, Dallas, p.18.
14. Wang, J. J. H., and Tripp, V. K. (1989) Design of Multi-Octave Spiral-Mode Microstrip Antennas Submitted to *IEEE Trans. Ant. Prop.*
15. Wang, J. J. H., and Tripp, V. K. (1990) Spiral Modes and the Design of Multi-Octave Microstrip Antennas Submitted to *Journal of EM Waves and Applications*.
16. Hofer, D. A., Kesler, O. B., Loyet, L. L., (1989) A Compact, Multi-polarized, Broadband Antenna, *1989 Antenna Appl. Symp.*, EM Laboratory, Univ. of IL, Urbana, IL.

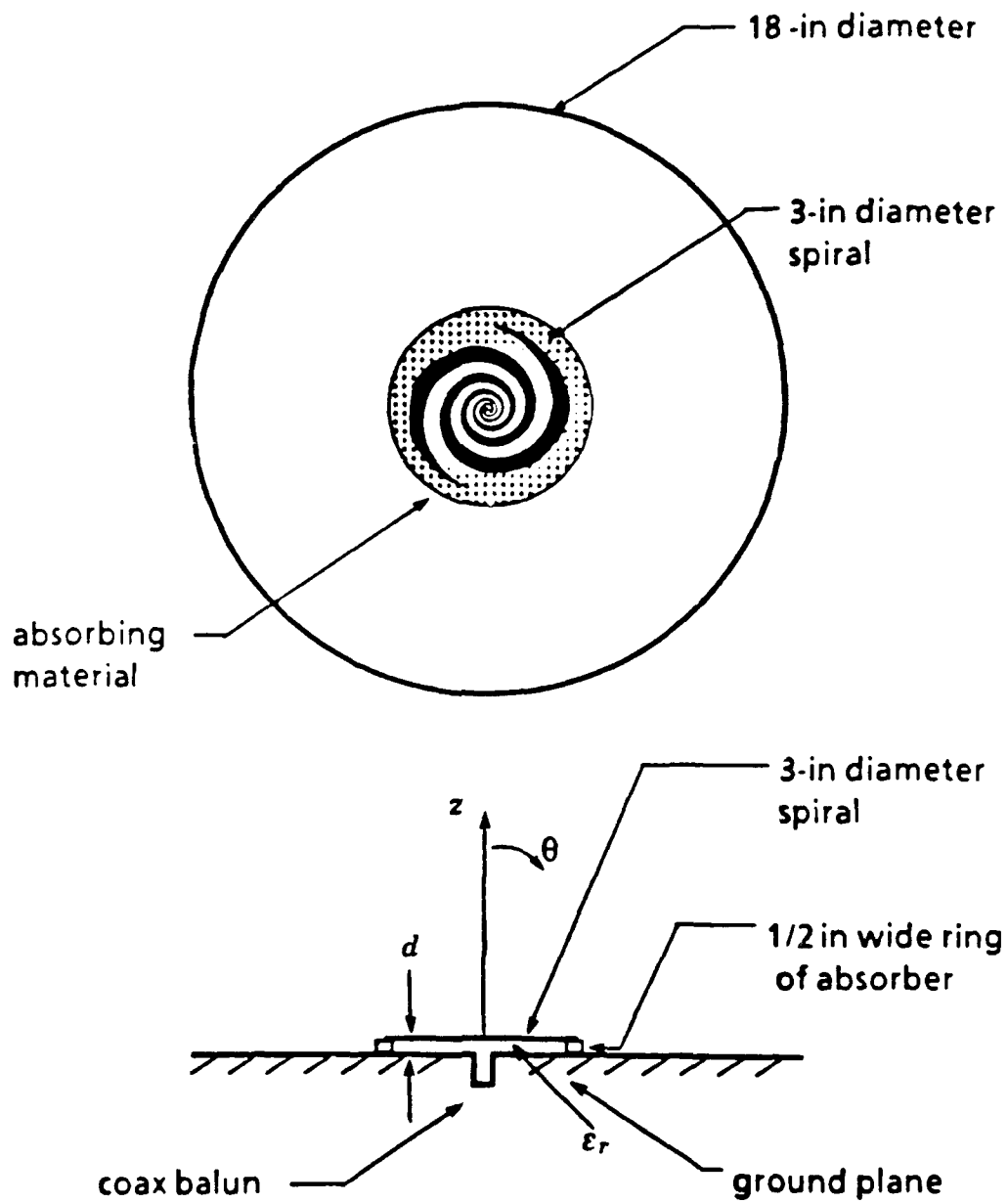


Figure 1. A spiral microstrip antenna configuration.

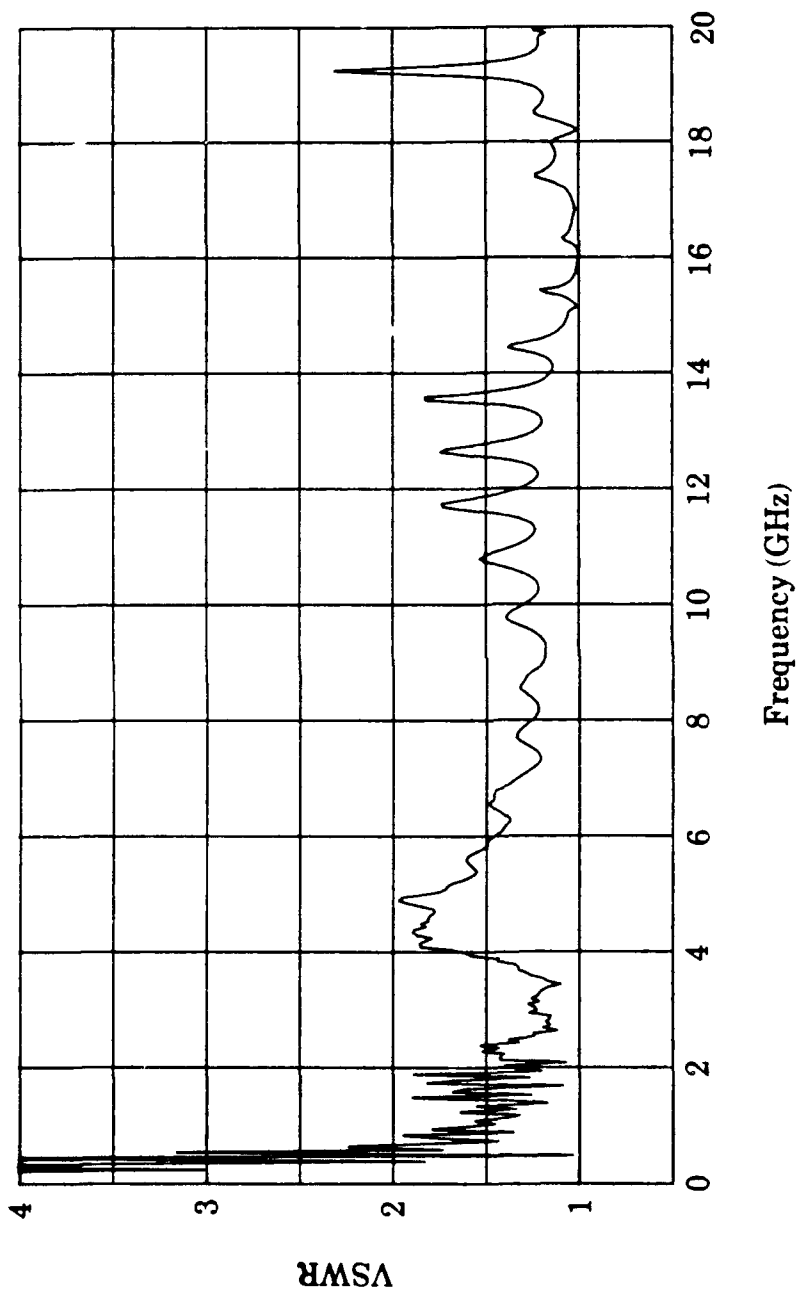


Figure 2. Measured VSWR of the spiral microstrip antenna of Figure 1.

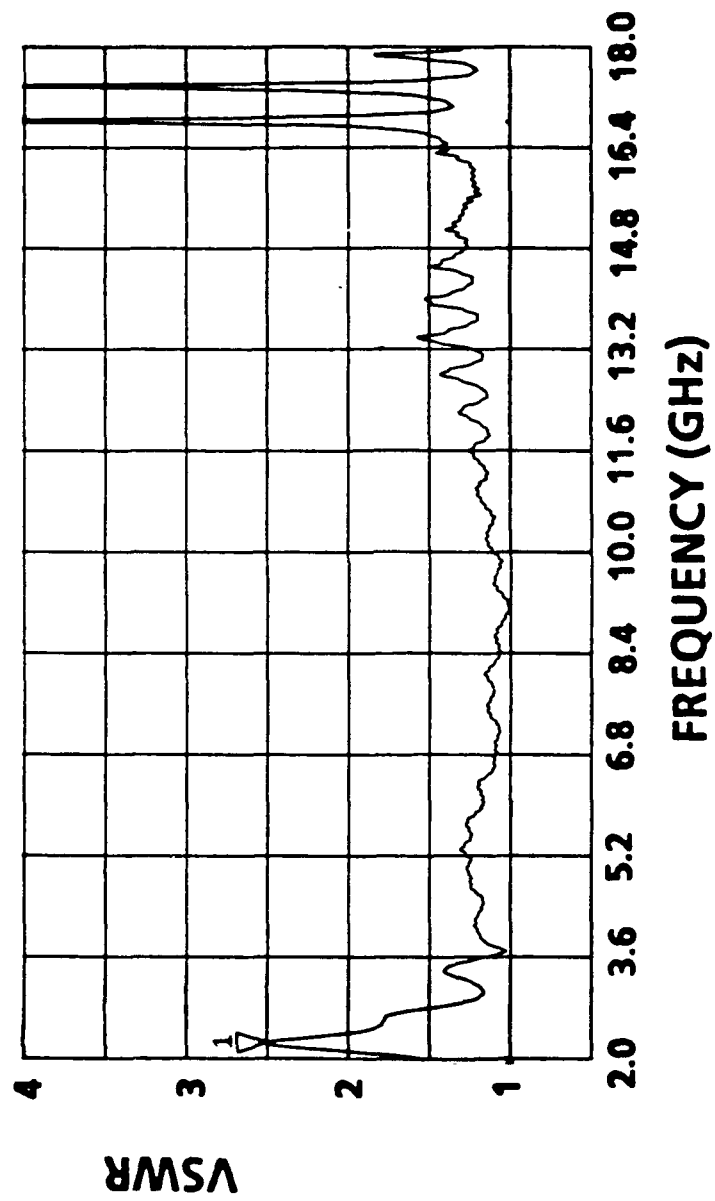


Figure 3. Measured VSWR of another spiral microstrip antenna configuration.

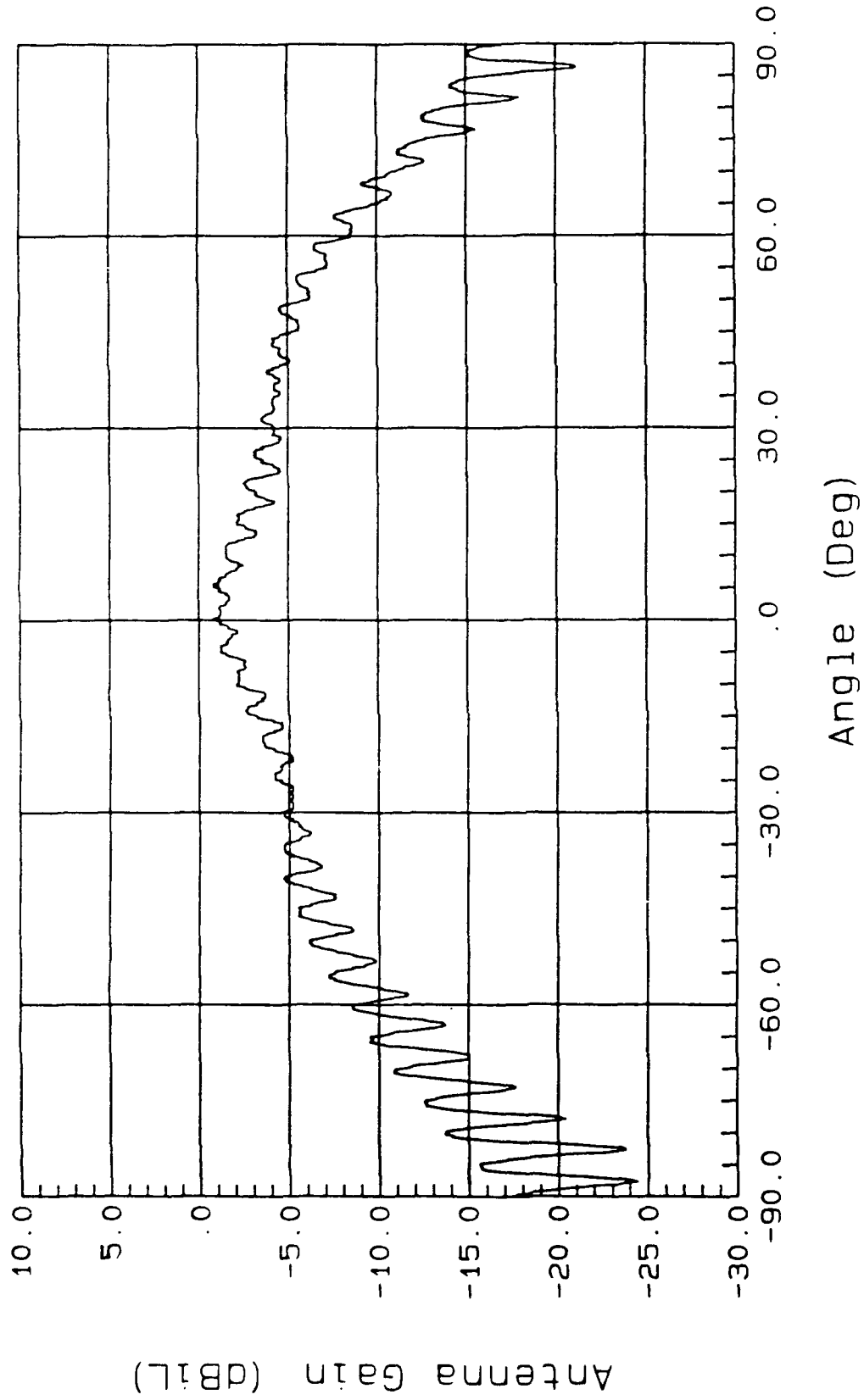


Figure 4. Measured radiation pattern for the Figure 1 antenna at 2 GHz.

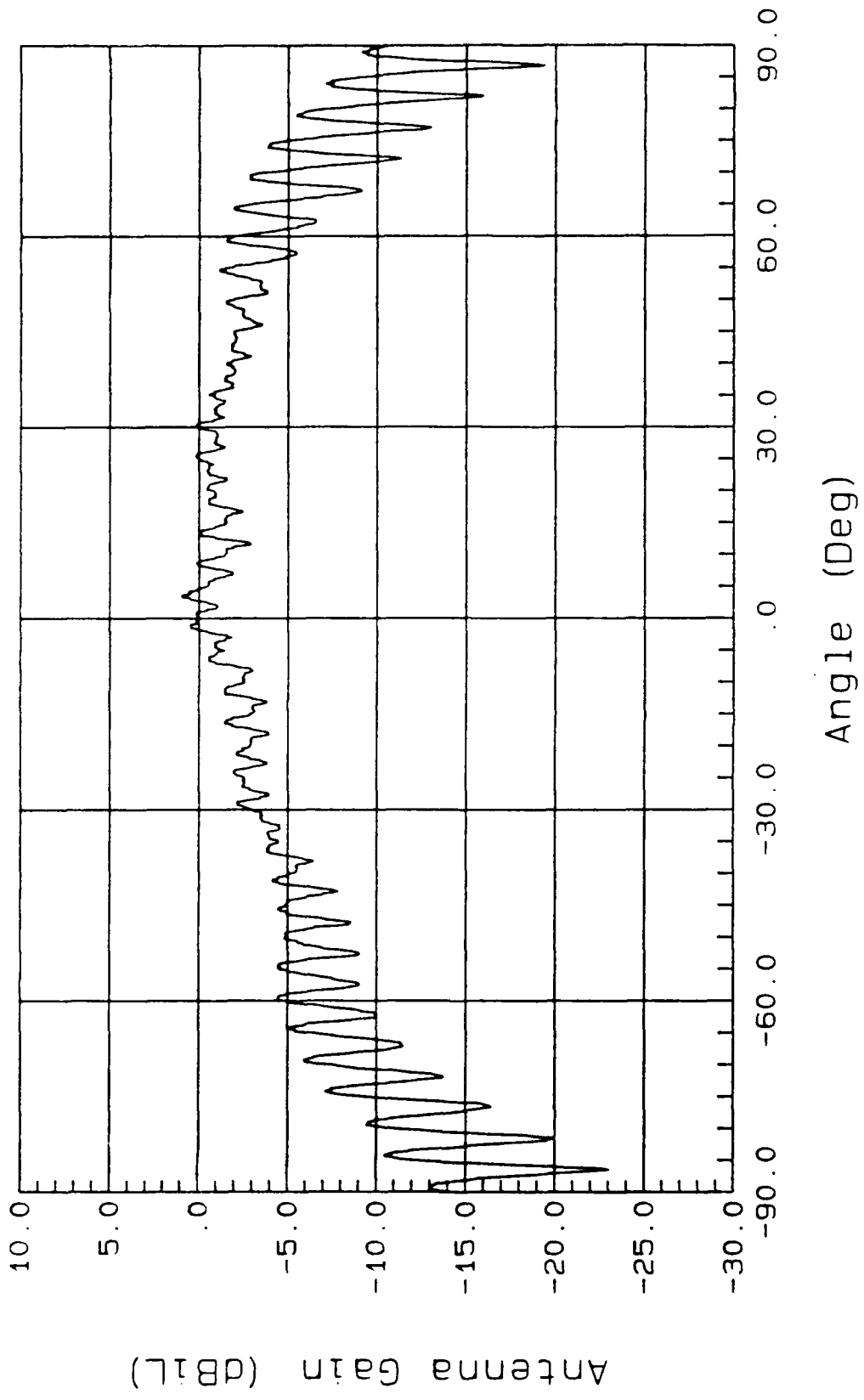


Figure 5. Measured radiation pattern for the Figure 1 antenna at 3 GHz.

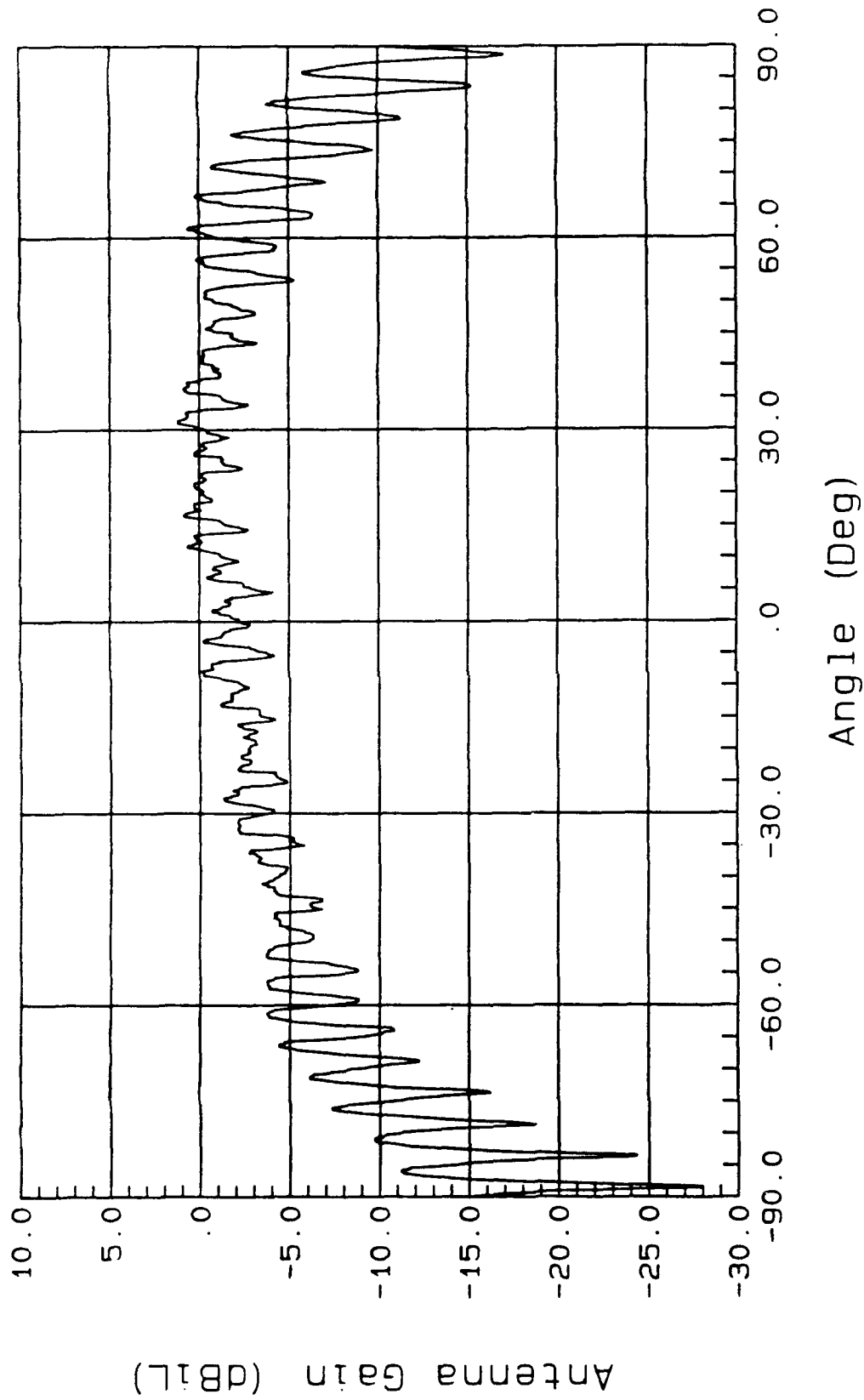


Figure 6. Measured radiation pattern for the Figure 1 antenna at 4 GHz.

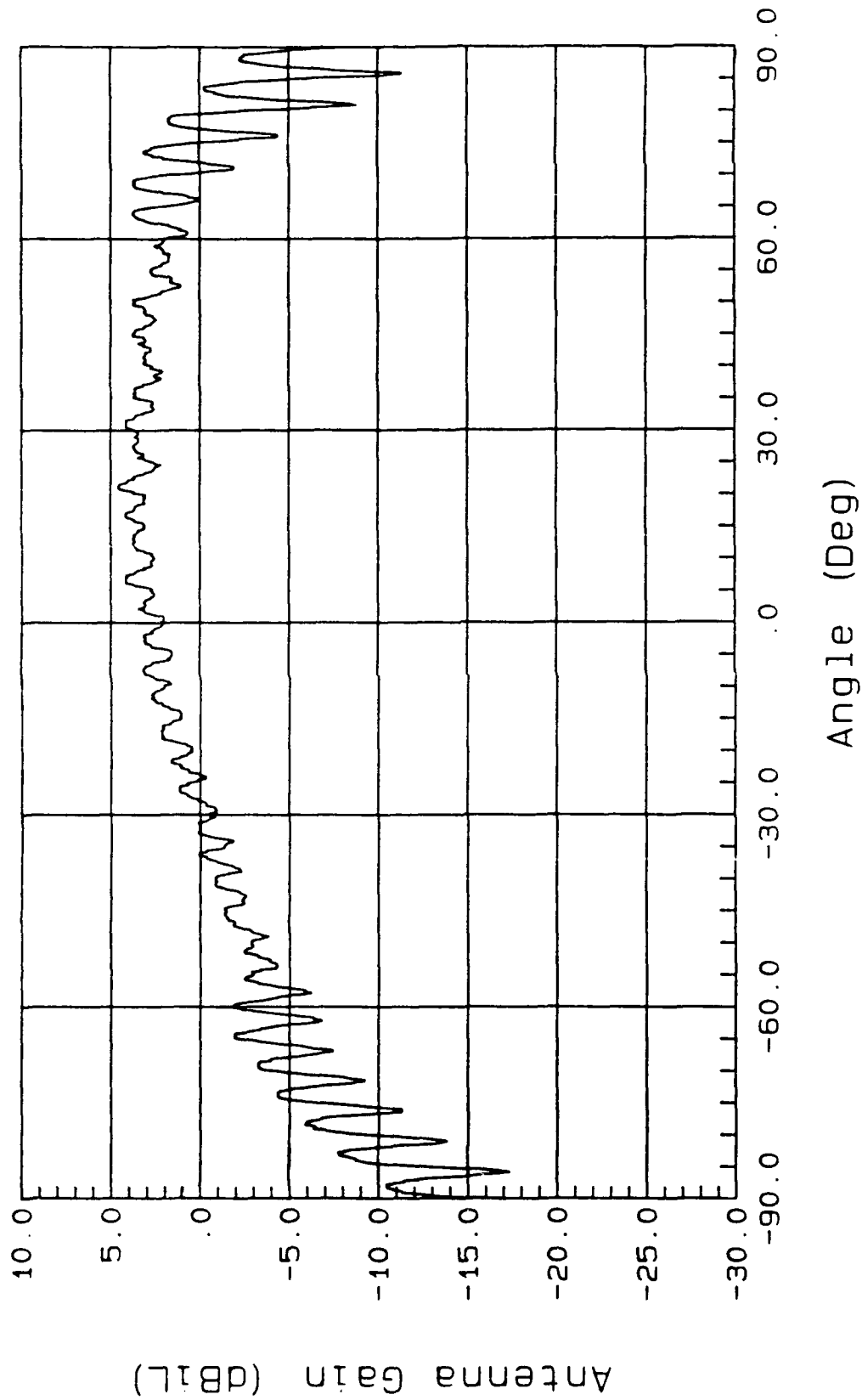


Figure 7. Measured radiation pattern for the Figure 1 antenna at 6 GHz.

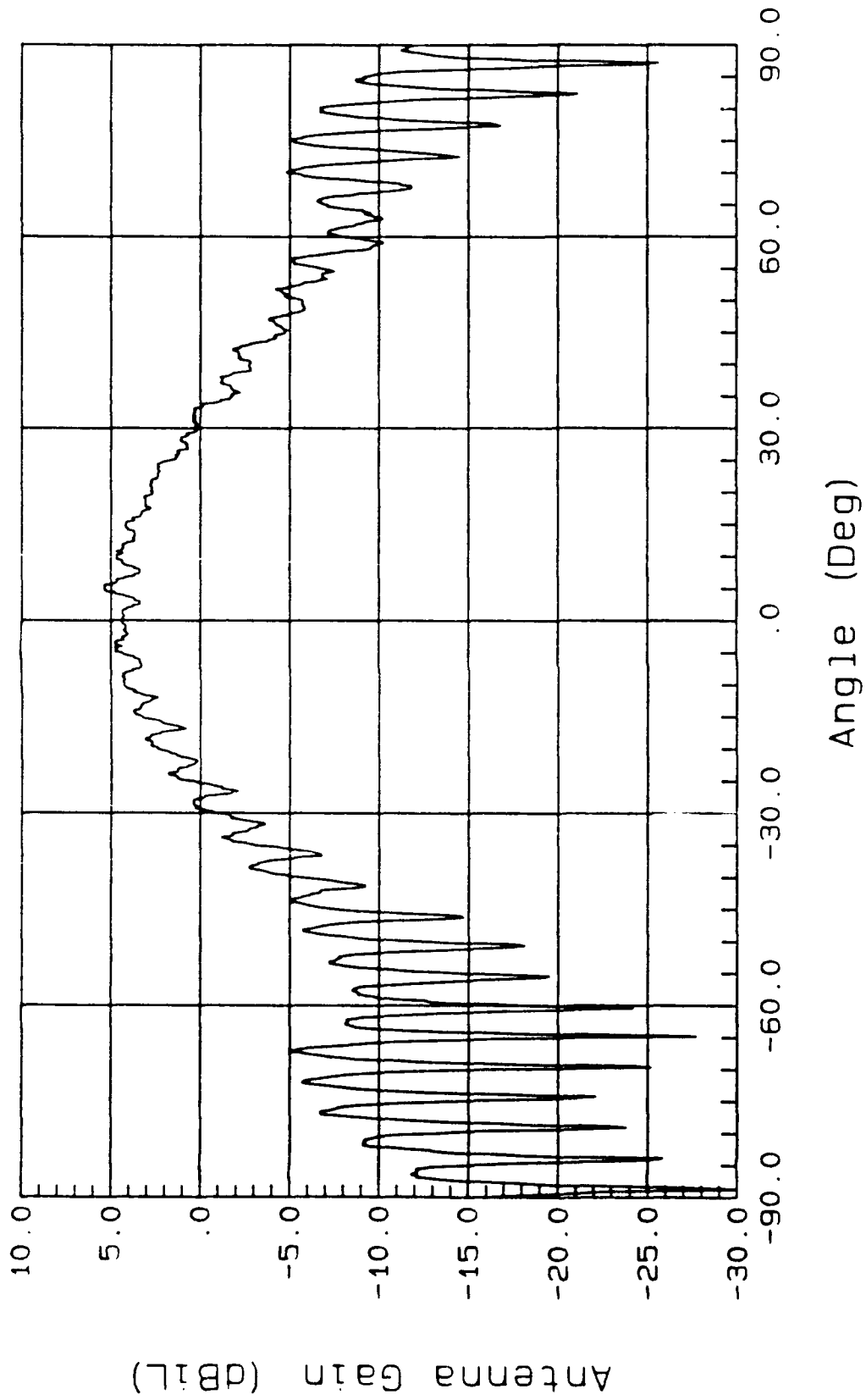


Figure 8. Measured radiation pattern for the Figure 1 antenna at 8 GHz.

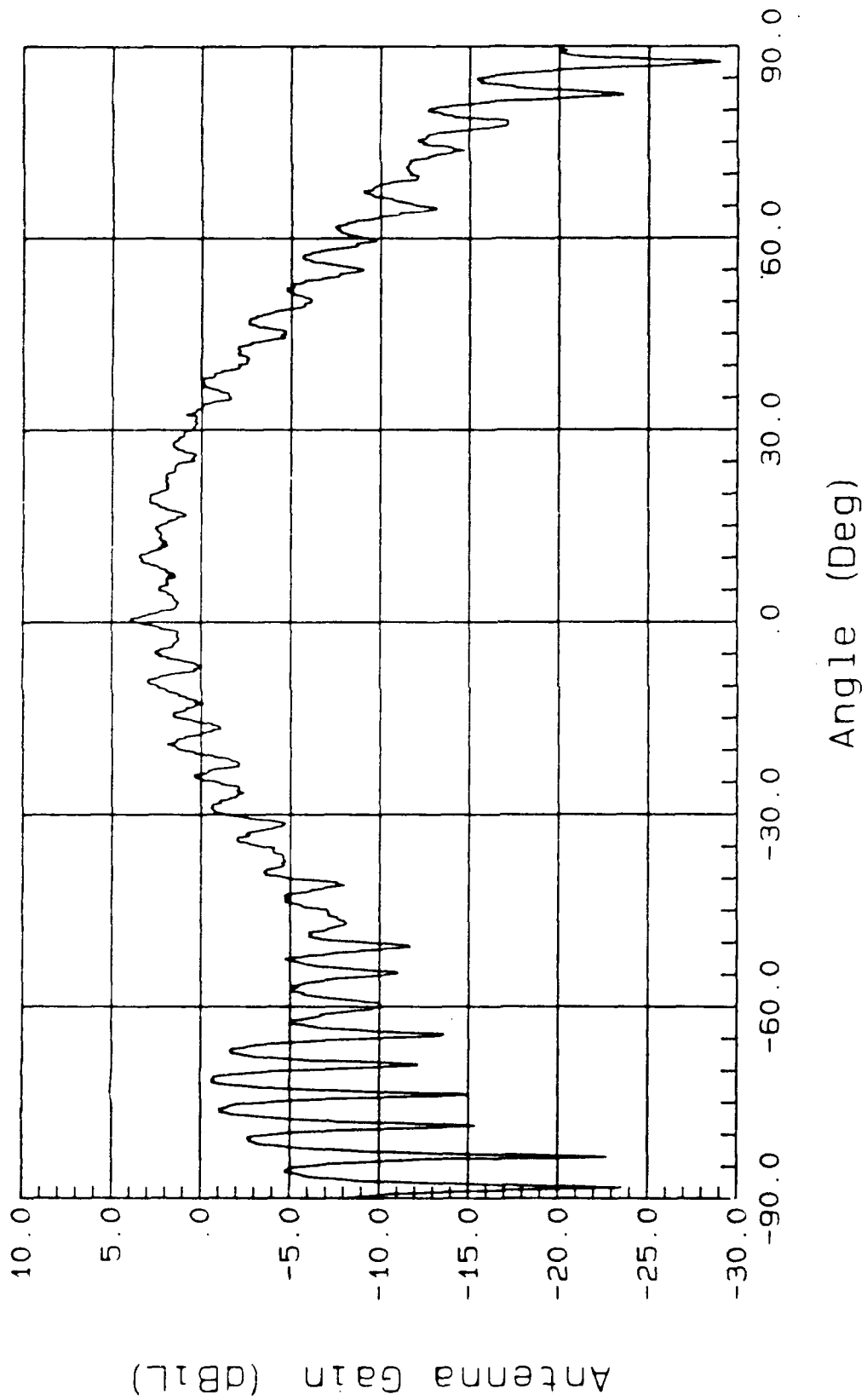


Figure 9. Measured radiation pattern for the Figure 1 antenna at 10 GHz.

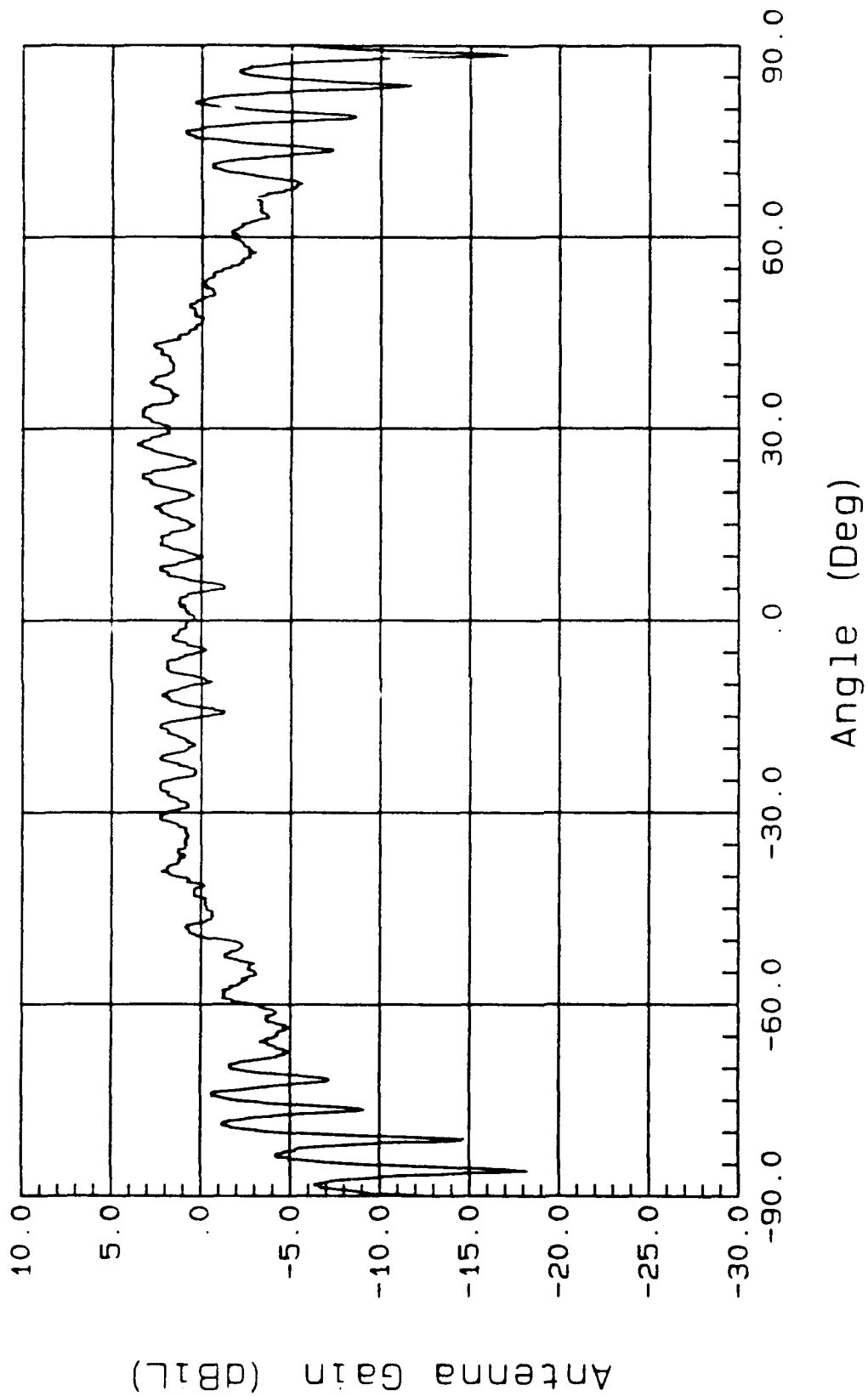


Figure 10. Measured radiation pattern for the Figure 1 antenna at 12 GHz.

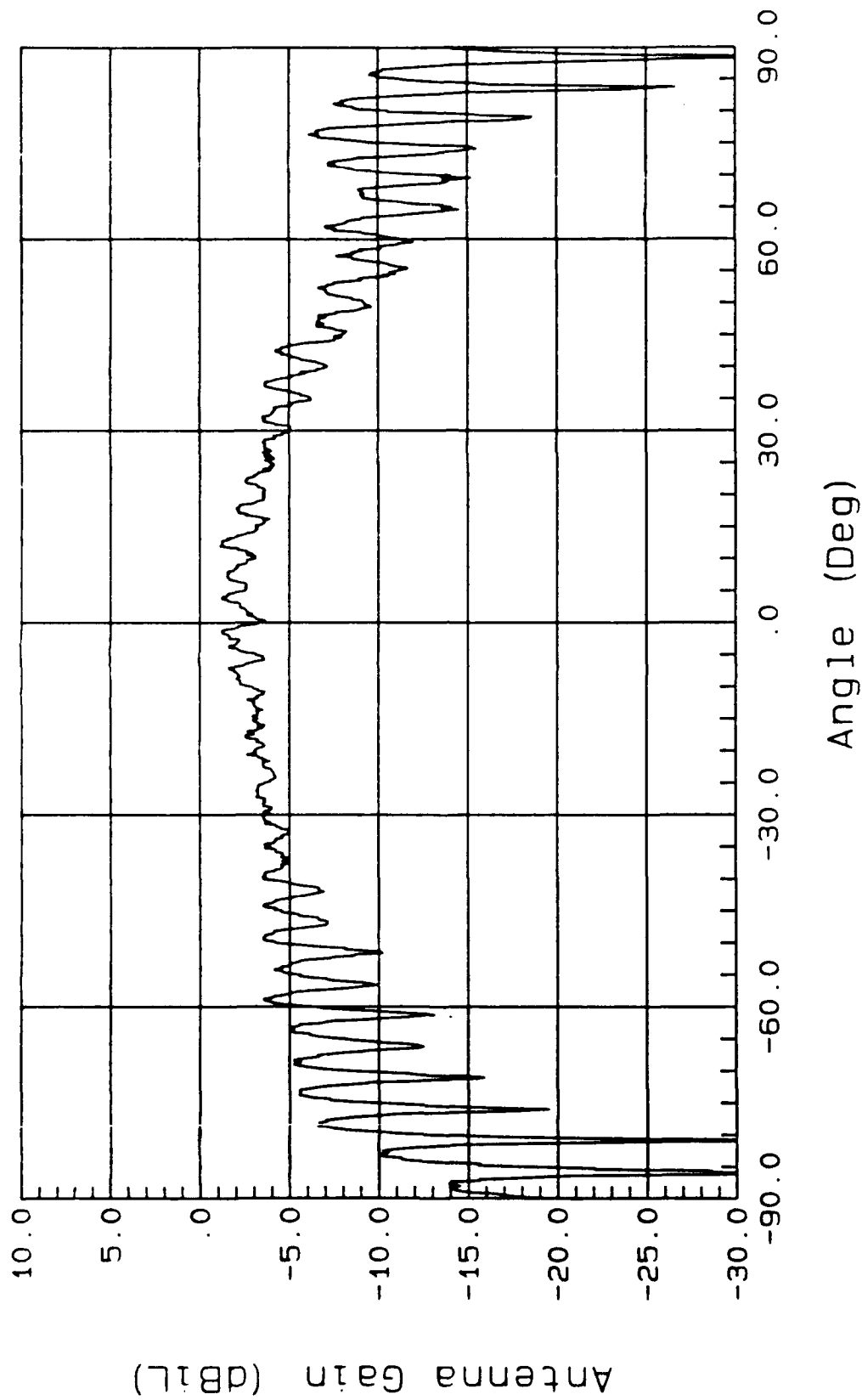


Figure 11. Measured radiation pattern for the Figure 1 antenna at 14 GHz.

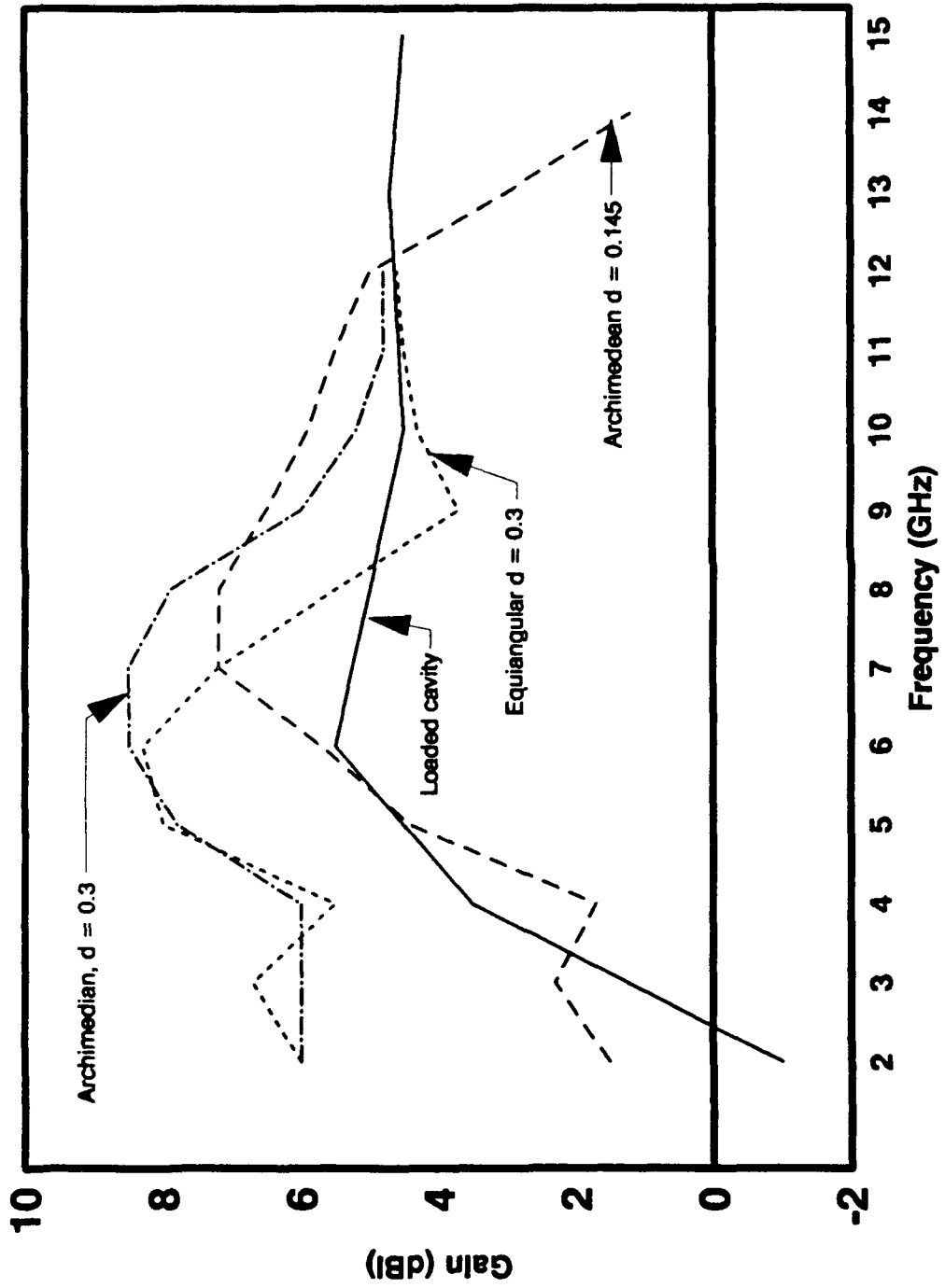


Figure 12. Comparison of gain curves for various microstrip configurations and the loaded cavity spiral.

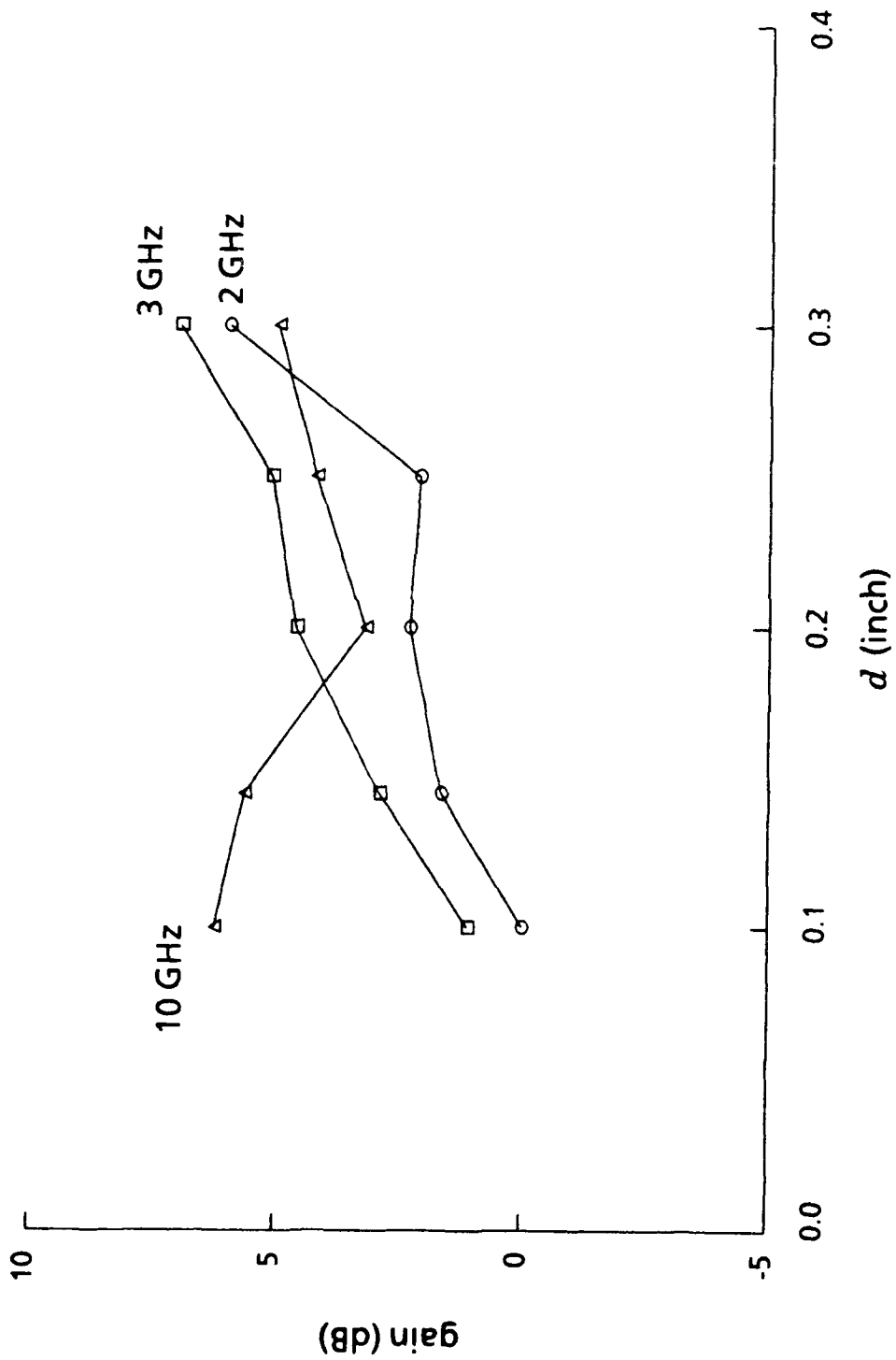


Figure 13. Effect of ground plane spacing on antenna gain.

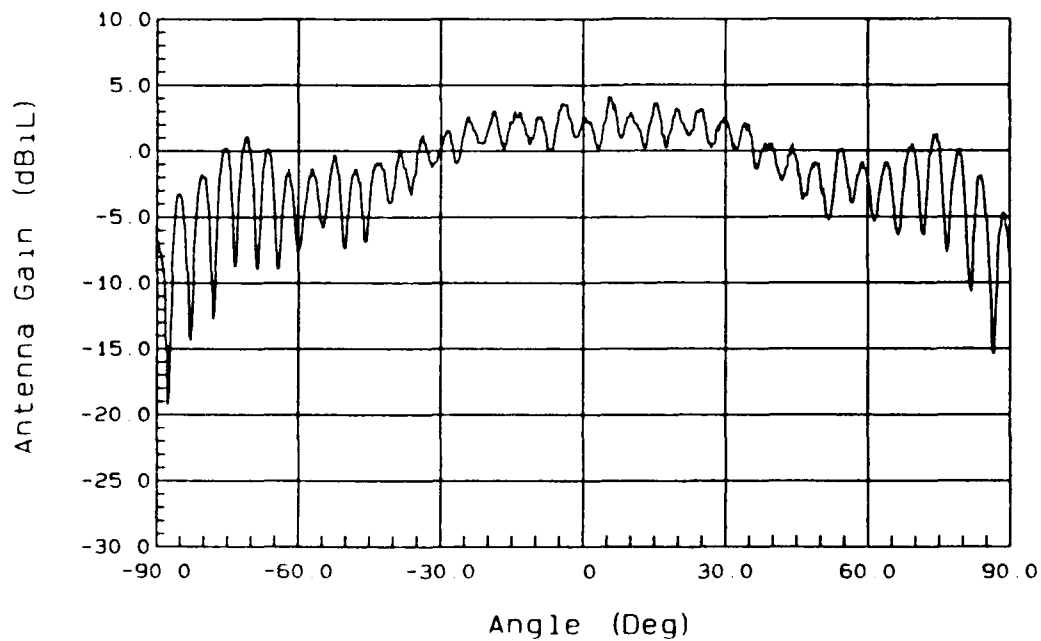
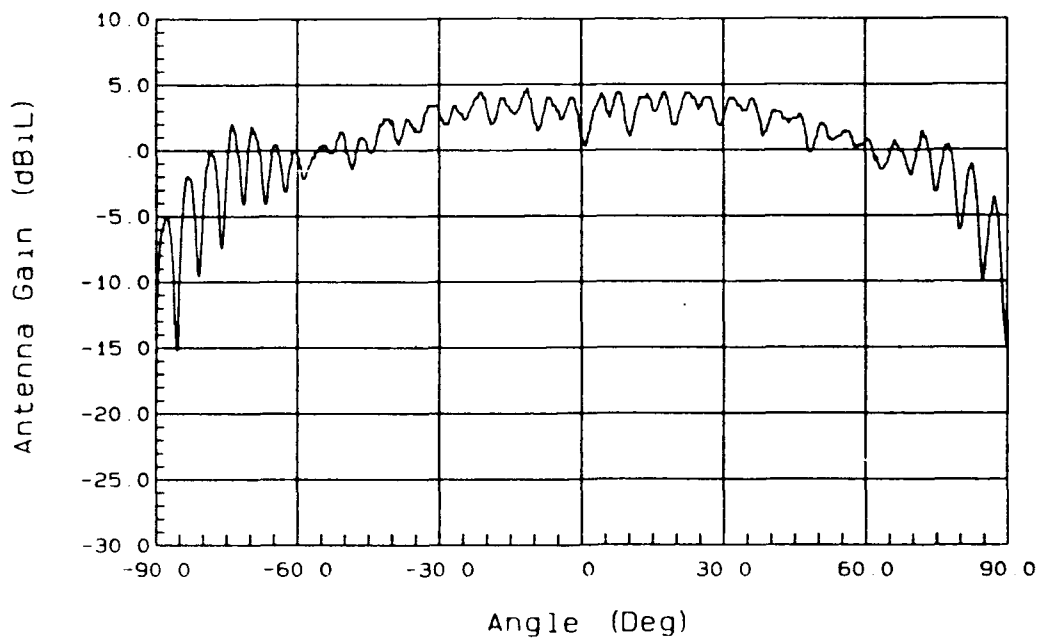


Figure 14. Effect of $\epsilon = 4.37$ substrate on patterns at 9 GHz.

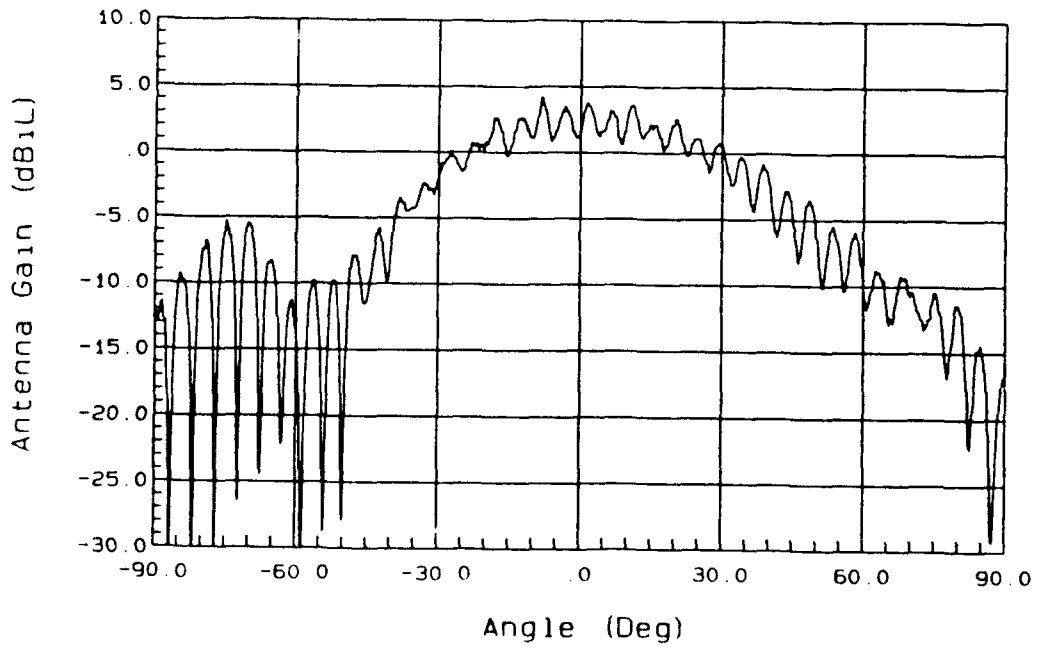
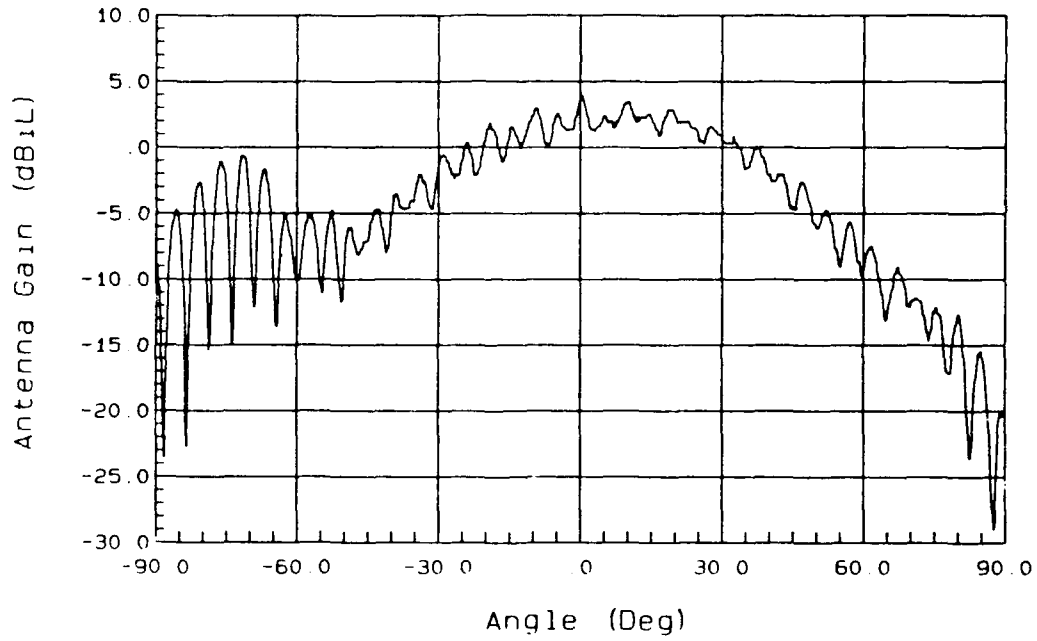


Figure 15. Effect of $\epsilon = 4.37$ substrate on patterns at 10 GHz.

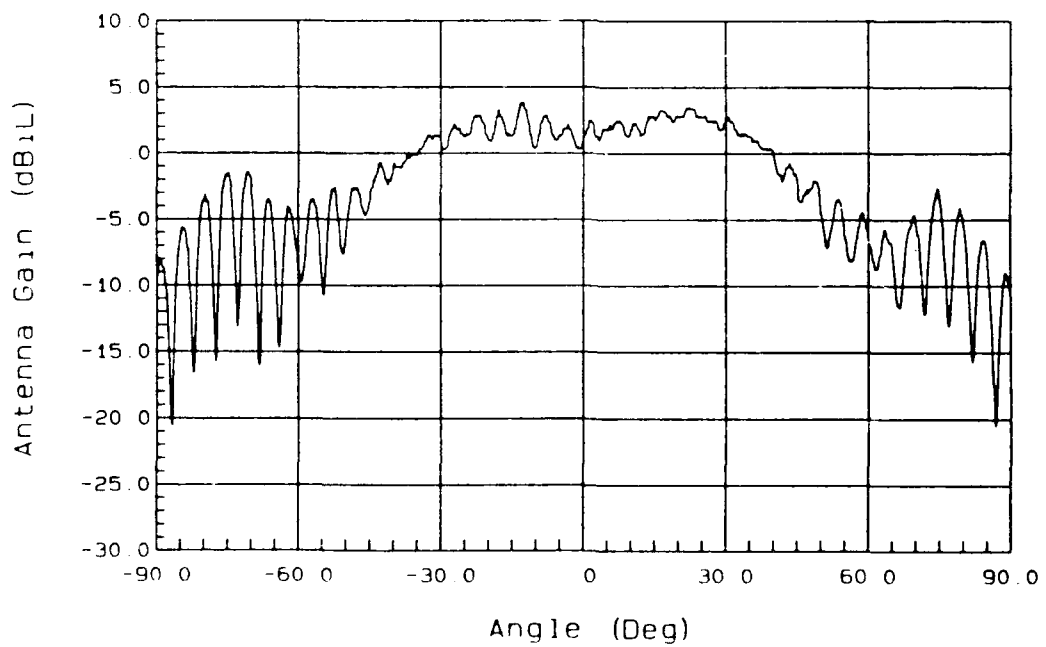
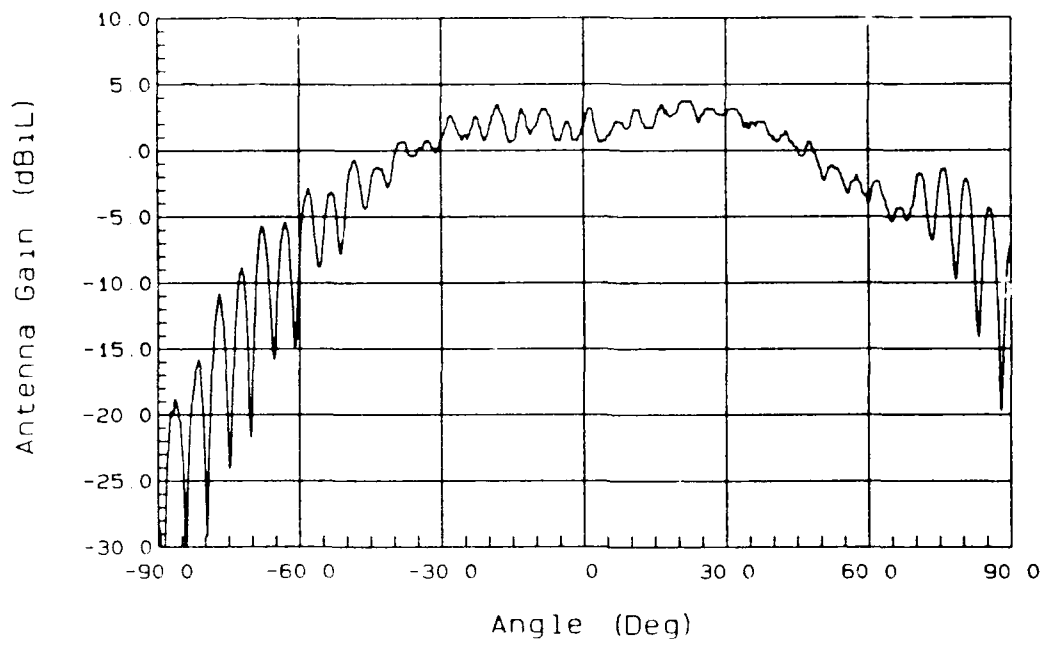


Figure 16. Effect of $\epsilon = 4.37$ substrate on patterns at 11 GHz.

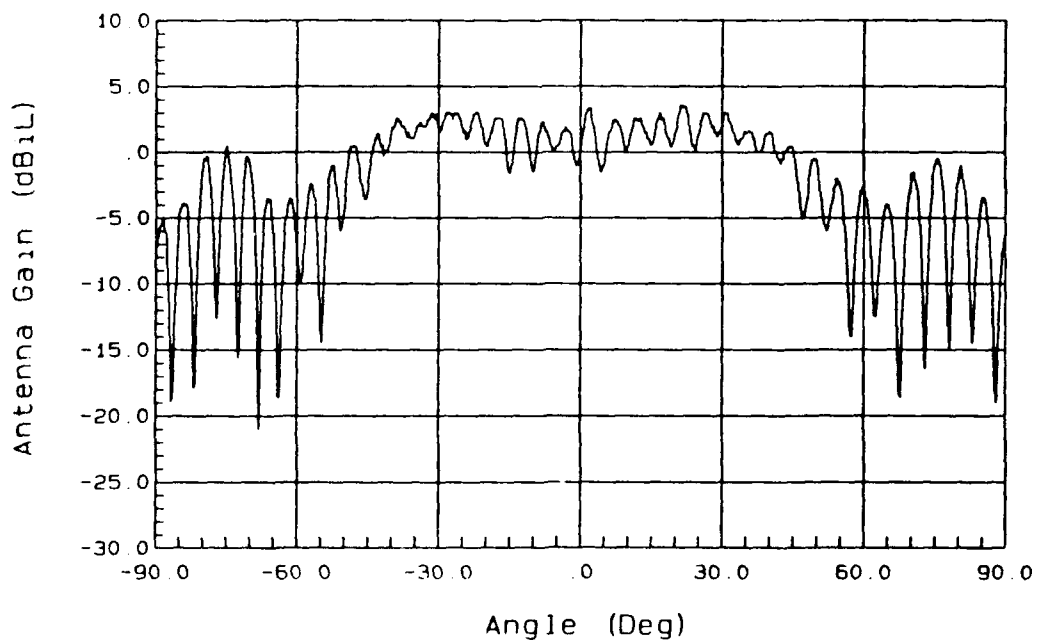
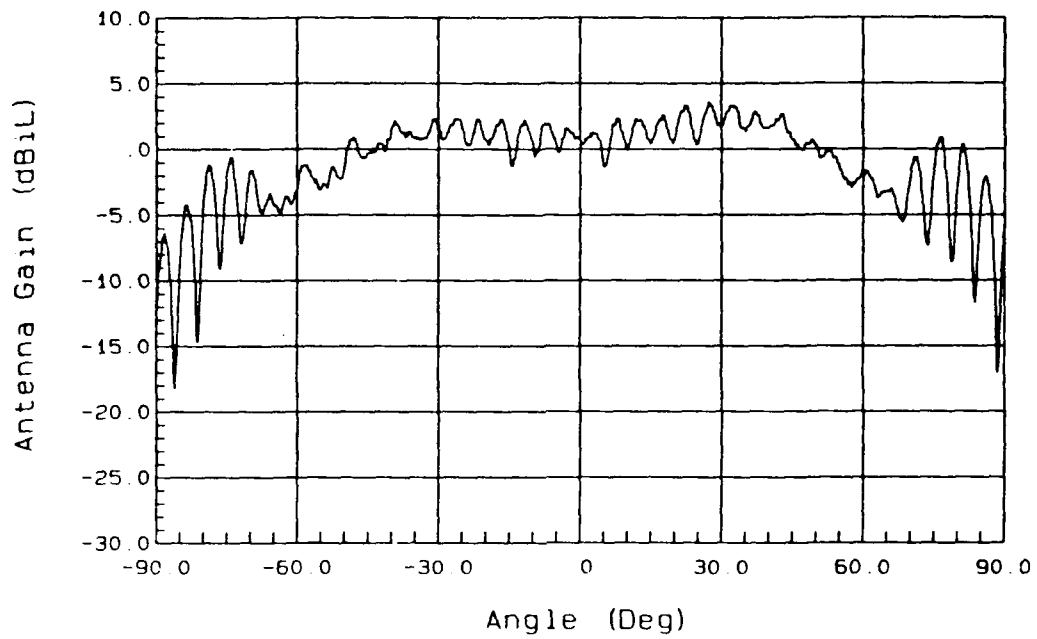


Figure 17. Effect of $\epsilon = 4.37$ substrate on patterns at 12 GHz.

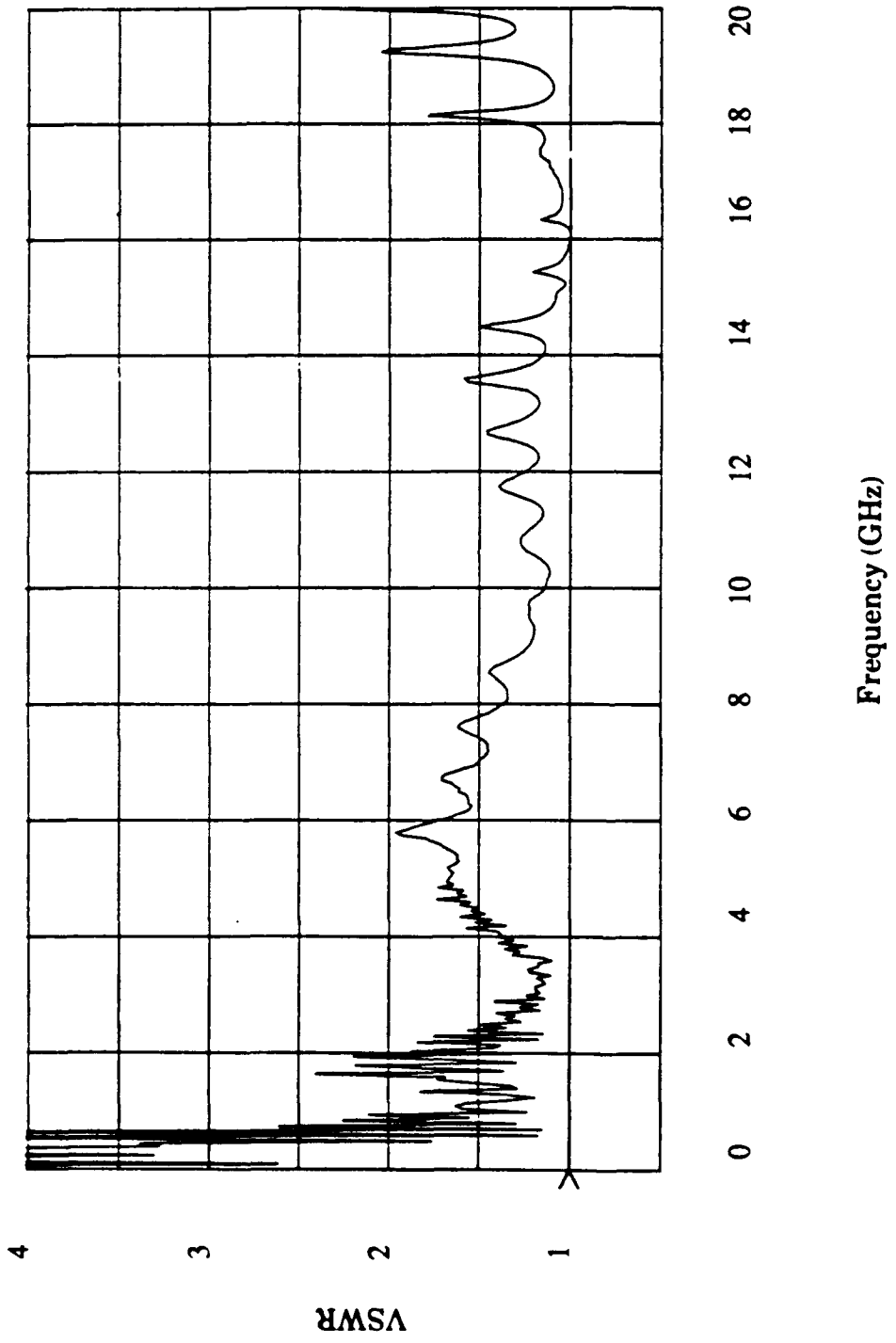


Figure 18 - Measured VSWR for a microstrip spiral with foam edge loading.

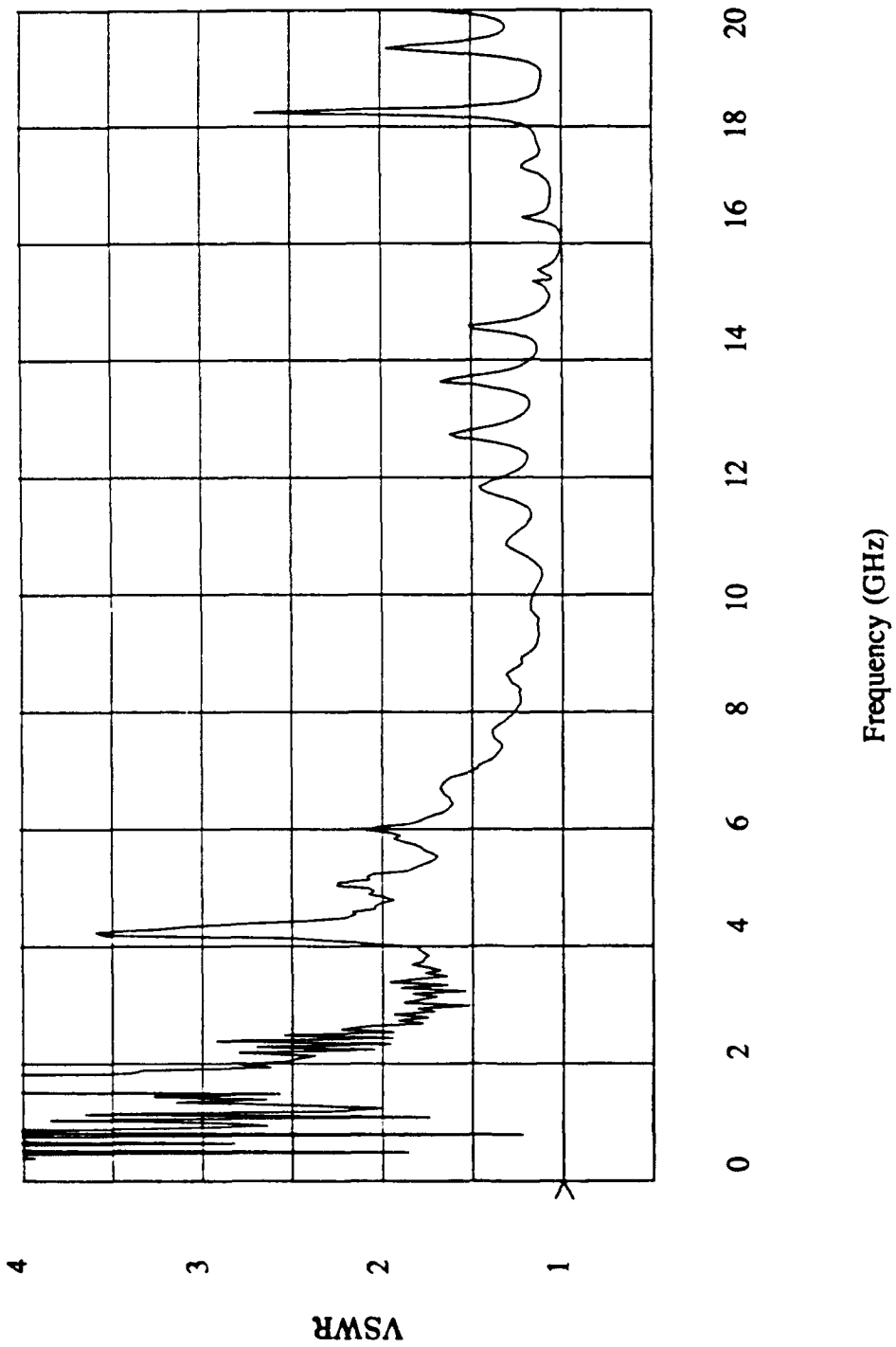


Figure 19 - Measured VSWR for a microstrip spiral with magnetic RAM edge loading.

ABSTRACT

**EXTERNAL LENS LOADING OF CAVITY-BACKED
SPIRAL ANTENNAS FOR IMPROVED PERFORMANCE**

George J. Monser

The Raytheon Company
Electromagnetic Systems Division
Goleta, CA

This paper presents the results of an empirical study to improve the performance of a log-spiral, cavity-backed antenna.

It is shown that an external lens over the antenna can be designed to yield improved on-axis gain at F_{LOW} , minimum perturbation over the middle of the band, and improved off-axis gain at F_{HIGH} (approximately $2 \times F_{LOW}$).

Four antenna/lens assemblies were evaluated to support the reproducibility of the design.

EXTERNAL LENS LOADING OF CAVITY-BACKED
SPIRAL ANTENNAS FOR IMPROVED PERFORMANCE

George J. Monser

The Raytheon Company
Electromagnetic Systems Division
Goleta, CA

SUMMARY

This paper presents the results of an empirical study effort to improve performance of a cavity-backed spiral antenna by external loading.

Data and analysis are presented showing that the technique is feasible and attractive, yielding gain improvements of 1 to 2 dB over conventional techniques.

1.0 INTRODUCTION

This paper describes the empirical development of an external lens over a cavity-backed spiral antenna. The purpose of the lens was to reshape the radiated energy to achieve the required minimum gain on antenna boresight and at $\pm 60^\circ$ with respect to boresight.

Uniquely, the lens was required to slightly narrow the pattern at F_{LOW} for more on-axis gain, minimally perturb the patterns midband, and at $2 \times F_{LOW}$ to achieve significant beam-broadening for more off-axis gain.

2.0 BASIC ANTENNA

Figure 1 shows a photograph of the antenna without any lens over the circuit-board. Here, a log-spiral was printed on the Duroid 5880 substrate, and only slight absorber loading was used within the cavity so as not to reduce the forward gain.

The basic antenna was fed through two equal-length, 0.085 inch diameter semi-rigid cables and an external Magic-Tee so that maximum effort could be given to developing the lens. Figure 2 shows a cross-section of the basic antenna.

3.0 LENS

Two candidate materials were chosen for the lens: acrylic with dielectric constant of about 2.7; and Teflon with a dielectric constant of about 2.04. Both materials had low-loss tangents over the frequency band, and both materials were easily machined to size and contour.

Figure 3 shows a photograph of some of the lenses evaluated with the antenna. Each lens had a small clearance area around the feed-points. For preliminary tests, the lenses were taped in position. For final tests, they were cemented in position.

4.0 TEST RESULTS (BASIC ANTENNA)

Figure 4 shows how the 3 dB beamwidth varies with frequency without any lens over the antenna. Figure 5 shows on-axis gain versus frequency.

Analysis of the beamwidth and gain data confirmed that the requirements could not be met without a lens.

The lens would be required to accomplish the following objectives:

- (1) Provide beamwidth narrowing over the lower part of the band to improve on-axis gain without significantly affecting the edge-of-view gain.

- (2) Over mid-band, the lens should leave the patterns and gain unchanged.

- (3) Provide significant beam-broadening over the upper part of the band, trading on-axis gain for edge-of-view gain.

5.0 TEST RESULTS (LENS-LOADED ANTENNA)

Figure 6 shows the minimum linear gain on-axis and at the edge of the field of view. Both curves represent performance to the 90 percentile levels (i.e., 90% of the data equals or exceeds the required data). This data was achieved using the serrated, contoured Teflon lens.

Figure 7 shows the VSWR for the individual arms of the spiral. Figure 8 shows the on-axis axial ratio.

Figure 9 shows on-axis gain versus frequency for the lens-loaded antenna.

6.0 DISCUSSION

The basic antenna showed deficiencies versus the requirements when evaluated without a lens. In particular, the beamwidths showed considerable variability and narrow pattern coverage near F_{HIGH} . Here, absorber loading within the cavity could have been used at the expense of gain for improved pattern performance. However, from a gain viewpoint, it appeared that a better approach would be to use an external lens.

Analysis of the data led to the following requirements: (1) The lens should provide for a slight gain improvement near F_{LOW} ; (2) the lens should not perturb mid-band performance; and (3) the lens should yield significant beambroadening near F_{HIGH} .

In the design process, the lens dielectric loading near the periphery and near the center were used, but for different reasons (see Figure 10). The peripheral loading objective was to enhance gain near F_{LOW} while the center-loading objectives were to broaden the beamwidth and reduce on-axis gain near F_{HIGH} .

The extent of realizing the above objectives is illustrated in Figure 4. Here, the beamwidths with lens

loading (dotted curves) are shown for ready comparison to the basic antenna without any lens. Figures 5 and 9 can also be compared. There, the effects of the lens on on-axis gain are apparent. Namely, the lens improves gain near F_{LOW} .

7.0 CONCLUDING REMARKS

This effort has shown the following results.

- (1) A simple external lens can be used to improve cavity-backed spiral antenna performance.
- (2) In particular, the lens simultaneously improves gain over the lower part of the band and broadens the coverage over the upper part of the band.
- (3) Compared to conventional techniques (such as absorber loading in the cavity and lossy terminations of the spiral windings, both of which improve pattern performance at the expense of gain), the lens-loading achieves the same results without reducing gain.
- (4) A total of four antennas with lenses were evaluated. Three of these units are shown in Figure 11. Results showed excellent correlation supporting the reproducibility of the empirically-designed lens.

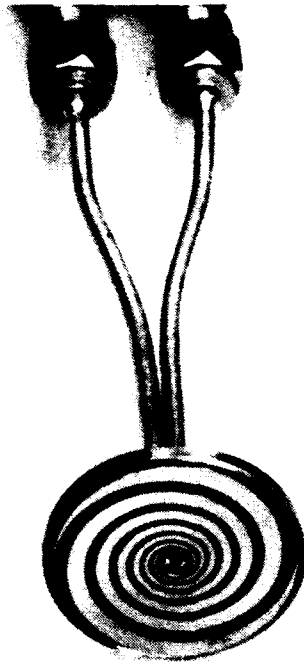


Figure 1. Antenna Without Lens

N29370

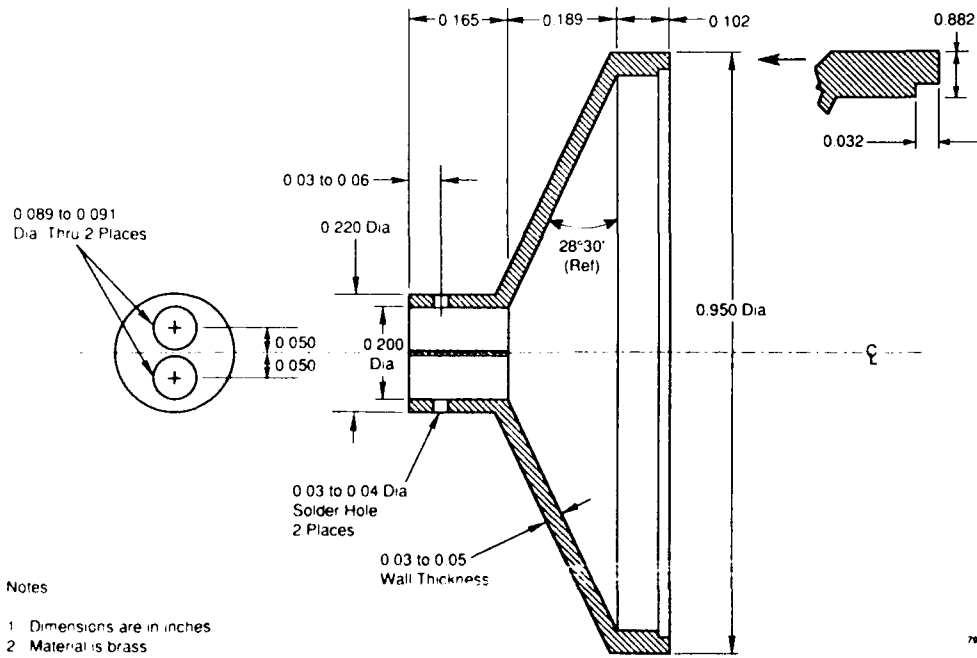


Figure 2. Antenna (Cavity) Cross Section

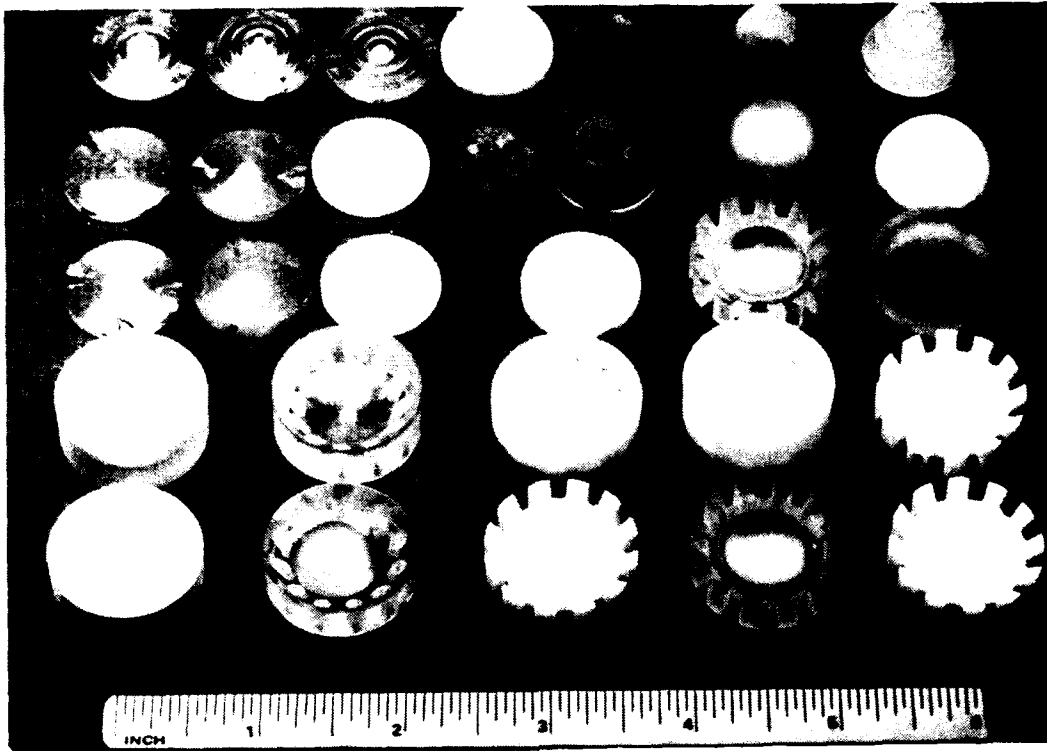


Figure 3. Lenses Evaluated with Cavity-Backed Log-Spiral

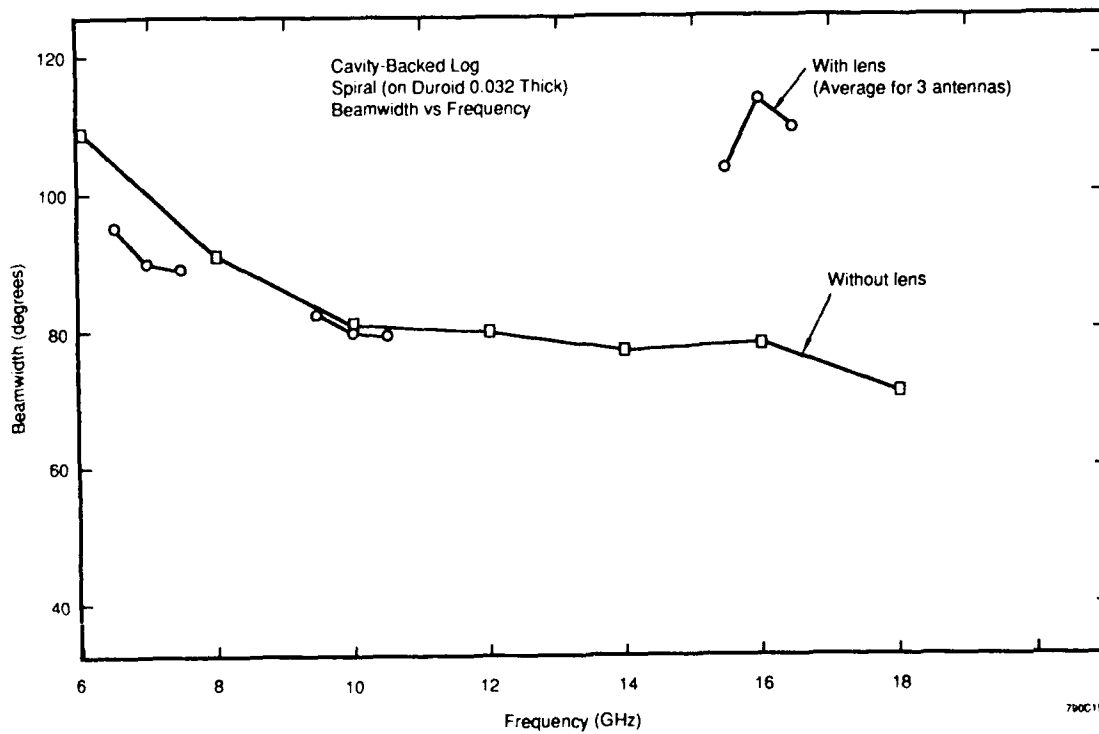


Figure 4. Beamwidths, With and Without Lens

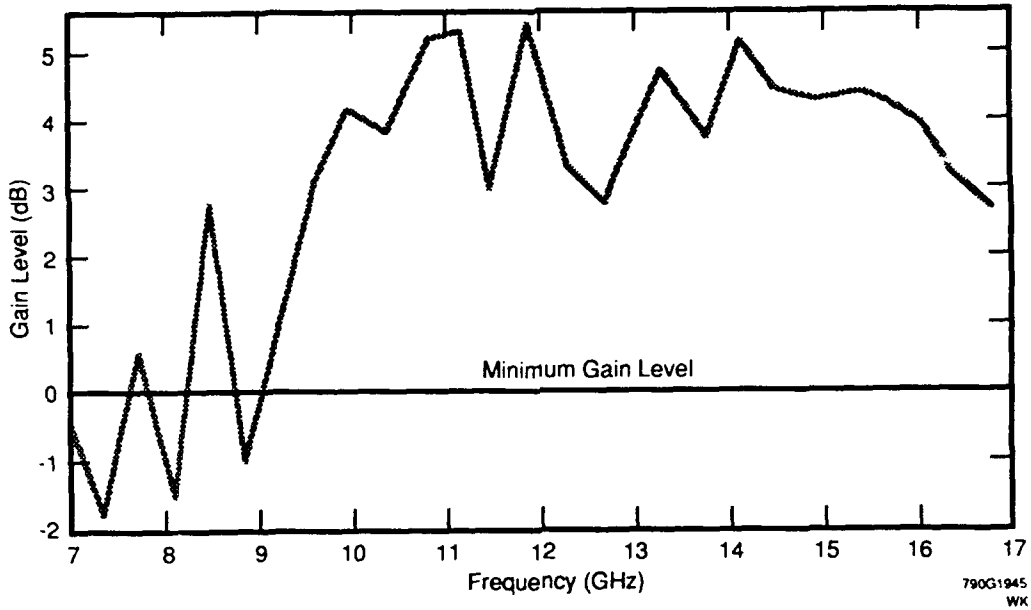


Figure 5. Boresight Matched Gain vs Frequency (Without Lens)

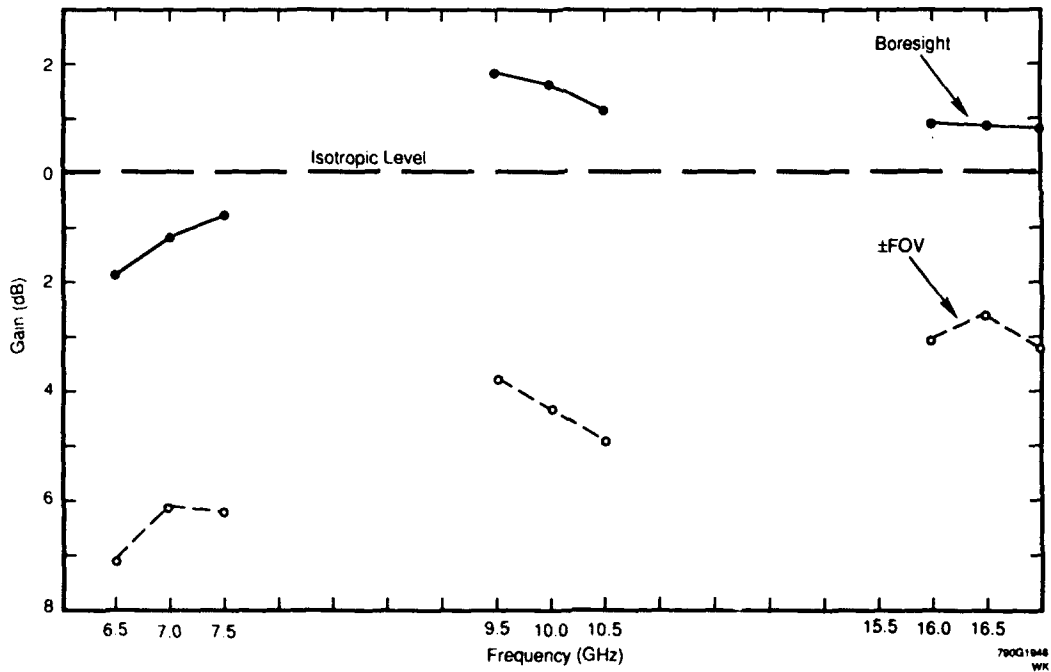


Figure 6. Average Linear Gain (Three Test Models)

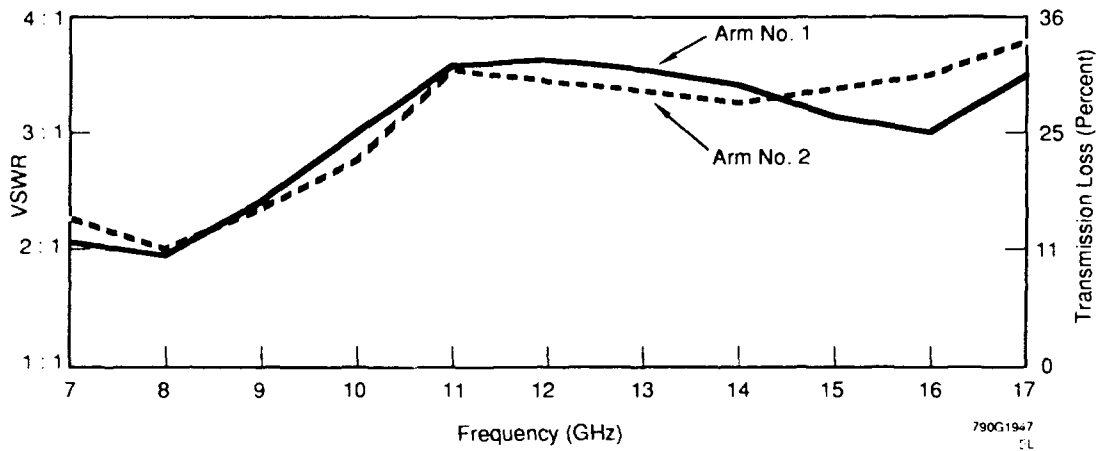


Figure 7. Individual Arms of Spiral, VSWR, and Transmission Loss vs Frequency

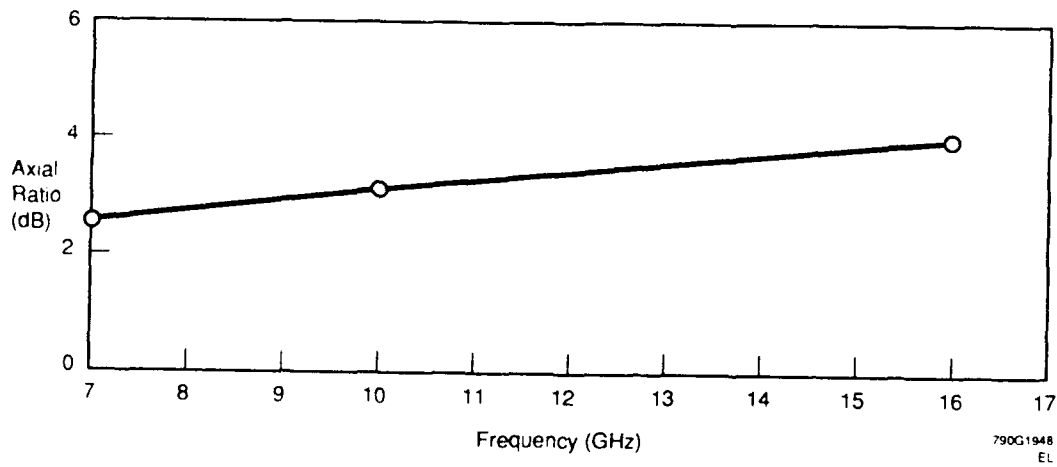


Figure 8. Boresight Axial Ratio vs Frequency

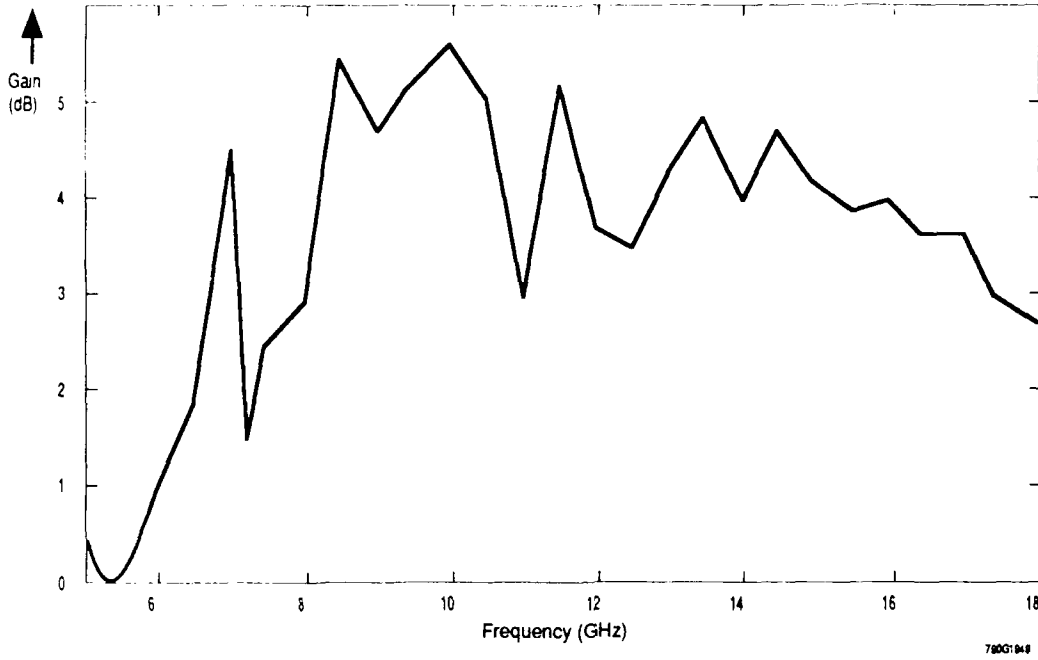


Figure 9. Matched Gain versus Frequency (Boresight) (With Lens)

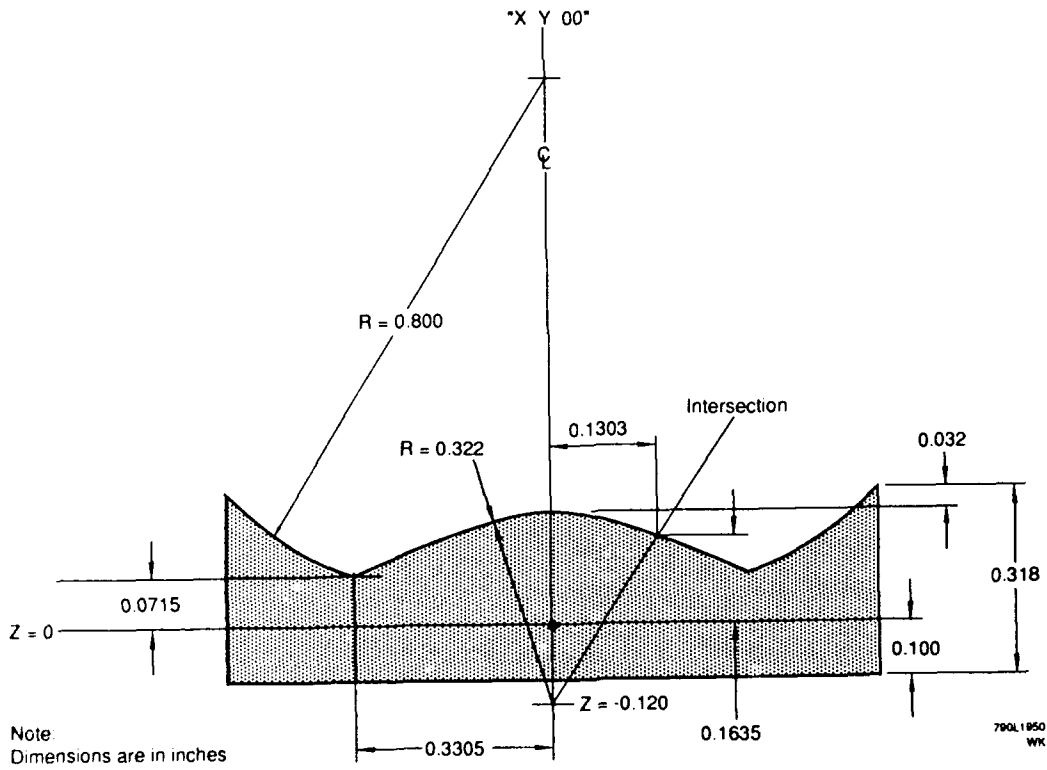


Figure 10. Lens Cross Section

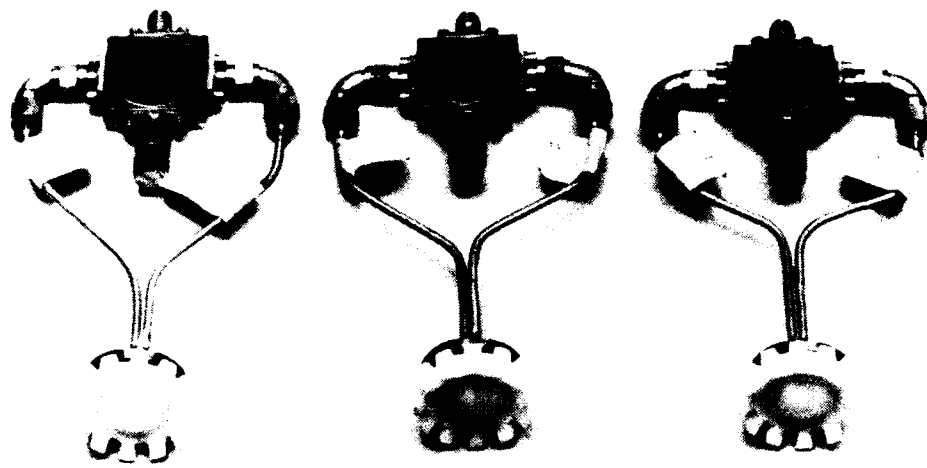
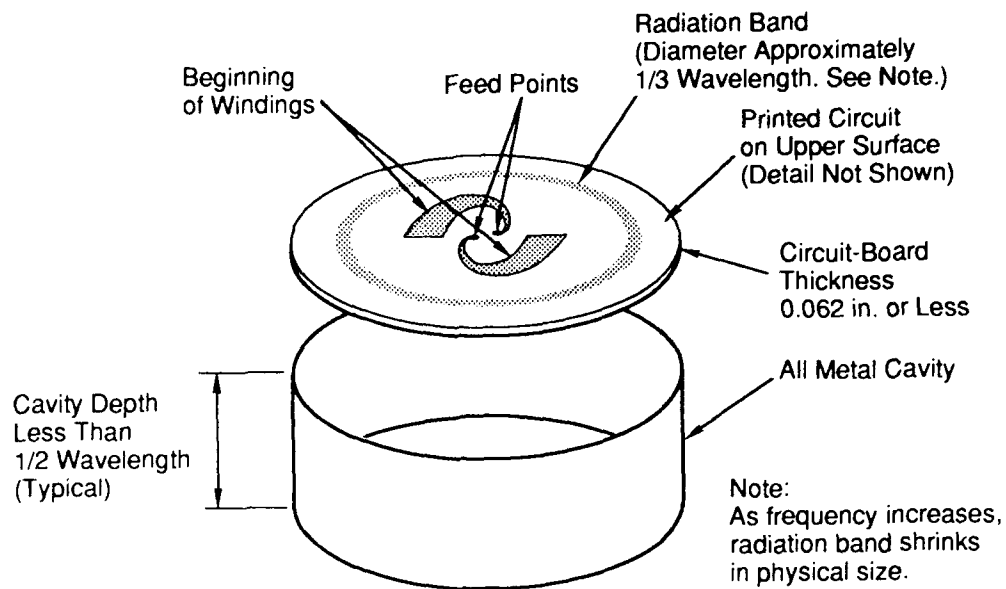


Figure 11. Antennas with Lenses

N30192



790L1968

Figure A-1. Cavity-Backed Spiral Antenna, Basic Elements (Illustrative)

A COMPACT BROADBAND ANTENNA

Sam C. Kuo and Warren Shelton
GTE Government Systems
100 Ferguson Drive
P.O. Box 7188, Mt. View CA 94039

The log-periodic dipole antenna (LPDA) theoretically provides an infinite bandwidth; therefore, it is invariably proposed when an application demands broadband antennas. In practice, the lowest frequency at which LPDAs are able to operate is limited by the length of the largest dipole. For a conventional LPDA that uses linear wire dipoles as radiators, the length of the largest dipole is on the order of one-half wavelength at the lowest operating frequency. This physical requirement precludes the use of LPDAs in some circumstances.

The conventional LPDA, shown in Figure 1, is defined primarily by two design parameters: alpha, the enclosed half angle, and tau, the ratio of the distance between or the lengths of adjacent dipoles. Alpha controls the length of the antenna structure, and tau determines the number of dipole elements. LPDAs with alpha smaller than 15° and tau greater than 0.9 generally exhibit moderate gain and directivity. These LPDAs also characteristically provide uniform performance because a relatively large tau provides many nearly resonant dipoles in the active region of the structure.

For each alpha, there exists an optimum value of tau. Deviation from the optimal value tends to result in a degradation in antenna performance. However, for alpha less than 15° , the LPDA will tolerate a relatively large range of tau without significant performance degradation. For these reasons, most size-reduction experiments in the microwave frequency region have been conducted on LPDAs with relatively small alpha angles. An example is the reduced-size antenna described in a U. S. Patent by J. C. Pullara¹. The antenna disclosed therein is characterized by an alpha angle of 12° and a tau of 0.95.

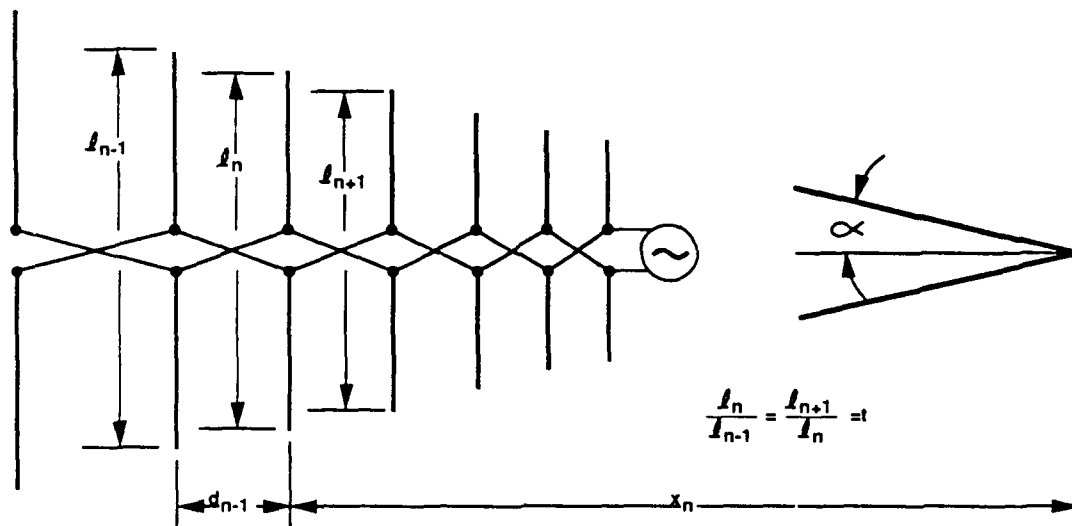


Figure 1. Design Parameters of the Log-Periodic Dipole Antenna

The difficulty in reducing the width of the LPDA increases as the alpha angle of the LPDA increases. To date, I am not aware that anyone has yet successfully reduced the width of microwave LPDAs to 50 percent with an alpha equal to or greater than 45° . The difficulty in foreshortening a LPDA with an alpha of about 45° lies in the conventional LPDA itself. As a result, broadband LPDAs with alphas greater than 45° are not commercially available for operating up to Ku-band frequency range.

The incentive to develop a broadband LPDA with a large alpha becomes apparent when it is understood that the boom length of an LPDA with a 45° alpha is approximately one-fifth that of an LPDA with an alpha of 12° . There are instances when the size restrictions will apply to both the length and the width of the LPDA. Specifically, when a short LPDA is required due to space limitation, alpha has to be

increased. In order to optimize performance, the value of tau must be decreased if the alpha is increased much over 15°.

The art of designing antenna structures with short booms and large alphas is not well known; and there has been very limited investigation of the performance and anomalies of these LPDAs. One study by Bantin and Balmain resulted in an outstanding paper². The authors, however, did not provide any practical solutions. (They did recommend using extremely large values of taus, such as 0.96, for LPDAs with larger alpha; however, this is very difficult to achieve in practice, especially in the microwave frequency range.)

The anomalies associated with the LPDAs mentioned above, however, do not apply to those operating at HF or low VHF because these LPDAs are excited differently from the microwave ones. The LPDA is a balanced antenna and, therefore, must be excited by using a balun for coaxial (unbalanced) systems. LPDAs operating at HF or low VHF are usually excited by a combined balun/transformer attached to the small end of the structure because the size of the balun/transformer is small compared with the lengths of the small dipole radiators. This gives low-frequency LPDAs an advantage over microwave antennas because the balanced transmission line used to excite the dipoles can be made to have a very high characteristic impedance. The higher the characteristic impedance of the LPDA feedline, the easier it is for the excitation currents to be coupled into the dipole radiators. A broadband LPDA operating at microwave frequencies, unfortunately, cannot tolerate such a large device at the small end of the antenna and, thus, is usually excited by using the "infinite balun" technique. Since the infinite balun is usually

made of 50-ohm coaxial cable, which is also an integral part of the feedline, a balanced feedline with high characteristic impedance will introduce high VSWR.

For conventional LPDAs with relatively small alphas and appropriate taus, it is generally adequate to excite the antenna with a balanced feedline with a characteristic impedance as low as 100 ohms because there are sufficient nearly resonant dipoles in the active region to radiate most of the excitation current. The amount of residual current, which goes on to excite the larger dipoles, will not degrade the performance of the antenna. However, when the alpha is 45° or more, LPDAs with linear dipoles and low feedline characteristic impedances will have anomalies caused by too few nearly resonant dipoles in the active region. Some of the excitation current will pass through the active region and introduce anomalies at other frequencies. These anomalies can be in the form of high backlobe levels which occur at frequencies where the active region is approximately $(2n+1) \lambda/4$ from the open truncation of the balanced feedline. If a shorted termination is used instead of an open at the end of the feedline, the anomalies will shift to different frequencies.

Another form of anomaly is the excitation of the $3/2$ - or $5/2$ -wavelength dipoles by the residual currents. When this happens, the E-plane radiation patterns will have narrower beamwidth and sidelobes. These can be eliminated by simply increasing the characteristic impedance of the balanced feedline (i.e., increasing the spacing of the feedline). A higher-impedance feedline will allow more energy to be coupled to the dipoles, thus decreasing the residual current. This can be demonstrated by an LPDA with a 45° alpha and a tau of 0.80. When a relatively low-characteristic impedance feedline (90 ohms) is used, the swept-frequency gain and radiation patterns both show anomalies. The dips in the swept-frequency gain,

shown in Figure 2, represent an increase in the backlobe level of the radiation pattern at those frequencies. The radiation pattern measured at a gain-dip frequency is shown in Figure 3 and is characterized by a very high backlobe. When the characteristic impedance of the feedline is increased to 200 ohms, the anomalies are gone, as shown in Figure 2. However, this technique can be used only for LPDAs operating at relatively low frequencies where a balun/transformer can be placed at the feedpoint without perturbing the antenna performance.

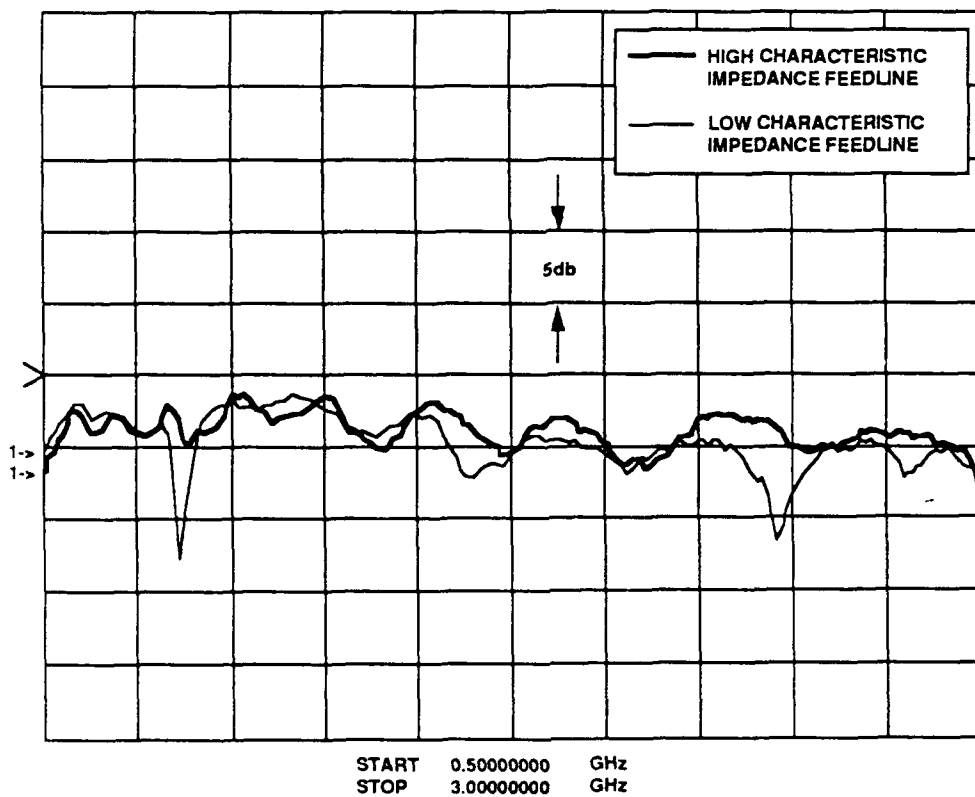


Figure 2. Swept Gain of a Short, Microwave LPDA with Linear Dipoles

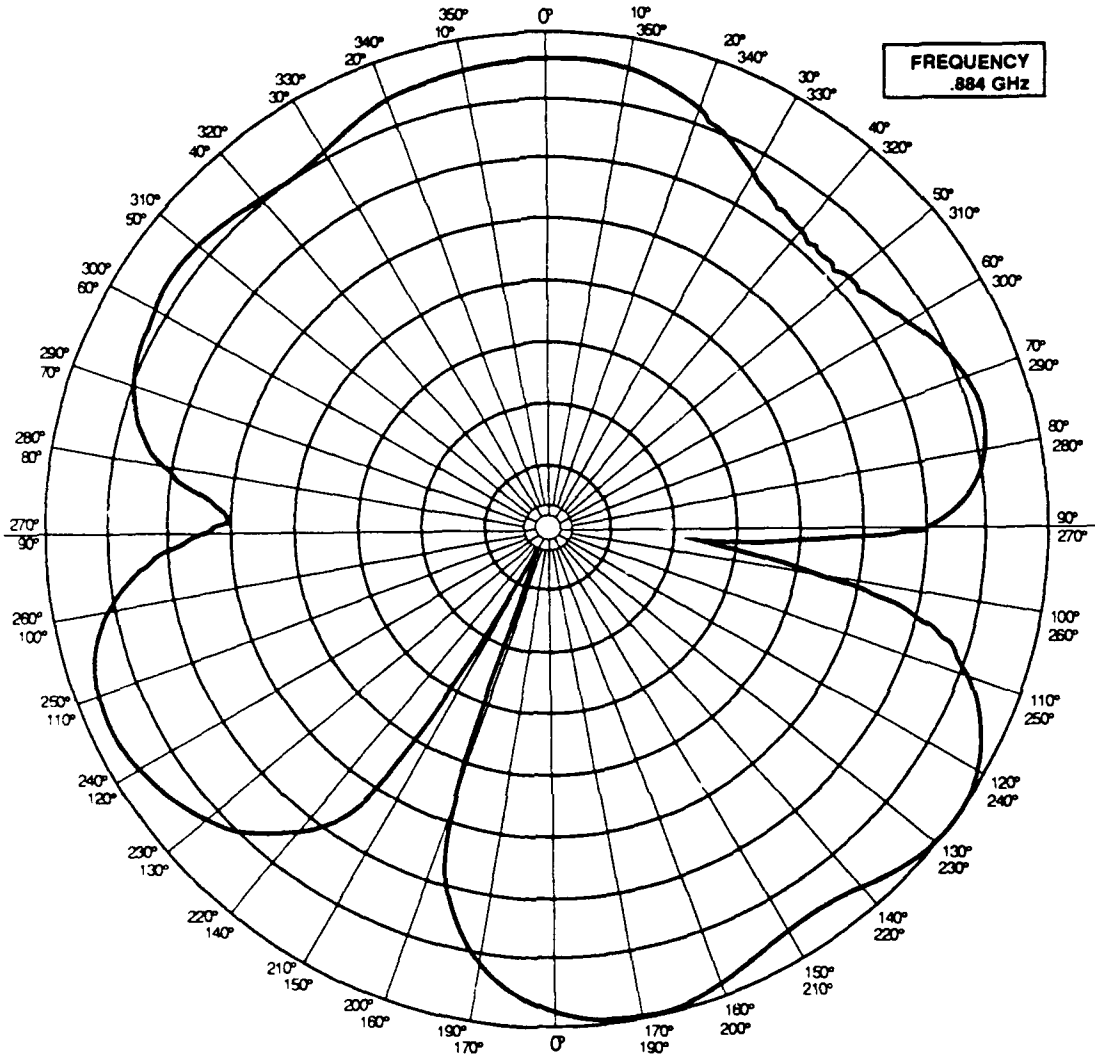


Figure 3. Radiation Pattern at the Gain-Dropout Frequency

New techniques that can eliminate these anomalies in short, microwave frequency, broadband LPDAs, are very desirable. An in-line transformer, formed by tapering the center conductor of the feedline, can provide some limited impedance transformation, but the cost is high, and the fabrication is difficult. Another design method is to replace the linear dipoles with radiators having a lower Q, such as the

triangular dipole. The Q of the dipole decreases as the base of the triangle increases. These lower-Q, triangular radiators will couple more energy from the feedline than will linear dipoles, with an effect identical to that achieved by introducing additional radiators into the active region. LPDAs with triangular dipoles and alphas smaller than 25 degrees have more uniform pattern and VSWR performance than those with linear dipoles. Feedlines with characteristic impedances as low as 75 ohms (which provides a nearly optimum match to the 50 ohm coaxial cable) have been used without any noticeable anomalies. Triangular-tooth LPDAs with alphas of 45° and with variable-impedance feedlines have also been built and tested at GTE, with no anomalies observed.

A disadvantage of the triangular-dipole, however, is that it resonates at frequencies higher than a linear dipole of the same length. For a triangular-dipole having a height-to-base ratio of 5 : 1 (where "height" is defined as one-half of the dipole length), the triangular dipole is approximately 20 percent longer than a linear dipole that resonates at the same frequency. Thus, an LPDA with such triangular-elements must be 20 percent wider and longer than one with linear dipoles operating over the same frequency range. This clearly is not desirable, inasmuch as the prime purpose of using the triangular-elements is to reduce the size of the antenna.

We developed a new configuration to reduce the width of a short LPDA with the goal of making one whose physical size is equal to or smaller than 6 inches by 6 inches and that will cover the frequency range of 0.5 to 18.0 GHz. This proposed antenna has a mixture of triangular, linear, and size-reduced dipole elements and may be viewed as being divided into four regions as shown in Figure 4. Region 1 includes a group of solid triangular dipoles. Region 2 is a

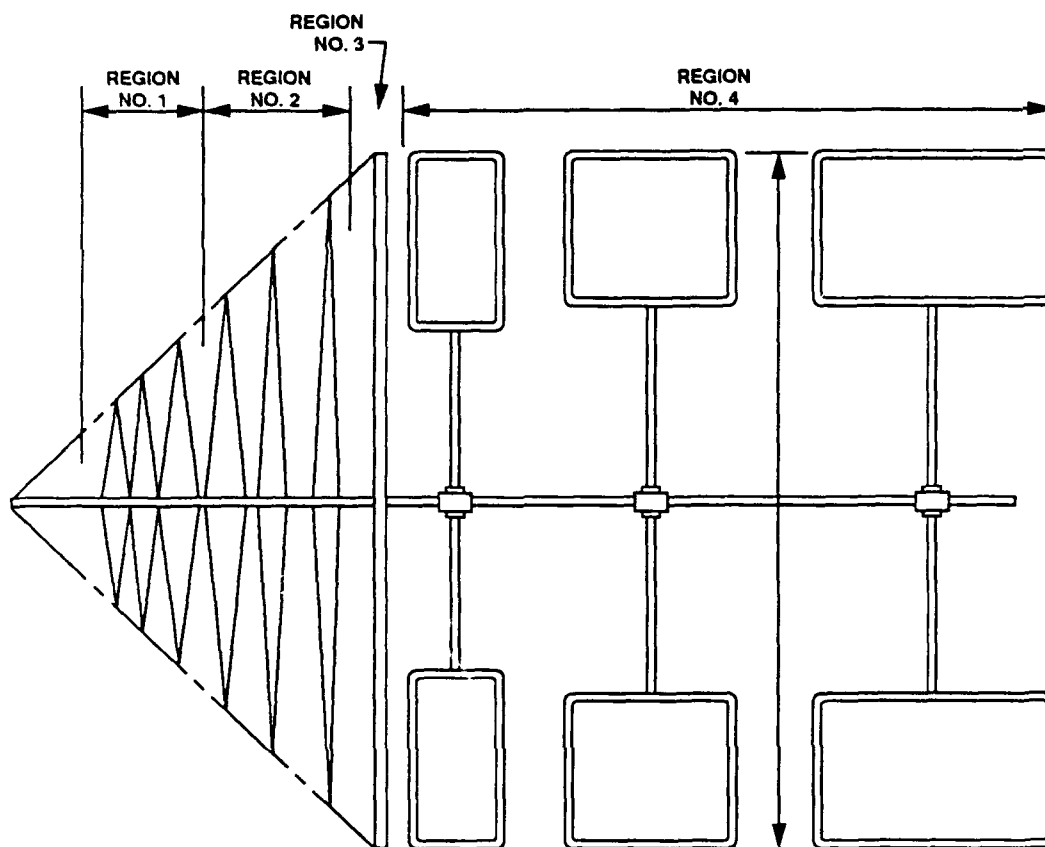


Figure 4. Configuration of the Proposed Antenna

transition region consisting of triangular dipoles that exhibit a gradually decreasing base-to-height ratio as the lengths of the dipoles increase. Thus, the triangular dipoles gradually become linear dipoles. Region 3 contains conventional linear dipoles (possibly just a single linear dipole). Region 4 contains size-reduced dipoles where the width reduction of the LPDA is achieved.

In order to demonstrate this technique, an LPDA with this configuration was fabricated and tested using an alpha with 45° and a tau of 0.80. (See

Figure 5.). Some of the size-reduced dipoles used in this investigation were of the type introduced in "Size-Reduced Log-Periodic Dipole Array Antennas," Microwave Journal, Dec. 1972. This type of size-reduced dipole, can in practice, achieve a maximum size reduction of 40 percent; so only two of these are used in Region 4. Since the last radiator requires reduction up to 50 percent, one of two other types of size-reduced dipoles must be used.

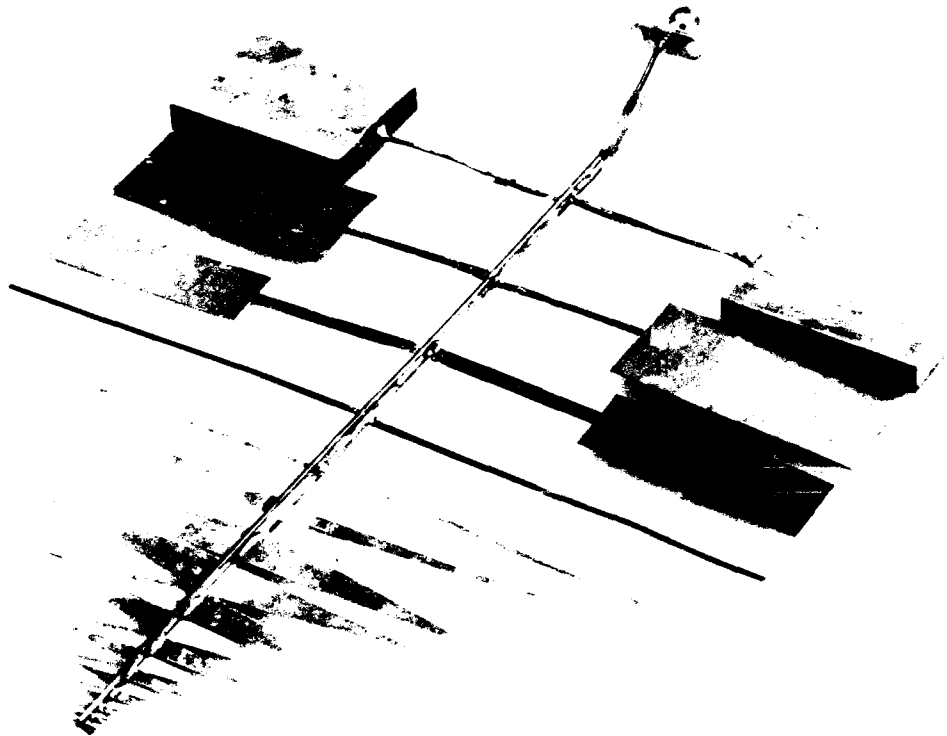


Figure 5. Picture of the Proposed LPDA

The first type is similar to the above-mentioned foreshortened dipole except that the thickness of the rectangular-shaped portion is increased, as shown in

Figure 6. The reduction factor increases as the thickness of the fat part of the dipole increases, while the size of the stem is kept constant. However, the thickness of the loaded section is limited to 0.25 inch for this application in order to keep the LPDA from being too bulky or heavy.

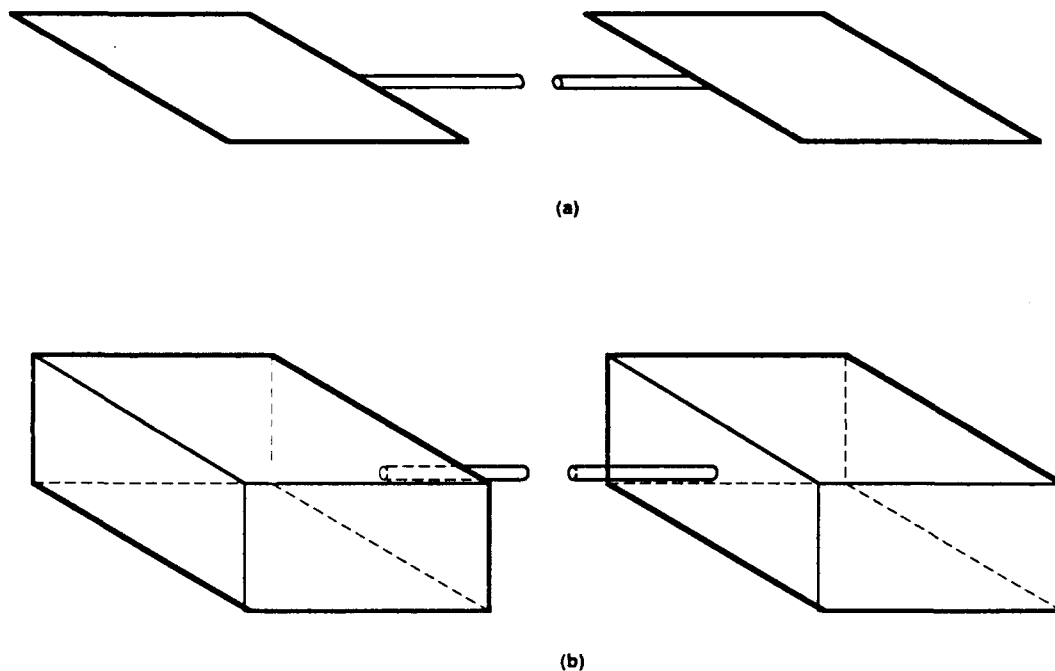


Figure 6. Size-Reduced Dipole

The other type of size-reduced dipole, which can be used as the largest linear dipole and can achieve a size reduction greater than 50 percent, is shown in Figure 7 (US Patent, 4,814,783). This type of dipole can be made to have the same resonant frequency as a linear dipole that is 2.5 times longer. If this second type of size-reduced dipole is used for the last radiator, the thickness of the LPDA

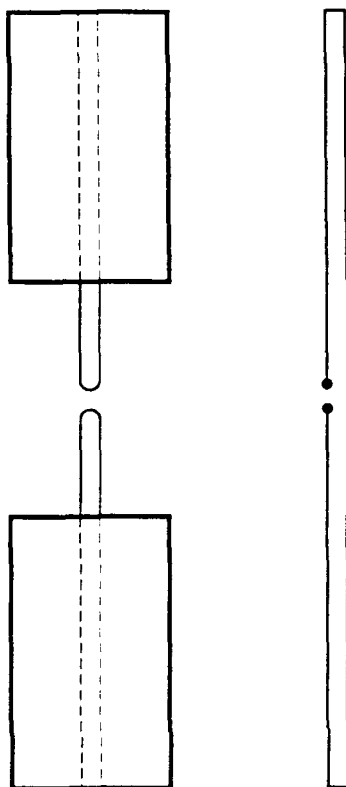


Figure 7. A Size-Reduced Dipole

can be limited to approximately 0.10 inch as compared with 0.25 inch when the structure of Figure 6 is used.

Another novel feature of this antenna is the use of a balanced feedline with variable characteristic impedance. At the feed point, the characteristic impedance is 100 ohm or less. The characteristic impedance of the feedline is increased by increasing the spacing of the balanced two-wire feedline. Thus, the characteristic impedance of the feedline near Region 2 is over 200 ohms and is even higher in

Regions 3 and 4. This configuration of feedline will provide a good match to the 50-ohm coaxial line at the feedpoint and yet have a higher characteristic impedance where the Q of the dipoles is also higher because of their shape change or fore-shortening. The gradual change of the feedline spacing provides a natural impedance transformation and will provide a good VSWR over the entire operating range. This can be seen from the measured VSWR as shown in Figures 8 and 9.

E-plane radiation patterns measured at frequencies in all four active regions are shown in Figure 10. Typical H-plane radiation patterns, measured in Regions 1 and 4, are shown in Figure 11 to demonstrate the change in directivity. The directivity of the radiation patterns decreases as the operating frequency decreases, because of the configuration change of the dipole radiators. The absolute gain of this antenna in Region 1 (above 2 GHz) is about 5 dBi and decreases to approximately 4 dBi in Region 3 and 3 dBi in Region 4 (below 1.0 GHz). At 500 MHz, the absolute gain is approximately 1 dBi. The swept-gain data showed no gain dropout anomalies.

These experimental results demonstrate that a 6" by 6" LPDA can be designed to operate over the 0.5-to-18 GHz frequency range with good electrical performance without anomalies. The reduction in gain and directivity at the lower operating frequencies is caused by the size reduction of the dipoles and should be accepted as the price paid for the reduced size.

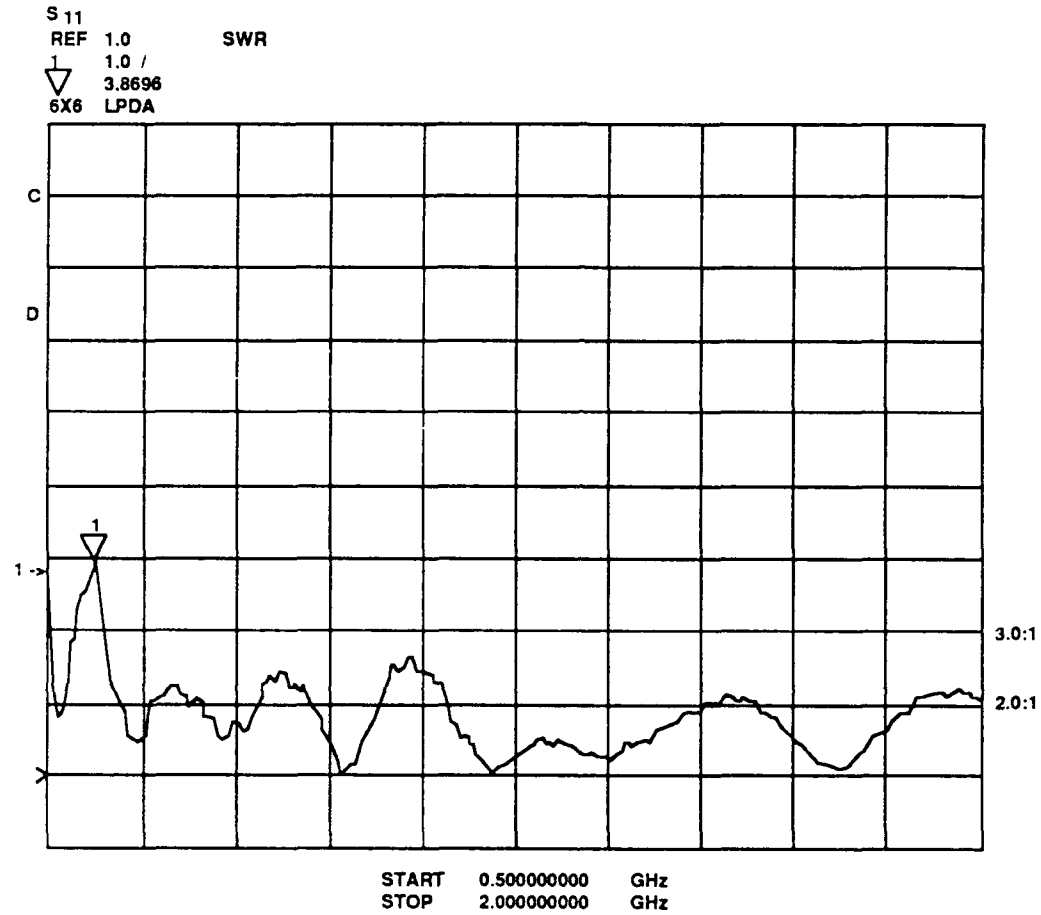


Figure 8. Measured VSWR

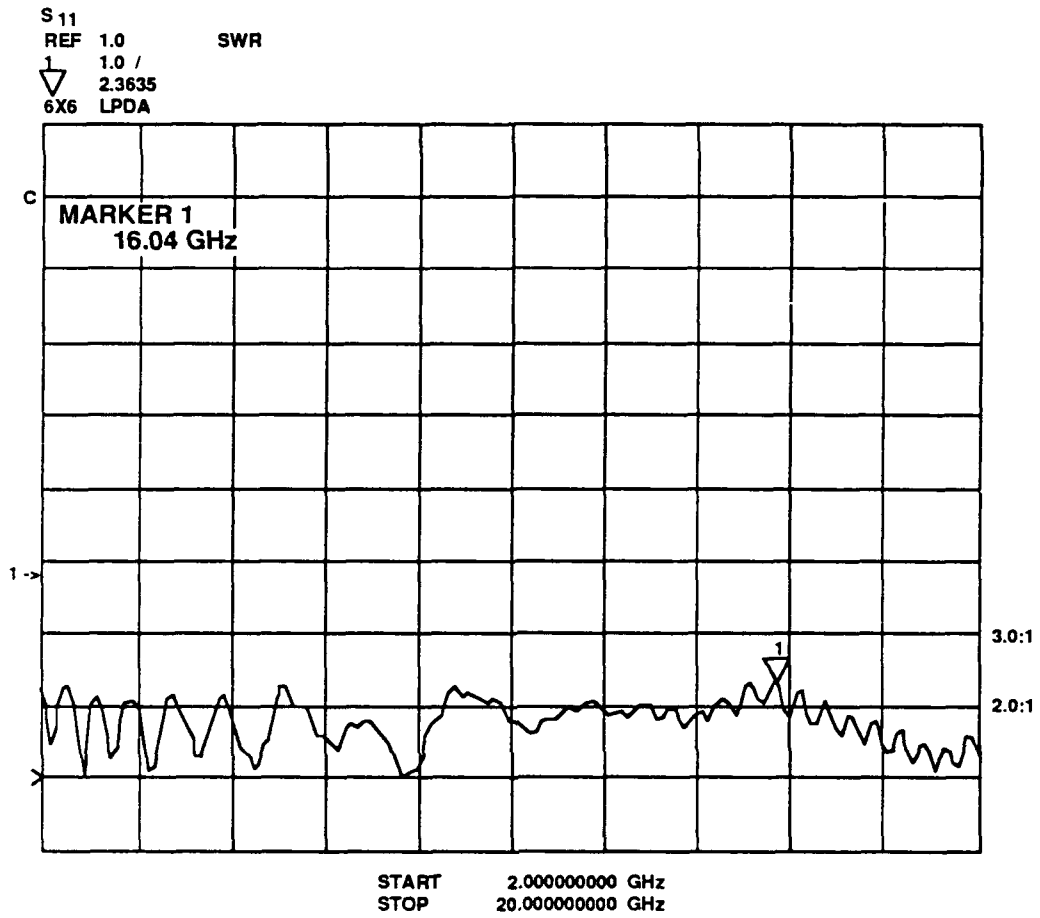


Figure 9. Measured VSWR

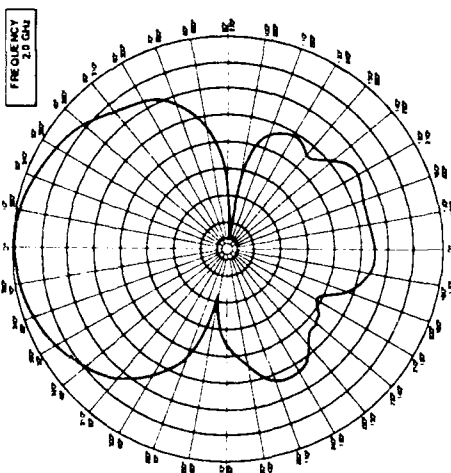
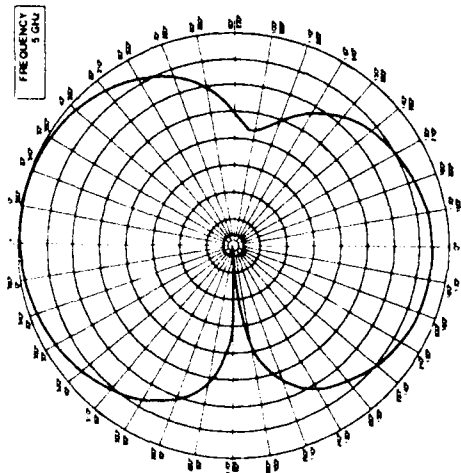
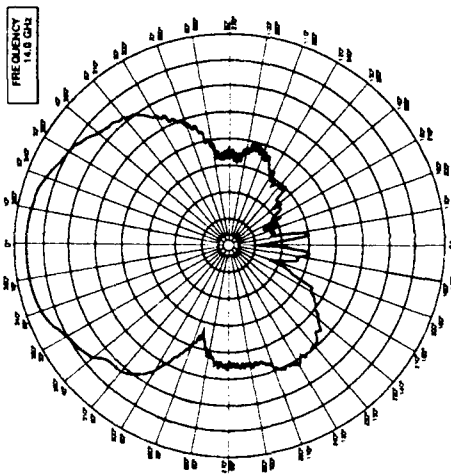
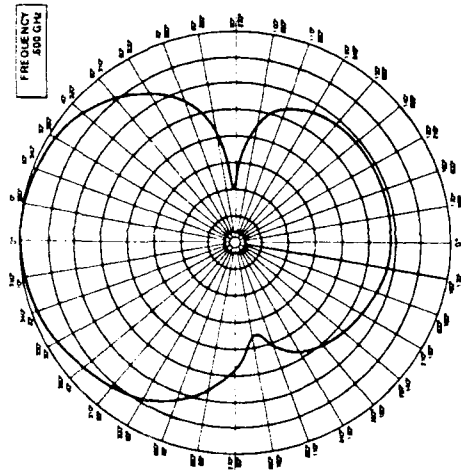
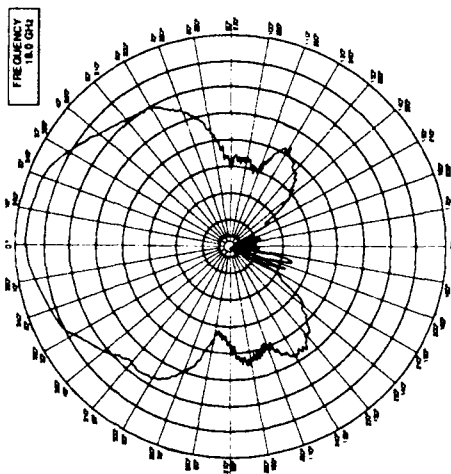
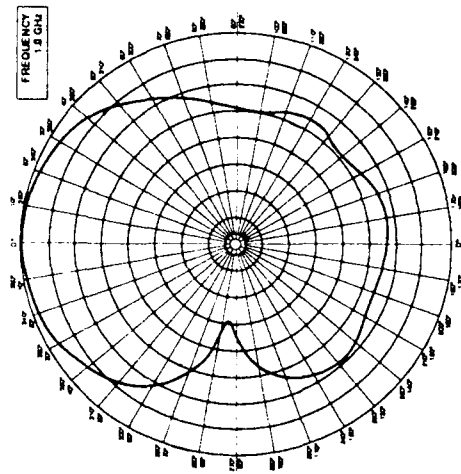


Figure 10. Measured Z-plane Patterns

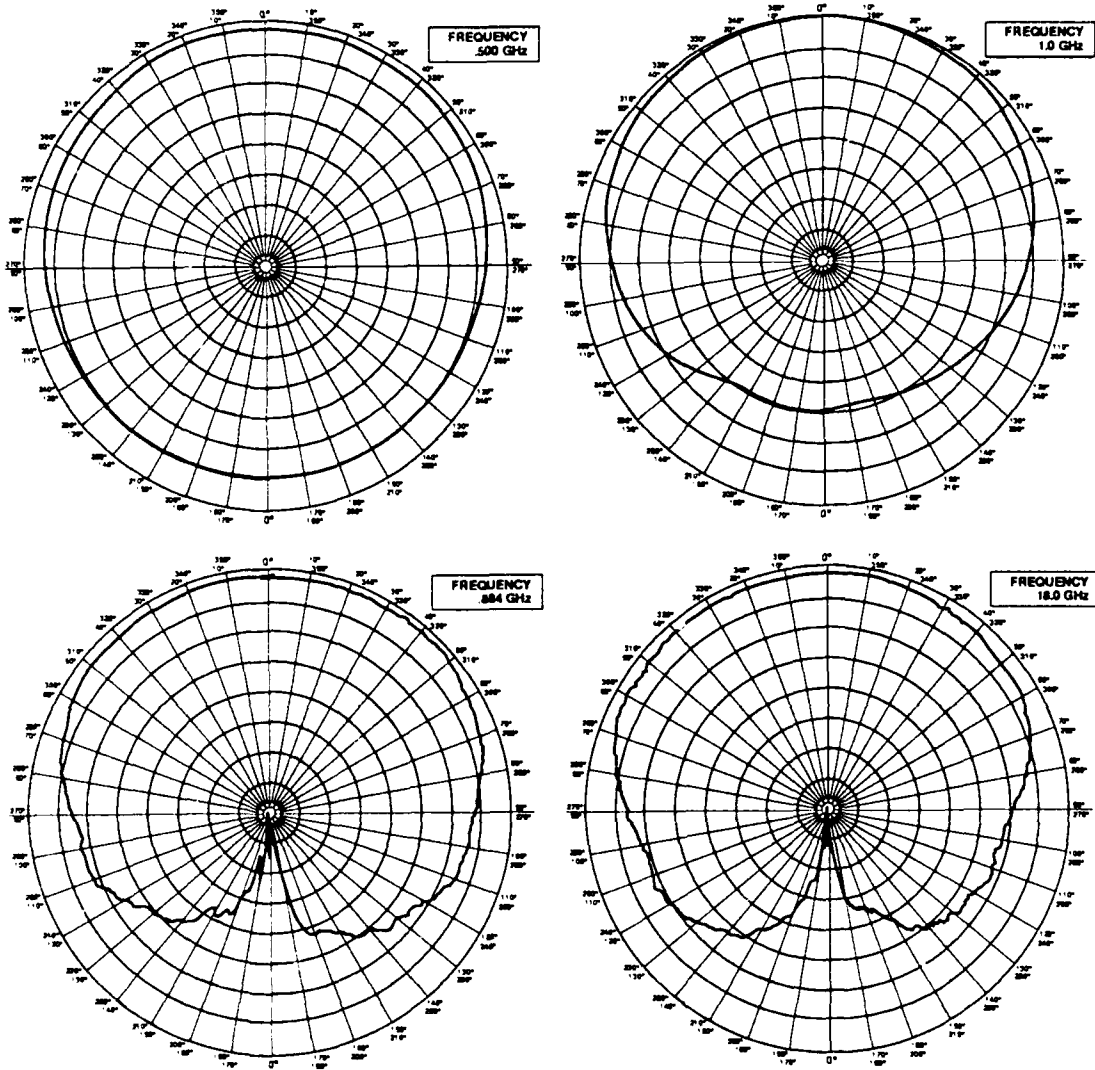
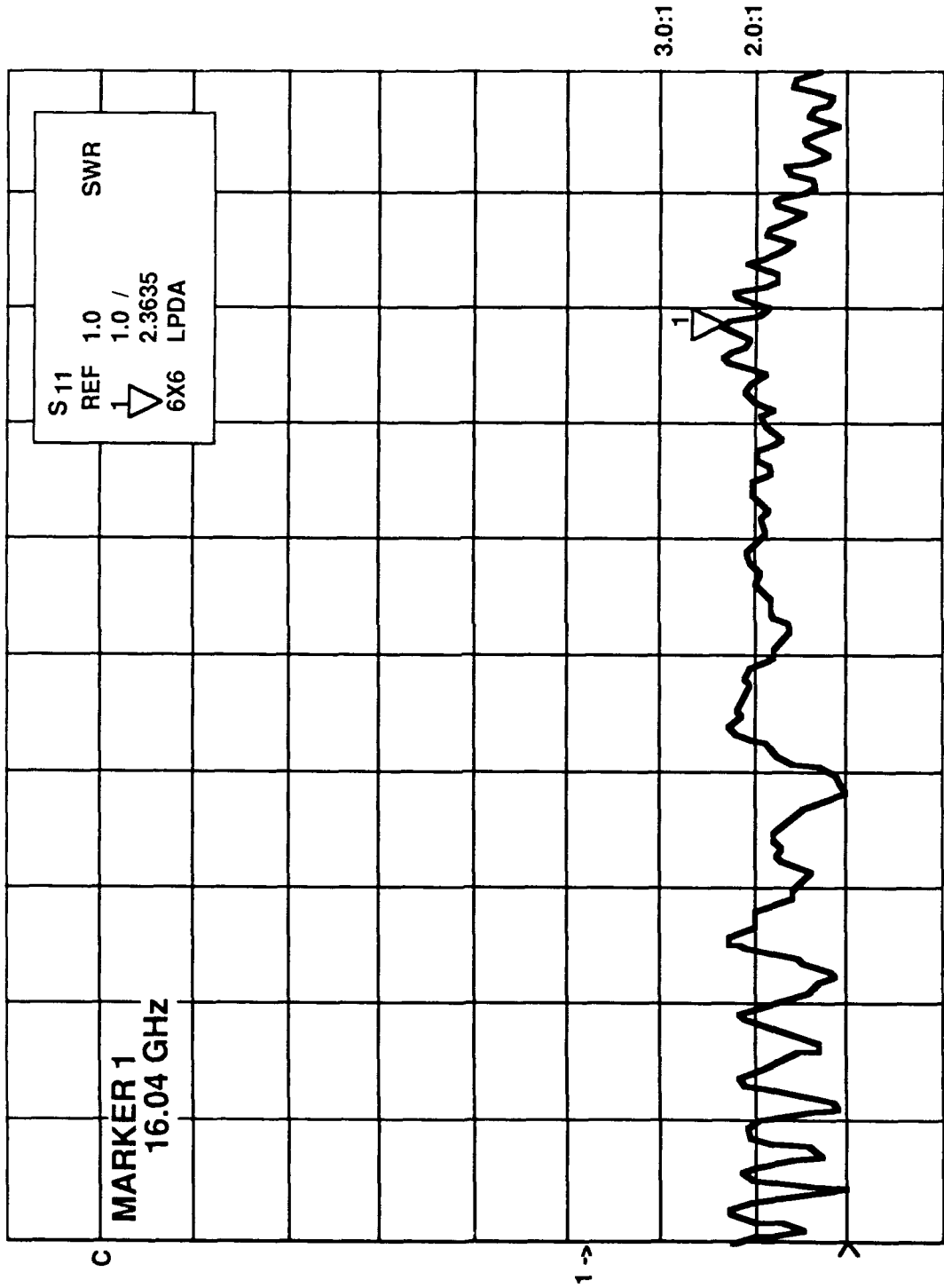


Figure 11. Measured H-plane Patterns

REFERENCES

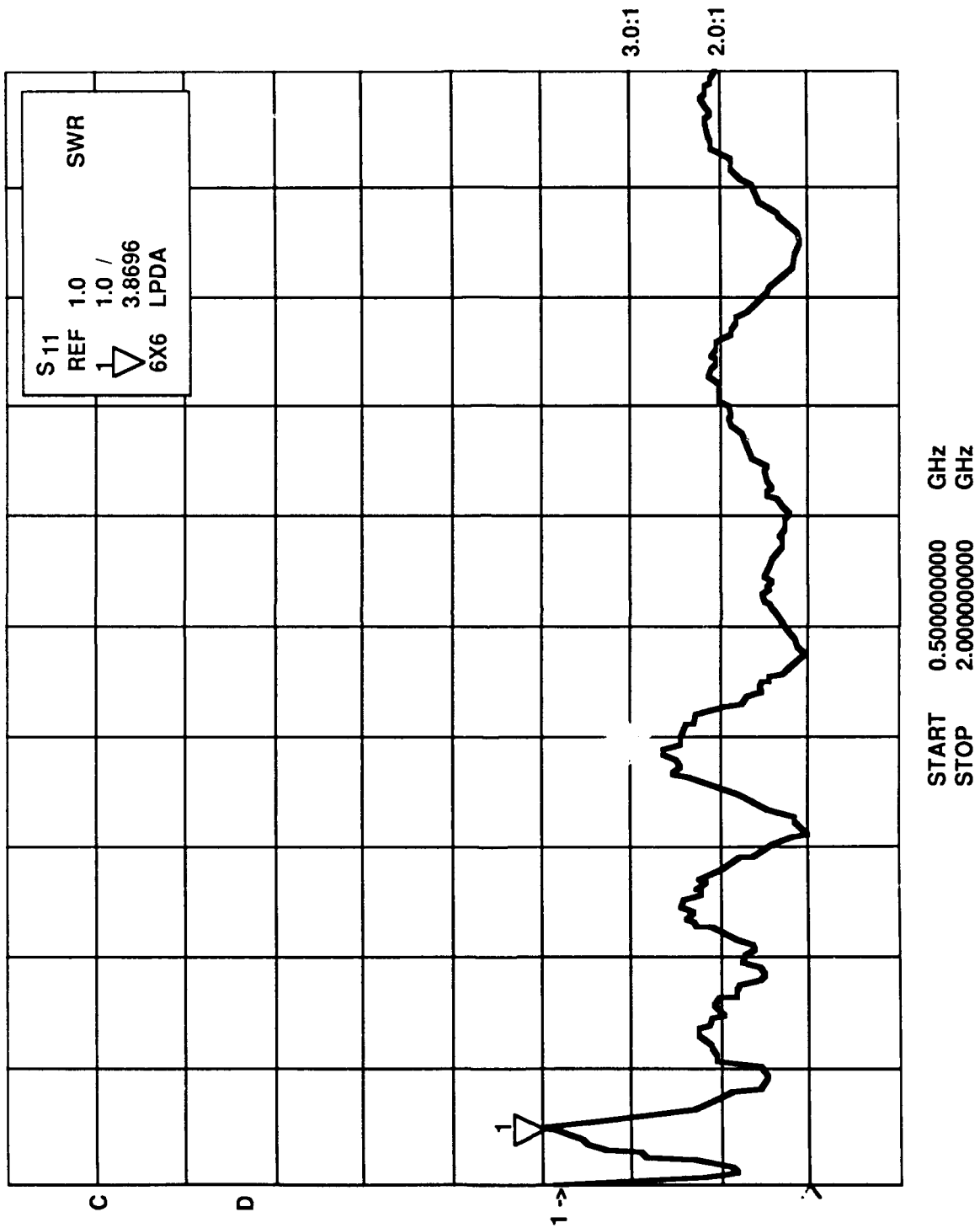
1. J. C. Pullara, J. C. "Reduced Size Broadband Antenna,"
U.S. Patent 3,543,277.
2. Bantin, C. C. and Balmain, K. G. "Study of compressed log-
periodic dipole antennas," IEEE Trans. Antenna Propagat. Vol. AP-18,
pp 195-203, March 1970.

MEASURED VSWR

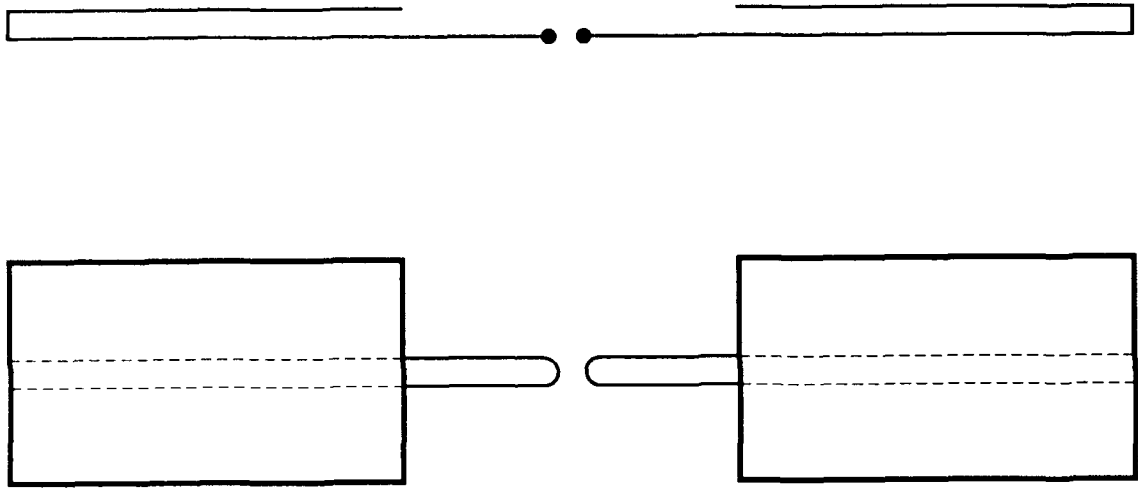


START 2.000000000 GHz
STOP 20.000000000 GHz

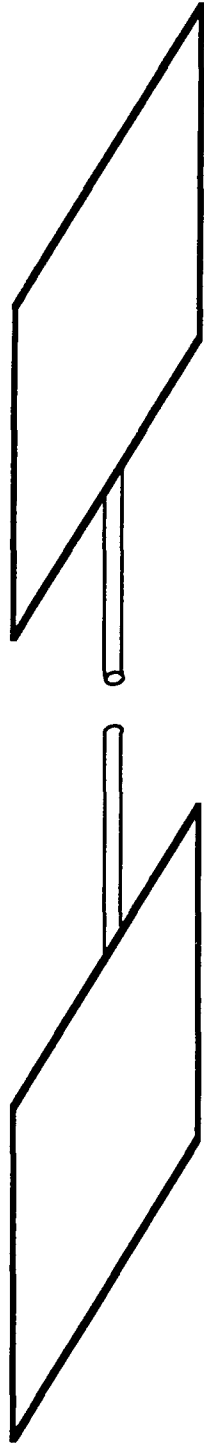
MEASURED VSWR



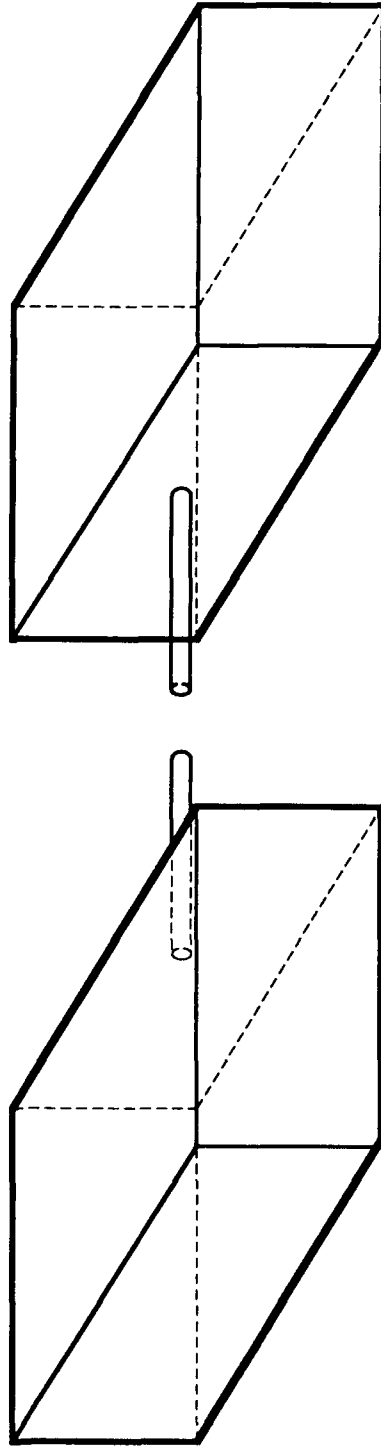
A SIZE-REDUCED DIPOLE



SIZE-REDUCED DIPOLE

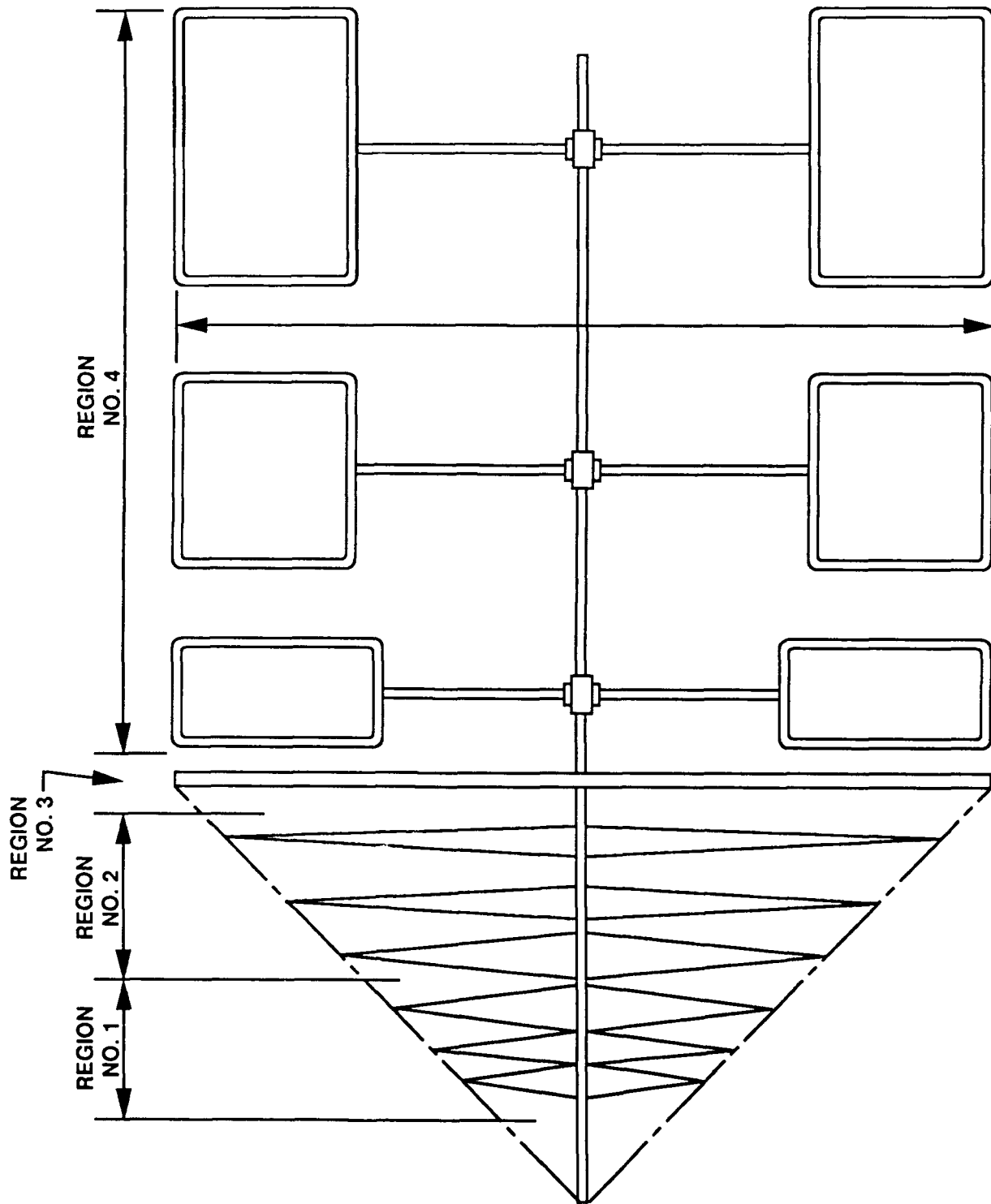


(a)

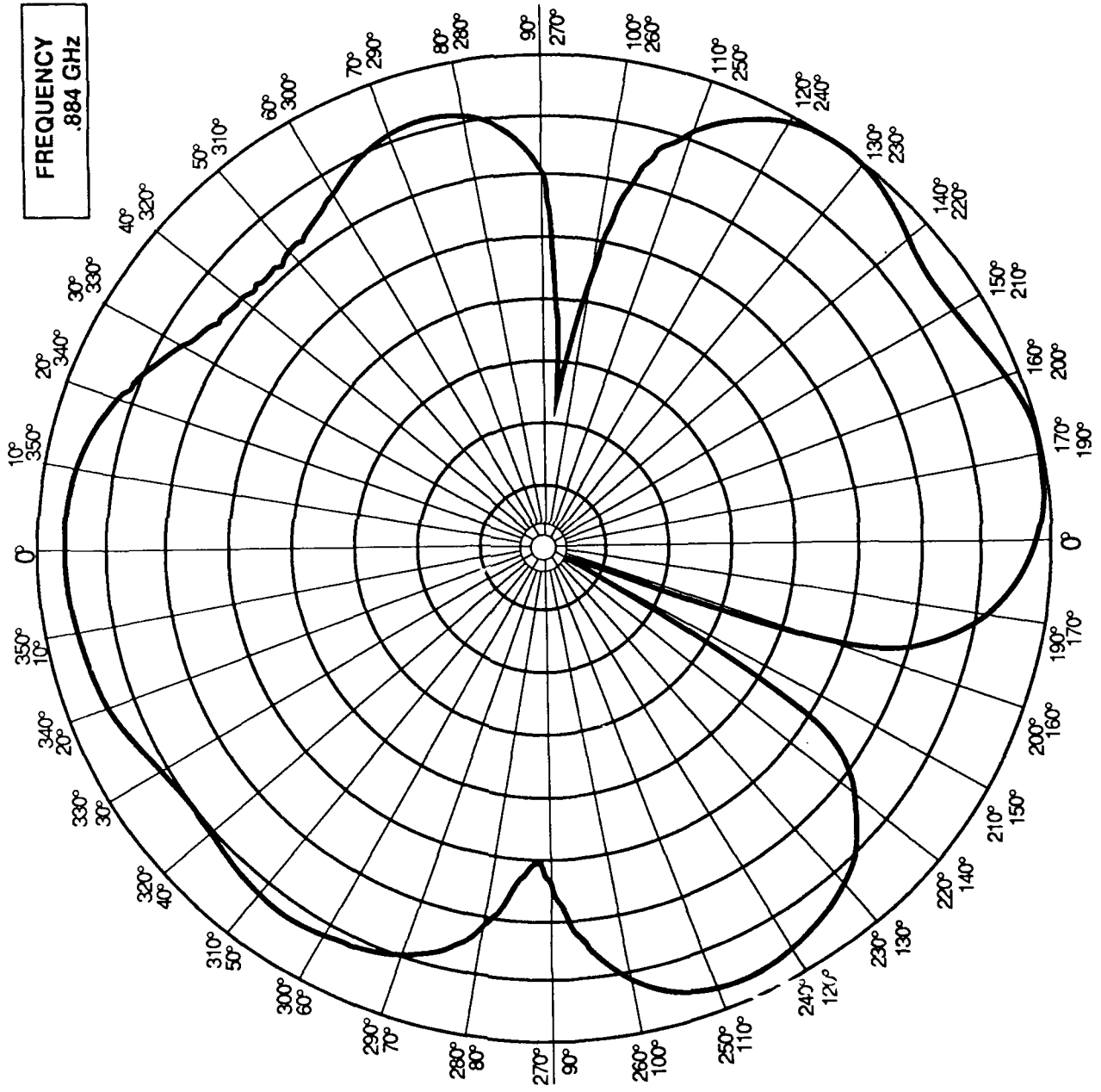


(b)

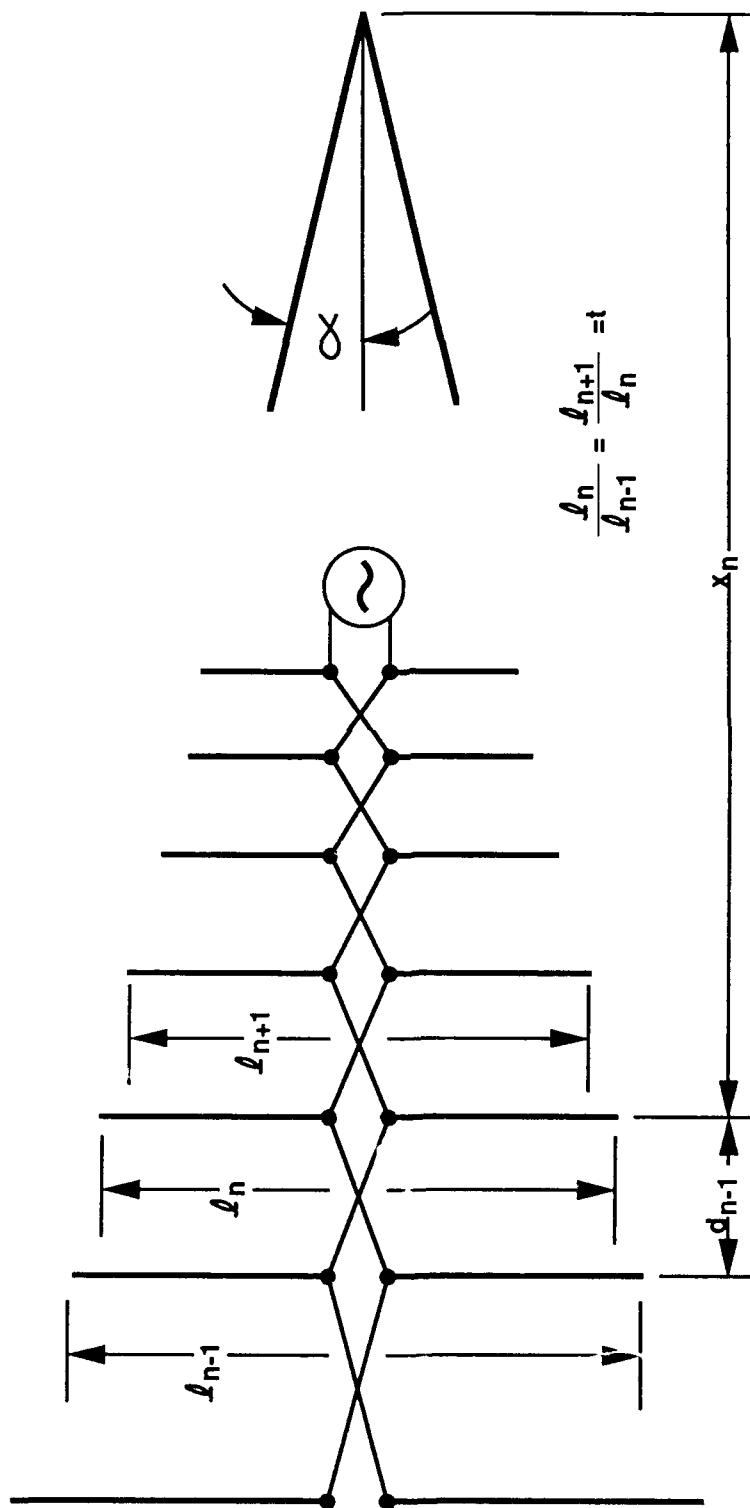
CONFIGURATION OF THE PROPOSED ANTENNA



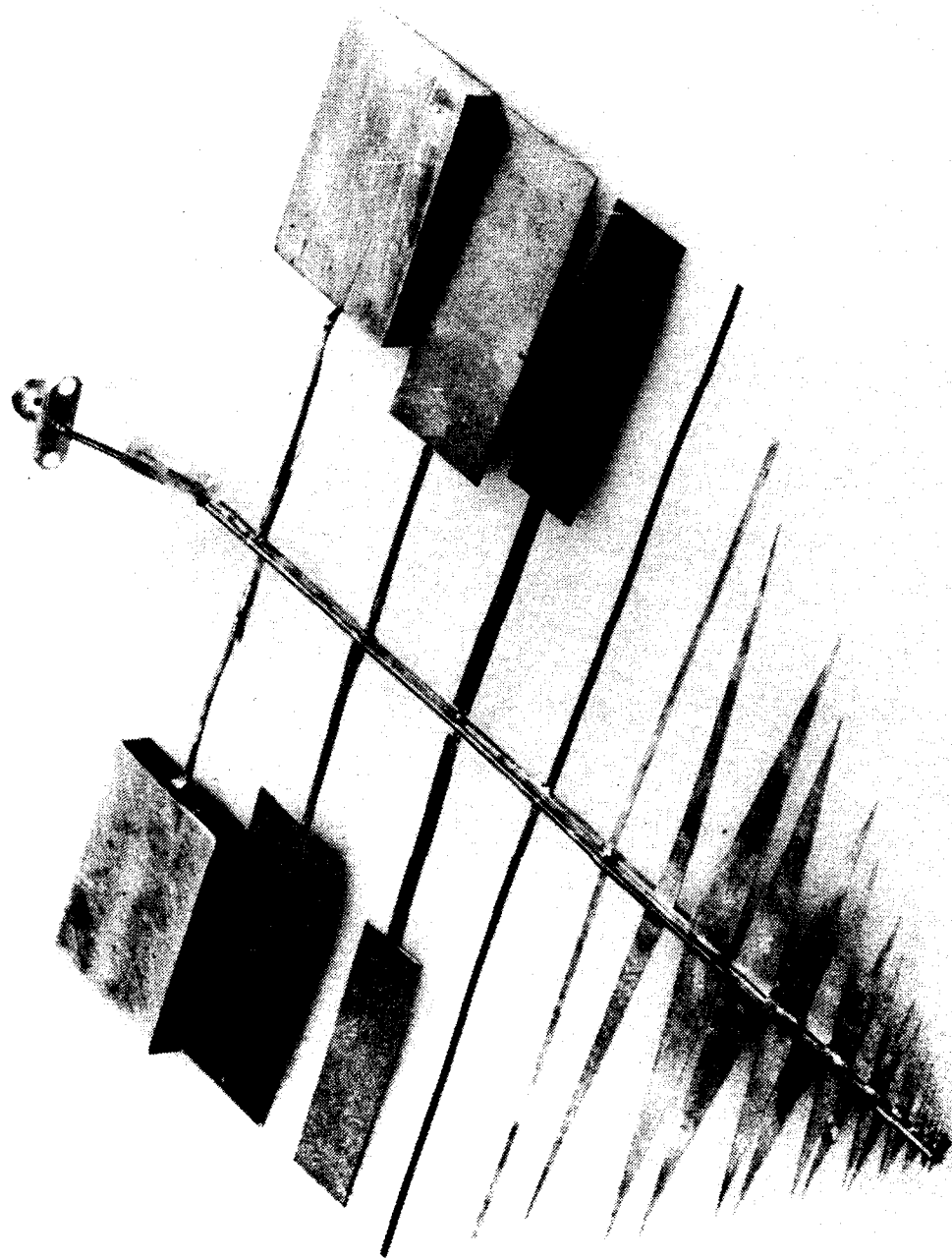
RADIATION PATTERN AT THE GAIN-DROPOUT FREQUENCY



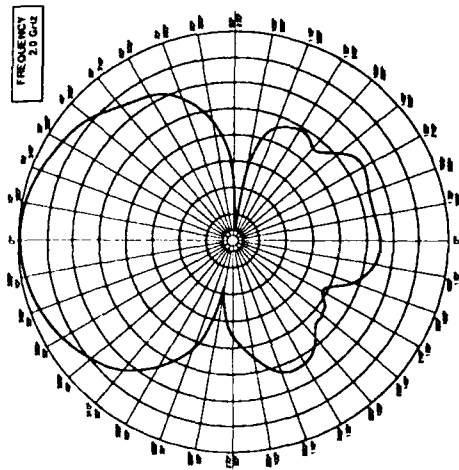
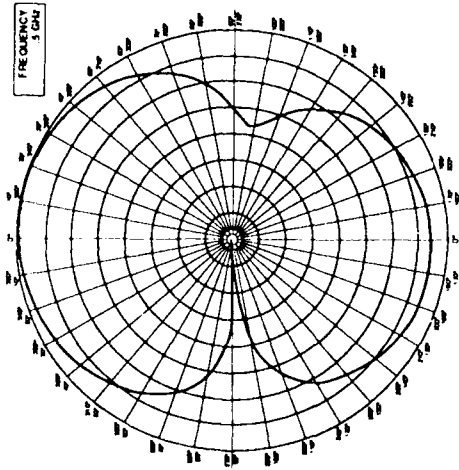
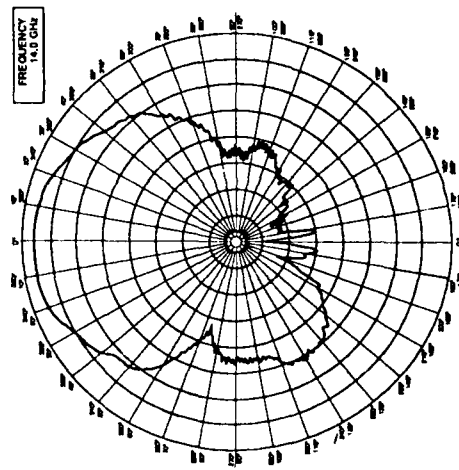
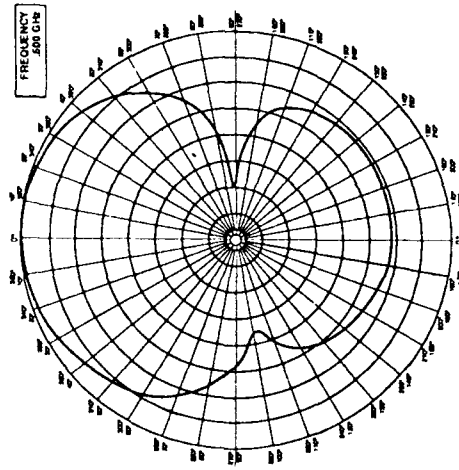
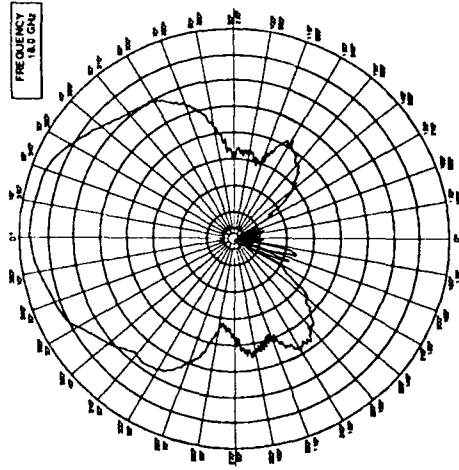
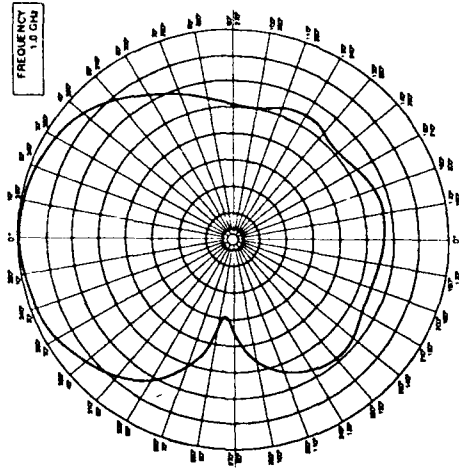
DESIGN PARAMETERS OF THE LOG-PERIODIC DIPOLE ANTENNA



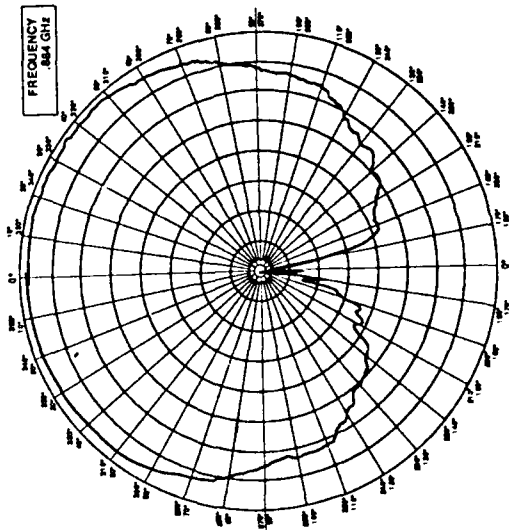
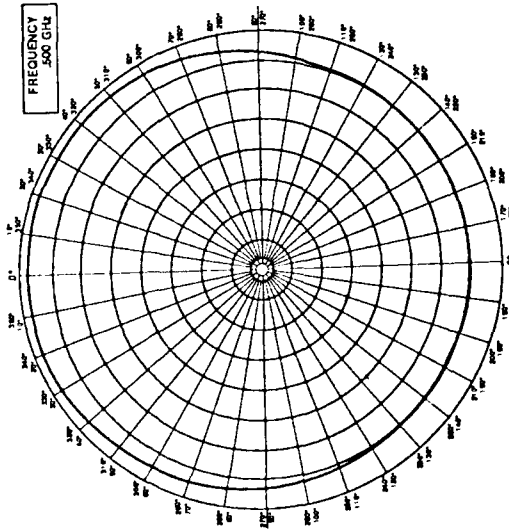
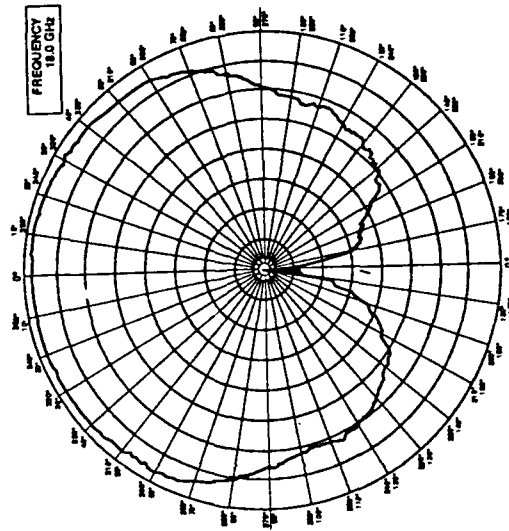
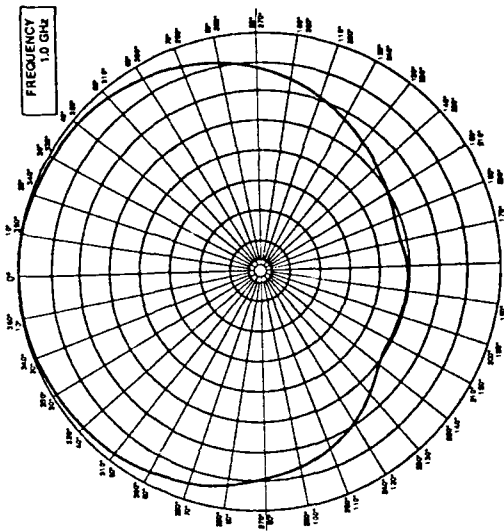
PICTURE OF THE PROPOSED LPDA



MEASURED Z-PLANE PATTERNS



MEASURED H-PLANE PATTERNS



**REDUCED PROFILE LOG PERIODIC DIPOLE ANTENNA
DESIGNED FOR COMPACT STORAGE AND SELF DEPLOYMENT**

G. D. Fenner, J. Rivera and P. G. Ingerson

TRW, INC.

Redondo Beach, California

ABSTRACT

A wideband, log periodic dipole antenna is designed for easy transportation and deployment requiring a significantly reduced unobstructed space for operation. The longest dipole elements are reduced in length and flattened and tapered in shape to allow bending for self-deployment. To maintain antenna performance in the frequency band of the foreshortened elements, several options were considered, including helices, "dumbbell" shaped elements, and inductive loads near the center of the dipole element lengths. Inductive loads at the base of the elements are selected to allow the elements to fold for temporary storage and to deploy easily. Results show that accounting for mutual coupling between elements has a negligible effect on the inductance values selected for optimum performance. The shaping of the dipole elements alters their characteristic impedance and requires compensation in the feeder impedance.

1.0 Background

A log periodic dipole array (LPDA) is a medium-gain, wide bandwidth, linearly polarized antenna with relatively frequency-independent performance over its operating band. A standard LPDA is defined by its scale factor, τ , and its apex angle, α (Figure 1). The lengths of adjacent dipole elements are related by the scale factor τ , and their spacing is then determined by α .

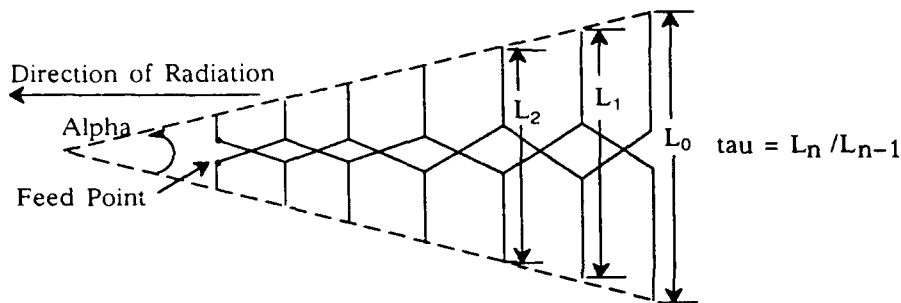


Figure 1. Standard LPDA Design

The LPDA is in a class of antennas known as “backfire”. It is fed at the front end (toward the apex), and a transmission line supports a slow wave moving from the front to the rear of the antenna. The energy is radiated back toward the apex when it reaches a section of the LPDA where the dipoles are nearly one-half wavelength long. The group of dipoles radiating energy at a given frequency is known as the “active region” and contains about three elements, depending on the design parameters. In a correctly designed LPDA, almost all of the energy is coupled from the feed line by the active region, which allows the antenna structure to be arbitrarily truncated at any point past the active region without reflected energy interfering with the radiation patterns or input impedance. The shorter elements preceding the active region act as shunt capacitive loads on the transmission

line, and are a primary factor in determining the input impedance of the antenna. Through the use of crossed dipoles, the antenna can be operated in circular polarization. The antenna's overall width is determined mainly by its low-frequency cutoff since the longest dipoles must be approximately one-half wavelength at cutoff.

The size of the LPDA can be significantly reduced by foreshortening and electrically loading the longer sets of dipoles, allowing the antenna to be deployed and operated in a smaller space. For operation in the Megahertz and lower frequency bands, this may offer a significant improvement in ease of handling and setup. The antenna can also be stored in a very compact configuration for transportation by folding the elements. The design of such an LPDA is discussed in this paper.

2.0 Foreshortened Elements

In an LPDA, the low-frequency cutoff is determined by the length of the longest dipole. To reduce the size of the antenna while maintaining the operational bandwidth of a full-size antenna, the elements are shortened and modified so that their electrical lengths remain unchanged.

Quite a few methods are available for shortening a dipole while maintaining its electrical length, including:^{1, 2}

- capacitive loading
- series inductive loading
- helices

each of which has advantages and disadvantages for this application.

Capacitive Loading

This type of loading can be accomplished in several forms, as shown in Figure 2.

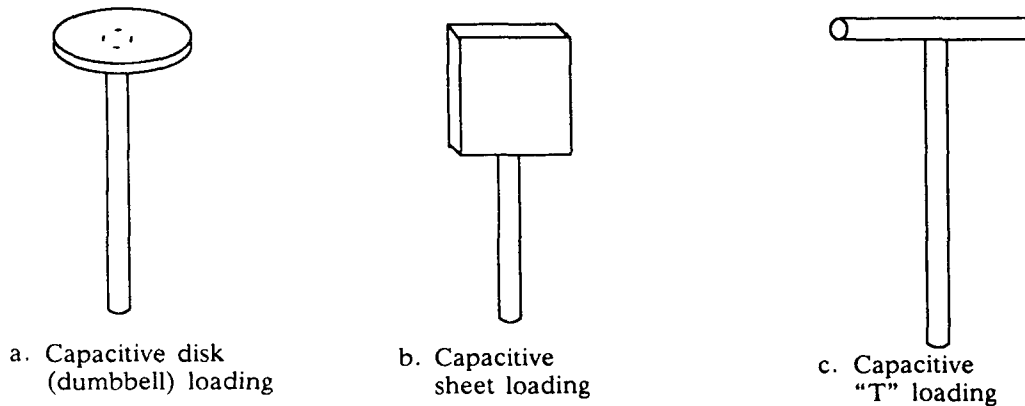


Figure 2. Capacitive Loading of Dipole Elements

Compared to series inductive loading and helices, capacitive loading results in the lowest values of element Q for a given amount of foreshortening. Low Q is desirable because high- Q elements reduce the number and bandwidth of elements in the active region of the LPDA and lead to variations in RF performance.

Series Inductive Loading

This type of loading can also be accomplished in several ways; either with a lumped element inductor or with a length of coaxial line in series with the element. Figure 3 illustrates these methods.

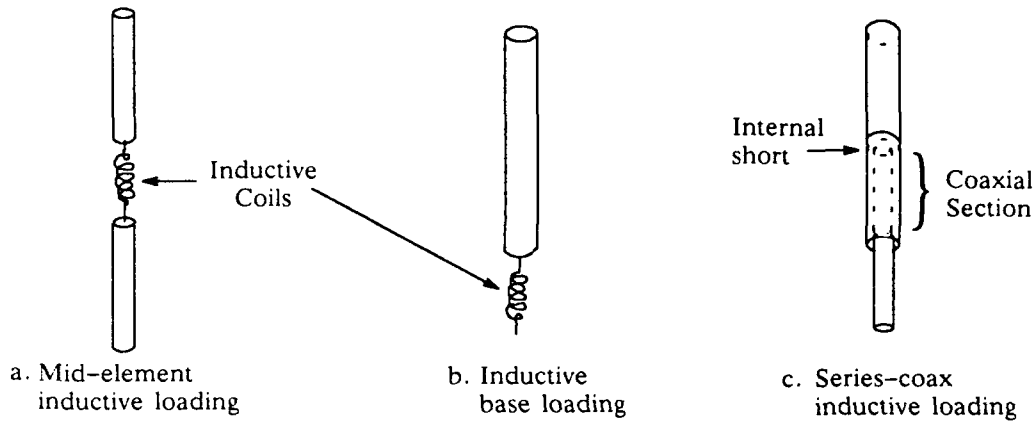


Figure 3. Series Inductive Loading

Helices

Helix wire dipoles are a version of inductive loading in which helical dipoles, rather than straight rods, are used as the elements. In this case the inductive loading is distributed along the length of the element rather than lumped as in inductive base-loading.

Of the loading methods considered, inductive base-loading is chosen for the reduced profile LPDA primarily for mechanical reasons. The dipole elements are made of thin strips of heat-treated beryllium-copper (BeCu) so that their mechanical properties are similar to that of a metal tape measure. To minimize design variations throughout the LPDA, BeCu was used for all of the antenna elements. By using heat-treated BeCu, the elements can be easily folded for storage. Series-coax inductive loading would be difficult to implement with such elements. Capacitive loading would put too much weight at the ends of the elements, causing them to collapse. In addition, most of the capacitive loading methods would likely cause damage or tangling of the elements during deployment. Mid-element inductive loading offers some improvement in radiation efficiency over base-loading,³ but at

the expense of mechanical complexity and added weight toward the ends of the elements. Helical dipole elements, though effective in reducing the required element length, would be extremely difficult to build so that they would fold for storage, and they would certainly tangle upon deployment.

3.0 Electrical Design

An LPDA design is driven by the performance required throughout the band. Based on the minimum operational space available in this application, it is necessary to shorten the four longest sets of dipole elements to the same length as the fifth set of elements (this is a maximum foreshortening of 31%). Space restrictions also drive the overall length of the antenna, even though it has been shown that extra sets of elements and an increasing tau through the truncated region improves performance.⁴

To analyze and implement the truncated design, the following steps were taken:

1. The design of a full-width LPDA is established. This sets the tau and alpha of the basic design.
2. The resonant frequency of the full length elements which are to be shortened is determined.
3. The elements are shortened to the desired length and the base impedance of each element is adjusted until they resonate at the same frequency as the corresponding full length element.

This method provides the amount of inductance necessary to resonate each shortened element at the same frequency as its full length counterpart.

This procedure was adopted after it was determined that the inductive loading at the base of each element has an insignificant effect on mutual

coupling between elements, and hence on performance. The coil is attached in series at the base of each shortened element. This assembly can be easily mounted on a ground plane to verify that it resonates at the desired frequency. It is then incorporated into the LPDA structure and is ready for evaluation as part of the array.

4.0 Mechanical Design

The antenna is illustrated in Figure 4 and consists of the following main components:

Stem. The stem is the central support structure for the entire LPDA. It is an aluminum tube designed for stiffness and light weight. Its diameter is chosen so that the separation between element pairs is a small fraction of the wavelength.

Feed Line. The dipole elements are fed by BeCu strips mounted along the outside of the stem. They function as strip transmission lines and use the stem as the return path. The height of the strip above the tube and the element configuration determine the antenna's input impedance.

Dipole elements. The antenna employs four sets of elements for circular polarization. The BeCu dipole elements are attached to opposite feed strips. Elements longer than six inches have a concave cross-section for stiffness and are heat-treated to allow them to spring straight after being bent for storage. The element width is gradually tapered, which moves the center-of-gravity of the elements away from the tips and reduces sagging. The longer elements are reinforced at their feed points with support collars attached to the stem. The heat-treated elements can be easily folded along the stem and the entire array enclosed in a cylinder for compact storage and

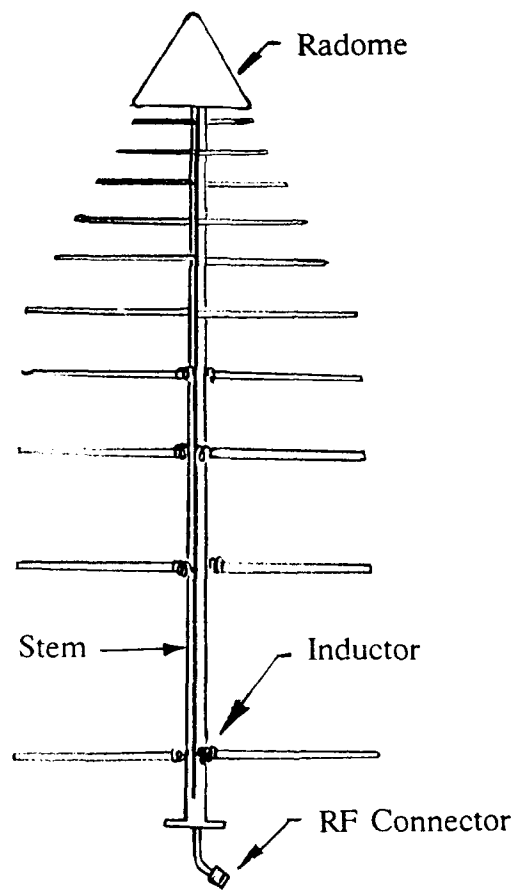


Figure 4. Reduced Profile Log-Periodic Dipole Antenna

easy transportation. The cylinder can be rigid or made of a suitable flexible material in which the elements are folded.

Radome. The fragile high-frequency elements are protected by a foam radome which does not affect performance.

Coax cables. Coaxial cables are located in the interior of the stem. They excite the four feed strips at the tip of the array, and provide a suitable RF connector at the back of the antenna. This method of exciting the antenna requires the use of a beamforming network to achieve circular polarization.

Inductors. The inductors consist of magnet wire wrapped around a threaded dielectric core and soldered in series between the feeder strip and the base of the elements. The core is threaded to assure repeatability of inductance values by maintaining uniform spacing between wire turns. The design is illustrated in Figure 5.

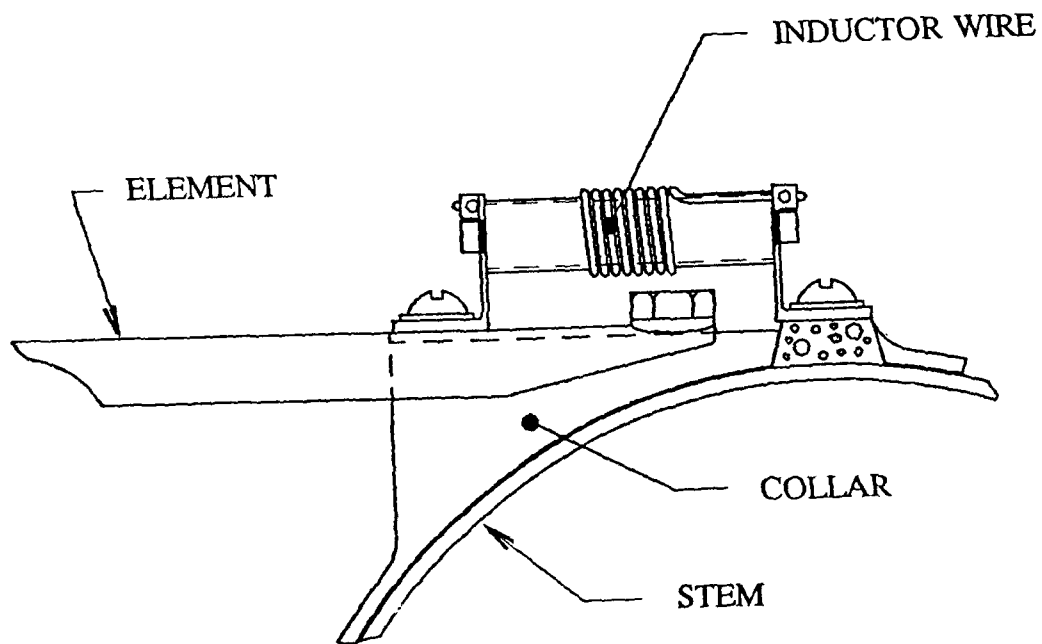
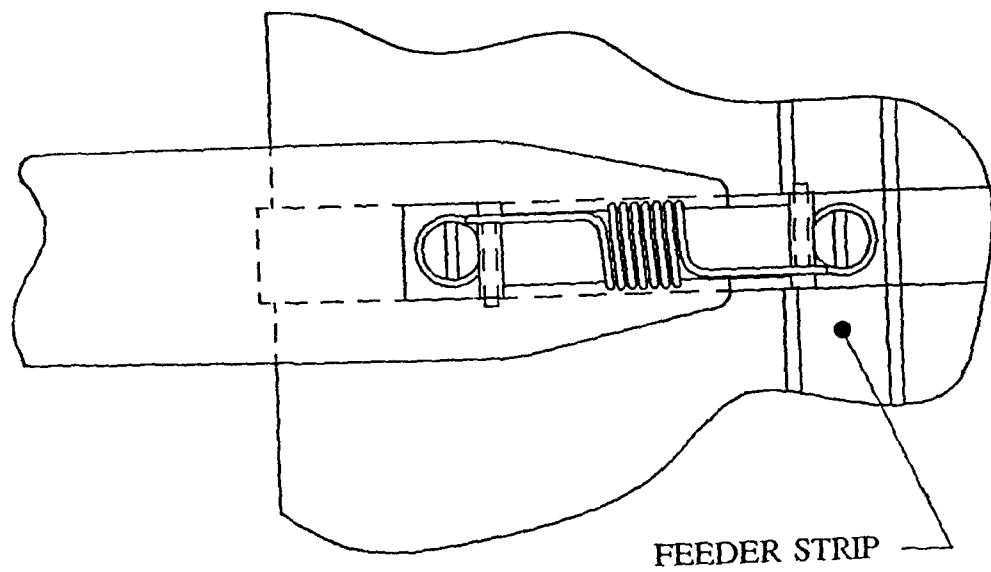


Figure 5. Inductor Coil

5.0 Characteristic Impedance of Shaped Elements

As stated in the previous section, the dipole elements are tapered in width and are semi-flat, rather than being uniform round rods as in most LPDAs. Both the flattening and the tapering have an influence on the characteristic impedance of the dipole elements. This is significant because the feed line impedance required to achieve a desired antenna input impedance is a function of the element characteristic impedance.⁵ The average characteristic impedance, Z_a of a dipole element is

$$Z_a = 120[\ln(h/a) - 2.25] \quad (1)$$

where h/a is the length-to-radius ratio for a circularly cylindrical dipole element. For elements that are not circularly cylindrical (see Figure 6), an "equivalent h/a " is required, $(h/a)_{eq}$. Elliott⁶ examines this for an elliptically shaped dipole, which leads to the following expression for equivalent h/a :

$$(h/a)_{eq} = h/[(b+c)/2] \quad (2)$$

The elliptically shaped dipole is actually a general case which includes the special cases of circular (where $c=b$) and flat rectangular (where $c \ll b$). For the latter case, the equation reduces to

$$(h/a)_{eq} = 2h/b. \quad (3)$$

Since $w_r = 2b$, the above can be expressed as

$$(h/a)_{eq} = 4h/w_r \quad (\text{flat rectangular element}). \quad (4)$$

Testing of circular, flat rectangular and flat tapered monopole elements on a ground plane verifies the above relation experimentally, and also provides an empirical relation for flat tapered elements,

$$(h/a)_{eq} = 8h/w_t \quad (\text{flat 4:1 tapered elements}). \quad (5)$$

The strip transmission line is designed using the above relation to achieve the desired antenna input impedance.

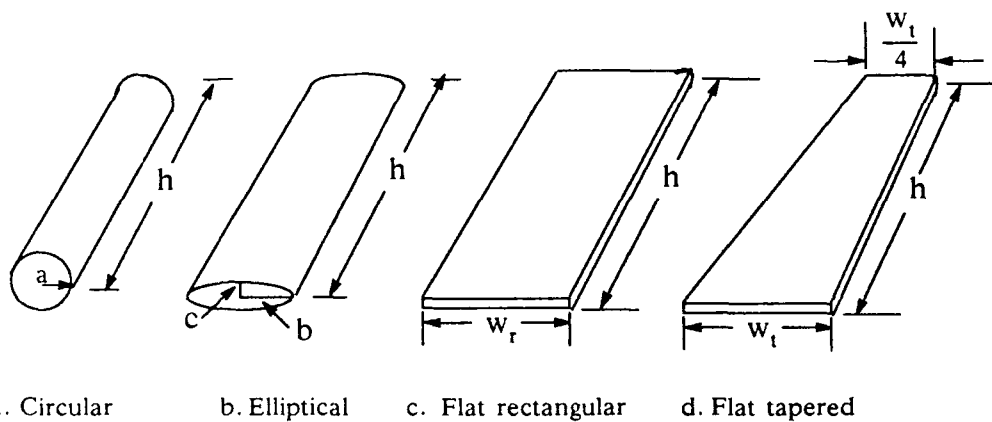


Figure 6. Dipole Element Types

6.0 Measurements and Results

The antenna's radiation patterns (contours) and input impedance (VSWR) were measured. Figures 7 and 8 show sample contours. The first contour is for the LPDA with full-length elements, the second is at the same frequency for the LPDA with truncated and base-loaded elements. Figure 9 illustrates the measured VSWR in the truncated region of the LPDA compared to the predicted VSWR, showing good agreement.

7.0 Conclusions

Profile reduction of a large LPD antenna has shown itself to be feasible and practical. Designing the elements for compact storage is an attractive

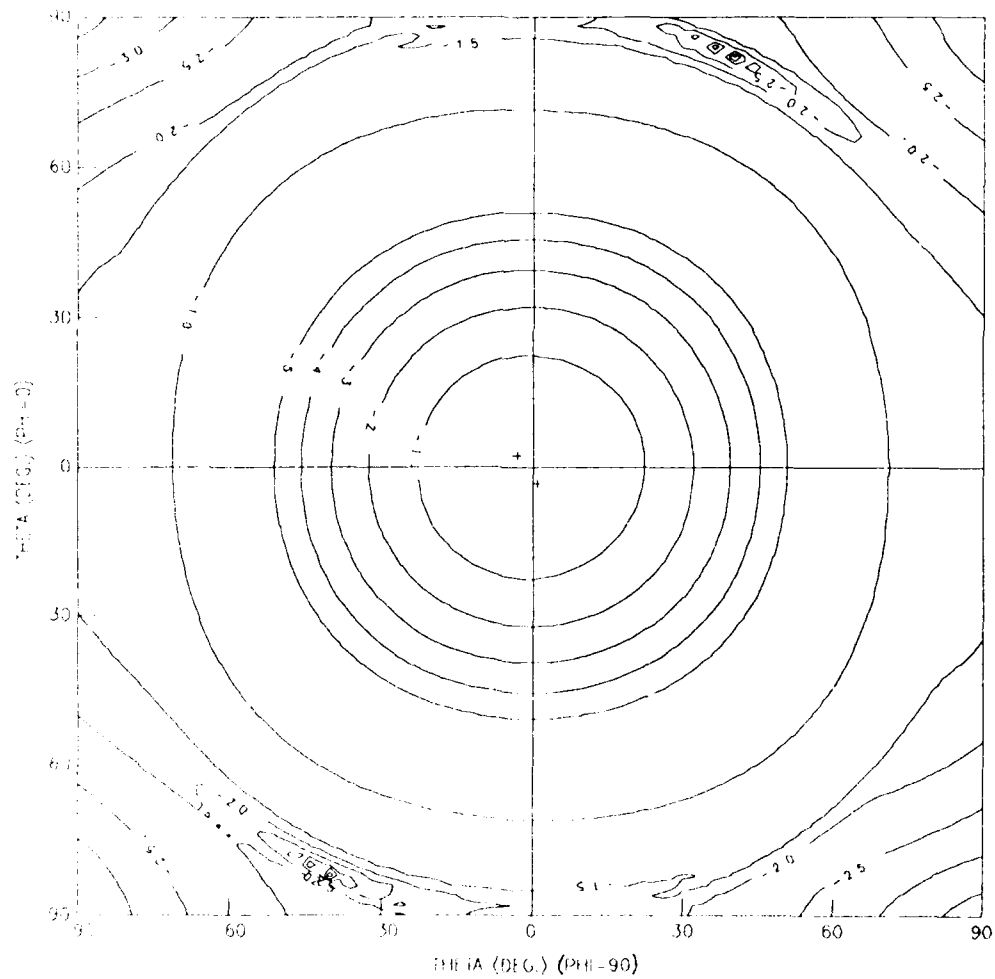


Figure 7. Sample Contour of Untruncated LPDA

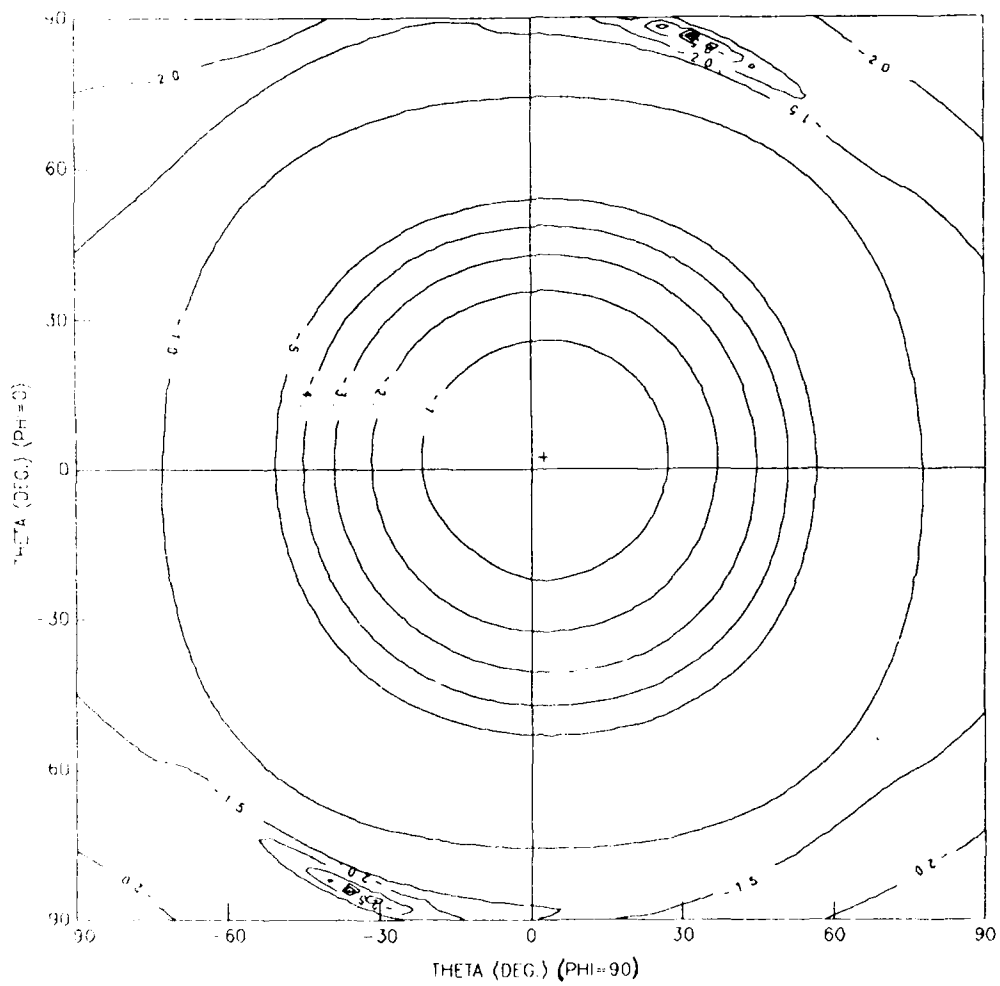


Figure 8. Sample Contour in Truncated Region of LPDA—Same Frequency as Figure 7.

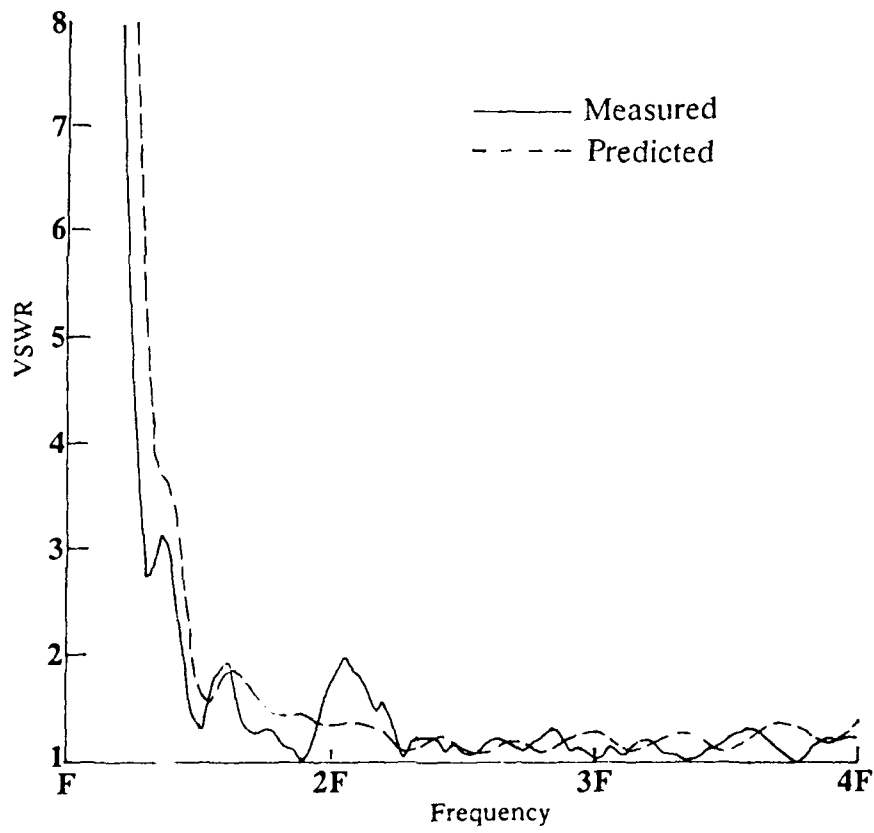


Figure 9. Measured and Predicted VSWR in Truncated Region.

feature which does not sacrifice too much in RF performance. Inserting inductive coils at the bases of the elements allows the antenna size to be reduced, and does not prevent the elements from folding.

Analysis and tests show that the base loading does not significantly affect the mutual coupling between elements. Hence, the procedure for determining the amount of inductance required is straightforward; choose an inductor which forces the shortened element to resonate at the same frequency as its full-length counterpart. The inductor design is quite simple and straightforward; no ferrite cores are required and there is no risk of damaging the inductors or elements as the antenna is unfolded.

This technique can be attractive for low-frequency LP antennas. Folding the elements in a cylindrical shell allows the antenna to be easily transported in a minimum amount of space.

The shape of the elements affects their characteristic impedance and must be considered in designing the antenna for a desired input impedance.

References

1. DiFonzo, D. F. (1964) Reduced Size Log Periodic Antennas, Micro-wave Journal, December: 37–42.
2. Kuo, S. C. (1972) Size-Reduced Log-Periodic Dipole Array Antenna, Microwave Journal, December: 27–33.
3. Hansen, R. C. (1975) Efficiency and Matching Tradeoffs for Inductively Loaded Short Antennas, IEEE Transactions on Communications 23 (No. 4): 430–435.
4. Elfving, C. T. (1963) Foreshortened Log Periodic Dipole Array. Paper presented at the WESCON convention, San Francisco.
5. Carrel, R. L. Analysis and Design of the Log-Periodic Dipole Antenna, Technical Report No. 52, Contract AF33(616)–6079, University of Illinois, Urbana, Illinois
6. Elliott, R. S. (1981) Antenna Theory and Design, Prentice-Hall, Englewood Cliffs, NH, 321–325.

A PRINTED CIRCUIT LOG PERIODIC DIPOLE ANTENNA WITH AN IMPROVED STRIPLINE FEED TECHNIQUE

Jeffrey A. Johnson

GE Aerospace
Aerospace Electronic Systems
Utica, NY 13501

ABSTRACT

A printed circuit log-periodic dipole antenna with 100 percent bandwidth is introduced. This antenna has an improved stripline feed technique that differs from those previously found in the literature. A method of reducing the antenna width to less than $\lambda/6$ at the lowest frequency is also presented to permit the antenna to operate in a grating lobe free phased array. Return loss, gain, and beamwidths are also presented.

1.0 INTRODUCTION

Operation of an active phased array over a wide bandwidth places severe requirements on the individual radiators. Such radiators must demonstrate good impedance characteristics, high gain, broad beamwidths, and be easily manufactured. In addition, for bandwidths approaching the order of 100 percent, the element width must be less than a half-wavelength at the low frequencies to fit into a grating lobe free array.

This paper presents a printed circuit log-periodic dipole (LPD) antenna designed to meet these requirements. The design introduces a stripline feed technique that differs from those previously found in the literature. This technique provides a wideband impedance match using substrates of equal thickness and readily available design data. The dipole lengths and separations were found by modifying the LPD spacing factor, σ , to account for the effects of the dielectric. The design also presents a practical method of reducing the element width by shaping and loading the printed dipoles. Test results for a 6 to 18 GHz design are also presented.

2.0 FEED DESIGN

The basic geometry of the feed structure along with the dipole placements is shown in Figure 1. It should be noted that there are three major transitions required for the feed structure: the connector-to-stripline interface, stripline-to-parallel wire feed line balun at the apex, and the termination of the parallel wire feed line beyond the largest radiating dipole. For the printed circuit LPD antenna, the transition between the stripline (SL) and parallel wire (PW) line becomes the most challenging. This is because the stripline, which brings the signal from the connector to the antenna apex, uses the two conductors of the PW feed as its two ground planes. A further constraint is that the SL-PW balun requires a four-to-one impedance transformation as outlined by Pantoja (1).

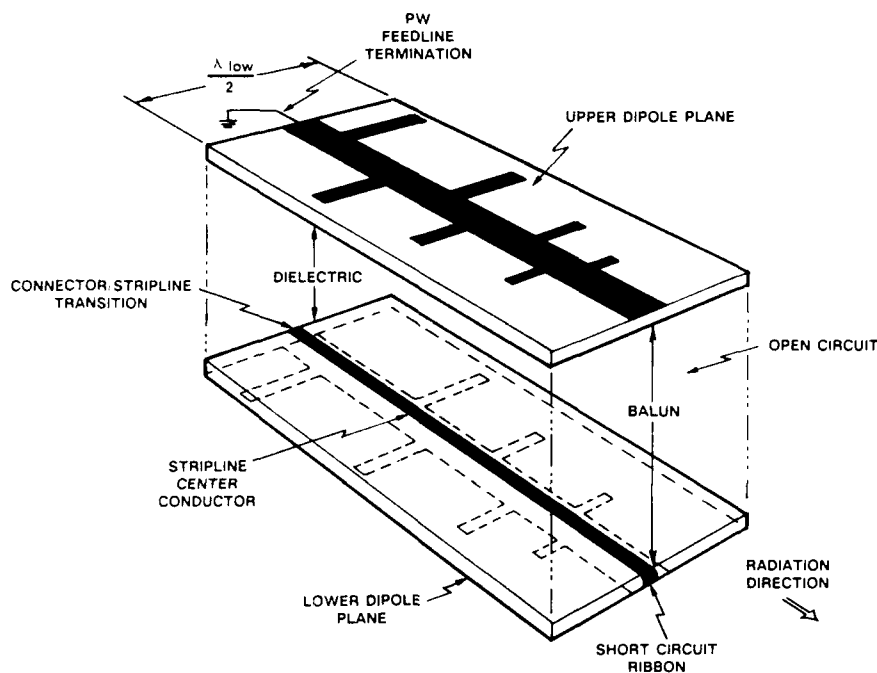


Figure 1. Printed Circuit Log-Periodic Dipole Antenna

Campbell (2) first presented the stripline feed design but neglected the required four-to-one impedance ratio. His design used a stripline feed with a narrow center conductor so that fringing fields of the noninfinite ground planes could be neglected. Also, with a narrow center conductor, its effects on the PW feeder line could be ignored. Two techniques have been proposed in the literature to account for the four-to-one impedance ratio at the balun. The first uses two substrates of unequal thickness to place the SL center conductor asymmetrically between its ground conductors (3), thereby lowering the SL impedance relative to the PW impedance. This method tends to be limited to approximately a three-to-one impedance ratio for practical substrate thicknesses. The second technique uses a wide center conductor but takes its effects into account by using finite element analysis to calculate the effective dielectric constants and characteristic impedances of the SL and the PW feed (1).

The design presented here retains much of the simplicity of Campbell's initial design by using three impedance transformers to permit both a four-to-one balun and a narrow center conductor. The first transformer converts a nominal 50-ohm impedance of a coax connector to a high impedance SL, thus creating a narrow center conductor. At the apex-balun region past the smallest dipole, the high SL impedance is lowered by increasing the center conductor width. Since the SL impedance was increased from 50 ohms at the connector, it would be difficult to lower the impedance of the SL to a quarter of the PW line impedance by only increasing the center conductor width. Therefore, to assist in the transi-

tion, the PW line has its impedance increased by reducing the outer conductor line widths at the balun.

The feed design, along with the printed dipoles, is shown schematically in Figure 2. The antenna structure consists of two laminated 0.015-inch polyimide substrates ($\epsilon_r = 4.5$, $\tan \delta = 0.01$). The input impedance of the LPD radiating structure was chosen to be 50 ohms, which corresponds to a PW impedance of 60 ohms and a conductor width of 0.065 inch. Each of the transformers was of a three-section Tchebyscheff design. The transformer at the connector raises the 50-ohm connector/stripline impedance to 75 ohms by decreasing the center conductor width from 0.035 to 0.005 inch. The two other transformers occur at the apex-balun. Here, one transformer decreases the SL impedance to 22 ohms by increasing the center conductor width to 0.040 inch; simultaneously, the two outer conductor widths are reduced to 0.040 inch to raise the input impedance of the LPD structure to 88 ohms. Subsequently, the four-to-one balun is created by shorting the center conductor of the 22-ohm SL to the bottom conductor of the 88-ohm PW feed and leaving the top conductor open circuited.

3.0. LPD DESIGN

The radiating structure design starts by finding the parameters for a free-space LPD antenna given the desired directivity, bandwidth, and input impedance. The design uses the work by DeVitto and Stracca (4,5) which is a refinement of the original design procedures (6,7). The directivity of the free space design was chosen as 9 dB; this corresponds to a scale factor, τ , of 0.88 and a relative spacing, σ , of 0.17. With these parameters, the number of dipoles, N , was found to be 12. The desired input impedance for the LPD structure was chosen to be 50 ohms. The dipole average characteristic impedance was determined to be 254 ohms, and the required feed line impedance was 60 ohms. From these values, the dipole lengths, spacing, and diameters were derived.

The second step in the design was to account for the effects of the dielectric on the dipole lengths and spacings. This was done by changing the spacing factor while maintaining the same scale factor for the above design. The value of σ was modified according to the equation:

$$\sigma_{\text{diel.}} = \sigma_{\text{air}} \frac{\sqrt{\epsilon_d}}{\sqrt{\epsilon_{pw}}}$$

where ϵ_{pw} is the effective dielectric constant of the PW feeder line. The value ϵ_d is the effective dielectric for the dipole on the substrate and was determined to be 1.9 by the method outlined by Campbell.

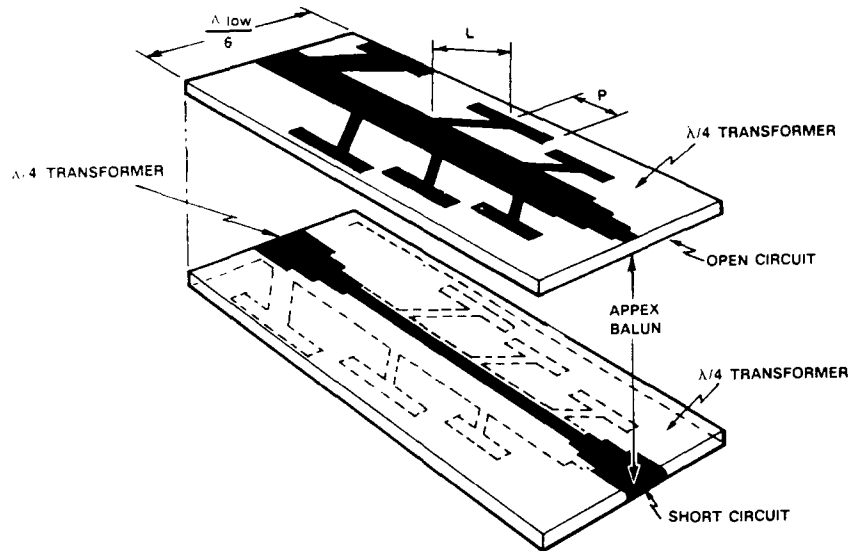


Figure 2. Electrically Narrow LPD with Transformer Feed

Since the center conductor is narrow relative to the two outer conductors, its effects on the PW feed line can be neglected. For this design, the value of ϵ_{pw} was determined to be 3.7 using Wheeler's (8) design data. The new value of σ was found to be 0.12. The method of modifying σ is equivalent to the procedure used by Pantoja, who reduced the dipole lengths and separation from the free space values by a factor of $1/\sqrt{\epsilon_d}$ and $1/\sqrt{\epsilon_{pw}}$, respectively

Using the new value of σ , the dipole lengths and separations can be calculated. The width of each dipole can be calculated as $4 \times a$, where a is the calculated radius for the dipole (9).

4.0 ELEMENT WIDTH REDUCTION AND PERFORMANCE

The goal of this LPD was to operate over the 6 to 18 GHz bandwidth and be able to fit into a grating lobe reduced array lattice. This required that the element be no more than 0.31 inch in total width, which is less than $\lambda/6$ at the lowest frequency. Several techniques were employed to achieve this dimension and maintain the $\lambda/2$ dipole resonance at the lower frequencies. The first technique was to use a substrate with a dielectric constant of 4.5 (polyimide). This reduced the width by approximately 20 percent over an equivalent design with a dielectric constant of 2.3 (PTFE). Although using an even higher dielectric constant would further reduce the width, an increase in substrate thickness would be re-

quired to maintain the desired SL and PW impedances. This increase in thickness could cause tilting of the element patterns (10) at the higher frequencies.

A further width reduction of approximately 30 percent was achieved by tilting the dipoles forward 45 degrees. Through a method of moment analysis (11) of a free space dipole, the beamwidth was broadened while only slightly raising the resonant frequency. The low frequency dipoles which were still too large were then truncated, and capacitive top-hat loading was applied.

After testing this design, it was determined that the top-hat loaded dipoles had improved patterns and gain over the straight tilted dipoles. Empirically it was determined that all dipoles should have a top-hat length, P , of about 35 percent of the total dipole length ($L + P$).

In order to meet the desired element width and to eliminate excessive overlap of the top-hats for adjacent dipoles, the last four dipoles had equal lengths (L) and top-hats (P). If left unaltered, these dipoles would have a desired resonant frequency around 8.9 GHz corresponding to the desired resonant frequency of the fourth largest dipole. To improve the low frequency performance, a thin coating (12) of high dielectric, electrically and magnetically lossy material (Eccosorb (13) CRS117, $\epsilon_r = 21.4 - j.42$, $\mu_r = 1.2 - j1.63$ at 8.6 GHz) was applied to the last three dipoles and the corresponding section of the PW feed line. The high dielectric constant lowers the magnitude of the reactance of the dipoles by lowering their resonant frequency. The high loss characteristics of the Eccosorb lossy material serves to raise the input resistance of the dipoles and increases the attenuation of the signal traveling towards the short circuit terminating the PW feed line. This attenuation is necessary to reduce the magnitude of the reflected signal from the short circuit, which can cause anomalous behavior (14) in the element performance.

The final design, with the addition of the load material, was fabricated and its performance was measured. Figure 3 shows the return loss, which was better than 10 dB from 6.2 to 18 GHz. The element gain was measured at 0.1 GHz increments and is shown in Figure 4. Also shown is the dielectric loss associated with the SL feed and caused by the high loss tangent of the material. This loss accounts for the decrease in gain at the higher frequencies. Patterns were measured at 0.5 GHz increments, and showed cross-polarization levels better than 20 dB down from the main polarization over 120° beamwidth. E- and H-plane beamwidths are shown in Figure 5.

5.0 CONCLUSIONS

A printed circuit log-periodic dipole antenna operating over a 100 percent bandwidth was presented. The design introduces an alternative stripline feed technique which uses three impedance transformers to achieve the required four-to-one impedance ratio at the balun. The dipole lengths and separations were found by a method similar to those previously reported. The design was electrically narrow at the low frequency so that it could

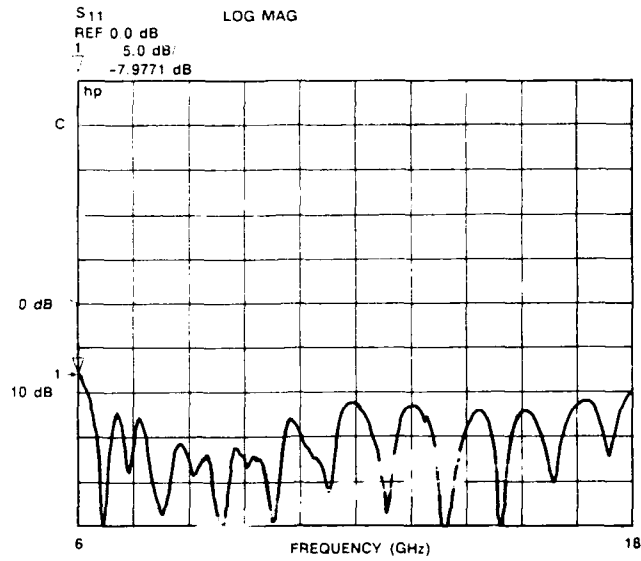


Figure 3. Return Loss

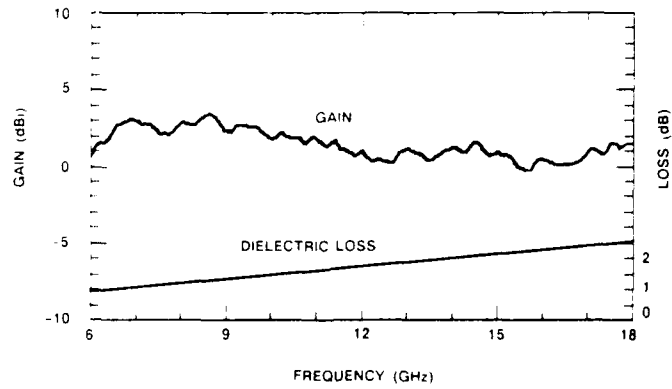


Figure 4. Element Gain

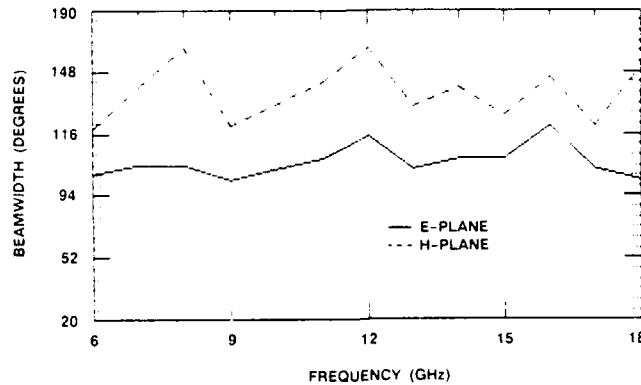


Figure 5. 3 dB Beamwidths

fit into a grating lobe reduced lattice. Measured performance of the radiator was shown to demonstrate the usefulness of the design.

Future work for this element will involve finding a lower loss substrate, modifying the balun area to reduce its length and maintain its performance, and increasing the parallel wire feed impedance and scale factor to improve the efficiency. Also, a small test array will be fabricated to verify its performance in an array environment.

6.0 ACKNOWLEDGMENT

The author wishes to thank Richard Jacobson for his assistance and helpful suggestions during the testing phase of this project.

7.0 REFERENCES

1. R. R. Pantoja, A. R. Sapienza, and F. C. Medeiros, "A Microwave Printed Planar Log-Periodic Dipole Array Antenna," *IEEE Trans.*, 1987, AP-35, No. 10, pp. 1176-1778.
2. C. K. Campbell, I. Traboulay, M. S. Suthers and H. Kneve, "Design of a Stripline Log-Periodic Dipole Antenna," *IEEE Trans.*, 1977, AP-25, No. 5, pp. 718-721.
3. F. I. Sheftman and L. H. Yorinks, "A Printed Circuit Log-Periodic Radiating Element for Wideband Phased Arrays," *1986 Int. IEEE Antennas Propagat. Soc. Symp. Dig.*, June 1986, pp. 753-756.
4. G. DeVitto and G. B. Stracca, "Comments on the Design of Log-Periodic Dipole Antennas," *IEEE Trans.*, 1973, AP-21, pp. 303-308.
5. G. DeVitto and G. B. Stracca, "Further Comments on the Design of Log-Periodic Dipole Antennas," *IEEE Trans.*, 1974, AP-22, pp. 714-718.

6. R. H. Du Hanel and D. E. Isbell, "Broadband Logarithmically Periodic Antenna Structures," IRE Nat. Conv. Rec. 1957, pt. 1, pp. 119-128.
7. R. L. Carrel, "Analysis and Design of the Log-Periodic Dipole Antenna," Antenna Lab., University of Illinois, Urbana, Tech. Rept. 52, 1961.
8. H. A. Wheeler, "Transmission-Line Properties of Parallel Strips Separated by a Dielectric Sheet," IEEE Trans., MTT-13, No. 2, March 1965, pp. 172-185.
9. C. M. Butler, "The Equivalent Radius of a Narrow Conducting Strip," IEEE Trans., 1982, AP-30, No. 4, pp. 755-758.
10. B. G. Evans, "The Effects of Transverse Feed Displacements on Log-Periodic Dipole Arrays," IEEE Trans., 1970, AP-18, No. 1, pp. 124-128.
11. G. B. Burke, and A. J. Poggio, "Numerical Electromagnetic Code (NEC) - Method of Moments," NOSC Tech. Doc. 116, Jan. 1980.
12. J. P. Y. Lee, and K. G. Balmain, "Wire Antennas Coated with Magnetically and Electrically Lossy Material," Radio Science, Vol. 14, No. 3, pp. 437-445, May-June 1979.
13. Eccosorb is a Registered Trademark of Emmerson and Cummings Corp.
14. C. C. Bantin and K. G. Balmain, "Study of Compressed Log-Periodic Dipole Antennas," IEEE Trans., 1970, AP-18, No. 2, pp. 195-203.

HALF WAVE "V" DIPOLE ANTENNA

Valentin Trainotti, Senior Member IEEE
Carlos Calvo 665-1°
1102 Buenos Aires, Argentina

ABSTRACT

Half wave dipole antenna has been used during many years in free space and over artificial or physical ground in HF, VHF and UHF operations. It was used alone or in large arrays, because of its simplicity and high radiation efficiency. Nevertheless half wave "V" dipole and its performance are not so well treated in technical literature. For this reason characteristics of this useful antenna are presented here where input impedance and radiation patterns are treated in theoretical and practical form for different dipole wing angle " α " and length-diameter relationship.

INTRODUCTION

Half wave dipole antenna has been studied since long time ago and it is one of the most popular, efficient and used antennas all over the radioelectric spectrum. Lots of papers have been written analyzing their

impedance and radiation properties for several length-diameter relationship. Different approaches have been developed in order to obtain their characteristics as exact as possible compared with the measured practical models. These characteristics depart quite a lot from the theoretical very thin dipoles especially in VHF and UHF. In these particular cases length-diameter relationship is generally low and the dipole has the mechanical properties of self supporting in space with only the feeding line structure. For moderate to low length-diameter relationship the sinusoidal current theory fails completely to determine their characteristics and for this reason one of the best approaches used lately is the method of moment theory.

Several computer programs have been made to analyze them even for P.C. Nevertheless measurements are always useful in order to know the under test antenna characteristics and especially those of very complicated mechanical structures whose analysis is quite difficult to simulate or in other cases to compare with theoretical approaches.

FREE SPACE HALF WAVE "V" DIPOLE CHARACTERISTICS

Analysis of a free space input impedance and radiation pattern using moment method theory is made in classical form where the linear dipole is placed along the Z axis. Figure 1 shows the "V" dipole geometry in free space. "V" dipole is contained in the YZ plane and the " θ " wing angle is taken from the Z axis because the classical linear dipole is taken as reference and its " θ " angle is zero. "H" is the half antenna length and "a" is the wire radius. Generally half wave antenna "H" is always a little bit shorter than $0.25\lambda_0$ in order to obtain dipole resonance depending on the length-diameter relationship. Here its value is taken as $0.24\lambda_0$ for any practical or theoretical cases. Figure 2 shows the input impedance values of a typical dipole as a function of " θ " angle and H/a relationship for center band frequency f_0 . It can be seen that an increase in " θ " angle leads to a decrease of input resistance values and an increase of input capacitive reactance typical of shorter antennas. Hence this effect produces a de-

crease in radiation resistance and directivity. To compensate this effect larger H values must be used as " δ " angle is increased. Nevertheless is important not use very high " δ " angle values because the "V" dipole transforms itself in a parallel wire transmission line with very low radiation resistance and almost no radiation. Figure 3 shows input impedance values near center frequency for a typical HF and VHF "V" dipole where H/a is 3600 and 100 respectively. Figure 4 shows calculated typical input impedance referred to 50 ohms as a function of " δ " angle and frequency for several H/a relationship. These H/a relationship are among those most used in practice, so a general view of a "V" dipole behavior can be seen. In the same figure, " δ " angle curve for 40 degrees and for any value of H/a relationship gives the best match to 50 ohms feeding lines. Figure 5 shows a comparison of measured and calculated input impedance values for " δ " 40 degrees where good agreement is achieved. Some departure can be seen for low H/a relationship due to the feeding point geometry effects. Nevertheless good matching to 50 ohms is obtained near

center frequency band without any other additional matching system as measured models suggested. Similar results for other " γ " angles are obtained. "V" dipole radiation patterns are modified as " γ " angle is increased in both horizontal and vertical plane. Nulls of vertical plane radiation patterns are filled in and departure from omnidirectionality in horizontal plane radiation patterns are obtained. Fill in in vertical radiation pattern nulls is due to a decrease in cross polarization relationship for $\theta = 0^\circ$ and $\theta = 180^\circ$. Calculated cross polarization is very low (less than -40 dB) for $\theta = 90^\circ$ for any " γ " angle and for any H/a relationship. Figure 5 and table 1 show radiation patterns in horizontal and vertical planes and directivity in equatorial plane as a function of ϕ angle and H/a Relationship. Very small directivity variations (less than a tenth of dB) are obtained for any value of H/a and these variations are even smaller as " γ " angle is increased.

TABLE 1
CALCULATED DIRECTIVITY dBi
"γ"

	0	10	20	30	40	50	60	70
$\theta = 90^\circ$ H/a=3600 H=0.24 λ_0								
0	2.13	2.11	2.04	1.94	1.82	1.68	1.55	1.44
45	2.13	2.09	1.99	1.85	1.67	1.49	1.32	1.17
90	2.13	2.08	1.95	1.77	1.54	1.31	1.08	0.89
135	2.13	2.09	1.99	1.85	1.67	1.49	1.32	1.17
180	2.13	2.11	2.04	1.94	1.82	1.68	1.55	1.44
225	2.13	2.10	2.02	1.88	1.71	1.52	1.34	1.18
270	2.13	2.10	1.99	1.82	1.60	1.36	1.12	0.91
315	2.13	2.10	2.02	1.88	1.71	1.52	1.34	1.08
$\theta = 90^\circ$ H/a=500 H=0.24 λ_0								
0	2.13	2.11	2.05	1.94	1.82	1.68	1.55	1.44
45	2.13	2.09	1.99	1.84	1.67	1.48	1.30	1.16
90	2.13	1.08	1.95	1.76	1.53	1.29	1.07	0.88
135	2.13	2.09	1.99	1.84	1.67	1.48	1.30	1.16
180	2.13	2.11	2.05	1.94	1.82	1.68	1.55	1.44
225	2.13	2.11	2.03	1.89	1.72	1.53	1.34	1.18
270	2.13	2.11	2.00	1.83	1.61	1.36	1.12	0.91
315	2.13	2.11	2.03	1.89	1.72	1.53	1.34	1.18
$\theta = 90^\circ$ H/a=100 H=0.24 λ_0								
0	2.15	2.12	2.06	1.95	1.82	1.68	1.55	1.44
45	2.15	2.10	1.99	1.83	1.65	1.46	1.28	1.14
90	2.15	2.08	1.94	1.74	1.50	1.26	1.04	0.86
135	2.15	2.10	1.99	1.83	1.65	1.46	1.28	1.14
180	2.15	2.12	2.06	1.95	1.82	1.68	1.55	1.44
225	2.15	2.13	2.05	1.91	1.74	1.54	1.32	1.18
270	2.15	2.13	2.03	1.85	1.63	1.37	1.10	0.91
315	2.15	2.13	2.05	1.91	1.74	1.54	1.32	1.18
$\theta = 90^\circ$ H/a=20 H=0.24 λ_0								
0	2.18	2.16	2.08	1.97	1.82	1.67	1.54	1.44
45	2.18	2.11	1.98	1.80	1.60	1.40	1.22	1.10
90	2.18	2.09	1.92	1.69	1.43	1.17	0.95	0.79
135	2.18	2.11	1.98	1.80	1.60	1.40	1.22	1.10
180	2.18	2.16	2.08	1.97	1.82	1.67	1.54	1.44
225	2.18	2.18	2.11	1.97	1.78	1.57	1.36	1.19
270	2.18	2.18	2.09	1.92	1.69	1.42	1.14	0.91
315	2.18	2.18	2.11	1.97	1.78	1.57	1.36	1.19

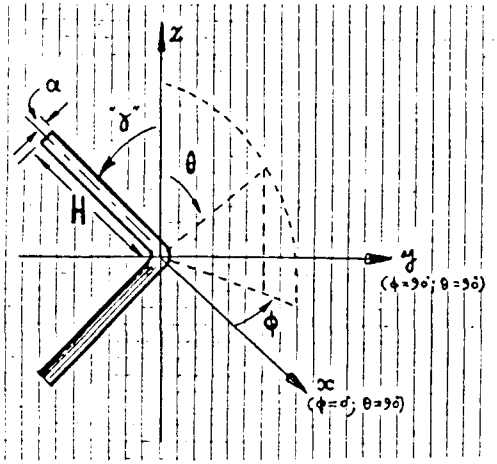


Figure 1. Free Space "V" dipole coordinates.

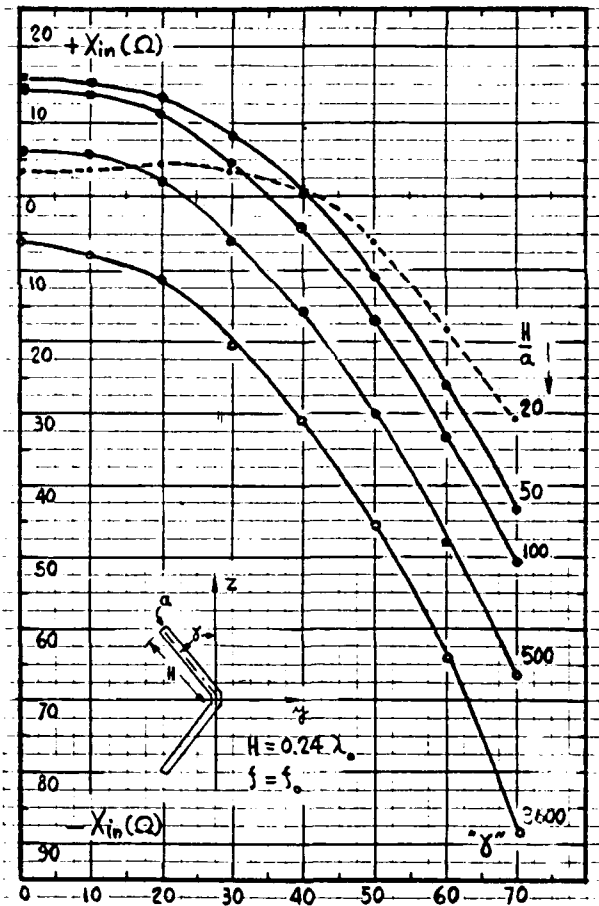
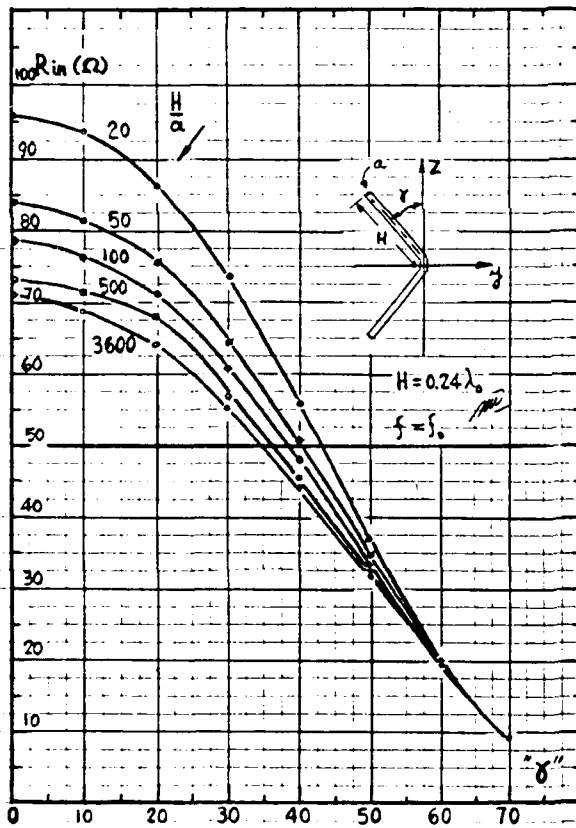


Figure 2. Free space "V" dipole input impedance as a function of " δ " and H/a .

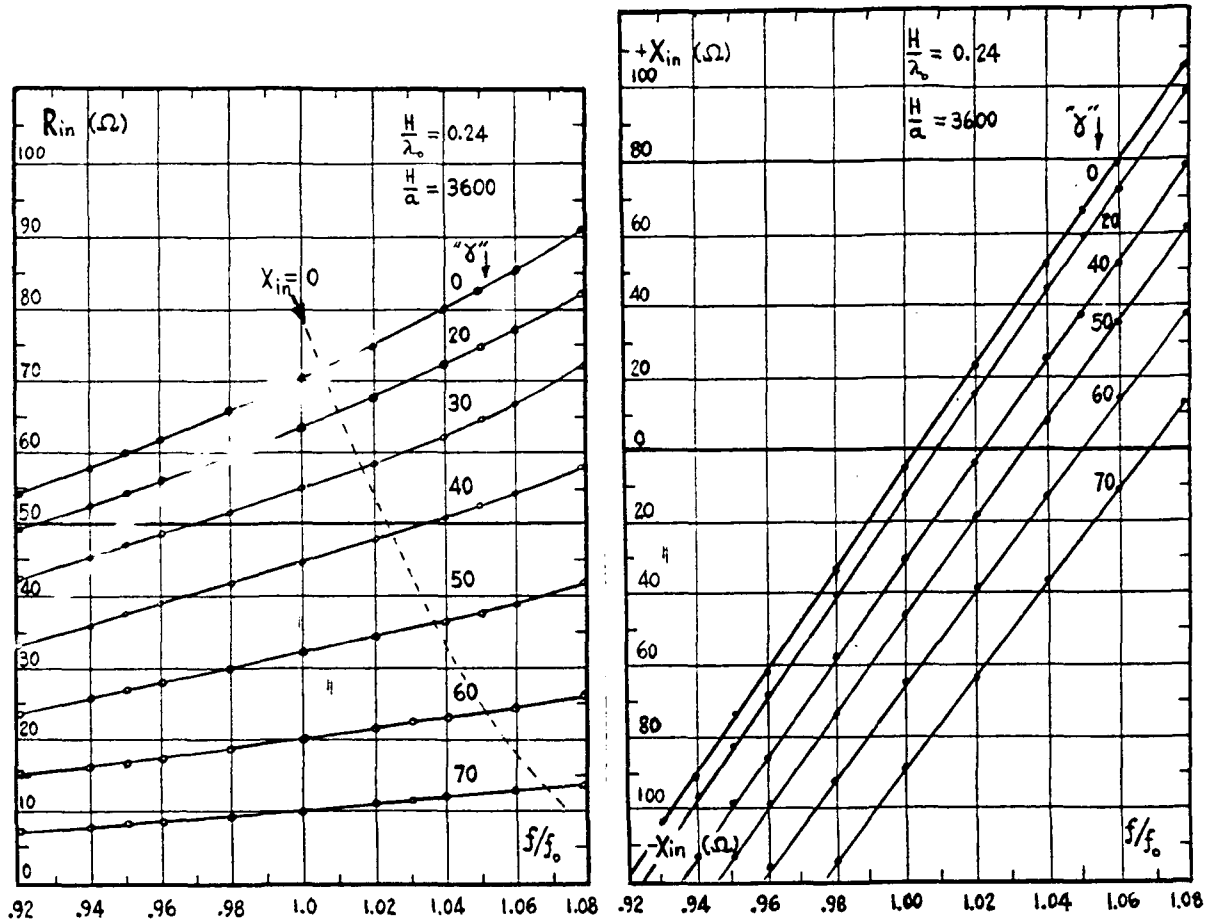


Figure 3 a. Free space "V" dipole input impedance near center frequency as a function of " δ " angle.

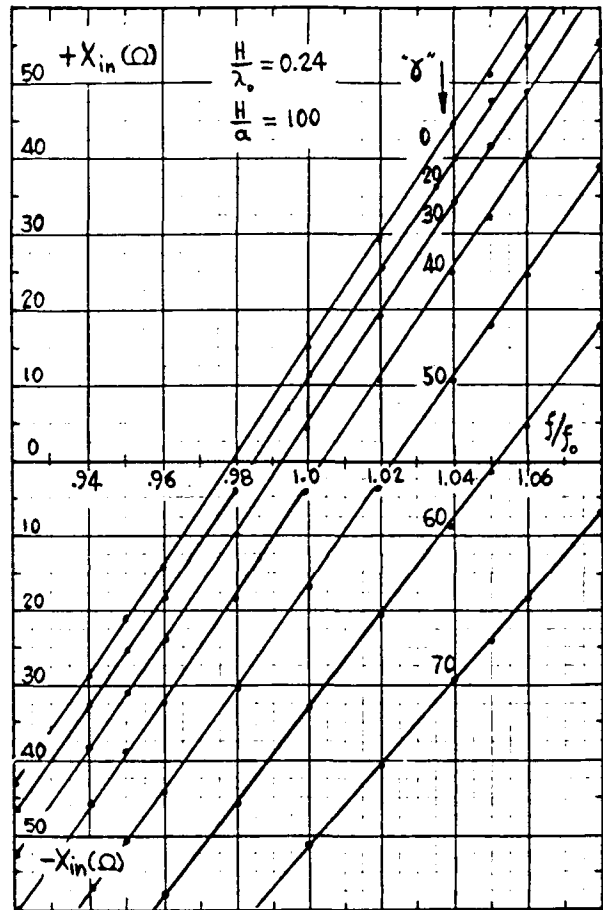
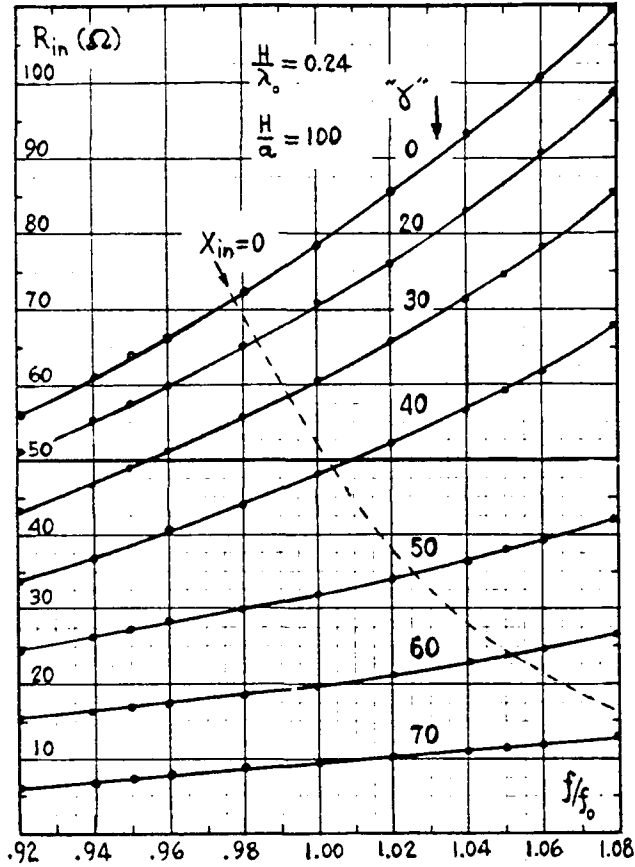


Figure 3 b. Free space "V" dipole input impedance near center frequency as a function of " δ " angle.

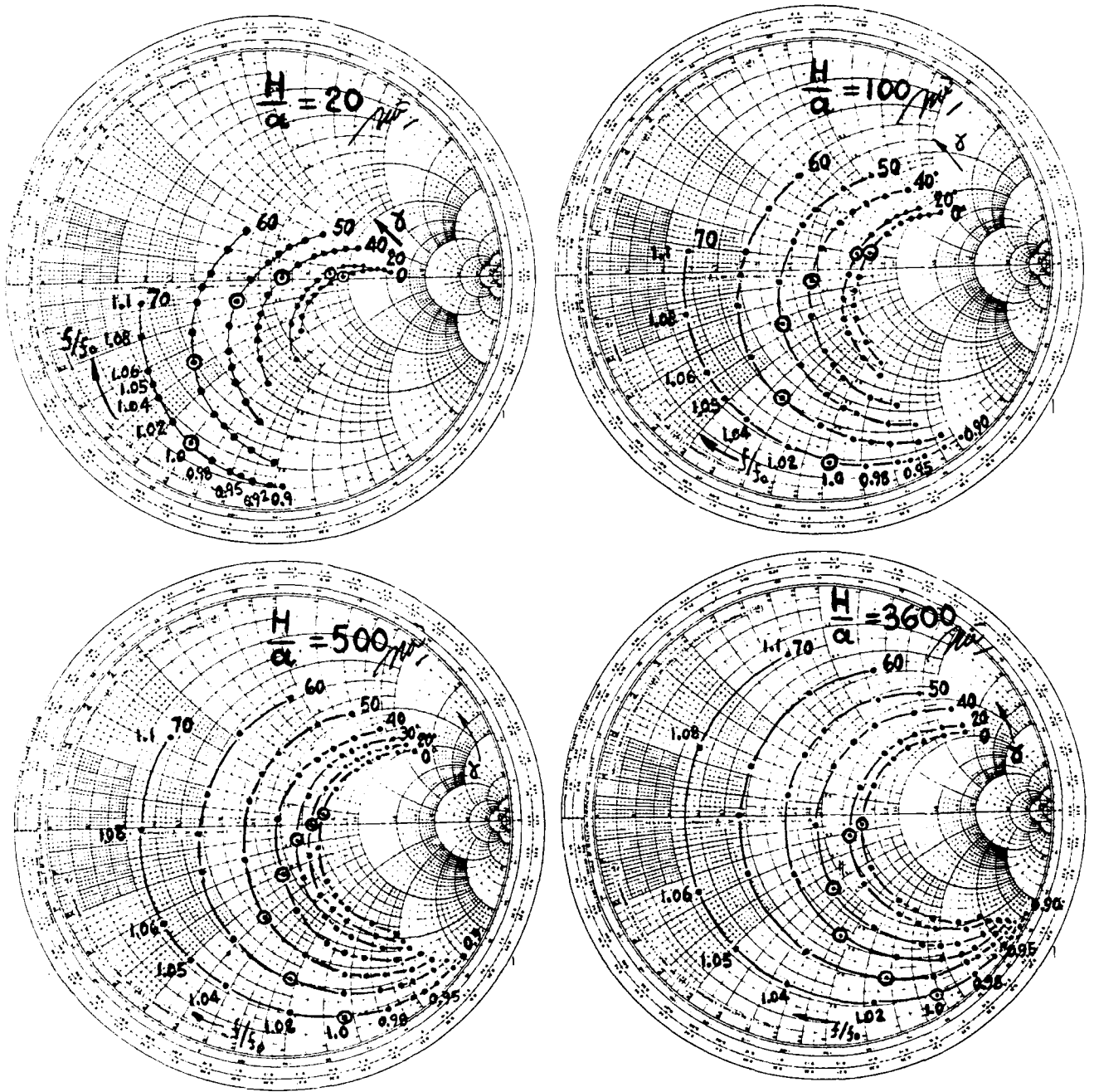


Figure 4. Free space "V" dipole input impedance as a function of frequency and " δ " angle.

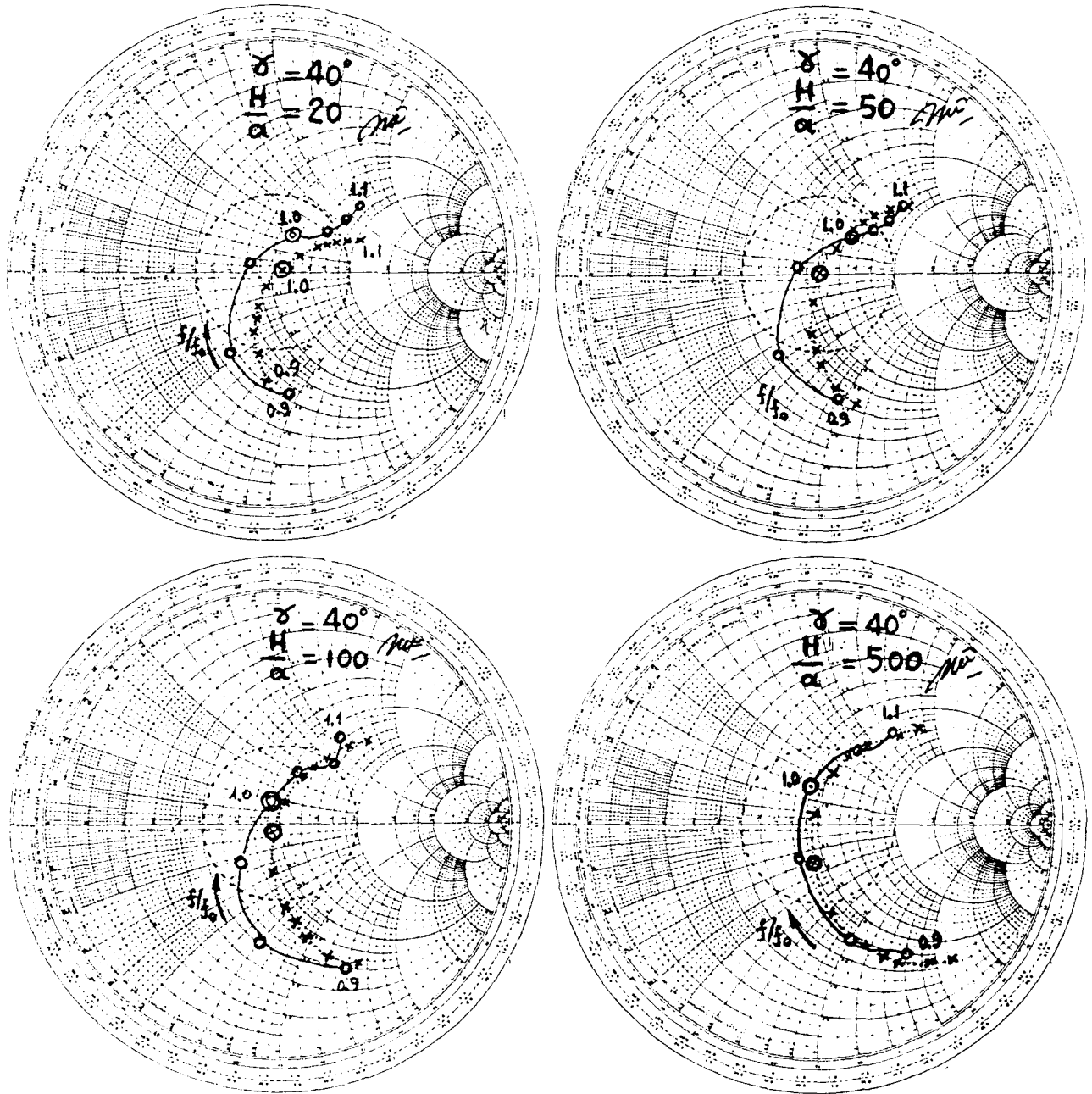


Figure 5. Comparison between calculated and measured free space "V" dipole input impedance.
o—o—o Measured x--x--x Calculated

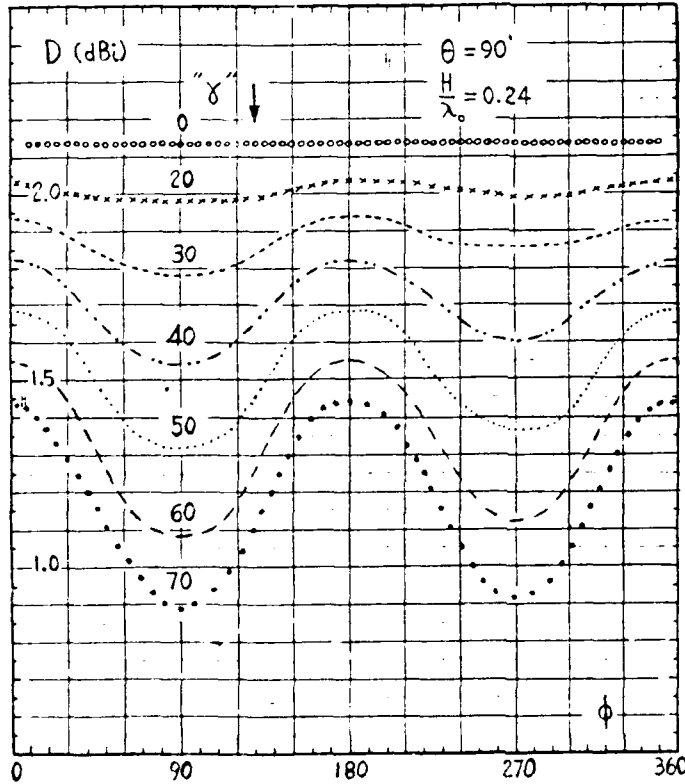
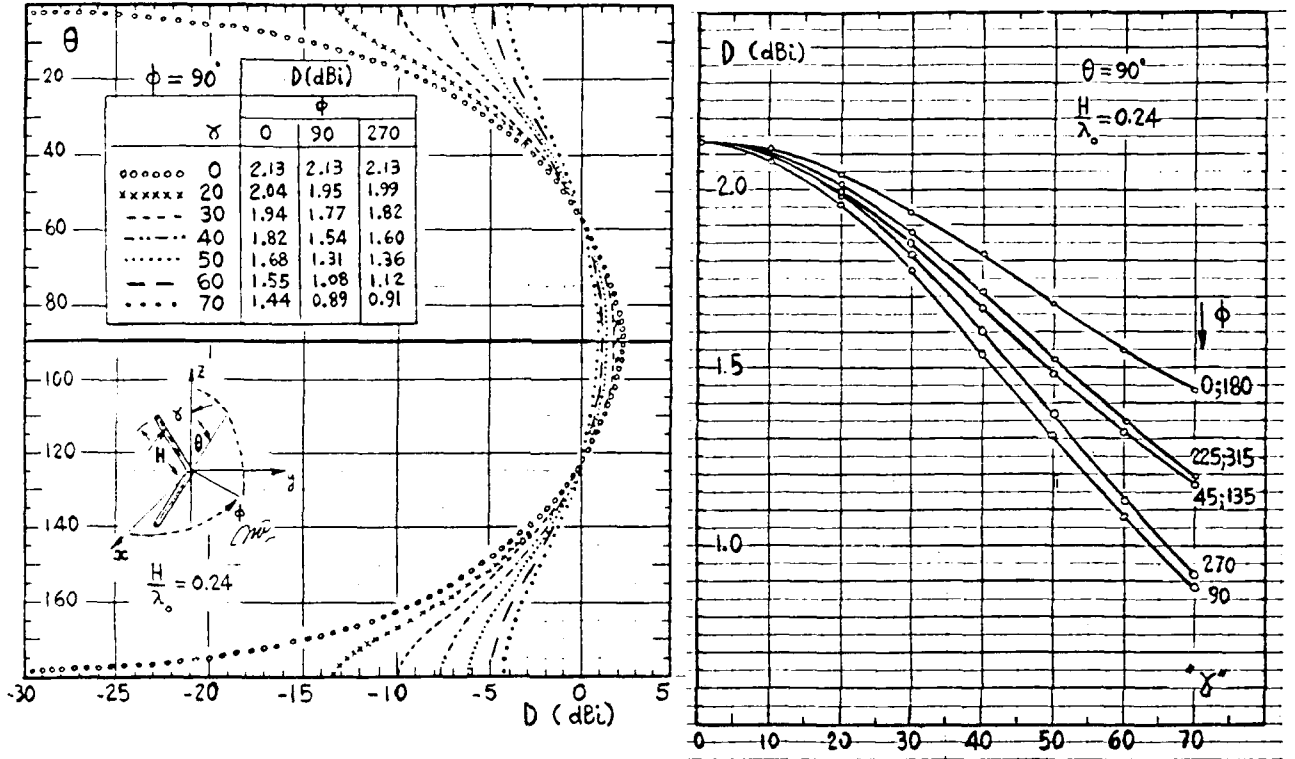


Figure 6. Free space "v" dipole radiation patterns and directivity as a function of " δ " angle.

GROUND PLANE "V" DIPOLE CHARACTERISTICS

To determine the radiation and impedance characteristics the half wave "V" dipole is placed over a ground plane whose conductivity is varied from infinity to low values typical of low conductivity soils. " θ " angle is varied from zero (classical horizontal half wave dipole) to 70 degrees if driving point height permits. In this case "V" dipole antenna is called generally inverted "V" dipole antenna and is very popular because it needs only one supporting pole. This makes it suitable for HF portable civilian and military communications and other applications. The center supporting pole permits to place a driving point balun on it improving the dipole radiation characteristics through outside shield line current elimination in coaxial feeding lines. For VHF and UHF applications half wave "V" dipole is placed generally over metal ground planes and its behavior is quite similar as infinite conductivity ground plane where radiation along the metal sheet is almost zero if size is very large in wavelengths. If not edge diffraction radiation will occur. Here infinite extension of

ground plane is considered. Figure 7 shows the "V" dipole geometry over ground. Input impedance values have been calculated and can be seen in figure 8 and 9 as a function of " θ " angle and height h over the ground plane for a typical HF and VHF inverted "V" dipole at center frequency. Among them a 40° " θ " angle inverted "V" dipoles have input impedance values close to 50 ohms for h/λ_0 between 0.2 and .55 and for any H/a relationship commonly used in practice. Input impedance as a function of frequency and " θ " angle can be seen in figure 10. Comparison between calculated and measured input impedance "V" dipole values is shown in figure 11 and typical HF "V" dipole input impedance as a function of height at center frequency can be seen in figure 12 for three values of dipole length and for a " θ " angle of 40 degree. In the same figure measured values for $h/\lambda_0=0.24$ can be seen too. Good matching to 50 ohms lines could be obtained without matching units, choosing the proper dipole length.

Inverted "V" dipole radiation properties depend on dipole driving point height over the ground plane and soil conductivity. Maximum directivity decreases as " θ "

angle increases due to an increase in radiation pattern beamwidth and null fill in. Calculated maximum directivity as a function of " α " angle and ground conductivity is shown in table 2 for different antenna height. In average soil conductivity and relative dielectric constant are taken as 0.01 siemens/m and 20 respectively and for poor soil 0.001 siemens/m and 4. Typical HF radiation patterns between 0.25 and 0.5 wavelength in height and for a " α " 40° inverted "V" dipole are shown in figure 13. Loss of directivity is generally less or around 1 dB for " α " angles between 0 and 40 degrees and for soil conductivities higher than 0.01 siemens/m.

" α " angle effect on radiation patterns can be seen in figure 14 for a perfect conductivity soil. Similar effect for less conductive soils is obtained.

CONCLUSIONS

Half wave "V" dipole has been analyze in free space and over ground plane. Results can be very useful in designing HF or VHF-UHF systems in order to choose a self impedance matching for 50 ohms lines or to obtain the proper radiation pattern. Input impedance, radiation

or directivity pattern have been determined in any case and only few cases can be seen here in order to be synthetic. Nevertheless given data intend to be as complete as possible in all aspects.

BIBLIOGRAPHY

1. Jordan, E.C. "Electromagnetic waves and radiating systems"
Prentice Hall, Inc. Englewood Cliffs, N.J. (1950).
2. Balanis, C.A. "Antenna Theory" Harper & Row Pub. N.Y. (1982)
3. Rockway, J.W. Tam, D.W.S. Logan, J.C. Li, S.T. "The Mininec"
Artech House, Norwood, MA. (1988)
4. Stutzman, W.L. Thiele, G.A. "Antenna Theory and Design"
John Wiley & Sons, Inc. N.Y. (1981).
5. Kraus, J.D. "Antennas" Mc. Graw Hill, Inc. N.Y. (1950).
6. Johnson, R.C. Jasik, H. "Antenna Engineering Handbook"
Mc. Graw Hill Co. N.Y. (1984)

TABLE 2

CALCULATED MAXIMUM DIRECTIVITY dBI

" δ "

	0	20	40	50	60	70
	$\phi = 90^\circ$		$h/\lambda_0 = 0.20$	$H/\lambda_0 = 0.24$		
$\alpha\alpha\alpha = \infty$	8.10	7.83	6.99	6.42	----	----
$\alpha\alpha\alpha = 0.01$	6.37	6.14	5.36	4.83	----	----
$\alpha\alpha\alpha = 0.001$	4.69	4.61	4.06	3.66	----	----
	$\phi = 90^\circ$		$h/\lambda_0 = 0.25$	$H/\lambda_0 = 0.24$		
$\alpha\alpha\alpha = \infty$	7.46	7.46	7.00	6.65	6.30	5.99
$\alpha\alpha\alpha = 0.01$	5.70	5.70	5.26	4.93	4.59	4.29
$\alpha\alpha\alpha = 0.001$	3.93	3.96	3.59	3.31	3.01	2.74
	$\phi = 90^\circ$		$h/\lambda_0 = 0.30$	$H/\lambda_0 = 0.24$		
$\alpha\alpha\alpha = \infty$	6.95	6.85	6.60	6.40	6.16	5.94
$\alpha\alpha\alpha = 0.01$	5.50	5.30	4.92	4.67	4.43	4.20
$\alpha\alpha\alpha = 0.001$	3.95	3.68	3.26	3.01	2.76	2.54
	$\phi = 90^\circ$		$h/\lambda_0 = 0.35$	$H/\lambda_0 = 0.24$		
$\alpha\alpha\alpha = \infty$	6.88	6.56	6.03	6.00	5.50	5.25
$\alpha\alpha\alpha = 0.01$	5.59	5.27	4.74	4.45	4.20	4.00
$\alpha\alpha\alpha = 0.001$	4.10	3.78	3.28	3.00	2.75	2.55
	$\phi = 90^\circ$		$h/\lambda_0 = 0.40$	$H/\lambda_0 = 0.24$		
$\alpha\alpha\alpha = \infty$	7.16	6.77	6.30	6.05	5.82	5.63
$\alpha\alpha\alpha = 0.01$	6.03	5.59	5.01	4.75	4.51	4.32
$\alpha\alpha\alpha = 0.001$	4.73	4.20	3.61	3.33	3.07	2.87
	$\phi = 90^\circ$		$h/\lambda_0 = 0.45$	$H/\lambda_0 = 0.24$		
$\alpha\alpha\alpha = \infty$	7.71	7.24	6.66	6.38	6.13	5.93
$\alpha\alpha\alpha = 0.01$	6.68	6.17	5.52	5.20	4.94	4.74
$\alpha\alpha\alpha = 0.001$	5.50	4.88	4.22	3.90	3.63	3.42
	$\phi = 90^\circ$		$h/\lambda_0 = 0.50$	$H/\lambda_0 = 0.24$		
$\alpha\alpha\alpha = \infty$	8.39	7.89	7.15	6.95	6.50	6.30
$\alpha\alpha\alpha = 0.01$	7.45	6.70	6.22	5.85	5.55	5.35
$\alpha\alpha\alpha = 0.001$	6.30	5.76	5.00	4.68	4.38	4.16

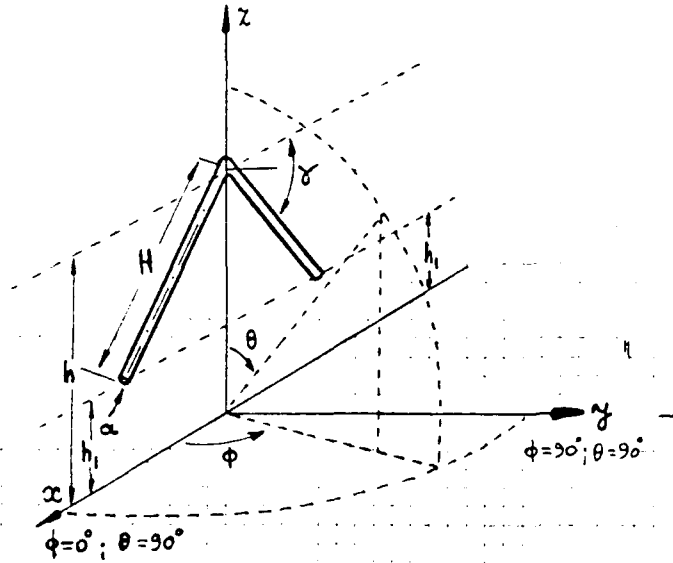


Figure 7. "V" dipole over ground plane coordinates.

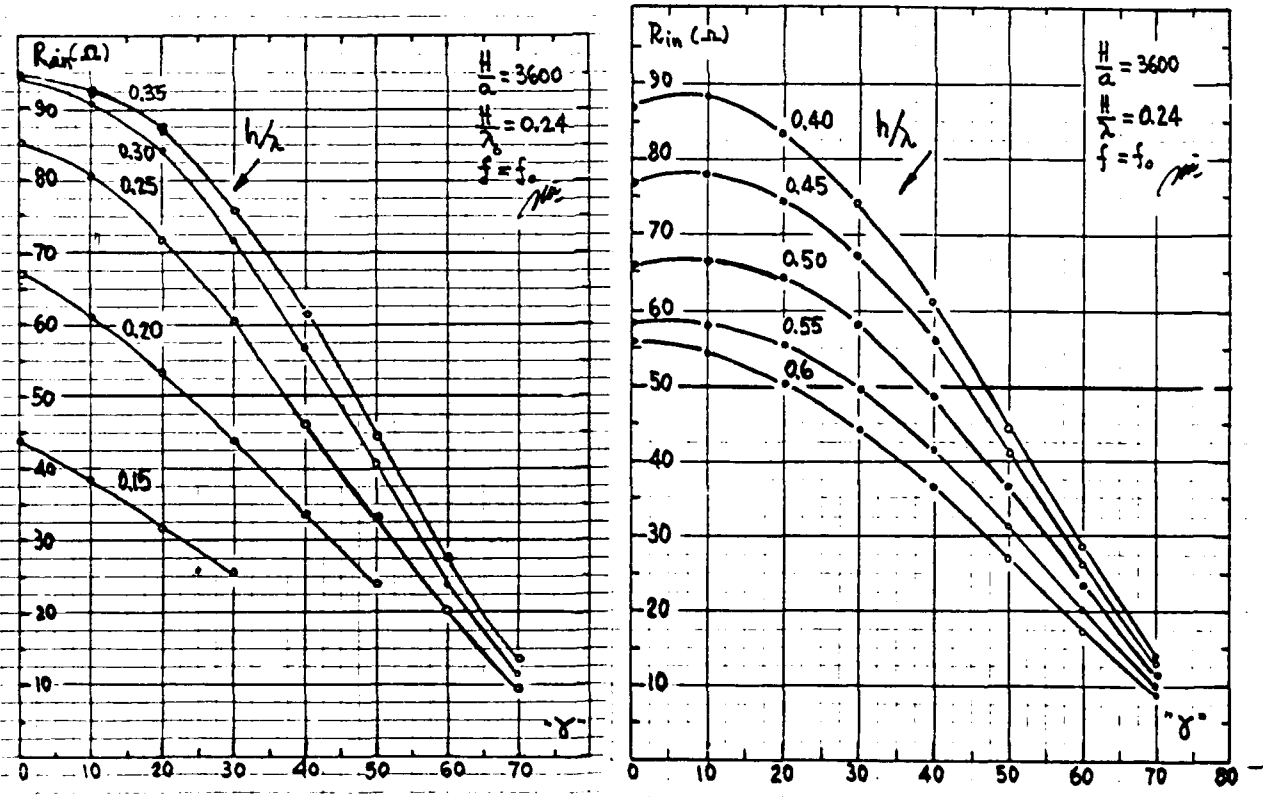


Figure 8. Inverted "V" dipole input resistance as a function of " δ " angle and Height h/λ .

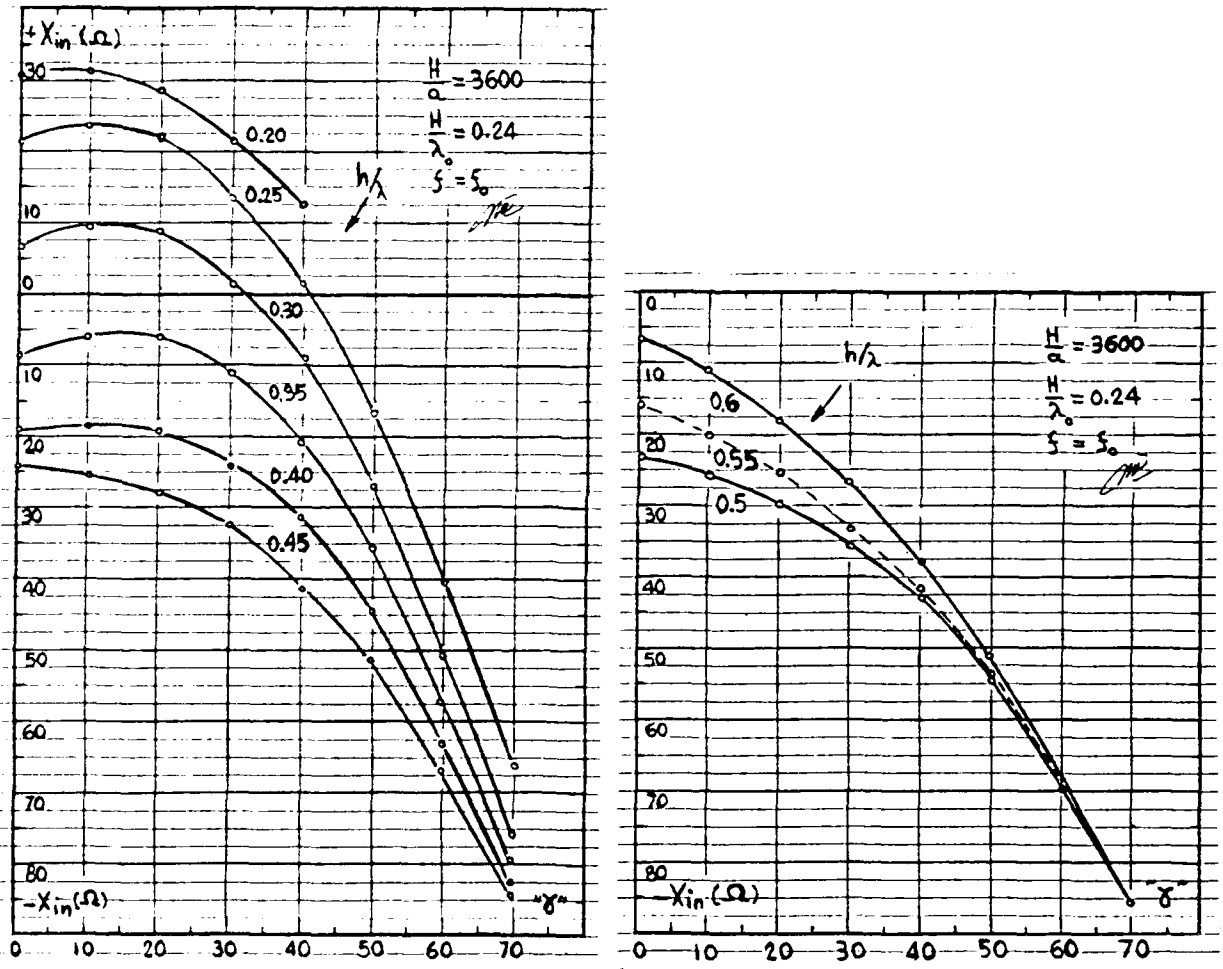


Figure 8 b. Inverted "V" dipole input reactance as a function of " γ " angle and height h/λ_0 .

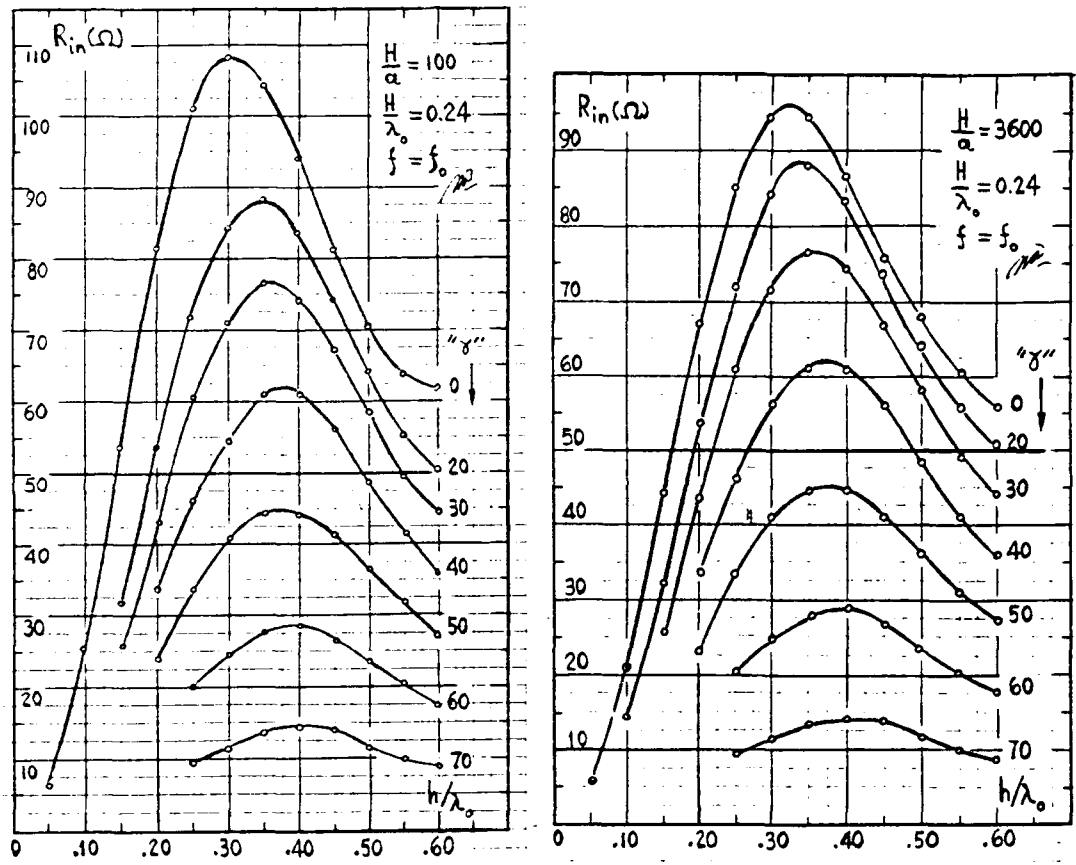


Figure 9 a. Inverted "V" dipole input resistance as a function of " δ " angle and height h/λ_0 .

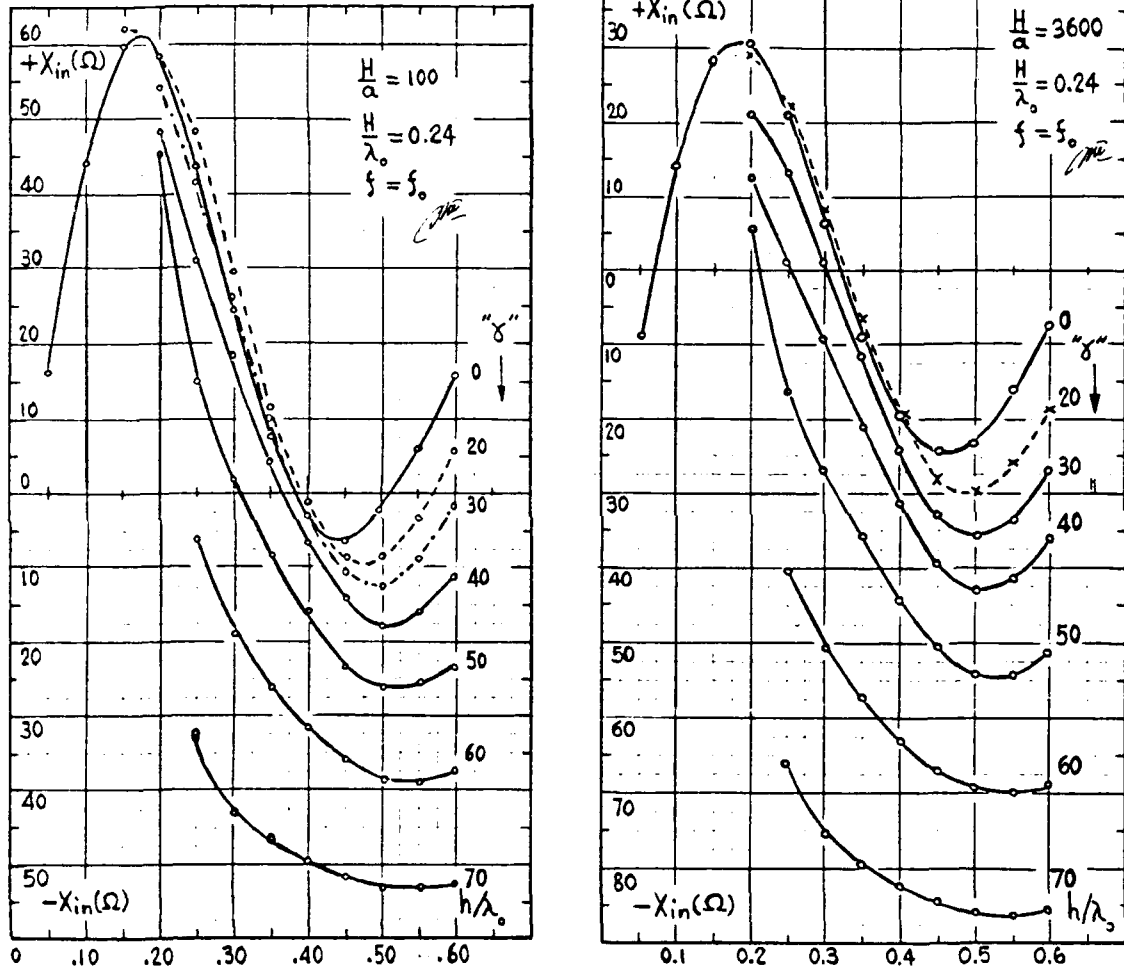


Figure 9 b. Inverted "V" dipole input reactance as a function of " δ " angle and height h/λ_0 .

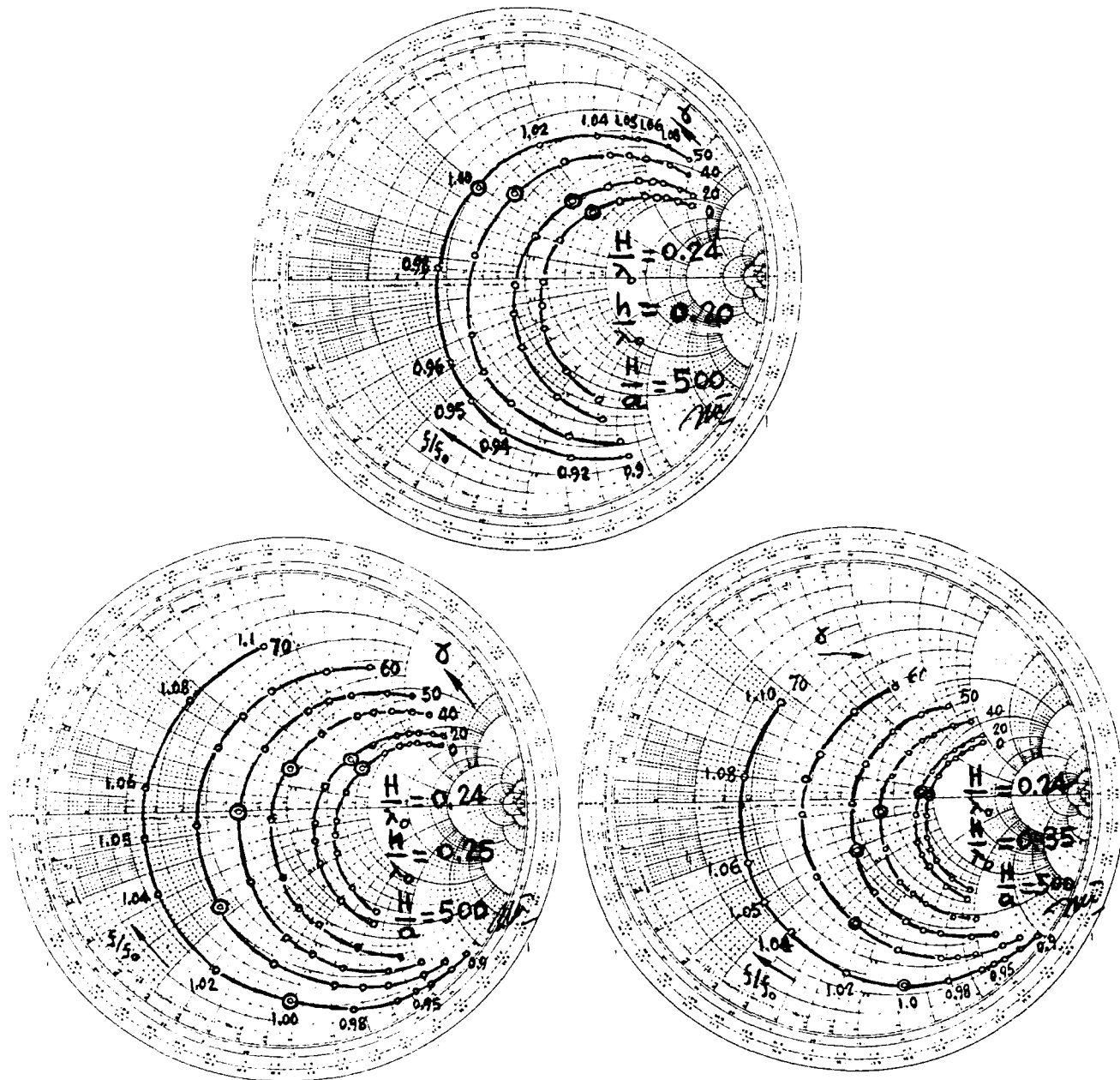


Figure 10. Typical HF inverted "V" dipole input impedance as a function of " δ " angle and frequency.

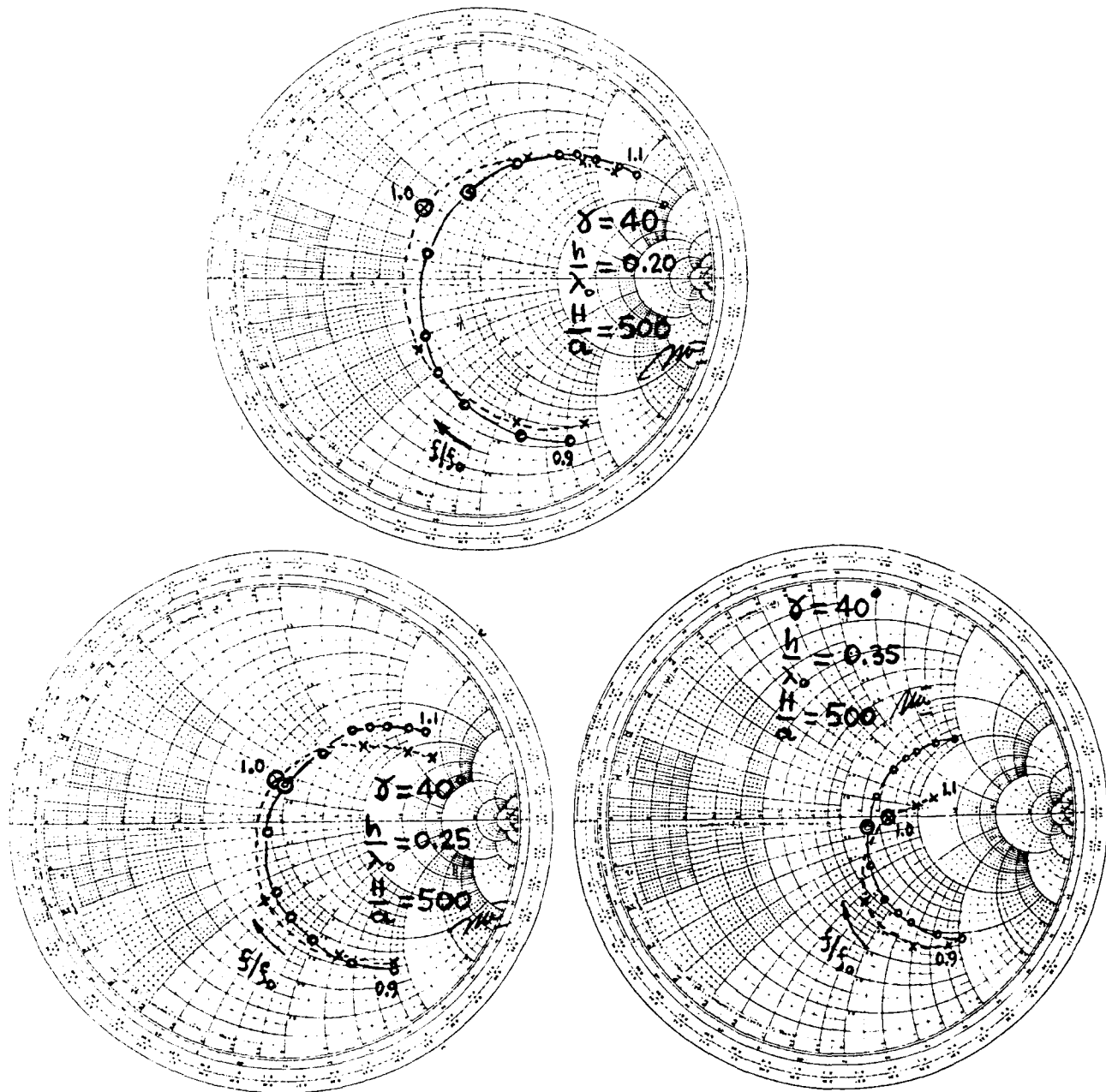


Figure 11. Comparison between measured and calculated inverted "V" dipole input impedance values.

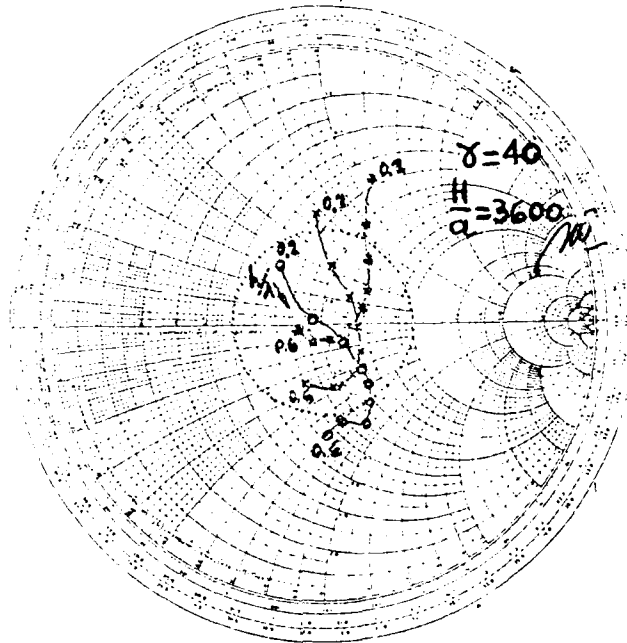


Figure 12 a. " δ " 40° inverted "V" dipole input impedance as a function of dipole length and height h/λ_0 .

H/λ_0 o—o—o 0.24 x—x—x 0.244 *—*—* 0.2475

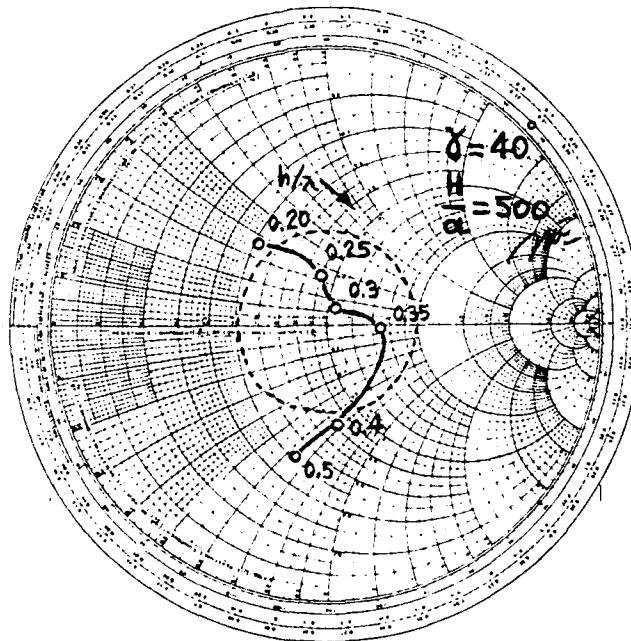


Figure 12 b. " δ " 40° inverted "V" dipole measured input impedance as a function of height h/λ_0 .

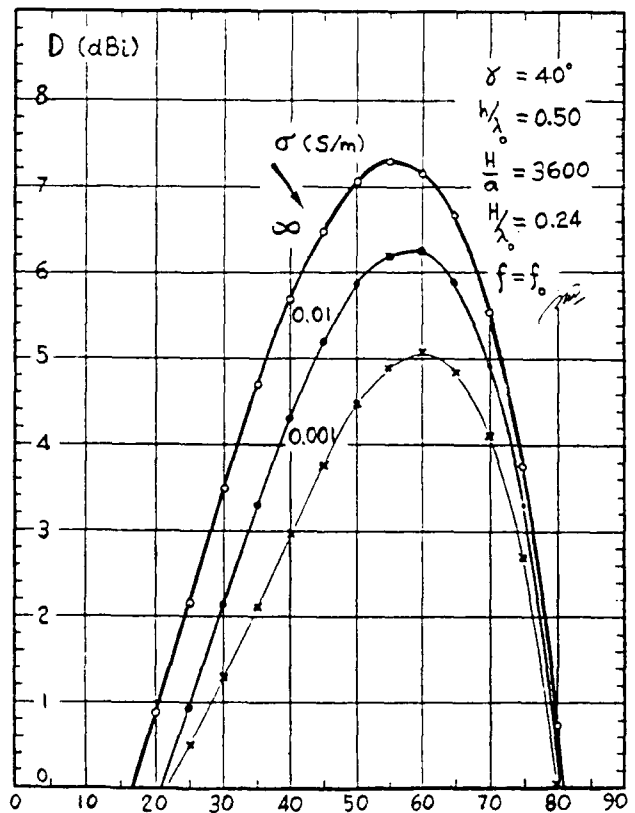
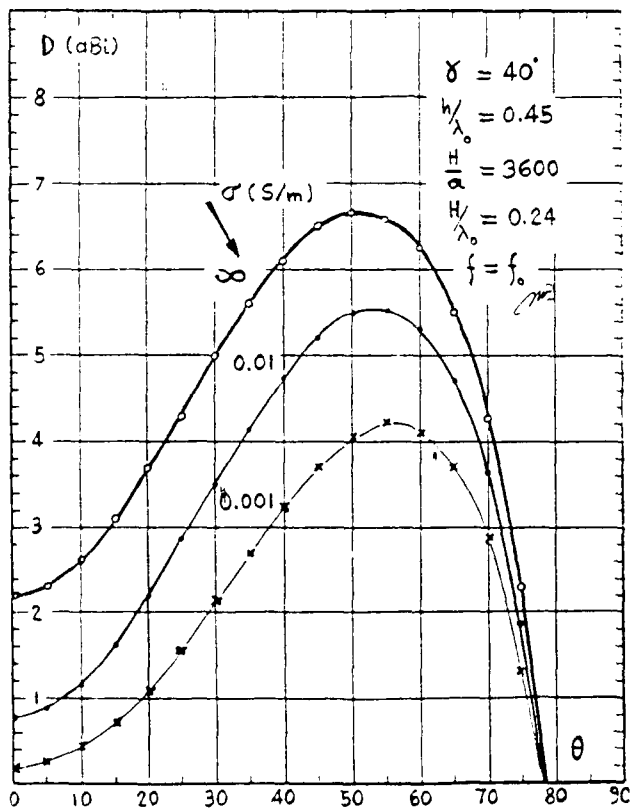
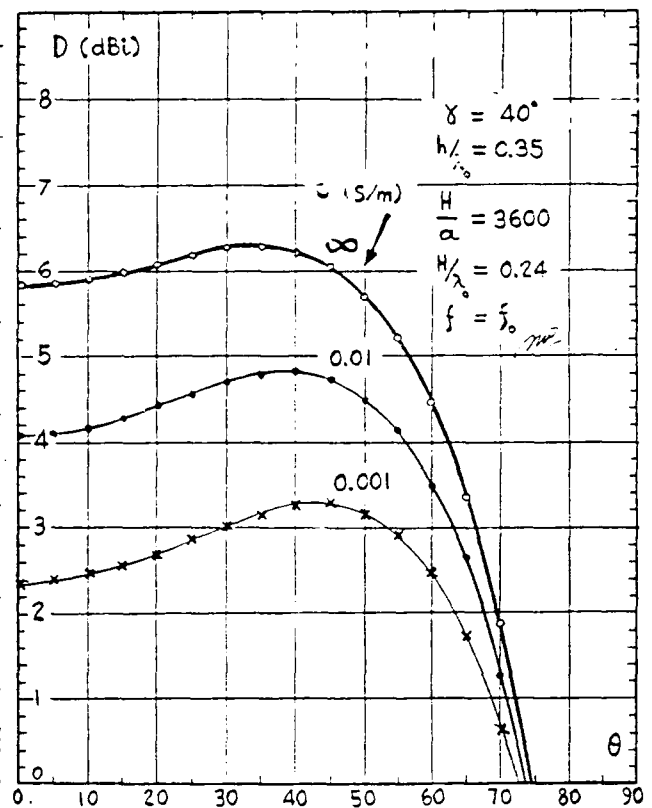
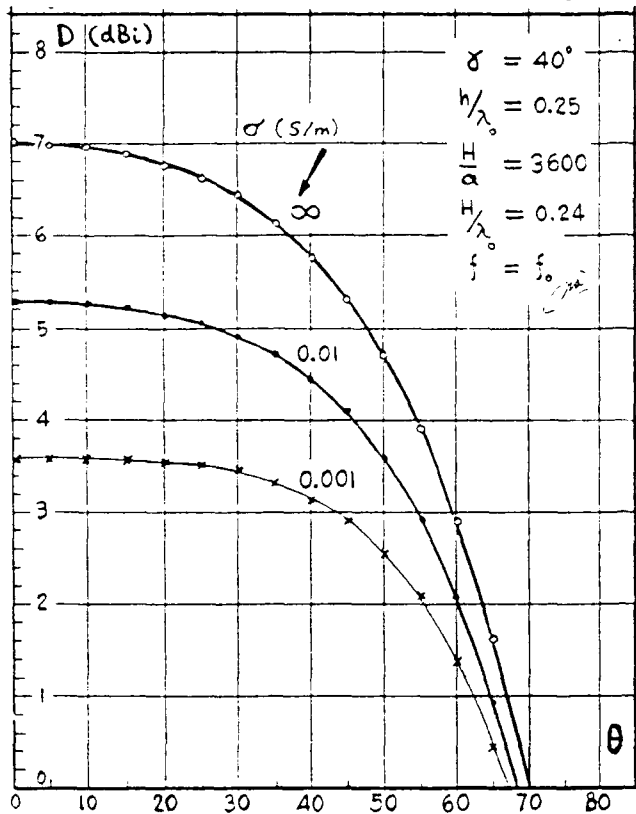


Figure 13. Inverted "V" dipole directivity as a function of " θ " angle and soil conductivity in siemens/m

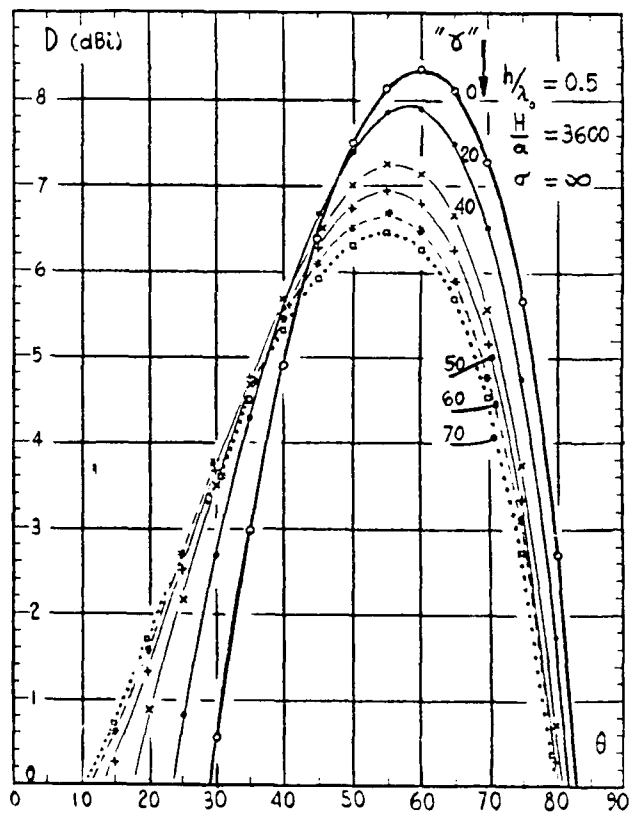
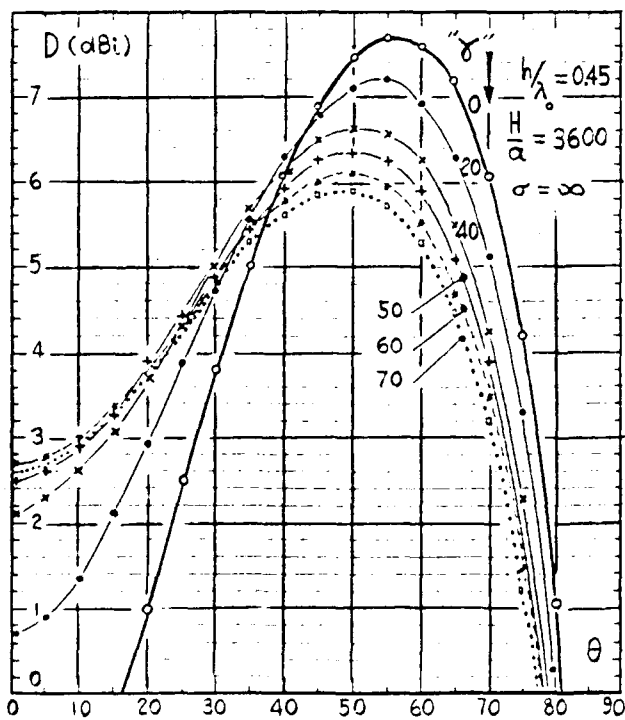
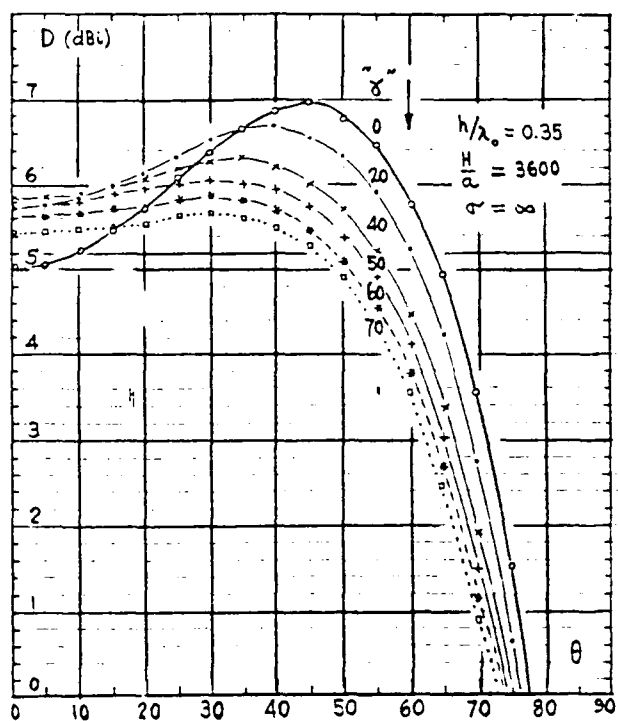
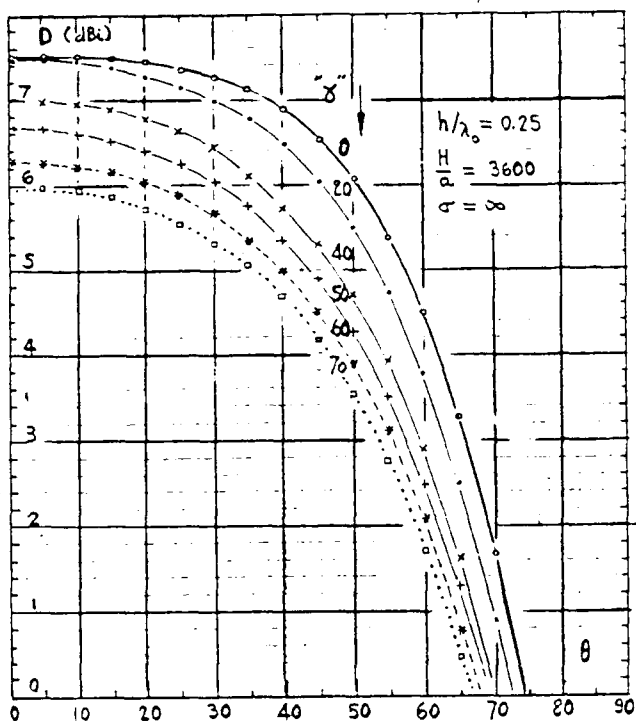


Figure 14. " δ " angle effect on inverted "V" dipole radiation pattern and directivity.

COMPACT HIGHLY INTEGRATED DUAL LINEAR ANTENNA FEED

Joseph A. Smolko

Daniel M. Earley

Daniel J. Lawrence

Michael J. Virostko

Raytheon Company

Missile Systems Division

Tewksbury, MA 01876-0901

Abstract

Active array antenna feed designs are facing increasingly severe design requirements. Microwave distribution networks are used to feed active element T/R modules in a prescribed fashion. A row/column architecture is often chosen to facilitate module cooling system design. This necessitates the need for multi-function linear feed assemblies. Typically these feeds require low-sidelobe receive sum and difference illuminations, along with a separate uniform transmit illumination in the interest of module efficiency. Perhaps the most stringent requirement is that the feed has to be extremely compact, not only in profile, but also in depth. A Compact Highly Integrated Dual Linear Antenna Feed was recently developed that meets all these contrasting requirements.

1. Introduction

This antenna feed, shown in Figure 1, provides independent transmit, receive sum and receive difference functions in an extremely compact design. The network is made compact primarily by taking advantage of a series architecture to reduce overall depth and by using specially designed feed-thru transitions so that the microwave signal can be routed vertically in addition to being routed

only horizontally as in conventional layouts. This particular design uses plug-in connectors to feed 10 T/R modules mounted on a coldplate cooling assembly. The feed has three channel interfaces (Transmit, Receive Sum, and Receive Difference) and 20 array interfaces (10 Transmit, 10 Receive) as illustrated in Figure 2. The feed architecture employs a separate 2:10 center-fed series receive feed and a 1:10 end-fed series transmit feed integrated into a single assembly with inputs and outputs occurring in the same plane. The series nature of the feed reduces the depth of the assembly at the expense of limiting the instantaneous bandwidth. The operating bandwidth exceeds 40 percent and is centered around 8.5 GHz.

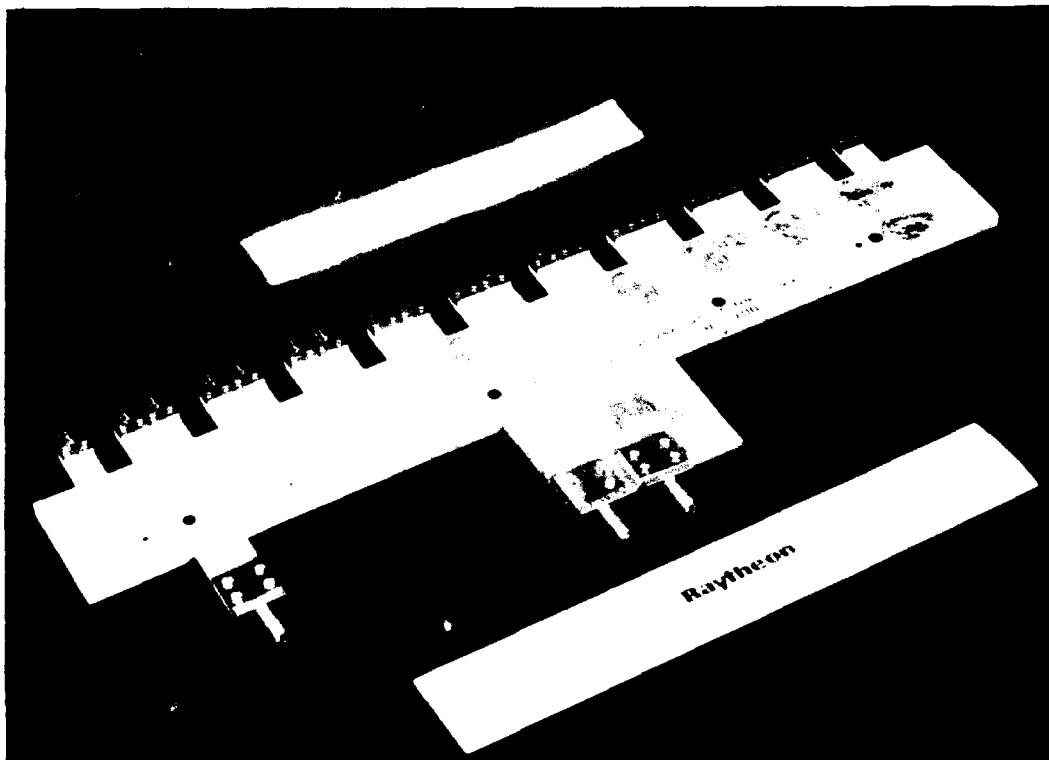


Figure 1. Compact Highly Integrated Dual Linear Antenna Feed

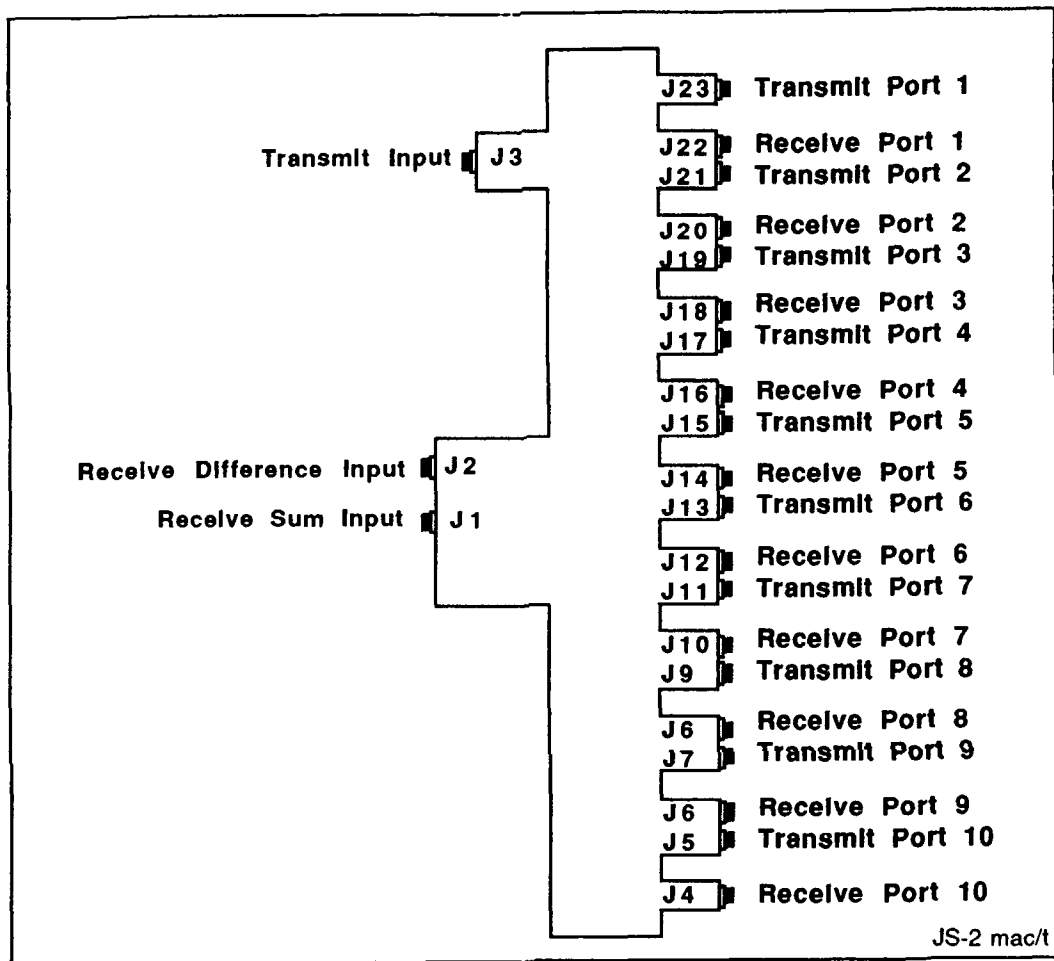


Figure 2. Feed Outline Drawing

2. Feed Architecture

The receive feed employs a center-fed series dual-rail ladder (more specifically Lopez¹) architecture as shown in Figure 3. The sum illumination is a 20 dB linear Taylor (NBAR=3) and the independent simultaneous difference illumination uses a sinusoidal ramp across the central elements to achieve a low-sidelobe difference pattern. In this configuration, the sum illumination appears wholly on the first, or primary rail, while the difference illumination is realized as a linear combination of coupled outputs from the primary and secondary rails. The secondary rail only spans the central elements, as the delta illumina-

tion tracks the sum identically at the outer elements of the array. Error-free predicted patterns for the receive illuminations are shown in Figure 4. The transmit feed utilizes an end-fed uniform series feed architecture as shown in Figure 5.

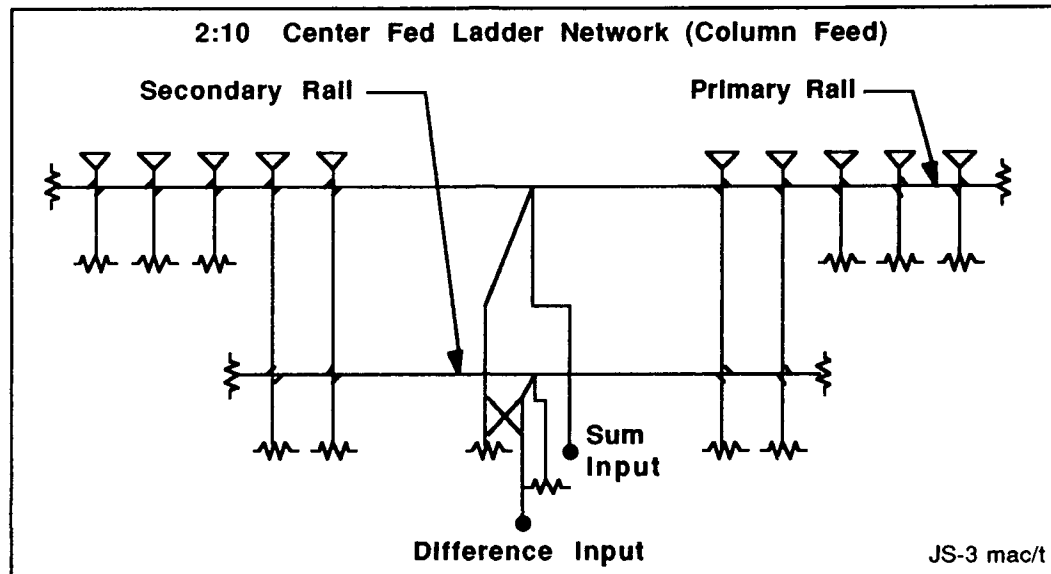


Figure 3. Receive Architecture

Thorough computer models to determine coupler values and interconnecting linelengths for these series feeds were developed under this effort. These models account for the coupler's ideal frequency characteristic and the frequency-dependent dissipative loss in the structure. The programs ultimately design the feed network and predict performance and errors as a function of frequency. These tools proved to be quite accurate as measured data on the completed feeds correlated well with predicted performance.

3. Implementation

Both transmit and receive feeds are implemented in a 0.067 in. (0.031 - 0.005 - 0.031) offset stripline medium; variable overlap couplers are used to direct energies in the desired fashion. Two of these 0.067 stripline assemblies are

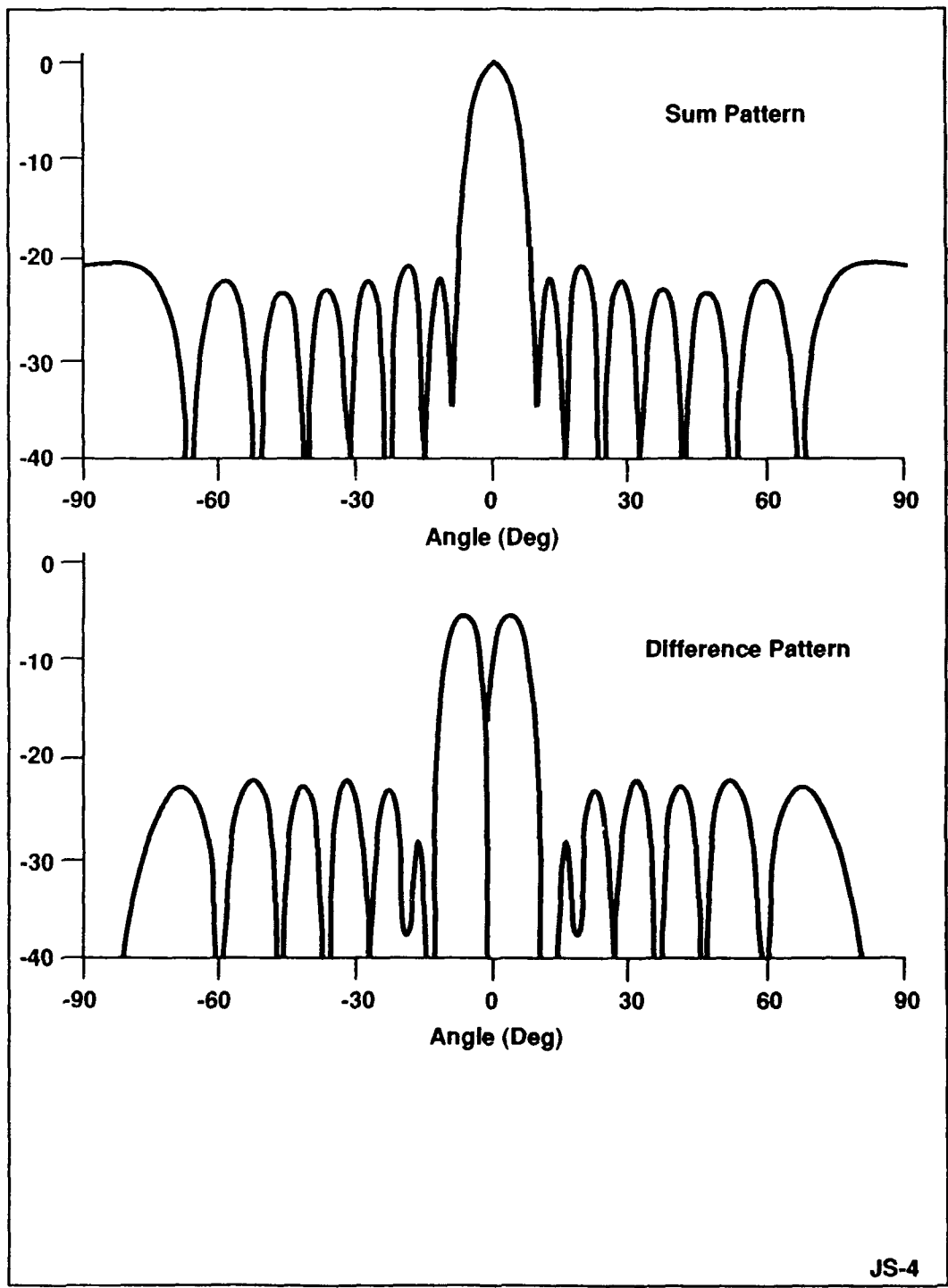


Figure 4. Error-Free Receive Patterns

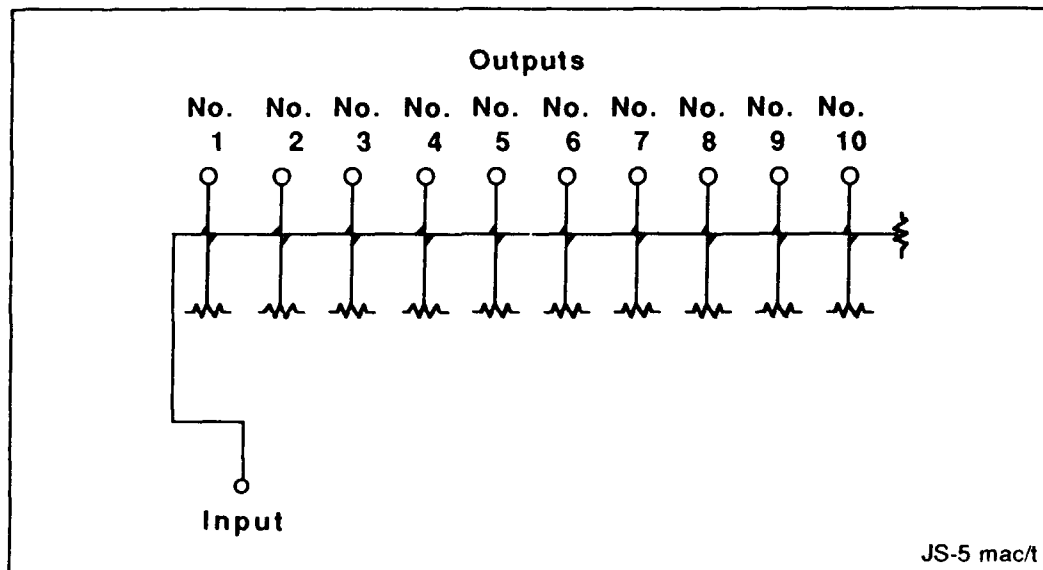


Figure 5. Transmit Architecture

then bonded together to form a single integral structure that includes both functions. The most innovative aspect of the design is that the transmit and receive feeds are not completely segregated each on their own stripline board, rather the microwave energy is routed back and forth between the layers to make the most efficient use of available real estate in a manner similar to that of a multi-layer low frequency printed circuit (PC) board. This "stitching" between layers is made possible by the development of a wideband microwave layer-to-layer ("piggyback") transition that behaves nearly as well as a pure TEM transmission line from 2 to 18 GHz. This inventive device performs the function of transitioning between two stripline boards that are bonded together, one atop the other. The transition is realized through simple sequential drilling and plating operations, which minimizes touch labor while maximizing producibility. A total of 13 of these transitions have been employed on the integrated feed assembly. The "piggyback" transition and measured VSWR on an isolated test piece are shown in Figure 6.

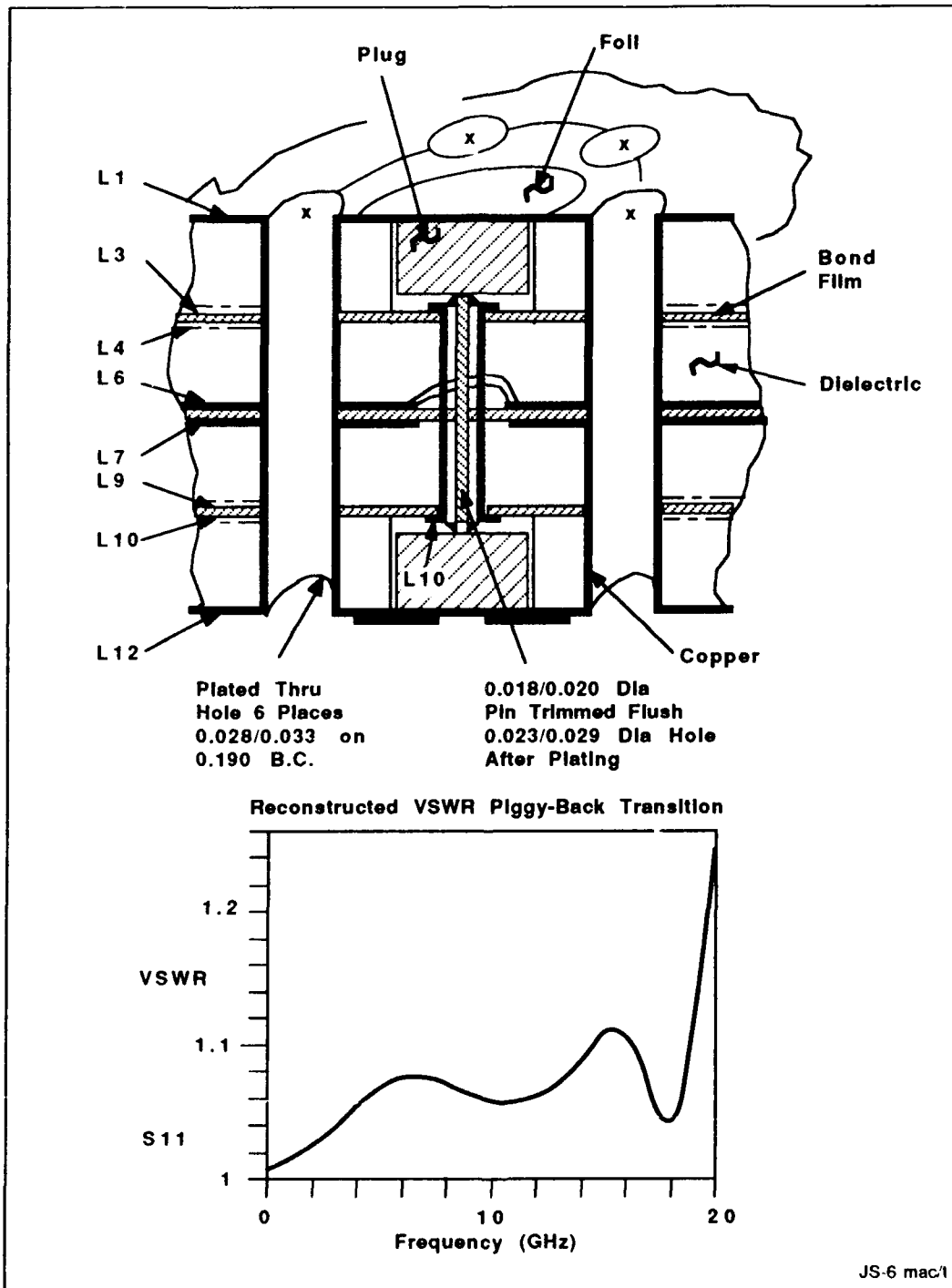


Figure 6. Feed Thru "Piggy-Back" Transition

Another component which is key to this feed network is the wideband, multi-section 180 degree hybrid used to realize the phase difference at the center of the feed. The classic ratrace device has only 10 percent bandwidth which is not adequate for this design. By adding another section to the ratrace, the bandwidth was extended to greater than 40 percent. The printed circuit representation of the hybrid along with its data are shown in Figure 7.

4. Measured Data

Measured data illustrates that the feed exhibits adequate performance over the specified bandwidth for all functions. From 6.5 GHz to 11.5 GHz, the average VSWR of the input and output ports is less than 1.4:1; with a maximum of 2.0:1. Figure 8 illustrates the uniform transmit illumination at 7, 8, 9 and 10 GHz. The progressive droop as frequency increases is due to both the coupler characteristics and the increasing dissipative loss with frequency. Figure 9 is the measured receive illumination also at 7, 8, 9, and 10 GHz; RMS errors across the ports relative to the ideal illumination range from 0.22 dB to 0.55 dB. Finally, Figure 10 shows the magnitude of the difference illumination across the band. This illumination shows more variation, and hence error with frequency, as a line-length dependent phase difference between the primary and secondary rail drives the function synthesis. This effect was predicted before the hardware was built and is deemed to be tolerable, as difference pattern sidelobes are still considerably better than could be realized with a simple phase difference. Overall, the feed provides all the functions required by the design criteria with accuracy that is suitable for feeding an active array of modules with additional amplitude and phase adjustment available. The design is not suited to passive arrays however, where extremely small errors are required to maintain sidelobe performance.

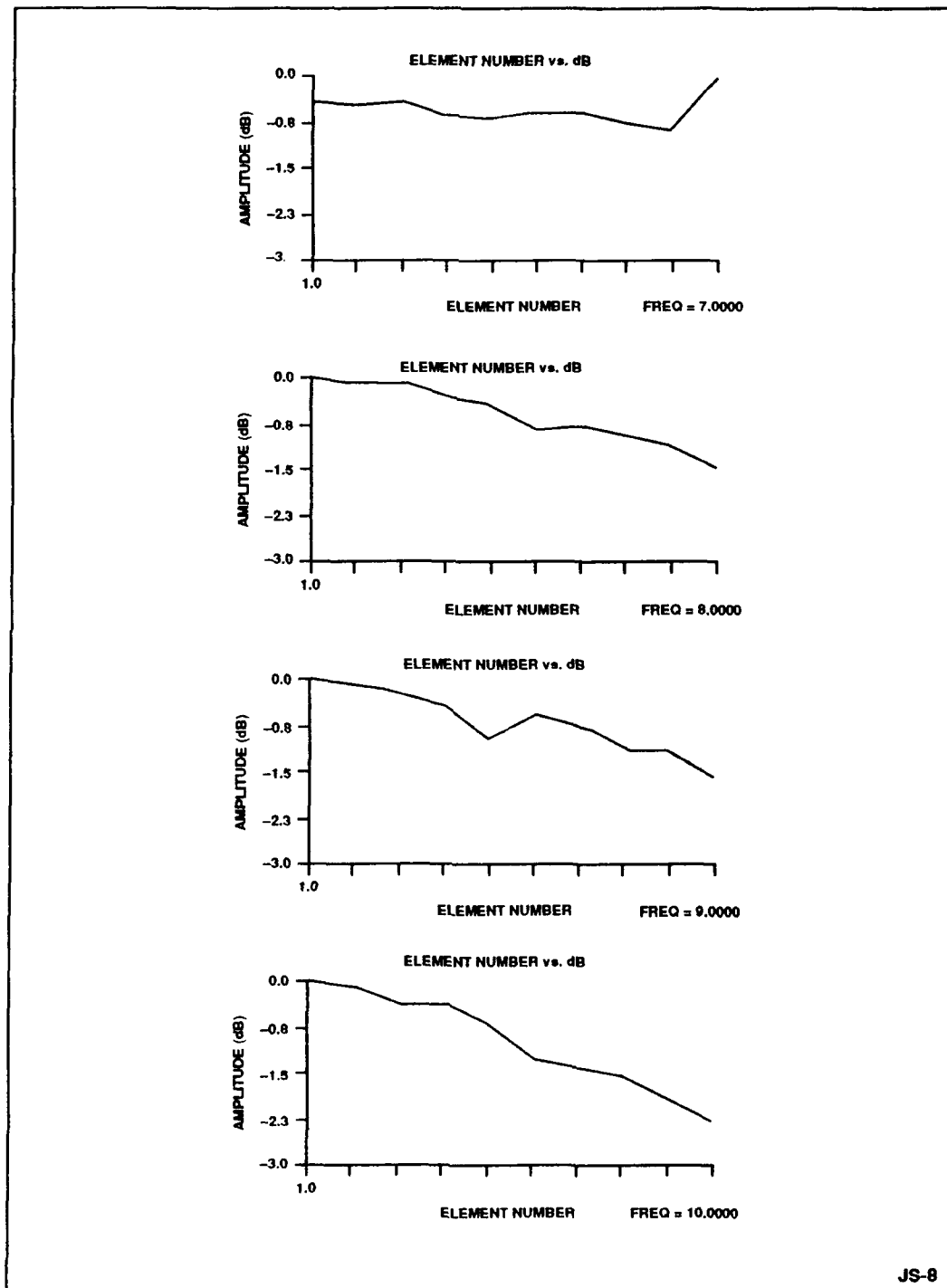


Figure 8. Measured Transmit Illumination

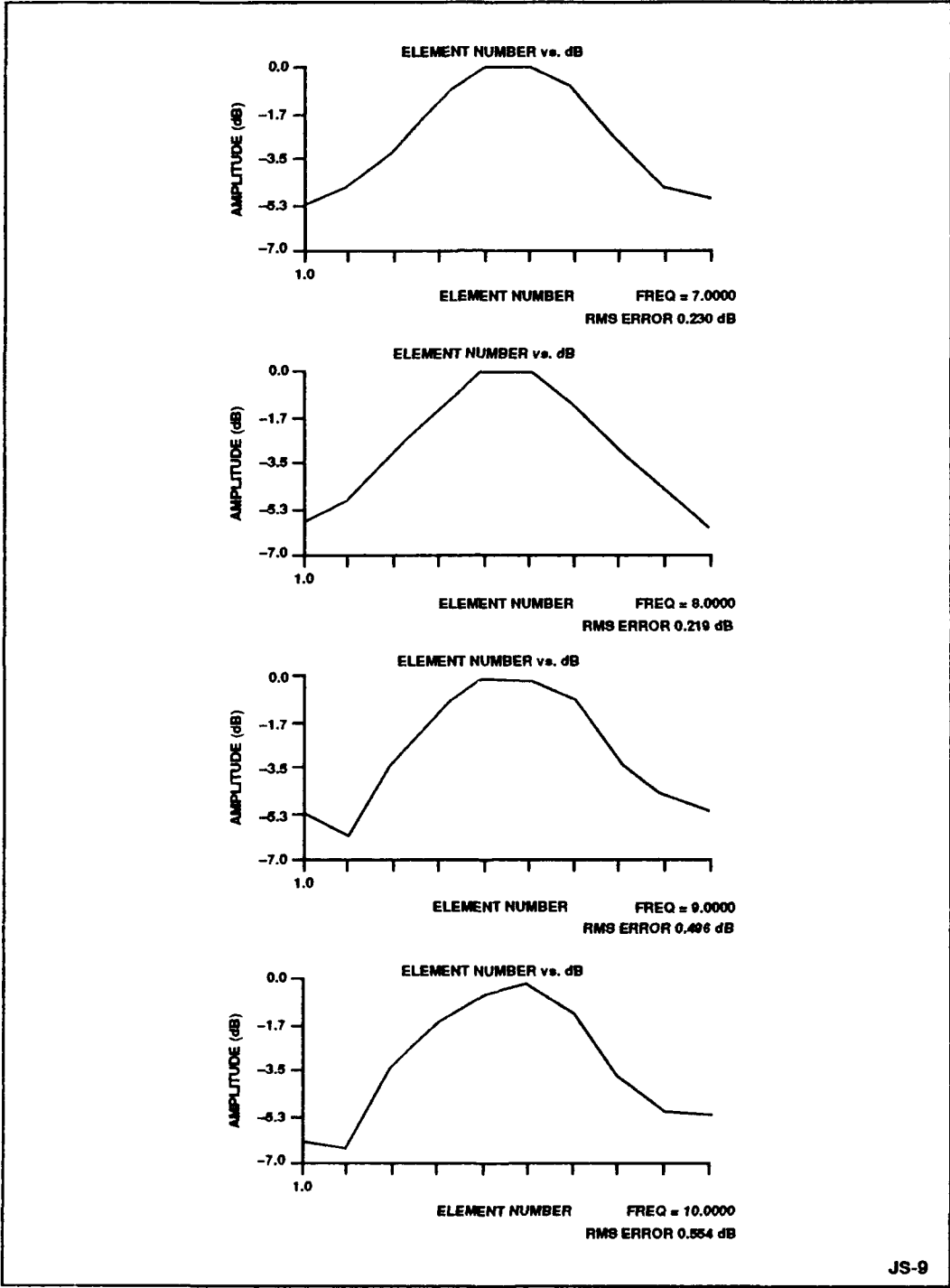


Figure 9. Measured Receive Sum Illumination

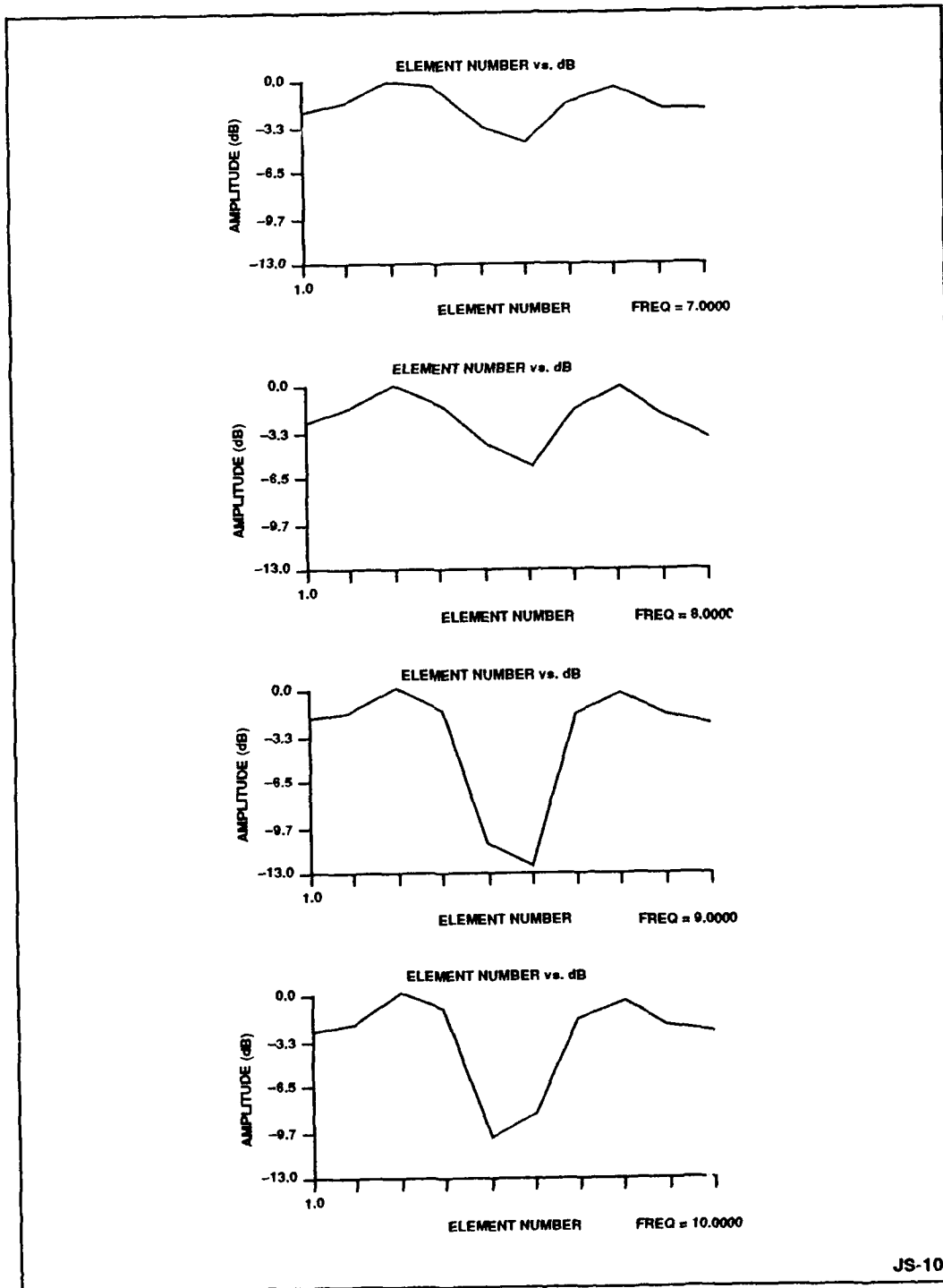


Figure 10. Measured Receive Delta Illumination

5. Conclusion

The novelty of the Compact Highly Integrated Dual Linear Antenna Feed is simply the extremely aggressive packaging of the distribution circuitry. The dense packaging is made possible primarily by the "piggyback" feed-thru design, and also by careful attention to detail in the multi-layer board layout and specially designed components. Figure 11 shows that, to achieve the desired functions, the assembly incorporates 24 variable overlap couplers, two 180 deg hybrids, one split-tee power divider, 27 resistive terminations, 13 piggy-back feed-thrus, and 23 input/output connectors into a package approximately 10 in. long x 3 in. deep x 0.150 in. thick. This package is thin enough to fit onto coldplates between columns of tightly spaced radiating elements and shallow enough so that it does not significantly degrade array depth. Although this feed was designed specifically for a small demonstration array, further work has recently been done which indicates that longer feeds (up to 40 elements), needed for full-sized arrays, are feasible with minor changes in the architecture. Feed designs of this type have potentially great utility for use in a variety of active array applications where multi-functionality is required but space is at a premium.

References

1. Lopez, Alfred, R., *Monopulse Networks for Series Feeding an Array Antenna*, T-AP, July 1968, p 436.

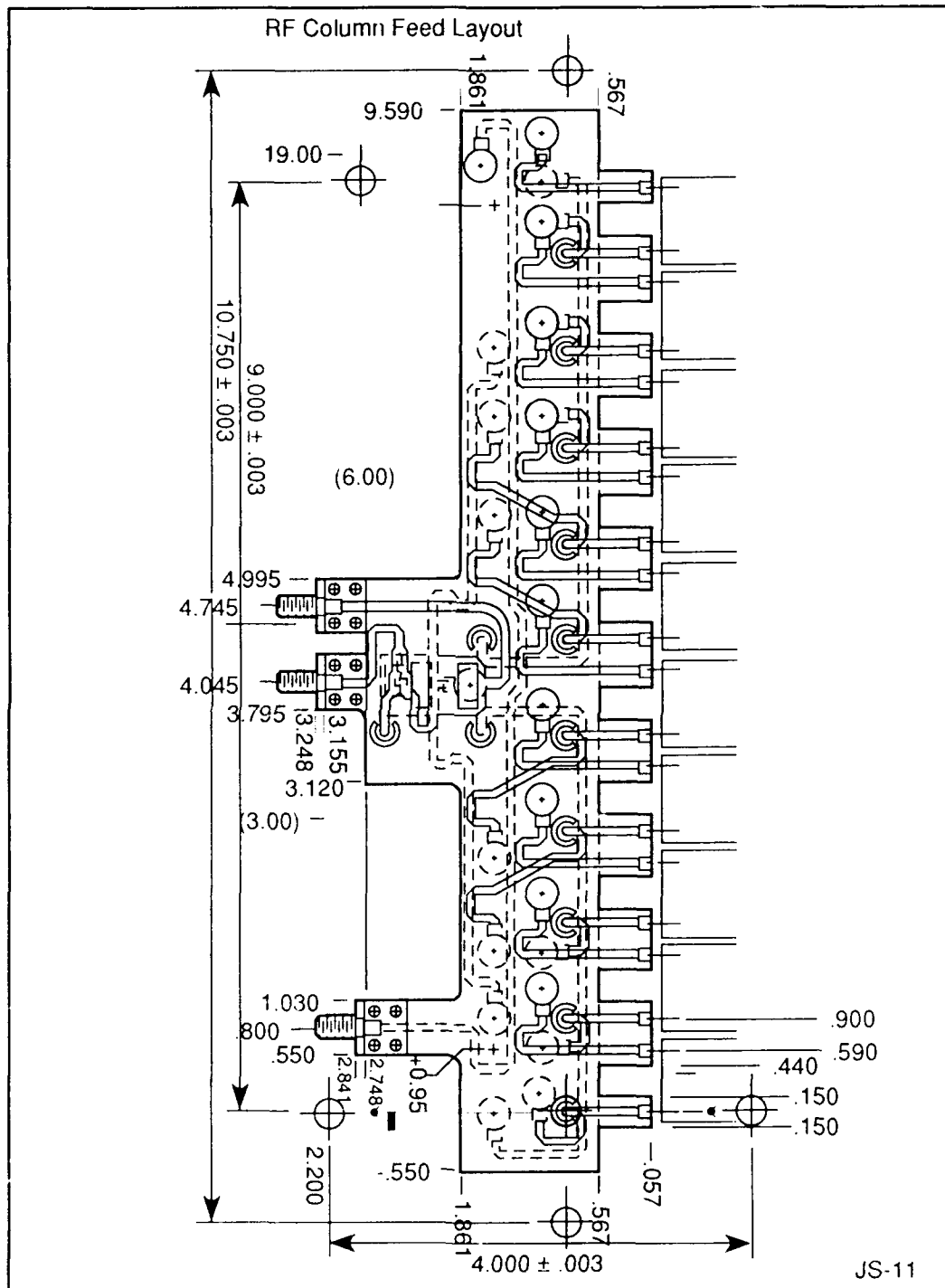


Figure 11. Feed Layout

SHAPED BEAM DESIGN WITH A LIMITED SIZED APERTURE

F. Rahman

Telesat Canada, Ottawa, Ontario, Canada.

INTRODUCTION

For satellite systems it is often necessary to plan the antenna coverage such that the satellite power distribution over the service area corresponds to that dictated by communications traffic and at the same time the spill over to the adjacent area where frequency and orbit is to be coordinated is minimal. In order to achieve these requirements shaped beam antennas are utilised. The most commonly used method of beam shaping in a satellite is to utilise an oversized reflector and illuminate it with an optimally excited feed elements. In its basic form each feed produces a circular elemental beam and the shaped beam is then produced through fitting of these circles to the service coverage area as seen from the satellite. Unfortunately, in most cases the service coverage areas are of irregular shapes. Therefore, the smaller the elemental beam the better is the beam shaping. Obviously, a smaller elemental beam demands a larger reflector size. For satellites the coverage is specified such that the compliance can be made with a reflector size that is compatible with satellite bus and launch vehicle constraints without significantly increasing the overall mass, cost and complexity. A design example for beam shaping under a situation where the reflector size is restricted by physical and economical limitations (as has been used for Anik E system definition) is presented.

REFLECTOR AND FEED ARRAY DESIGN

As stated previously, beam shaping is achieved by combining the elemental beams appropriately such that the composite beam becomes close to the desired service area as viewed from the satellite. An optimum reflector size is that

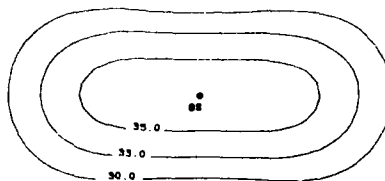
when a further increase in size would not improve the antenna performance by any appreciable amount because the gain area product [1] at the edge of coverage approaches the physical limit associated with the beam size and beam efficiency [2]. For a cost effective design of Anik E satellites the physical limitations imposed constraints on the maximum size of reflector which is far short of optimum size required for an efficient beam shaping. Under these circumstances a partial beam shaping can be obtained by an optimised phase distribution between feed elements. Such a beam however, do not correspond to maximised edge of coverage gain as can be achieved with the optimised larger reflector. But with proper design it can produce a gain close to above and best of all it generates a shaped beam matched to the coverage with minimal spillover to adjacent areas and a gain distribution close to that demanded by the traffic. The requirement on Anik E was a higher gain at the two coasts of U.S.A. and a minimal radiation to areas adjacent to Mexico for the purpose of frequency and orbital coordinations. A fully shaped beam with the above requirement demands a reflector size in the order of 1.5m to 2m. Such a shaped beam design although would produce a higher edge of coverage with a good gain distribution over the coverage area, was not feasible on Anik E since the satellite had to carry two other larger (2m) antennas for its prime coverage requirements.

The analysis uses physical optics aperture integration method [3]. The principle used is that when two adjacent elemental beams are combined in phase at feed array the composite beam becomes an ellipse. The shape of composite beam gradually changes to figure eight as the phase differential is increased from zero. As can be seen from the illustrations of Figure 1, the gain reduction is phase dependent. The gain at the edge of coverage is not reduced appreciable a phase differencial of upto 60 degrees. For phase difference above 60 degrees

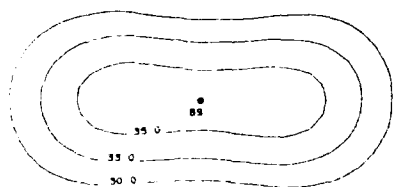
gain starts dropping significantly until the design becomes too inefficient. By a suitable algorithm a combination of amplitude and phase between multiple feed elements could be optimised so as to produce a shaped beam with a limited sized reflector without significantly compromising the performance. Maximum physical size available for Anik E was only 1m which is less than two third the optimum size for a gain maximized design. Figure 2 shows the performance that could be achieved with an edge of coverage gain maximized design using a 1.8m reflector with equiphase feed elements. A corresponding gain maximized design with 1m reflector is shown at Figure 3. As can be seen this does not provide the beam shaping requirements. A design example with phase adjustments is shown at Figure 4. The antenna geometry together with feed element phase and amplitude excitation coefficients are illustrated at Figure 5. This design was used as the basis for Anik E system definition and a contract was awarded for construction of two spacecrafts. The contractor provided the final design and a performance close to above was achieved [4]. The first Anik E will be launched in March 1991 and the antennas have been successfully tested and integrated.

REFERENCES :

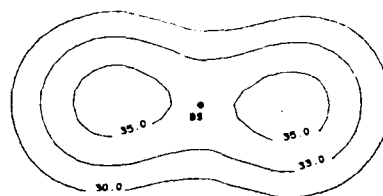
- [1] Stegen, R. : "The Gain Beamwidth Product of an Antenna", IEEE Trans. on Antennas and Propagations, Vol. AP-12, 1964, p. 505-508.
- [2] Rahman, F. : "Performance Evaluation of Spacecraft Antennas from Gain Contours", URSI Int. Symp. on E M Theory, August 25-29, 1986, Budapest, Hungary
- [3] Rudge, A.W., Adataia, A.N. : "Offset Parabolic Reflector Antennas - A Review", Proc. IEEE, Dec. 1978 p.1592-1618.
- [4] Whitehouse, R.C. : "Anik E Antenna Farm", 1989 IEEE International Symposium on Antennas and Propagation, p.503-506.



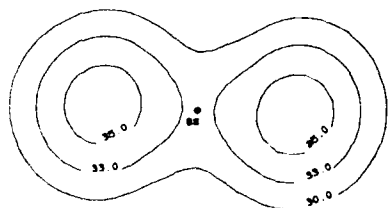
RELATIVE PHASE BETWEEN THE TWO HORNS = 0



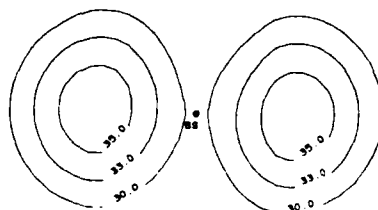
RELATIVE PHASE BETWEEN THE TWO HORNS = 30deg.



RELATIVE PHASE BETWEEN THE TWO HORNS = 60deg.



RELATIVE PHASE BETWEEN THE TWO HORNS = 90deg.



RELATIVE PHASE BETWEEN THE TWO HORNS = 120deg.

Figure 1 : An Illustrations of Impact of Phases On Gain Contours (Two Horn Case).

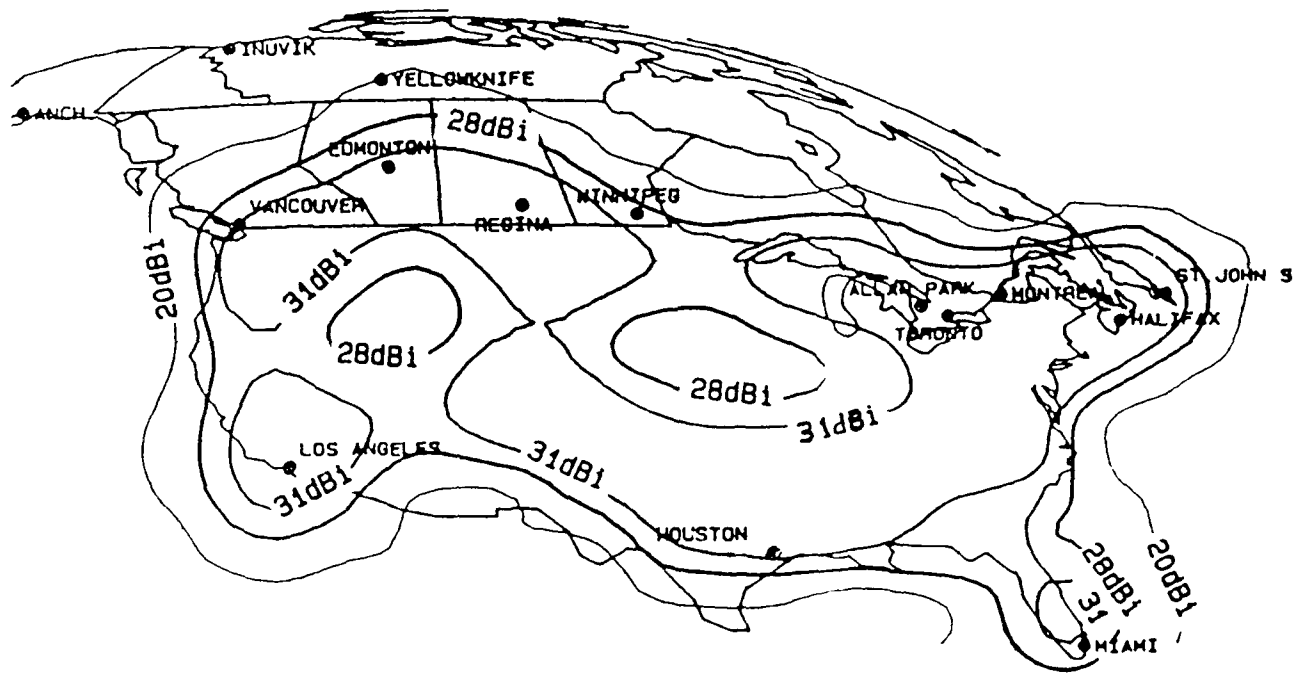


Figure 2 : Shaped Beam Coverage Performance Using a Full (1.8m) Sized Aperture.

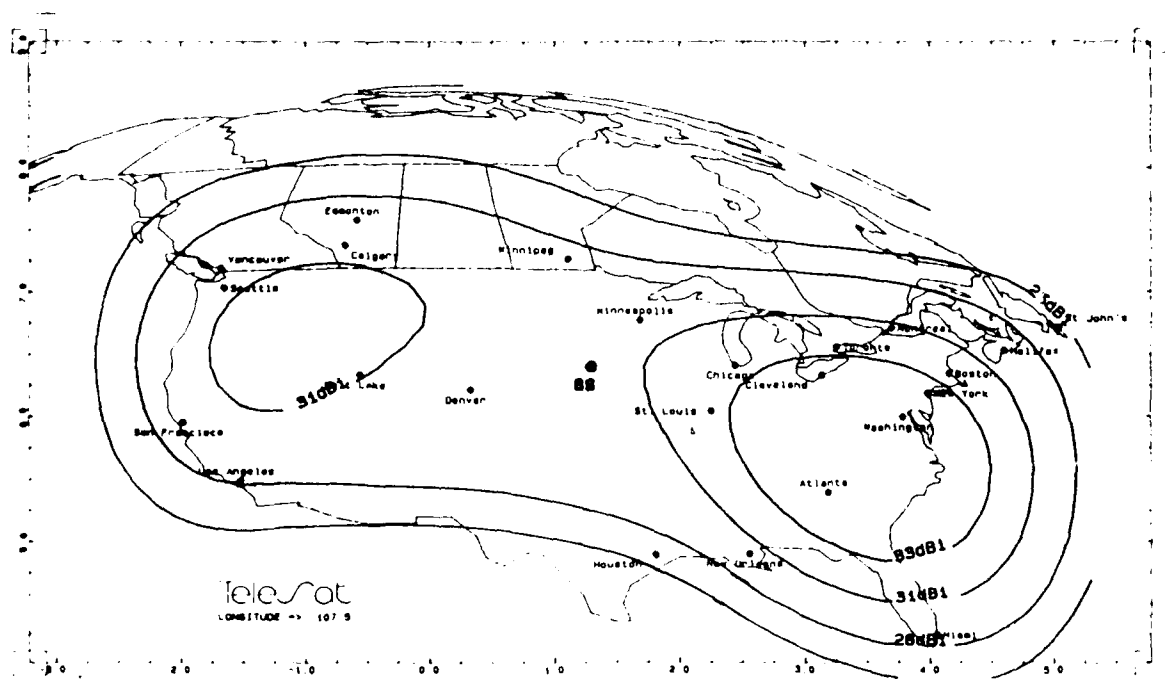


Figure 3: Coverage with Gain Maximized Design Using a 1m Diameter Reflector.

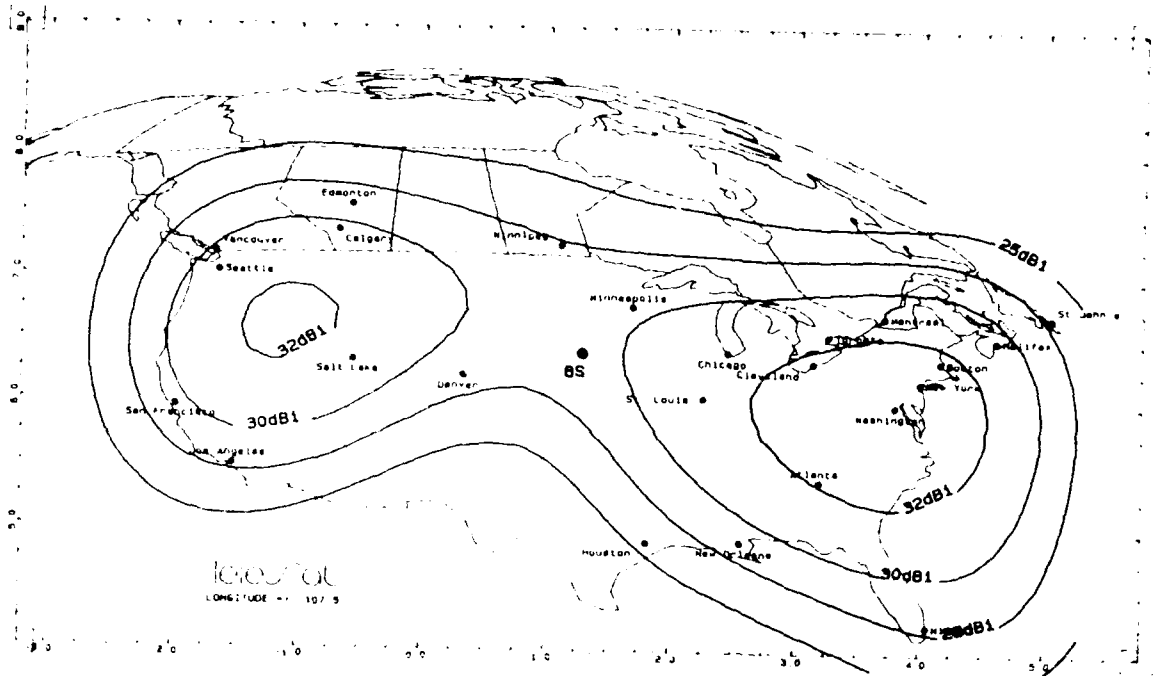


Figure 4: Shaped Beam Coverage Performance with the Limited Sized Reflector Design

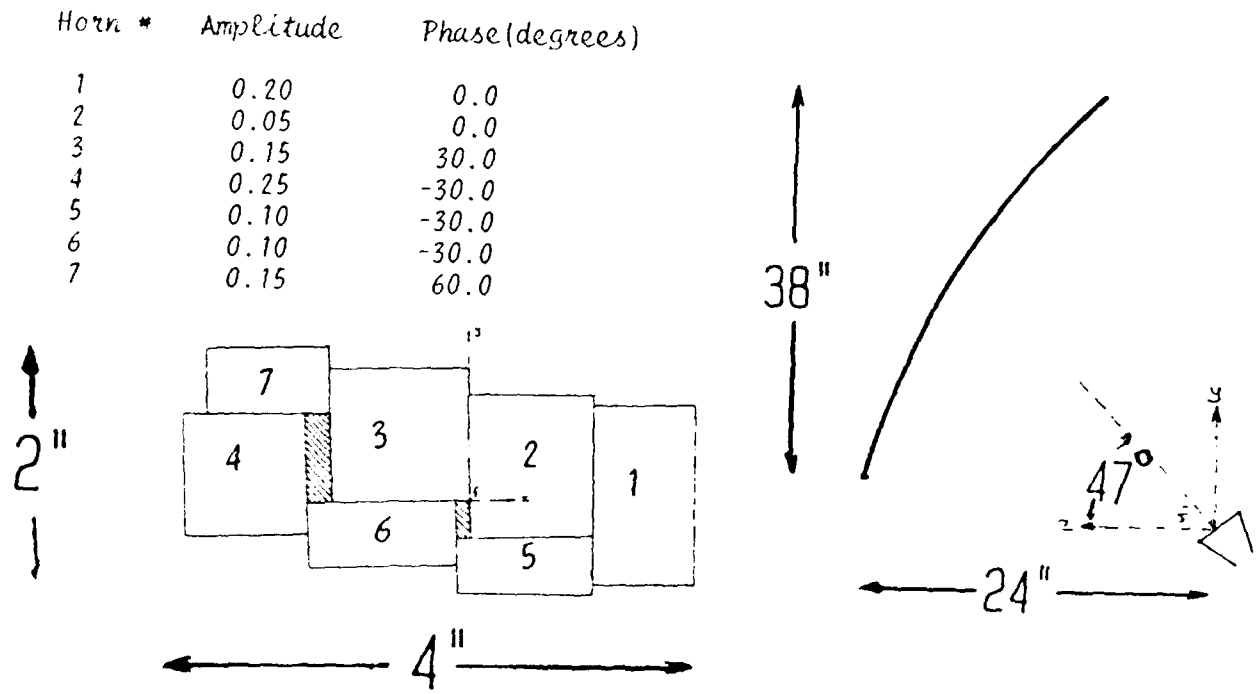


Figure 5: Reflector Configuration and Feed Layout for the Anik E Conceptual Design

ADAPTIVE ALGORITHMS FOR ENERGY DENSITY ANTENNAS IN SCATTERING ENVIRONMENTS

James P. Phillips Motorola
Dr. Donald Ucci Illinois Institute of Technology

ABSTRACT

Energy density antennas (EDA) provide independent outputs for the E-field and the H-field energy and have been described by Dr. William C.Y. Lee and others. These independent outputs can be selected or combined to enhance or diminish the strength of the scattered signal. In the scatter environment, the characteristics of the fields change so rapidly that even LMS methods of adaptation impose an impractical computational burden. The maximal-ratio combiner can optimally combine the signals but is hardware intensive. The use of sub-optimal adaptive algorithms reduces the computational burden and hardware complexity to an economical level and the algorithm can then be implemented with simple micro-controllers. The methods described here are based on a finite state machine. The hardware that is simulated and tested has 64 states created by four quadrature-phase shifters that process the signals from the energy density antenna. Algorithms which require memory are examined and compared to conventional algorithms. Algorithms with memory will find and attempt to track chaotic limit cycles. Adaptive antennas using these algorithms benefit in environments where there are a few major scatterers. As the number of scatterers increases, the limit cycles become too chaotic and convergence is not possible.

1.0 ANTENNA STRUCTURE

The energy density antenna [1] consists of four conductors arranged in loops or pairs of loops that can be connected in sum and difference modes to extract energy from both the electric and the magnetic field as shown in Fig 1. This antenna shows advantage in multipath propagation [2] such as mobile radio in which the receiving antenna is moving among many reflectors of the signal. In this environment, the plane-wave, relationship between the electric and magnetic fields is not valid. With these many sources, the electric and the magnetic field components from each add vectorially and produce independent random variables [3]. These random variables are functions of the antenna location (X,Y), a

random variable. If only the vertical E -field polarization, E_z , is considered, then the associated H -field consists of H_x , and H_y .

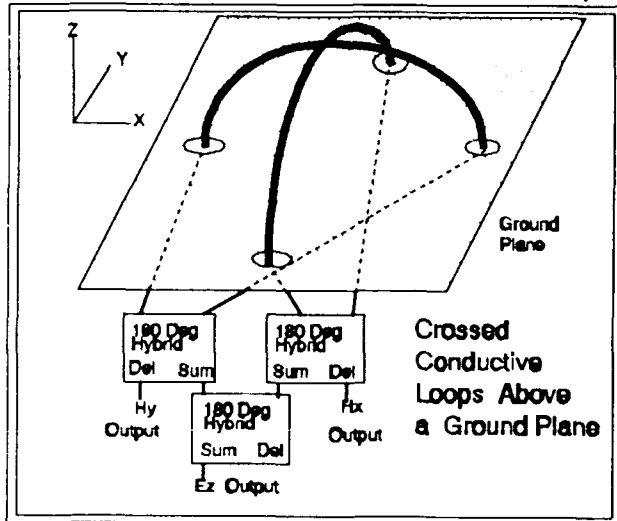


Figure 1. Energy Density Antenna.

These three fields, E_z , H_x , and H_y , are intercepted by the antenna structure and produce three outputs V_{Ez} , V_{Hx} , and V_{Hy} . A small loop in the x - z plane (Fig. 1) has a response pattern

$$|V_{Hy}| = K \cos \phi \quad (1)$$

$$|V_{Hy}|^2 = K^2 \cos^2 \phi \quad (2)$$

A similar loop in the y - z plane has a response pattern

$$|V_{Hx}| = K \sin \phi \quad (3)$$

$$|V_{Hx}|^2 = K^2 \sin^2 \phi \quad (4)$$

An Ez field probe has the response independent of angle ϕ as

$$|V_{Ez}| = K \quad (5)$$

$$|V_{Ez}|^2 = K^2 (\sin^2 \phi + \cos^2 \phi) = K^2 (|V_{Hx}|^2 + |V_{Hy}|^2) \quad (6)$$

The output power of the energy density antenna, V_{Ez}^2 , V_{Hx}^2 and V_{Hy}^2 , can be expressed in their quadrature components.

$$\begin{aligned} V_{Ez}^2 &= V_{Ez\text{-real}}^2 + V_{Ez\text{-imag}}^2 \\ V_{Hx}^2 &= V_{Hx\text{-real}}^2 + V_{Hx\text{-imag}}^2 \\ V_{Hy}^2 &= V_{Hy\text{-real}}^2 + V_{Hy\text{-imag}}^2 \end{aligned} \quad (7)$$

Each of the six quadrature voltages can be expressed as the sum or difference of the random variables, $S_{n,r}(X,Y)$ or $S_{n,i}(X,Y)$. This is accomplished using the weighting functions in Table 1 on the sources in the environment.

$$S_{n,r}(X,Y) = \sum_{j=1}^N W_n(\phi) \operatorname{Re}[\text{Source}_j] \quad (8a)$$

$$S_{n,i}(X,Y) = \sum_{j=1}^N W_n(\phi) \operatorname{Im}[\text{Source}_j] \quad (8b)$$

$n = 1,2,3,4$ $r = \text{real}$ $i = \text{imaginary}$

$W_n(\rho) = \text{Weighting Functions shown in Table 1}$

$\text{Source}_j = \text{scattering signal from source } j \text{ of } N$

The voltages can therefore be expressed as:

$$V_{Ez,r} = S_{1,r} + S_{2,r} - S_{3,r} - S_{4,r} \quad V_{Ez,i} = S_{1,i} + S_{2,i} - S_{3,i} - S_{4,i} \quad (9a)$$

$$V_{Hx,r} = S_{1,r} + S_{3,r} \quad V_{Hx,i} = S_{1,i} + S_{3,i} \quad (9b)$$

$$V_{Hy,r} = S_{2,r} + S_{4,r} \quad V_{Hy,i} = S_{2,i} + S_{4,i} \quad (9c)$$

$W_n(\phi)$	Range
$W_1(\phi) = \cos \phi$	for $-\pi/2 \leq \phi \leq \pi/2$ and 0 elsewhere
$W_2(\phi) = \sin \phi$	for $0 \leq \phi \leq \pi$ and 0 elsewhere
$W_3(\phi) = \cos \phi$	for $\pi/2 \leq \phi \leq 3\pi/2$ and 0 elsewhere
$W_4(\phi) = \sin \phi$	for $\pi \leq \phi \leq 2\pi$ and 0 elsewhere

Table 1. Weighting functions for Sources.

The probability density function (PDF), $f_{S_{n,r|i}}(S_{n,r|i})$, of each random variable, $S_{n,r|i}[X,Y]$, is Gaussian for an infinite number of reflectors [3]. However, for a small number of sources, the PDF can be approximated by a truncated Gaussian. In the limit of truncation, the PDF for each of the random variables, $S_{n,r|i}$, becomes uniform [4]. Thus, the quadrature components of $V_{Ez,r|i}$ are the sum of four RV's with uniform distribution. The PDF of $V_{Ez,r|i}$ is the convolution of four uniformly distributed RV's. It resembles the Gaussian as shown in Fig 2. The PDF of $V_{Hj,r|i}$, the sum of two uniformly distributed random variables, is triangular and yet still closely approximates Gaussian. This assumption conforms to measured data and conventional models [3]. The cumulative distribution function (CDF) of $|V_{Hj}|$ departs from the Rayleigh distribution by a maximum

of 0.56 Decibels (dB) as shown in Fig 3. The distribution of $|V_{Ez}|$ departs by 0.16 dB. This is well within the experimental error of propagation measurements. The correlation coefficient of the power envelopes $\{\rho_{P\alpha, P\beta}, \text{ where } P\alpha, P\beta = |E_z|^2, |H_x|^2, |H_y|^2\}$ of the three outputs from the energy density antenna determines the benefit of selecting or combining these together to avoid nulls in a fading environment [2].

$\rho_{Hx2, Hy2} = 0$ as seen by the orthogonality of the crossed loops. $\rho_{Ez2, Hk2}$ ($k=x, y$) is determined by the PDF of $f_{S_{n,r}|i}(S_{n,r}|i)$ and therefore the truncation point of the Gaussian PDF.

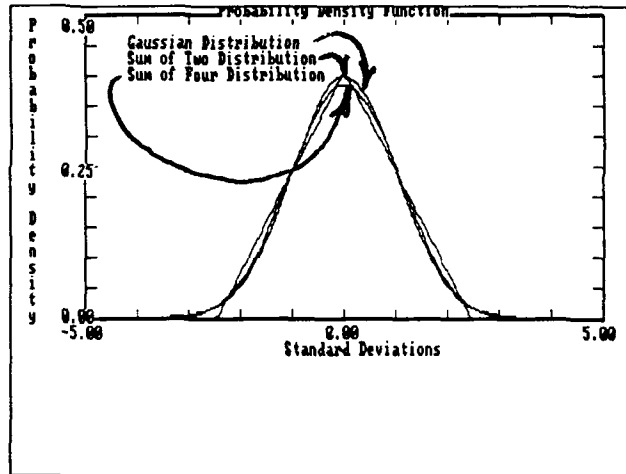


Figure 2. PDF's of Signals.

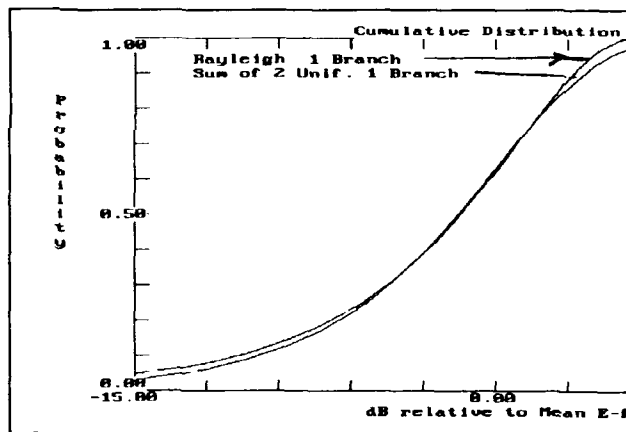


Figure 3. Rayleigh and Hy CDF.

$$\rho_{Ez^2, Hk^2} = \frac{\text{Cov}(V_{Ez}^2, V_{Hk}^2)}{\sqrt{\text{Var}(V_{Ez}^2)\text{Var}(V_{Hk}^2)}} \quad \text{where: } H_k = H_x \text{ or } H_y \quad (10)$$

The correlation coefficient is a function of the second and fourth moment of the components $S_{n,r|i}$ as shown below.

$$\rho_{V_{Ez}, V_{Hk}}^2 = \frac{E[S_{n,r|i}^4] - 3E[S_{n,r|i}^2]^2}{\sqrt{(E[S_{n,r|i}^4] + 5E[S_{n,r|i}^2]^2)(2E[S_{n,r|i}^4] + 2E[S_{n,r|i}^2]^2)}} \quad (11)$$

The correlation coefficient versus the truncation of the Gaussian PDF is shown in Table 2.

Truncate @ \pm Std. Dev.	Correlation $\rho_{Ez, Hk}^2$ for Sources	
	In all 4 sectors	In only 2 sectors
∞	0.0000000	0.0000000
5.0	-0.0000411	-0.0000822
4.0	-0.0017540	-0.0035111
3.0	-0.0221290	-0.0447505
2.5	-0.0505844	-0.1037599
2.0	-0.0901283	-0.1885627
1.5	-0.1316281	-0.2811517
1.0	-0.1657003	-0.3599927
0.5	-0.1871468	-0.4109525
Δ Unif	-0.1944611	-0.4285714

Table 2. Correlation Coefficient vs. the PDF of the $S_{n,r|i}$ Components.

The uniform PDF for the components, $S_{n,r|i}$, produces a correlation coefficient of -0.194 and thus offers greater diversity benefit than 3 independent antennas. For selection diversity, this advantage is equivalent to having four independent branches as shown in Fig. 4. If all of the sources are in only two of the four sectors, then the correlation coefficient is -0.428 and the benefit is greater. This advantage is based on the assumption of a uniform PDF for $S_{n,r|i}$.

If the number of reflectors or sources is reduced further to two and they have equal power, then the PDF of $|V_{Ez}|$ or $|V_{Hk}|$ is peaked at the ends and is shown in Fig 5. The envelope correlation coefficient is

$$\rho_{Ez2,Hk2} = -1 \quad (12)$$

With only two sources, the power output is constant. That is:

$$V_{Iz}^2 + V_{Ik}^2 + V_{Ily}^2 = K \quad (13)$$

Thus, for two sources, the energy density antenna lives up to its name and provides constant output power. For three sources, complete adaptation is still possible. In signal environments where there are four or more sources, the energy density antenna cannot avoid nulls [5] and can only adapt to an approximation based on the characteristics of the sources. The limitations of the EDA are due to the number of its available outputs. With only three outputs, the EDA has only two degrees of freedom for control of its response. Thus, the performance of the antenna is very dependent on the signal source environment.

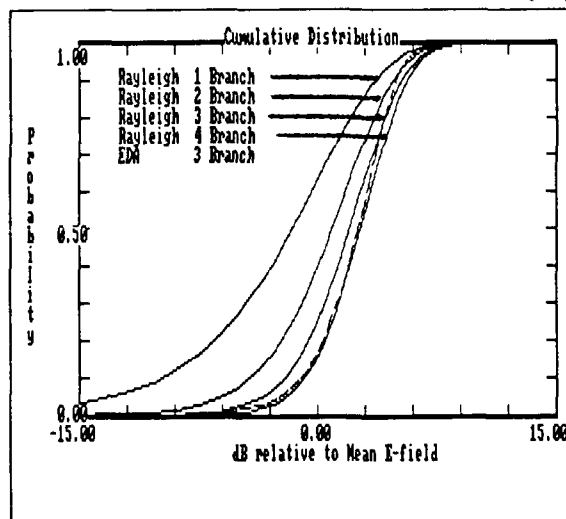


Figure 4. CDF of EDA and 1 - 4 Independent Channel Diversity.

2.0 Signal Source Environments

To quantify the signal environments where a finite number of sources are present, the parameter of source entropy is used. It is defined as

$$E_k = -\sum_1^N p_i \log_2\left(\frac{1}{p_i}\right) \quad (14)$$

where: E_k - Source Entropy
and $p_i = \frac{\text{power of source } i}{\text{Total Power of Sources}}$

This parallels the use of entropy in information theory [6] in that entropy is a measure of the randomness of the system. As the number of sources and the distribution of power among them increases, the entropy increases. How well the energy density antenna will reduce the fading of the signals will be determined by the entropy of the sources.

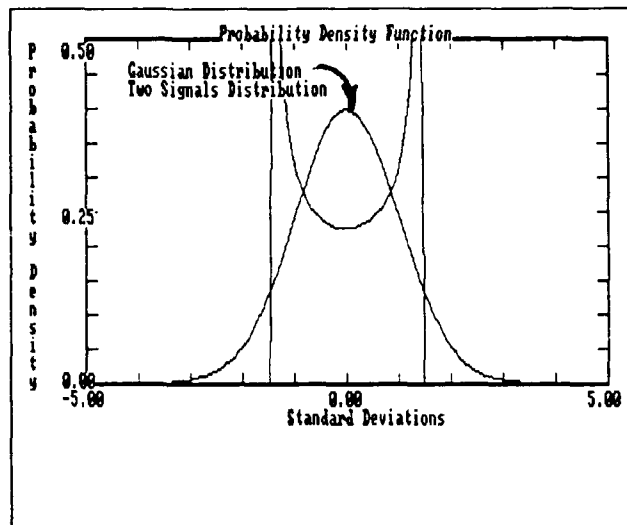


Figure 5. PDF of Two Signals.

For the energy density antenna to adapt to the environment and reduce the fading, a control mechanism needs to be added that can combine the outputs in a constructive manner.

3.0 Antenna Control Hardware

The adaptation of antennas in the multipath environment is very difficult due to the rapid changes in the signal characteristics. Least mean square algorithms (LMS) are too computationally intensive to be practical in the multipath environment [7]. Direct search algorithms are a possibility but require rapid sampling to determine the gradients. A first step to a practical controller is to construct it as a finite state machine.

The antenna combiner as shown in Fig. 6 uses only phase weighting and has steps of $\pi/2$ on each of the four inputs from the antenna. This controller has $2^8 = 256$ unique settings. Because only the relative phase among the four wire outputs (Fig 1.) is significant, there is a redundancy which reduces the number of unique states to $2^8/4 = 64$. This creates one more pair of adjacent states (total of eight) for each state. These additional adjacent states allow more flexibility in a stepped trajectory through state space. The importance of these trajectories will follow.

The 64 states are selected with a one-byte word. The penalty for this simplicity is two-fold. First, there is the lack of amplitude weighting and second, the phase

quantization is very coarse. The lack of amplitude weighting (equal gain combining [2]) sacrifices 0.98 dB of signal relative to an ideal combiner, a pre-detection maximal-ratio combiner [2]. This is calculated by finding the expected value of the square of the difference of two Rayleigh distributed random variables. This assumes that the two signals are co-phased before combining them in a Wilkinson Tee [8].

$$E[v_{\Delta}^2] = \int_0^{\infty} p_{\Delta}(v_{\Delta}) v_{\Delta}^2 dv \quad (15)$$

$$\text{where } v_{\Delta} = |V_1 - V_2| \text{ and } p_i(V_i) = 2e^{-V_i^2} \text{ for } 0 \leq v_i < \infty \\ i=1,2$$

$$E[V_{\Delta}^2] = 0.213 \quad E[V_1^2] = E[V_2^2] = 1$$

$$\text{LOSS} = \frac{E[V_1^2] + E[V_2^2] - E[V_{\Delta}^2]}{E[V_1^2] + E[V_2^2]} \quad (16)$$

$$\text{LOSS} = \frac{1 + 1 - 0.213}{2} = 0.8935 = 0.49 \text{ dB}$$

The four-way combiner consists of two 2-way combiners in series. The total loss is twice 0.49 dB or 0.98 dB.

The coarse quantization of the phase steps, $\pi/2$, also introduces losses of 0.87 dB as shown below.

$$E[v^2] = \int_{\cos(\pi/4)}^{\cos(0)} \frac{4X^2}{\pi \sqrt{1-X^2}} dx = 1 - 0.5 + \frac{1}{\pi} = 0.818 = 0.87 \text{ dB} \quad (17)$$

The analysis assumed that there would be a uniformly distributed phase error of $\pm \pi/4$ for each of the four inputs from the energy density antenna. The total loss is the sum of the loss due to equal gain combining and that due to large phase quantization and is equal to 1.85 dB. This loss has been verified as part of the

system simulation, see Fig. 9, and is described in section 5.0.

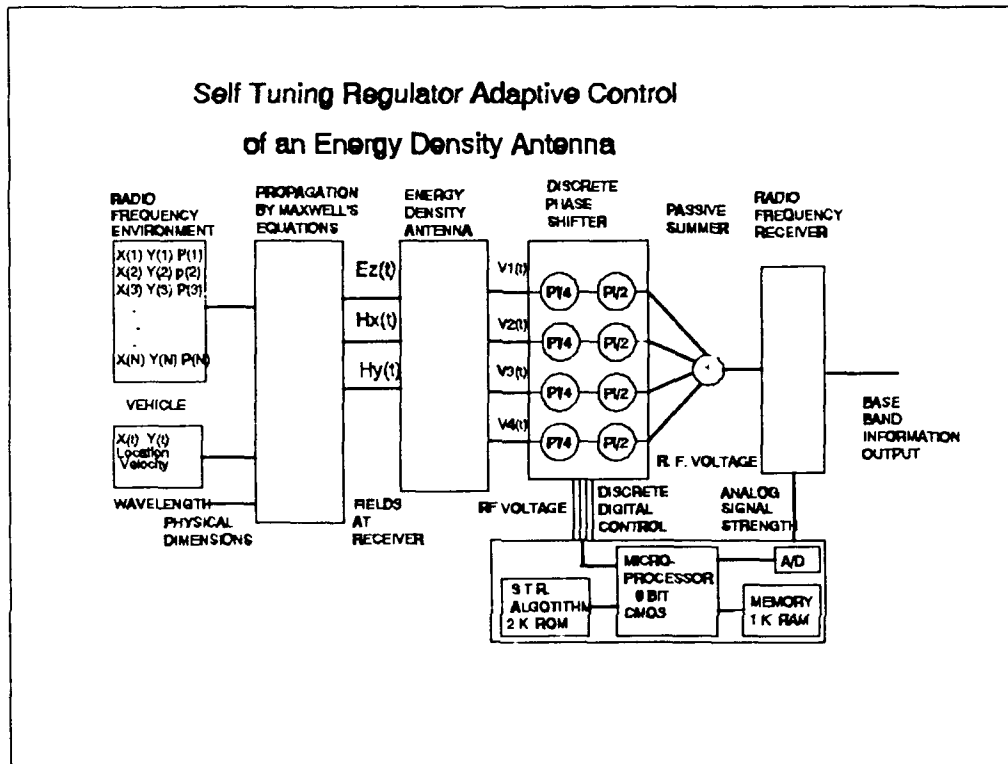


Figure 6. Antenna Controller.

The 64 states of the antenna can be diagrammed in a $4 \times 4 \times 4$ Euclidian state space cell as in Figs. 7 and 8. These cells are periodic in all three axes. Allowing the controller to step only to adjacent states limits the switching transients to small values compatible with analog and digital modulation [9]. These single step trajectories in state space are easy to incorporate into the control algorithm.

4.0 ADAPTIVE ALGORITHMS

The adaptation algorithms used with this antenna must be very simple. The intended application is small, battery powered equipment where size and power consumption must be minimized. There is no active processing (gain or

conversion) of the input signals before combining and the receiver itself provides evaluation of the combined signals. Two algorithms have been simulated and compared for use in this application, a direct search [7] and a newly developed, chaotic-cycle-tracking (CCT) routine.

The direct search is a simple routine in which the receiver samples all eight adjacent states and then switches whenever the criterion (signal strength, S/N, C/I, etc.) of any one of them exceeds that of the present state. This requires extensive sampling and is slow. However, it works well at low fading rates [9]. At higher fading rates, even this simple algorithm exceeds the capacity of the control hardware.

This study demonstrated that often multipath propagation has chaotic [10] rather than stochastic [3] characteristics. The existence of chaotic limit cycles has been demonstrated for many different environments by field measurement, Fig. 7, and computer simulation, Fig. 8. For each simulated physical path of the antenna, the "most traveled" closed path through state space was identified and showed the chaotic characteristic. This chaotic nature can be exploited allowing the use of a fast algorithm.

The chaotic-cycle-tracking (CCT) algorithm is fast because memory is used to model the environment and maintain an estimate of the

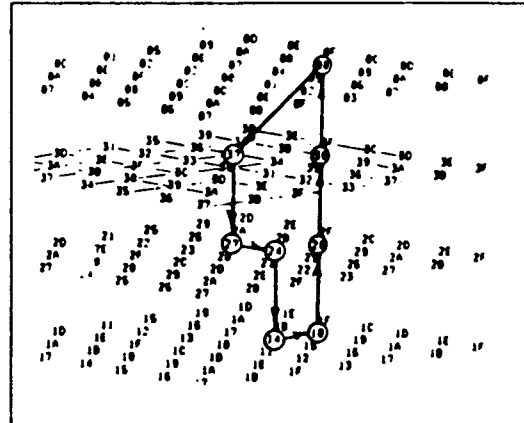


Figure 7. Limit Cycle from Measurements.

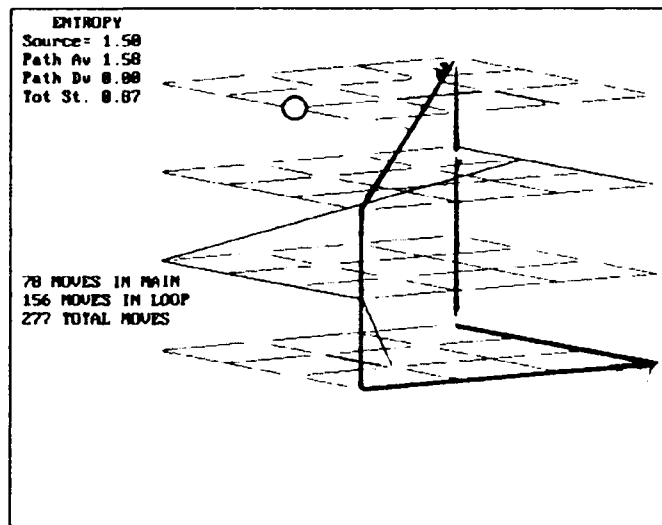


Figure 8. Limit Cycle from Simulation.

best next state for each present state. The system is modeled as a Markov chain [11, 12, 13] with a non-stationary transition matrix. The transition matrix is sparse and each row contains only two values, one on the major diagonal and the other in one-of-eight possible positions (adjacent states). The position of the latter is determined by the greatest element of the criteria benefit vector (CBV) for that state. The transitions occur when the criterion of the present state falls below a standard. If the switching is beneficial, then the new state is continued until the value of the criterion decreases. If the switching is detrimental, then the opposite adjacent state is selected.

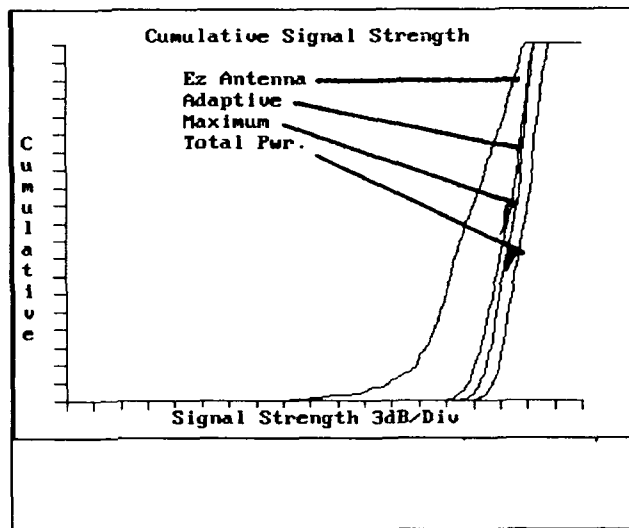


Figure 9 CDF of Antenna.

A criteria benefit vector (CBV) of length 8 is maintained for each of the 64 states of the antenna. The essence of the adaptive algorithm is the method of updating the elements of the CBV's. Each time the antenna changes state, the change in the value of the criterion is used to update the vector element, V_{ij} by

$$V_{ij} = (1 - \alpha_i) V_{ij} + \alpha_i (O_{j_i} - O_i)$$

where $0 < \alpha_i < 1$

O_i - output in state i

and O_{j_i} - output in state j
after transition from state i

(18)

The value of α_i is important as it is the "forgetting factor" [14, 15] of a self tuned regulator (STR) adaptive system. The value of α_i is a function of the Kolmogorov-entropy (K-entropy) [10] of state i .

All calculations are done while waiting for the delay caused by the IF filter of the receiver and the A/D conversion. The switching then occurs without having to do significant calculations because the next state is estimated while measurements are being done. This estimate is based on the past history of benefit or loss of this transition.

A series of the most beneficial estimates predict a closed path in state space [16, 17] while the antenna traverses the environment. This path is only an estimate of the ideal instantaneous path which shows wandering or chaotic behavior in most environments. This predicted closed path is defined as the limit cycle.

The use of the concept of chaos to describe the multipath environment is a departure from conventional thought. It requires an entropy value. The entropy of the system is the sum of the K-entropy for each state. One method of obtaining the entropy is to estimate the transition probabilities from a histogram. The histogram is only available during simulations and is not available during real-time operation of the algorithm. Another method of estimating the entropy is from the variance of the benefit of the criteria. This is available during real-time operation of the algorithm.

Those states with high entropy are steering states where the system may select quite different paths [18, 19, 20]. If the entropy of a state is low, then the next state is consistent. The forgetting factor for each state is made a function of the entropy of that state as estimated from the variance of the benefit to the criterion.

The variance for each element of the CBV's needs to be stored in addition to the value itself. If a single byte is used to store these variables, then the system can be defined within 1 K-Byte of memory. This is within the capability of low-cost, low current, CMOS controllers.

5.0 Results - Antenna Performance

The performance of the antenna is measured in the form of a cumulative distribution function of signal strength, see Fig. 9. This shows the overall effectiveness in reducing the multipath fading. For any particular probability level, e.g. 5%, the advantage can be expressed in dB of signal strength. This dB advantage can be used in any other part of the system, e.g. lower transmitter power. The advantage of the antenna is shown in Table 3. The benefit is that relative to an E-field antenna.

Difference in Signal Levels Relative to an E-Field Antenna when Fades Occur Five Percent of the Time				
Environment	Combining Algorithm			
Source Entropy	Maximal Ratio	Equal Gain	Direct Search	Cycle Track
0.5	11.5 dB	9.6	8.6	8.5
1.0	11.5 dB	9.6	8.6	8.3
1.5	11.5 dB	9.6	8.6	7.4
2.0	11.5 dB	9.6	8.6	6.4
2.5	11.5 dB	9.6	8.6	5.5
3.0	11.5 dB	9.6	8.6	3.2
4.0	11.5 dB	9.6	8.6	2.4
5.0	11.5 dB	9.6	8.6	1.5

Table 3. Benefit of the Adaptive Energy Density Antenna with Various Algorithms.

6.0 Conclusions

1. The energy density antenna is an effective receptor in a multipath fading environment. It is a single antenna structure which provides three independent outputs that can be selected or combined to provide a diversity gain of typically 12 dB. The entropy of the scattering environment determines the improved performance of energy density antenna relative to that of three independent antennas. For scattering environments with high entropy the performance is equivalent. For environments with low entropy the energy density antenna performance far exceeds that of three and approaches that of an infinite number of independent antennas.
2. A simple, phase only, 64-state antenna controller and combiner can be used with the energy density antenna and invokes a mean loss of performance of 1.9 dB resulting in a typical net diversity gain of 10 dB.

3. The scattering environment often produces fields that have chaotic characteristics when viewed in the state space of the energy density antenna. The periodicity of the fields becomes more apparent when viewed in three-dimensional state-space rather than in scalar time plots.
4. An adaptive algorithm which uses memory to retain an estimate the gradients and converge to a limit cycle is effective in a scattering environment. In many environments the penalty is less than 2 dB when compared with a continuous direct search algorithm. The benefits include operation at mobile vehicle speeds, reduced switching transients and low power consumption.
5. This algorithm can be run on very low-cost, low-power CMOS controller chips, such as the 68HC04, for antennas on moving vehicles at highway speeds. It is effective in systems with voice bandwidth channels at 900 MHz.

ACKNOWLEDGEMENTS

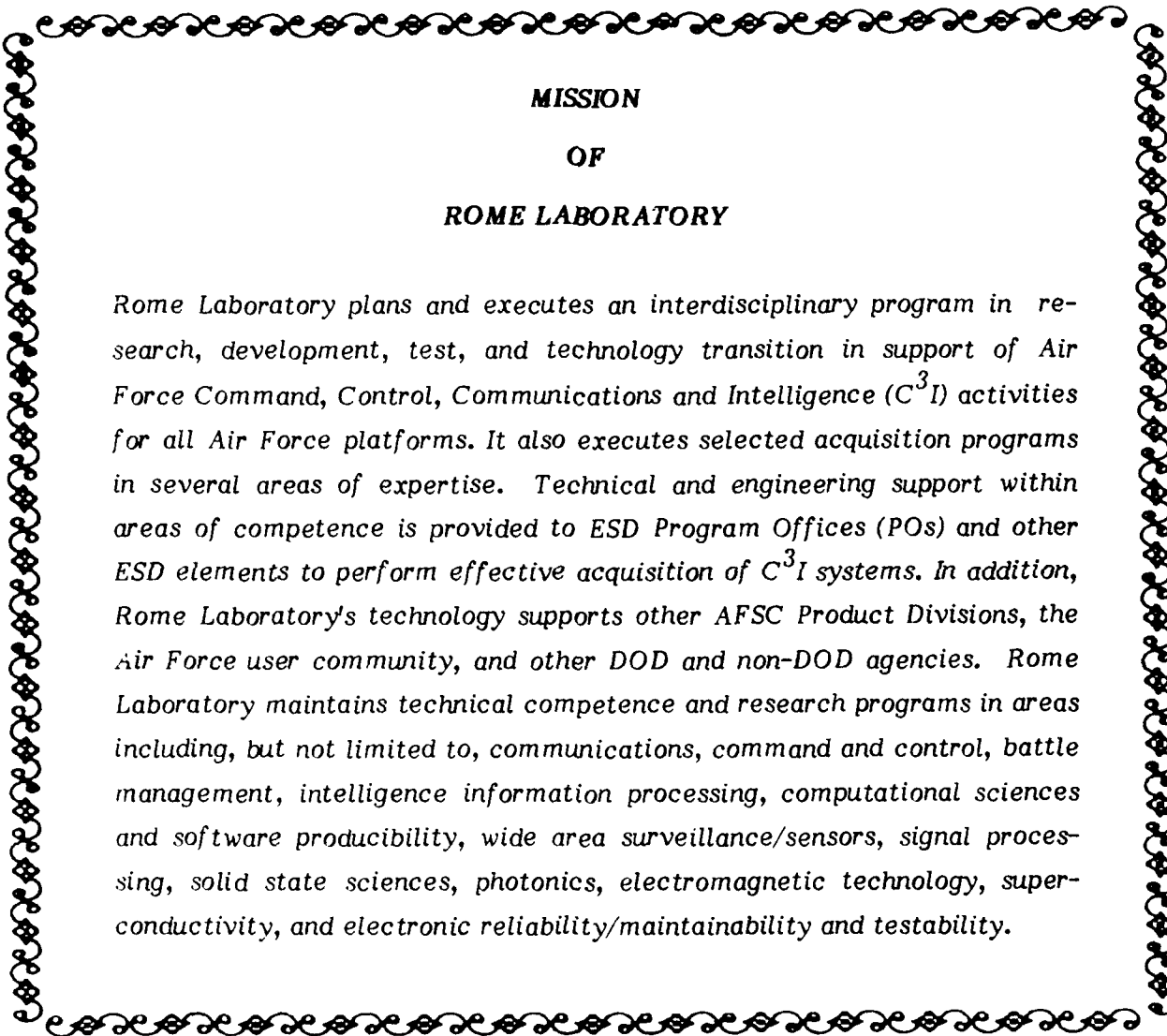
We wish to thank Dr. Peter Clarkson of Illinois Institute of Technology and Donald L. Linder and Albert Leitich of Motorola for their support on this project and Sharon Phillips for her proofreading contribution.

REFERENCES

1. Lee, William C. Y. (1967) An Energy Density Antenna for Independent Measurement of the Electric and Magnetic Field, *Bell System Technical Journal*, Vol. 46, no. 7, September, pp. 1587 -1599.
2. Lee, William C.Y. (1982) *Mobile Communications Engineering*, McGraw-Hill Book Co., New York.
3. Jakes, William C. Jr.(1974) *Microwave Mobile Communications*, John Wiley & Sons, New York.

4. Rothchild, V. (1986) Probability Distributions, John Wiley and Sons, New York.
5. Gilbert, E. N.(1965) Energy Reception for Mobile Radio, *Bell System Technical Journal*, Vol. 45, no. 8, pp. 1179-1803.
6. Shannon, C. E.(1929) A Mathematical Theory of Communication, *Bell System Technical Journal*, 379-423 (Part I), 623-656 (Part II).
7. Vaughn, Rodney G.(1988) On Optimum Combining at the Mobile, *IEEE Trans. VTG*, Vol. 37, No. 4, pp 181-188.
8. Wilkenson, E. J. (1960) An N-Way Hybrid Power Divider, *IRE Trans*, Vol. MTT-8 pp. 116-118.
9. Meravi, Denise, et al. (1988) Results of Experiments Using an Adaptive Antenna in a 256 Kbps In-Building Data Transmission System, Motorola Internal Report.
10. Rasband, S. Neil (1990) *Chaotic Dynamics of Nonlinear Systems*, John Wiley and Sons Inc., New York.
11. Freedman, David (1971) *Markov Cha.* Holden-Day, San Francisco.
12. Wheeler, Richard M. and Kumpati S. Narendra (1985) Decentralized Learning in Finite Markov Chains, *Proceedings 24th Conf. on Decision and Control*.
13. Milito, Rodolfo A. and J. B. Cruz, Jr. (1985) An Optimization-Oriented Approach to the Adaptive Control of Markov Chains, *Proceedings 24th Conf. on Decision and Control*.
14. Favier, G. and A. Smolders (1984) Adaptive Smoother-Predictors for Tracking Maneuvering Targets, *Proceedings 23rd Conf. on Decision and Control*.
15. Chalam, V. V.(1987) *Adaptive Control Systems Techniques and Applications*, Marcel Dekker, Inc., New York.

16. Goucem, A. and D. P. Atherton (1986) Limit Cycles in Nonlinear Discrete Systems, Proceedings 23rd Conf. on Decision and Control.
17. Wang, Qinghong and Jason L. Speyer (1987) The Periodic Riccati Differential Equation and the Periodic Regulator, Proceedings 26th Conf. on Decision and Control.
18. Gleick, James (1987) Chaos - Making a new Science, Viking Press, 40 West 23rd St, New York.
19. Ralph H. Abram and Christopher D. Shaw (1984) Dynamics The Geometry of Behavior Part One: Periodic Behavior, 1984, Aerial Press Inc., Santa Cruz, Ca.
20. op. cit.(1984) Dynamics The Geometry of Behavior Part Two: Chaotic Behavior, 1984, Aerial Press Inc, Santa Cruz, Ca.



**MISSION
OF
ROME LABORATORY**

Rome Laboratory plans and executes an interdisciplinary program in research, development, test, and technology transition in support of Air Force Command, Control, Communications and Intelligence (C³I) activities for all Air Force platforms. It also executes selected acquisition programs in several areas of expertise. Technical and engineering support within areas of competence is provided to ESD Program Offices (POs) and other ESD elements to perform effective acquisition of C³I systems. In addition, Rome Laboratory's technology supports other AFSC Product Divisions, the Air Force user community, and other DOD and non-DOD agencies. Rome Laboratory maintains technical competence and research programs in areas including, but not limited to, communications, command and control, battle management, intelligence information processing, computational sciences and software producibility, wide area surveillance/sensors, signal processing, solid state sciences, photonics, electromagnetic technology, superconductivity, and electronic reliability/maintainability and testability.